5-2018

Extreme ultraviolet spectra of highly charged Y and Xe ions: line identification, diagnostic potential, and isotope shift

Roshani Silwal
Clemson University, rsilwal@g.clemson.edu

Extreme ultraviolet spectra of highly charged Y and Xe ions: line identification, diagnostic potential, and isotope shift

---

A Dissertation
Presented to
the Graduate School of
Clemson University

In Partial Fulfillment
of the Requirements for the Degree
Doctor of Philosophy
Physics

---

by
Roshani Silwal
May 2018

Accepted by:
Dr. Endre Takacs, Committee Chair
Dr. Chad Sosolik
Dr. Joan Marler
Dr. Mark Leising

Abstract

Highly charged ions have enhanced relativistic effects and compressed electronic wave functions, making their atomic transitions relevant in studies of fundamental atomic and nuclear properties. Accurate atomic data such as wavelengths, energy levels, and transition probabilities are vital to the plasma communities. We report the extreme ultraviolet spectroscopy (EUV) of highly charged yttrium and xenon ions that were produced and confined with an electron beam ion trap (EBIT). The EUV spectra from these ions were recorded with a flat-field grazing incidence grating spectrometer.

In the first part of this work, new and previously observed EUV spectral lines were identified corresponding to the L-shell and a few M-shell yttrium ions (Y^{26+} – Y^{36+}) in the wavelength range of 4 nm to 20 nm. The wavelength of the Li-like Y resonances, (2s - $2p_{1/2}$) and (2s - $2p_{3/2}$) and the Na-like D lines in Y, (3s - $3p_{1/2}$) and (3s - $3p_{3/2}$) were measured with an EBIT for the first time. The wavelength uncertainties of the identified transitions ranged between 0.0004 nm and 0.002 nm. Fifty nine spectral lines corresponding to Δ n = 0 transitions within the n = 2 and n = 3 shell were identified. Line identification was assisted by the collisional-radiative non-Maxwellian code NOMAD. A few magnetic-dipole lines were measured, and the potential application of these transitions in electron density and temperature diagnostics was analyzed.

In the second part of this work, we report a new method based on EUV spectroscopy of Na-like D transitions to measure the variation in mean square charge radii of Xe isotopes. The isotope shift of the Na-like D1 (3s - $3p_{1/2}$) transitions between ^{124}Xe and ^{136}Xe isotopes was measured and used to determine this variation by comparison with atomic structure

calculations. The calculations were performed using the Relativistic Many-Body Perturbation (RMBPT) and Multi-Configuration Dirac-Hartree-Fock (MCDHF) methods that were in excellent agreement with each other. The electron beam energy during the measurement was fixed at 6 keV. The difference in the mean-square charge radii, $\delta < r^2 >$ was determined to be 0.269(0.042) fm^2, which agrees well with previous measurements and a recommended value reported by [AM13]. The Mg-like ($3s^2$ - 3s3p) transitions were also employed to determine the differences in the mean square charge radii. Systematic studies of the measured shift were performed, providing confidence in the obtained results.

Dedication

This work is dedicated to my family. A special shout-out to my friend Nirmal Nischal and sisters Deepti Silwal and Dipika Silwal for their constant support and love.

Acknowledgments

I would like to thank the Department of Physics and Astronomy at Clemson University for their support throughout my degree. My sincere gratitude to advisor Dr. Endre Takacs for giving me an opportunity to work with him and conduct exciting research with multiple collaboration opportunities. I have learned a lot from him in past couple of years. His enthusiasm for research and hard work has always motivated me. He has always supported my work and encouraged me to learn new things. I want to thank my committee members Dr. Joan P. Marler, Dr. Chad Sosolik and Dr. Mark Leising for their suggestions and feedback that has continuously guided me in conducting my research. Special thanks to Dr. Marler for helping me build my resume and for providing great suggestions.

My research was funded by the Measurement Science and Engineering (MSE) Research Grant Programs of the Department of Commerce at the National Institute of Standards and Technology (NIST). I am grateful to Dr. Yuri Ralchenko at NIST for providing most of the theoretical data relevant to our work. He has constantly supported my work and taught me a lot about atomic structure and collisional/radiative processes in plasmas. His sense of humor, readiness to explain things in detail have made working with him a very fun and rewarding experience. I am thankful to Dr. Joan M. Dreiling from NIST for assisting me during experiments, data analysis and manuscript preparation. She is a very good friend and she has always helped and encouraged me. Her discipline for work and everything in life has always inspired me. Also, thanks to Dr. Dipti Goyal from NIST for her hard work and for providing calculations that assisted our measurements. I appreciate her help with writing and editing the theory section for my publications. I would like to

thank Dr. Tapasi K. Das for helping me in the calibration work during the beginning of my research work at NIST.

I express my gratitude towards collaborators Dr. John Gillaspy, Dr. Alain Lapierre, Dr. Gerald Gwinner, Dr. Antonio Villari, Dr. Alexandar Borovik Jr., for their valuable suggestions and feedbacks during data analysis and preparation of the manuscripts. In particular, Dr. Gillaspy and Dr. Lapierre have assisted me and encouraged me to perform more tests and ask more questions. I am grateful to Dr. Steven Blundell for providing calculations for Na-like Xe ions and Dr. Marianna Safronova for providing the theory for Ne-like Y ions. I would like to thank David Takacs for his help with the python code during the initial data analysis.

I am very gratified to have friends like Amy C. Gall and Samuel Sanders for the past few years. They have always helped me figure out both research related and not related problems. I want to thank them for helping me edit the dissertation. Amy constantly supported and motivated me to do better. I am very thankful for her friendship and all the good times. A big thanks to the Professional Enrichment Grant (PEG) at Clemson, which allowed me the opportunity to attend multiple conferences and workshops. This is a great effort conducted by the graduate school government and I hope it continues providing funding to students seeking opportunities as such in the upcoming years.

I am indebted to my parents and my sisters for believing in me and always encouraging me to pursue academia. The five year long journey has been hard since they weren't here with me, but their love and support has kept me going on. I feel lucky for everything I have been able to achieve. None would have been possible without them. Special thanks to Anamika Rimal for her friendship. Lastly, I want to thank my friend Nirmal Nischal for walking this journey with me and helping me out in everything possible. His belief in me and pushing me to work harder has always helped me a lot.

Table of Contents

List of Tables

List of Figures

Chapter 1

Introduction

1.1 Motivation

The electron beam ion trap (EBIT) is a small-scale laboratory device known for producing and trapping highly ionized plasmas. Most of the matter in the universe is highly ionized and the study of highly charged ions helps to unveil new information about the universe. The research of highly charged ions is of interest as they exist in numerous astrophysical systems such as active galactic nuclei and supernova remnants. In fact, our sun produces highly charged plasma known as the solar wind that interacts significantly with the earth's atmosphere. The study of highly charged ions is also of great importance to fusion device development. The EBIT allows for controlled laboratory studies of these highly ionized systems that experience extreme electric fields, an effect that is amplified for atoms with increasing nuclear charge. These systems also exhibit enormous potential energies (of the order of keV) that increases with the nuclear charge. This is because more energy is required to remove more electrons from an atom. Electric potentials of similar order can be applied with an EBIT, allowing for the successful creation and confinement of such highly charged systems.

The slit-like EBIT plasma makes this device suitable for spectroscopic measurements of the radiation emitted by the plasma in various wavelength regions. The highly charged

Table 1.1: Z dependence of the probabilities of different atomic structure effects along the hydrogen isoelectronic sequence. E1 is the electric dipole transition, M1 is the magnetic dipole transition, E2 is the electric quadrupole moment, E1M1 is the two-photon E1+M1 process and QED stands for quantum electrodynamics. From [ZH12].

E1 (Δ n = 0)	Z
E1 (Δ n $\neq$ 0)	Z^4
M1 (Δ n = 0)	Z^3
M1 (Δ n $\neq$ 0)	Z^6
M1 (within fine structure)	Z^{12}
E2 (Δ n = 0)	Z
E2 (Δ n $\neq$ 0)	Z^6
E2 (within fine structure)	Z^{16}
2E1	Z^6
E1M1	Z^6
Hyperfine Splitting	Z^3
QED effect	Z^4
Parity violation	Z^5

.

ions are also relativistic in nature, magnifying the effects of quantum electrodynamics (QED) and parity-violations for high Z species. Given the extreme electric fields, highly charged ions provide unique tests of the limits of QED. [Gil10]. The dependence of various atomic structure effects in highly charged systems with increasing Z along the hydrogen isoelectronic sequence is shown in Table 1.1 [ZH12]. Details of this dependence in highly charged systems is given in Chapter 3.

The scientific need of spectroscopic data of the highly charged ions is therefore imperative. Studies of these plasmas can provide a better understanding of the dominant physical processes that occur within the plasma [RDT$^+$08]. Fusion devices, such as tokamaks, contains highly charged impurities of different trace elements resulting in emissions in various wavelength regions. Such radiation from contaminating ions can lead to significant negative effects on the performance of fusion plasma devices, such as power loss. The electron density, rotation velocities, temperature, and impurities transport are some of the parameters necessary to characterize the plasma. The study of the spectral lines that are radiated from the plasma can be used to determine such parameters. Spectroscopic research represents an invaluable diagnostic tool for fusion device development in the hopes of pro-

ducing a sustainable, clean energy source. For instance, detailed studies of the radiation from highly charged tungsten has been conducted recently due to its relevance in tokamaks such as ASDEX [BR09] and ITER [RDT$^+$08]. The significance of highly charged ions in energy diagnostics relies on the behavior of forbidden transitions in highly ionized systems. As seen from Table 1.1, the forbidden magnetic-dipole M1 transitions are strong in highly charged plasmas and the intensity ratio of such transitions to the allowed electric dipole E1 transitions can be used to deduce plasma temperatures and densities.

Scientific research can be limited by the lack of atomic data as this leads to difficulties in the proper identification of processes. Figure 1.1 shows the available atomic data for the elements in the periodic table. The color index represent the number of lines present in the atomic spectra database with the blue color being non-available data. The amount of unavailable atomic data is significant and depicts the need for more spectroscopic measurement of the higher charged states of these elements. Furthermore, complex atomic models that are used to fit the atomic spectra require verification of the theoretical data from laboratory measurements. Measurements of atomic data in multi-electron ions can provide benchmark tests of the existing theoretical framework.

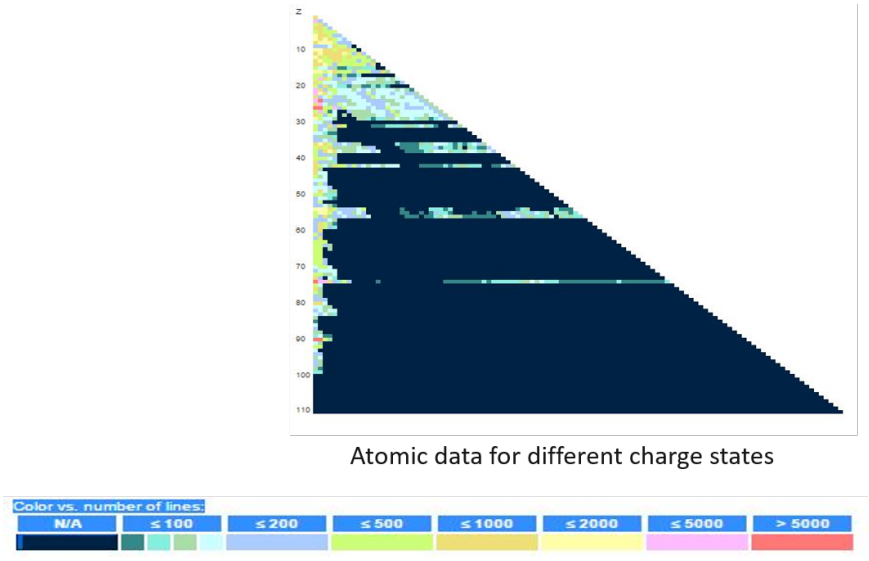

Figure 1.1: Available atomic data for different charge states. From [ASD].

Atomic spectroscopy played a significant role in the discovery of quantum mechanics. The discovery of Bohr's atomic model, Einstein's photoelectric effect, and Planck's black-body radiation were key to the concept of quantization. In highly charged high-Z systems, the study of atomic transitions can reveal information about not just the atomic structure, but the nuclear structure as well. The transitions in highly charged systems become highly sensitive to the presence of the finite nucleus size. This is due to the reduced size of the atom and the strong overlap of the electronic orbitals with the nucleus. As a result, atomic transitions of high-Z highly charged ions can be a good probe of nuclear properties such as mass and size of the nucleus. In a recent study of of Na-like D transitions by Gillaspy *et al.* [GOR$^+$13], the authors reported that the uncertainty in the theoretical transition energy is dominated by the uncertainty in the value of the nuclear charge radius, suggesting that the atomic transitions of the Na-like systems are sensitive to nuclear size. In their work, the authors also highlighted the use of Na-like D transitions to provide a test of QED to 0.4 %.

Nuclear charge radius is a key nuclear parameter that carries information about the nuclear structure. For radioactive elements with Z higher than Bi (Z = 83), no experimental absolute nuclear charge radii have been reported except for U and Th. This is because most of these elements are unstable and the conventional electron scattering [Hof56] and muon spectroscopy [FBH$^+$95] methods require large quantities of the element. There are other methods that have been used for relative nuclear radii measurement such as K_α spectroscopy [BBH65], optical laser spectroscopy (OLS) [LRS07], x-ray spectroscopy [EBC96], and dielectronic recombination measurements [SLM$^+$05, BKM$^+$09]. However, there are regions in the chart of nuclides where both absolute and relative nuclear charge radii measurements are missing. This only substantiates the importance of new methods for the measurement of the absolute and nuclear charge radii. The OLS method in particular, is experimentally very precise. However, the difficult atomic structure calculations of the complex atomic configurations for neutrals or singly charged ions can contribute to systematic offsets in the extracted value of the relative nuclear radii. A new method to determine the

nuclear radii for radioactive isotopes would provide more data of the measured radii values. These data are necessary to calibrate the atomic structure calculations and therefore complements the optical measurements.

The EBIT facility at NIST has been used to perform spectroscopic measurements over the past two decades. The device is capable of creating high charge states of practically all the elements. NIST EBIT is very well suited for atomic spectroscopy because of its slit-like plasma source. In addition, various high efficiency and moderate to high resolution spectrometers are installed to the observation port in different wavelengths regions. The current research is mainly focused on exploring the spectral lines in the EUV region and makes use of the flat-field grazing incidence grating EUV spectrometer installed at one of the observation port of the NIST EBIT. The EUV spectrometer employs reflection grating with increased groove spacing. The grazing incidence geometry of the spectrometer enhances the reflectivity. The EUV spectrometer therefore provides high counting statistics with a moderate resolution and is significant in spectroscopic measurements in the EUV region. Previous measurements in the EUV region performed at NIST consist of a wide variety of studies of different elements of which we list a few here [ORGR12, GDR$^+$09, RRP$^+$07, FSO$^+$07, PGRR14].

In the first part of this work, we have continued similar measurement with the mid-Z element yttrium with an atomic number of 39. The study of yttrium was motivated by its relevance in tokamaks such as the the Joint European Torus (JET) tokamak [JMD90], Texas Experimental tokamak (TEXT) [SKIR89, RKS$^+$87], and the Princeton Tokamaks [Hin76, HBC$^+$86, SHC$^+$82]. Moreover, it can be seen from Fig. 1.1 that the atomic data for highly charged yttrium is missing in the atomic database. With this measurement, the EUV spectral lines corresponding to the Li-like Y through Al-like Y transitions were identified. Identification of unknown features and previously known features can provide tests of accuracy of theory. The study of magnetic dipole transitions that are amplified in highly charged plasmas can provide diagnostic studies of the plasma parameters.

In the preceding paragraphs, the use of atomic transitions to extract information

of the nuclear structure was discussed. The necessity for a new method to determine the nuclear charge radius of radioactive isotopes was highlighted and the sensitivity of the Na-like D transitions to nuclear size was explored. Driven by these rationale, we developed a new method based on EUV spectroscopy of the Na-like D transitions between the Xe isotopes ^{124}Xe and ^{136}Xe in the second part of this work. The method utilizes the advantage of the enhanced field shift effects in the Na-like systems in combination with the very accurate atomic structure calculations provided by the simplified quasi-hydrogenic electronic structure of these systems. The Na-like D transitions in particular are of significant interest as these transitions are very intense and can be easily created in an EBIT and recorded with the high counting statistics EUV spectrometer. Only two measured values of the relative nuclear charge radii $\delta < r^2 >$ for xenon isotopes have been reported. This measurement will provide a new value of $\delta < r^2 >$. Such data is necessary for the evaluation of the nuclear radii values for instance, the compilations conducted by Angeli *et al.* [AM13].

The outline of the dissertation is as follows. Chapter 2 contains the details of the atomic theory pertinent to this work. Highly charged ions and the Na-like systems are briefly described in Chapter 3. Chapter 4 contains the explanation of the collisional-radiative processes that occur in high-temperature plasmas, the model used to describe such processes and a brief description of plasma diagnostics using intensity ratios. The description of the electron beam ion trap design, operational details and the source of neutrals and singly charged ions in the device are presented in Chapter 5. In Chapter 6, we describe the spectrometers used during the data acquisition as well as discuss the spectral line shape and line broadening. Chapter 7 summarizes the results and data analysis of the investigation of highly charged yttrium. In this chapter, we describe the identification of new and known spectral features of the L-shell ions and a few M-shell ions of highly charged yttrium (Y^{26+} - Y^{36+}). We expand the discussion to the use of the line intensity ratios of the identified magnetic-dipole and electric-dipole transitions as a potential tool to diagnose the electron density and temperature. In Chapter 8, the measurement of the isotope shift of the Na-like D transitions between xenon isotopes ^{124}Xe and ^{136}Xe is presented. We

describe the use of this new method based on EUV spectroscopy in the determination of the difference in the mean square nuclear charge radii. Chapter 9 contains the conclusions and discussions pertaining to the study. Finally, the appendices include the publications, abstract of presentations at various conferences and the python script that were used for data analysis.

Chapter 2

Atomic Structure

This chapter describes the theory of atomic structure and the description of the isotope shift. The details of the atomic theory are given in [Foo05, Gri97, Kun09, Ral16] and a summary of the methods relevant to this work is presented in this chapter.

2.1 Basic Considerations

An atom consists of a heavy positive nucleus surrounded by negatively charged electrons. This was demonstrated by Rutherford's experiment in 1911. He provided the analogy of the motion of the electrons around the central nucleus with the planetary motion. This interpretation did not make physical sense in regards to the stability of the atom, because the electrons in circular orbits undergo acceleration and would radiate and collapse to the nucleus eventually. In 1913, Bohr defined an atomic model by incorporating quantum mechanics to characterize the behavior of electrons around the nucleus. The idea of discrete energy levels was introduced to describe the quantization of the orbits. According to Bohr's model, the electrons revolve around the nucleus in discrete orbits and jump from one orbit to the other by radiating energy based on the quantization rule ($m_e vr = \mathrm{n}\hbar$). His model assumed the orbits to be circular. Sommerfield later applied this quantization to elliptical orbits, which was consistent with the special theory of relativity. The relativistic effects

were seen to cause differences in the energy of the elliptical orbits by an order of α^2 times the gross energy, ($E_n = -\frac{e^2/4\pi\epsilon_0}{2a_0}.\frac{1}{n^2}$). Here α is the fine-structure constant given by $\alpha = (e^2/4\pi\epsilon_0)/\hbar c$. The quantum mechanical description provided by Bohr-Sommerfield theory is applicable to classically treated electronic orbits, but fails to describe atoms with more than one electron. Bohr's model was extended to elements with higher Z by Moseley where the electronic charge e for the hydrogen atom was replaced by charge Ze for heavier atoms. His law defined that the frequency of the X-ray emitted by an atom is proportional to the square of the atomic number Z.

Proper quantum mechanical description of atoms was provided by Schrödinger in 1925 with the use of wave-functions. The wave functions carried much more information about the atoms and the radiated transitions, than just the energies. The solution to the Schrödinger equation resulted in eigen-energies that have dependence only on the principal quantum number n. This indicates that for different orbital quantum numbers l with same n, the energy levels are degenerate. The non-relativistic Schrödinger equation does not take into account the relativistic nature of the electrons. The relativistic effects are known to cause splitting of the energy levels termed as fine structure. To treat the fine structure, relativistic effects have to be introduced as a perturbation to the Schrödinger equation. Furthermore, Schrödinger equation includes only the spatial part of the electron wave function and does not include the spin part that is responsible for the fine structure.

The observation of fine structure in the hydrogen atom provided evidence of the existence of electron spin. This splitting of the spectral line was a result of the interaction of the spin and the orbital angular momentum. Another experimental evidence of the spin was provided by the anomalous Zeeman effect. It was Goudsmit and Uhlenbeck who first proposed the existence of an intrinsic property of an electron, later termed as spin angular momentum by Pauli. Paul Dirac in 1928 formed a relativistic generalization of Schrödinger equation that takes into account the spin and magnetic moment known as the Dirac equation. The solution to Dirac equation in a Coulomb potential gives the dependence of energy on n and total quantum number j. According to the Dirac equation, the levels

with different l but same n and j should have degenerate energy levels. Dirac equation therefore implemented the fine structure effect in its definition.

In contradiction to Dirac's formalism, an experiment conducted by Lamb and Rutherford in 1947 showed that the n = 2 shell in hydrogen atom have an energy separation between the levels 2s $^2S_{1/2}$ and 2p $^2P_{1/2}$. The 2p $^2P_{1/2}$ level was observed at lower energy than the 2s $^2S_{1/2}$ level. According to Dirac's energy relation, the levels with same n and j are degenerate. The separation in these energy levels could not be explained by the relativistic quantum-mechanical explanation of atoms and needed the inclusion of quantum electrodynamics (QED) in the explanation of the atomic structure. To define the atomic structure, QED corrections need to be included, which is mostly contributed by the self-energy (SE) and vacuum polarization (VP) effects. These corrections are of the order of $\alpha^5 Z^4 m_e c^2$, and are the leading QED corrections for the highly charged ions. When an electron emits and reabsorbs a virtual photon, the process contributes to SE. When a photon produces a virtual electron-positron pair in vacuum, it contributes to VP. Figure 2.1 shows the fine structure separation of the n = 2 and n = 3 shells of hydrogen and the allowed atomic transitions between these energy levels. When the nuclear magnetic moment is also included in the description of the atomic structure, the energy levels become further divided to the so-called hyperfine structure. The nuclear spin I combined with the total angular momentum j of the electrons leads to the hyperfine structure.

2.2 Hydrogen Atom

The development of quantum theory and the advancement in atomic spectroscopy began with the study of hydrogen atom. The Schrödinger equation and Dirac equation can be solved exactly for the hydrogen atom. The Schrödinger equation for a hydrogen atom with one electron is given by:

$$-\frac{\hbar^2}{2m_e} \bigtriangledown^2 + V(r)\psi = E\psi \tag{2.1}$$

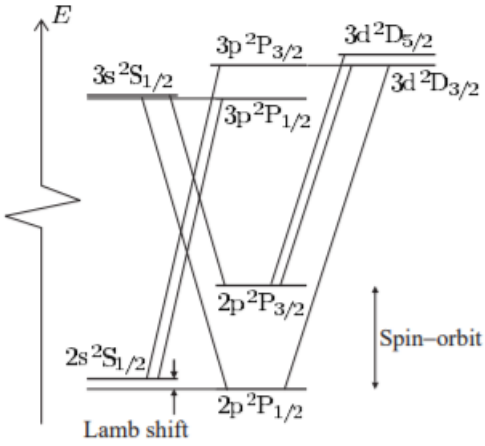

Figure 2.1: Fine structure of hydrogen atom for n =2 and n = 3 levels and the allowed transitions between the levels. From [Foo05].

The solution of the wave equation for a hydrogen atom in spherical coordinates is comprised of a radial part $R_{n,l}$ and an angular part $Y_{l,m}$. The resulting eigen-energies are of the form E = -$\hbar$ c R_∞ $1/n^2$. The solutions are standing waves for particular energies. When an atom interacts with the electromagnetic radiation it results in the transition between these stationary energy states governed by the selection rules. The selection rules are derived from the angular integral of the interaction.

Given a radiation defined by an oscillating electric field of the form:

$$E(t) =\mid E_0 \mid Re(e^{-i\omega t}\hat{e}_{rad}) \tag{2.2}$$

The Hamiltonian for the interaction of the electric dipole with the field E(t) is given by H = e$\mathbf{r} \cdot \mathbf{E(t)}$ and the transition rate, R for the interaction is approximately equal to:

$$R \propto \mid eE_0 \mid^2 \mid \int \phi_2(\mathbf{r} \cdot \hat{\mathbf{e}}_{\mathbf{rad}})\phi_1 d^3\mathbf{r} \mid^2 \tag{2.3}$$

This results in the angular integral component given by equation 2.4.

$$I_{ang} = \int_0^{2\pi} Y^*_{l_2,m_2}(\theta,\phi)\hat{r}\cdot\hat{e}_{rad}Y_{l_1,m_1}(\theta,\phi)\sin\theta d\theta d\phi \tag{2.4}$$

where, $\hat{e}_{rad}$ is the polarization vector, and $\hat{r}\cdot e_{rad}$ is the electric dipole operator that interacts with the oscillating electric field $\mathbf{E}$(t). The angular component $I_{ang} = 0$ unless the selection rules are satisfied. For π-transitions, where the polarization of the radiation is linear, the electric field component is along the z-axis and the selection rule is given by $\Delta\ m_l = 0$. For the σ-transitions, where the polarization is a superposition of two circular polarizations, the electric field is in the xy-plane and the selection rule is given by $\Delta\ m_l = \pm 1$. For an unpolarized light, the selection rule is given by $\Delta\ m_l = 0, \pm\ 1$.

Schrödinger wave equation is non-relativistic and the solution to the eigen-value equation resulted in energy that depends only on n. Dirac equation included the spin orbit interaction, which resulted in a solution given by .

$$E_{n,J} = m\left[1 + \frac{Z^2e^4}{(n-E_J)^2}\right]^{-1/2} \tag{2.5}$$

where,

$$E_J = J + 1/2 - \sqrt{(J+1/2)^2 - Z^2e^4} \tag{2.6}$$

This provided the energy dependence on both n and J.

2.2.1 Spin-Orbit Interaction

The magnetic moment due to the spin of the electron is affected by the orbital field and the interaction of the electron and the magnetic field. This interaction is caused by the electric field of the nucleus and results in the Hamiltonian of the form,

$$H = -\mu\cdot B = g_s\mu_B\mathbf{s}.\frac{\hbar}{m_ec^2}(\frac{1}{er}\frac{\partial V}{\partial r})\mathbf{l} \tag{2.7}$$

Here, B is the field experienced by moving electrons in an atom and μ is the magnetic moment of the electron due to its spin. Equation 2.7 doesn't include Thomas precession that leads to a splitting twice larger than the observed splitting. The spin-orbit interaction including the Thomas precession results in equation 2.8.

$$H = (g_s - 1)\frac{\hbar^2}{2m_e^2c^2}\left(\frac{1}{r}\frac{\partial V}{\partial r}\right)\mathbf{s}\cdot\mathbf{l} \tag{2.8}$$

where, the Coulomb potential is given by: $\frac{1}{r}\frac{\partial V}{\partial r} = \frac{e^2/4\pi\epsilon_0}{r^3}$. This results in the energy for the spin-orbit interaction of the form .

$$E = \frac{\hbar^2}{2m_e^2c^2}\frac{e^2}{4\pi\epsilon_0}\left\langle\frac{1}{r^3}\right\rangle\mathbf{s.l} \tag{2.9}$$

From the definition of total angular momentum, $\mathbf{j} = \mathbf{l} + \mathbf{s}$, we can write, $\mathbf{s.l} = \mathbf{j^2} - \mathbf{l^2} - \mathbf{s^2}$ = 1/2j(j+1)-l(l+1)-s(s+1). This results in the energy shift due to spin-orbit interaction given by equation 2.10.

$$E_{s-o} = \frac{\beta}{2}j(j+1) - l(l+1) - s(s+1). \tag{2.10}$$

The energy interval between levels $j = l + 1/2$ and $j = l - 1/2$, where the spin s =1/2 is then given by:

$$\Delta E_{s-o} = \beta(l + 1/2) = \frac{\alpha^2 hcR_\infty}{n^3 l(l+1)} = \frac{\alpha^2}{nl(l+1)}E(n). \tag{2.11}$$

2.3 Many-electron systems

For many-electron systems, the interaction potential is no more given by just the Coulomb potential V(r) as the interaction between electrons become important. So, the Hamiltonian will have an interaction term e^2/r_{ij} and cannot be solved analytically anymore. Brief overview of the theory of atomic structure in many-electron systems have been provided in the following subsections.

2.3.1 Non-Relativistic Atomic Structure

The Hamiltonian for N electrons around a nucleus for many-electron atoms can be written as:

$$H = H_{KE} + H_{electron-nucleus} + H_{electron-electron} + H_{spin-orbit} + ...$$

$$= \sum_{i=1}^{N} \frac{-\hbar^2}{2m} \bigtriangledown_i^2 - \sum_{i=1}^{N} \frac{Ze^2/4\pi\epsilon_0}{r_i} + \sum_{i>j}^{N} \frac{e^2/4\pi\epsilon_0}{r_{ij}} + H_{spin-orbit} + ...$$

A standard procedure to treat such systems is provided by the use of the central-field approximation. In this approximation, the majority of the electron-electron repulsion is attributed to arise from the the central potential S(r) assuming a spherical charge distribution of the core. The resulting interactions are also spherically symmetric in this assumption. The central-field potential can then be written as:

$$V_{CF}(r) = -\frac{Ze^2/4\pi\epsilon_0}{r} + S(r) \tag{2.12}$$

The Hamiltonian looks like equation 2.13 if we neglect the spin-orbit part .

$$H_{CF}(r) = \sum_{i=1}^{N} \frac{-\hbar^2}{2m} \bigtriangledown_i^2 + V_{CF}(r_i) \tag{2.13}$$

The N electron Schrödinger equation $H\psi = E\psi$ can be treated by N one electron Schrödinger equations of the form:

$$\frac{-\hbar^2}{2m} \bigtriangledown_1^2 + V_{CF}(r_1)\psi_1 = E_1\psi_1 \tag{2.14}$$

2.3.2 Relativistic Atomic Structure

Two methods of relativistic atomic structure calculations were used to determine the isotope shift of the Na-like, Mg-like and Al-like Xe ions. The calculations were performed by our collaborators Dr. Dipti Goyal and Dr. Steven Blundell. Here we present a brief

description of the atomic theory for the two methods.

2.3.2.1 Multi-configuration Dirac-Hartree-Fock (MCDHF) method

The multi-configuration method was implemented with the relativistic atomic structure GRASP2K package described in detail in references [JHFG07, JGR+17]. The Hamiltonian in the relativistic Dirac-Fock formalism can be written as:

$$H_{DC} = \sum_{i=1}^{N}(c\alpha_i.\mathbf{p}_i + V_{nuc}(r_i) + (\beta_i - 1)c^2) + \sum_{i>j}^{N} 1/r_{ij} \tag{2.15}$$

where, $\alpha_\mathbf{i}$, β_i are the 4 $\times$ 4 Dirac matrices, $\mathbf{p_i}$ is electron momentum operator, $V_{nuc}(r_i)$ is the extended nuclear charge distribution, and r_{ij} is the distance between i and j electrons. GRASP2K package was used to get the atomic state function (ASF) $\psi(\gamma PJM_J)$ assumed to be a linear combination of the configuration state functions (CSF) $\phi(\gamma_j PJM_J)$ written as:

$$\psi(\gamma PJM_J) = \sum_{j=1}^{N_{CSF}} c_j \phi(\gamma_j PJM_J) \tag{2.16}$$

Among the N CSFs, only the ones with same parity and angular momentum will contribute to the ASF. Here, the labels γ_j refer to the properties of the CSFs such as sub-shell quantum numbers and the occupancy of the orbitals. The CSFs are antisymmetric and coupled state functions given by the products of one-electron Dirac spinor, also known as Slater determinant. And c_i's are the expansion coefficients obtained from the solutions of the relativistic configuration interaction (RCI) problem $Hc = E\mathbf{c}$, H being the RCI matrix with elements:

$$H_{ij} =< \phi(\gamma_i PJM_J)|H_{DC}|\phi(\gamma_j PJM_J) > \tag{2.17}$$

Before doing the RCI module to obtain the final wave-function by including the contribution of Breit and QED contribution, we need the initial estimate of radial function that are done in extended optimal level (EOL) scheme. To include the relativistic QED effects, vacuum polarization, self-energy and Breit interactions that are necessary for the proper treatment

of the electron correlation effects, RCI calculations are used.

$$H_{DCB} = H_{DC} - \sum_{i<j}^{N} \left[\alpha_i.\alpha_j \frac{cos(\omega_{ij} r_{ij}/c)}{r_{ij}} + (\alpha_i.\bigtriangledown)(\alpha_j.\bigtriangledown) \frac{cos(\omega_{ij} r_{ij}/c) - 1}{\omega_{ij}^2/c^2} \right] \tag{2.18}$$

These calculations are based on the Dirac-Coulomb-Breit Hamiltonian given in equation 2.18 and was used with the GRASP2K package. The advantage of using this method is that it is computationally more efficient and can handle millions of CSFs.

2.3.2.2 Relativistic Many-Body Perturbation Theory (RMBPT)

The many-electron systems are complex due to the strong electron correlation effects that cannot be properly accounted for in the Dirac-Hartree-Fock (DHF) wave functions. The many-body perturbation theory (MBPT) does so by treating these effects as a perturbation to the DHF wave function. The complexity with this method increases with each order of MBPT. A description of the MBPT formalism has been provided by Avgoustoglou [AJP$^+$92]. To summarize the idea, a general way to treat electron correlations can be achieved by assuming that each electron moves independently in a central potential U(r) and the interaction can be treated as a perturbation to the central potential by setting H $= H_0$ + V, where,

$$H_0 = \sum_{i=1}^{N} hr_i + \sum_{i=1}^{N} U(r_i) \tag{2.19}$$

$$V = -\sum_{i=1}^{N} U(r_i) + \sum_{i<j}^{N} \frac{e^2}{r_{ij}} \tag{2.20}$$

where, h(r) = cα.$\mathbf{p}$ + βmc^2 + V$_{nuc}$(r) is the relativistic Hamiltonian. The negative energy terms are excluded from the atomic structure calculations. The solution for $H_0\psi_0 = E_0\psi_0$ is then given by anti-symmetric product of one particle wave functions. Both H_0 and V are written in quantized form in terms of the creation and annihilation operators and the Hartree-Fock potential is defined in terms of a Coulomb potential. The manipulation of these operators is used to determine the higher-order corrections to the energy. A new

diagrammatic approach was used to obtain an analytic formula of MBPT with the use of well-defined Feynmann diagrams, the details of which has been provided in references [JBS88b, AJP+92, GOR+13]. The RMBPT terms are built from perturbations to the DHF potential, where the electron-electron interaction consists of both the Breit and Coulomb interactions.

2.3.3 $LS-$ Coupling Scheme

The Hamiltonian for N electrons is defined by the sum of central field Hamiltonian, H_{CF} and the residual electrostatic repulsion Hamiltonian, H_{re}:

$$H = H_{CF} + H_{re} = \sum_{i=1}^{N} \Big[-\frac{\hbar^2}{2m} \bigtriangledown_i^2 + V_{CF}(r_i) \Big] + \sum_{i=1}^{N} \Big(\sum_{j>i}^{N} \frac{e^2/4\pi\epsilon_0}{r_{ij}} - S(r_i) \Big). \qquad (2.21)$$

When two electrons with orbital angular momentum $\mathbf{l_1}$ and $\mathbf{l_2}$ interact, the electrostatic repulsion between them results in the change in their individual orbital angular momenta, but the total angular momenta L given by $\mathbf{l_1} + \mathbf{l_2}$ remains conserved. This interaction leads to the the precession of $\mathbf{l_1}$ and $\mathbf{l_2}$ around the resultant $\mathbf{L}$. Similarly, the spin angular momentum of the two electrons $\mathbf{s_1}$ and $\mathbf{s_2}$ also precess around the resultant total spin angular momentum $\mathbf{S}$. The quantum mechanical operators L^2, L_z and S^2, S_z commute with H_{re}, and the quantum numbers L, M_L, S and M_S are the good quantum numbers for the Russell-Sanders coupling or LS coupling. The eigenstates of H_{re} is given by $|LM_LSM_S>$. The energy levels given by L and S are referred as terms and are given by ^{2S+1}L in LS coupling. The total orbital angular momentum, $\mathbf{L}$ and the total spin angular momentum, $\mathbf{S}$ then precess around the total angular momentum, $\mathbf{J}$.

The fine-structure in hydrogen arises due to the spin-orbit interaction that results in a shift of $E_{s-o} = \beta_{LS}$¡S · L¿. This leads to an energy interval between adjacent levels to be $\Delta E_{FS} = E_J$ - $E_{J+1} = \beta_{LS} J$. The spin-orbit interaction is added as a perturbation to the term ^{2S+1}L to describe the fine structure in LS coupling, and is valid when $E_{re} \ll E_{s-o}$, that is applicable for light atoms.

For equivalent electrons in LS coupling, the lowest-energy term is determined by the Hund's rule. There are three rules according to which the energy levels are arranged. The first rule requires that the term with the largest S value has the lowest energy. Second rule requires that for a given multiplicity, the level with largest L has the lowest energy. According to the third rule, for atoms with less than half-filled shells, the energy level with the lowest J has the lowest energy and in case of atoms with more than half filled shells, the energy level with largest J has lowest energy. For example, if we look at the $3p^2$ configuration of two electrons with angular momentums l_1=1, l_2=1, s_1=1/2, and s_2=1/2. The electrons couple to the total angular momentum values L of 0, 1 or 2 and S of 0 or 1. The terms corresponding to this configuration are given by ^{2s+1}L. For the $3p^2$ configuration in a silicon atom, the energy terms are therefore ^1S, ^1P, ^1D, ^3S, ^3P and ^3D. Since, the two electrons are equivalent they can only have the terms ^1S, ^3P, and ^1D due to Pauli's exclusion principle. These three terms are arranged according to the Hund's rule. Since, the highest S of 1 lead to the term ^3P, it will have the lowest energy. For S =0, the two terms possible are ^1S and ^1D. Since D has largest L, the term ^1D has lower energy than ^1S. For the term ^3P, lowest J has lowest energy. This can be seen from Table 2.1.

Table 2.1: Energies of the three terms for $3p^2$ configuration in silicon.

Configuration	**Term**	**J**	**Level (eV)**
$3s^2 3p^2$	^{3}P	0	0.0000000
		1	0.0095610
		2	0.0276679
$3s^2 3p^2$	^{1}D	2	0.7809579
$3s^2 3p^2$	^{1}S	0	1.9086586

2.3.4 $jj-$ Coupling Scheme

For heavy atoms, LS coupling is not a good approximation as E_{s-o} increases with Z and becomes scalable with E_{re}. In some cases E_{s-o} is even greater than E_{re}. This means that for heavier atoms, spin-orbit interaction has to be considered before the electrostatic repulsion. In this coupling scheme, **l** and **s** couple together to give the total angular mo-

Table 2.2: Selection rules for atomic transitions. From [sel].

Transitions		Electric dipole (E1)	Magnetic dipole(M1)	Electric quadrupole(E2)	Magnetic quadrupole(M2)
Rigorous rules	1	$\Delta J = 0, \pm 1$		$\Delta J = 0, \pm 1, \pm 2$	
		(J = 0 $\not\leftrightarrow$ 0)		(J = 0 $\not\leftrightarrow$ 0, 1; 1/2 $\not\leftrightarrow$ 1/2)	
	2	$\Delta M_J = 0, \pm 1$		$\Delta M_J = 0, \pm 1, \pm 2$	
	3	Parity changes	Same parity	Same parity	Parity changes
LS coupling	4	One electron jump	No electron jump	None or one electron jump	One electron jump
		$\Delta L = \pm 1$	$\Delta L = 0$, n = 0	$\Delta L = 0, \pm 2$	$\Delta L = \pm 1$
	5	$\Delta S = 0$		$\Delta S = 0$	
		$\Delta L = 0, \pm 1$	$\Delta L = 0$	$\Delta L = 0, \pm 1, \pm 2$	
		(L = 0 $\not\leftrightarrow$ 0)		(L = 0 $\not\leftrightarrow$ 0, 1)	

mentums $\mathbf{j_1}$ and $\mathbf{j_2}$ given by $\mathbf{j_1} = \mathbf{l_1} + \mathbf{s_1}$ and $\mathbf{j_2} = \mathbf{l_2} + \mathbf{s_2}$, respectively. In the $jj-$ coupling scheme, the individual $\mathbf{l}$ and $\mathbf{s}$ precess around $\mathbf{j}$ and the individual angular momenta, $\mathbf{j_1}$ and $\mathbf{j_2}$ are coupled to give the resultant momentum $\mathbf{J}$.

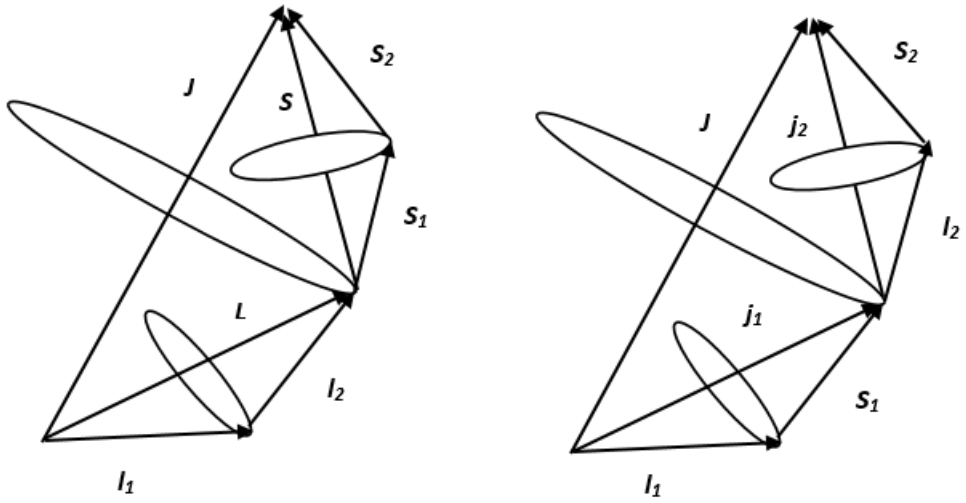

Figure 2.2: *LS*- coupling scheme (left) and *jj*- coupling scheme (right).

2.4 Isotope Shift

This section summarizes the details provided by Adriana Pálffy [Pál10]. Different isotopes of the same element (same Z) have a slight difference in the wavelengths of their

electronic transitions. This shift is termed as the isotope shift and it arises from the finite mass of the nucleus (the mass shift) and finite nuclear size (the field shift). Mass shift arises due to nuclear recoil corrections and is usually strong in light atoms. The field shift is due to different nuclear charge distributions in different isotopes and is large in heavy atoms as it scales as Z^5 or Z^6. As the electron wave-functions penetrate the nucleus, the field shift arises and this shift increases with the increase in the penetration. As a result, s orbitals have larger field shift compared to p and d orbitals [TSC+03]. The isotope shift for a specific atomic transition k for 2 isotopes with mass numbers A and A' is given by the sum of mass shift and field shift.

$$\delta\nu_k^{A,A'} = \delta\nu_{k,MS}^{A,A'} + \delta\nu_{k,FS}^{A,A'} \tag{2.22}$$

The review of various theoretical and experimental approach applied to evaluate this shift have been discussed by A. Palffy [Pál10].

2.4.1 Mass Shift

The nucleus is assumed to be infinitely heavy in most of the cases, but the nuclear motion or recoil needs to be considered for a better description of the system. This can be done in hydrogen-like ions, by considering the reduced mass, μ defined as:

$$\mu = \frac{mM}{m+M} \tag{2.23}$$

instead of electron mass, m_e in the Schrödinger equation. For many-electron systems, there is also a mass polarization term in the Schrödinger equation, given by:

$$-\frac{\hbar^2}{M}\sum_{i<j} \bigtriangledown_{\mathbf{r_i}} \cdot \bigtriangledown_{\mathbf{r_j}} \tag{2.24}$$

where i and j denote ith and jth electrons, respectively. The non-relativistic theory of the mass shift was developed by Hughes and Eckart in 1930 [HE30]. It consists of two parts:

normal mass shift (NMS) (one-body part) that comes from the inclusion of reduced mass and specific mass shift (SMS) (two-body part) that comes from the mass polarization shown in 2.24. The normal mass shift and the specific mass shift operator is given by 2.25 and 2.26 respectively.

$$H_{NMS}^{(nr)} = \frac{1}{2M} \sum_i \mathbf{p_i}^2 \tag{2.25}$$

$$H_{SMS}^{(nr)} = \frac{1}{2M} \sum_{i \neq j} \mathbf{p_i} \cdot \mathbf{p_j} \tag{2.26}$$

Here M is the nuclear mass and $\mathbf{p_i}$, $\mathbf{p_j}$ is the momentum operator for ith and jth electron. But the non-relativistic description applies only if we consider the nucleus to be point-like. The full relativistic theory for nuclear recoil can be formulated only within quantum electrodynamics [SAB$^+$94, Pal87]. Mass shift can be obtained within the lowest-order relativistic approximation ($\sim v^2/c^2$) and to the first order in (m/M) by evaluating the expectation of relativistic recoil Hamiltonian given by:

$$H_{RMS} = \frac{1}{2M} \sum_{i,j} \left[\mathbf{p_i} \cdot \mathbf{p_j} - \frac{Z\alpha}{r_i} \left(\alpha_\mathbf{i} + \frac{(\alpha_\mathbf{i}.\mathbf{r_i})\mathbf{r_i}}{\mathbf{r_i^2}} \right) \cdot \mathbf{p_j} \right] \tag{2.27}$$

Here, $\mathbf{p_i}$ and $\mathbf{r_i}$ represent the momentum and coordinate of i^{th} electron respectively. α is the fine structure constant and $\alpha_\mathbf{i}$ are the 4x4 vector Dirac matrices . Equation 2.27 can be split to one-body part (i=j) and two-body part (i $\neq$ j) such that the NMS and SMS are defined by equation 2.28 and 2.29 respectively.

$$H_{RNMS} = \frac{1}{2M} \sum_i \left[\mathbf{p_i}^2 - \frac{Z\alpha}{r_i} \left(\alpha_\mathbf{i} + \frac{(\alpha_\mathbf{i}.\mathbf{r_i})\mathbf{r_i}}{\mathbf{r_i^2}} \right) \cdot \mathbf{p_i} \right] \tag{2.28}$$

$$H_{RSMS} = \frac{1}{2M} \sum_{i \neq j} \left[\mathbf{p_i}.\mathbf{p_j} - \frac{Z\alpha}{r_i} \left(\alpha_\mathbf{i} + \frac{(\alpha_\mathbf{i}.\mathbf{r_i})\mathbf{r_i}}{\mathbf{r_i^2}} \right) \cdot \mathbf{p_j} \right] \tag{2.29}$$

Expectation value of equations 2.28 and 2.29 is used to evaluate normal mass shift

that takes into account the nuclear mass and the specific mass shift that takes into account the electron correlation respectively.

2.4.2 Field Shift

The nucleus is usually treated to be point-like with the nuclear potential of the form 1/r. However, the nucleus has a finite size and the actual nuclear charge potential is given by the proton distribution in the nuclear matter, which will be different from the electrostatic Coulomb potential, V(r) = -Ze^2/r. The isotopes of same elements have different neutron numbers, that leads to a slightly different nuclear charge distribution contributing to shift in their electronic energy levels. This shift is termed as volume or field shift. The energy shift can be written as

$$\delta\nu_{k,FS}^{A,A'} = F_k\lambda^{A,A'} \tag{2.30}$$

where, $\lambda^{A,A'}$ is a nuclear parameter that depends on the nuclear charge distributions of the isotopes and F_k is the electronic parameter proportional to the electronic density change at origin between lower and upper state for a transition k and is given by:

$$F_k = \frac{Z}{3\hbar}\left(\frac{e^2}{4\pi\epsilon_0}\right)\Delta \mid \psi(0)^2 \mid \tag{2.31}$$

Usually, the shift is approximated as:

$$\delta\nu_{k,FS}^{A,A'} = F_k\delta < r^2 >^{A,A'} \tag{2.32}$$

to extract the information of the difference in the mean nuclear charge radii of isotope A and A', defined by $\delta < r^2 >^{A,A'}$ [Ang04].

Equation 2.30 is an approximation that doesn't take into account the higher order of nuclear moments. To perfectly treat the system, one has to define the nuclear parameter,

$\lambda^{A,A'}$ as:

$$\lambda^{A,A'} = \delta < r^2 >^{A,A'} + \frac{C_2}{C_1}\delta < r^4 >^{A,A'} + \frac{C_3}{C_1}\delta < r^6 >^{A,A'} + ... \tag{2.33}$$

Here, C_1, C_2, C_3 .... are the Seltzer coefficients, and $\delta < r^4 >^{A,A'}$, $\delta < r^6 >^{A,A'}$ are the higher order nuclear moments. These higher nuclear terms are important for heavier nucleus as they can contribute to the total field shift significantly. Field shift can also be evaluated directly from the difference in the transition energies of the two isotopes. This method involves calculating the wave function for each isotope. The electronic F factor is usually deduced from the semi-empirical calculations by the Goudsmit-Fermi-Segré formula or through Dirac-Fock methods. F factor can also determined from King plot analysis [LRS07, FBH$^+$95].

As stated earlier, the nucleus is generally treated as point like. To accurately define the nucleus, proper choice of the nuclear distribution needs to be addressed. Several nuclear charge distribution models have been used to describe the atomic nucleus [Pál10]. The nucleus can be treated as a homogeneously charged sphere with a constant charge distribution of the form $\rho(\mathrm{r}) = 3\mathrm{Ze}/4\pi\mathrm{R}^3$, and the potential is defined by:

$$V(r) = \frac{Ze^2}{2R}(\frac{r^2}{R^2} - 3), r \leq R; -\frac{Ze^2}{r}, r \geq R \tag{2.34}$$

It has been noted [FBH$^+$95] that the optical transitions and K X-rays are sensitive to the mean square charge radii difference $\delta < r^2 >$ and the radial moments are defined as:

$$< K(r) >= \frac{1}{Ze}\int \rho_N(r)K(r)d^3r;\ < r^2 >= \frac{1}{Ze}\int \rho_N(r)r^2d^3r;\ < r^n >= \frac{1}{Ze}\int \rho_N(r)r^nd^3r \tag{2.35}$$

The radial moment $< r^2 >$ is the most significant part and the higher order moments do not contribute much. The root mean square charge (RMS) radius is therefore important and the nuclear size depends on this term. As a result, most experiments extract the value

of the RMS radius to determine the nuclear charge distribution.

An even better approximation for the nuclear charge distribution is given by a two-parameter Fermi model [JS85] defined as:

$$\rho(r) = \frac{\rho_0}{1 + e^{(r-c)/a}} \tag{2.36}$$

Here, c is the half density radius and a is related to the surface thickness as t = $4aln3$. In this work, t = 2.3 fm is assumed in the MCDHF calcualtions. The Fermi model defined by equation 2.36 considers a spherical nucleus. However, to include a deformation in the nuclear size, the Fermi model can be modified as [ZST$^+$84]:

$$\rho(r, \theta, \phi) = \frac{\rho_0}{1 + e^{(r-c)/a}} \tag{2.37}$$

where,

$$c = c_0 \left(1 + \sum_{l=1}^{\infty} \sum_{m=-1}^{l} \beta_{lm} Y_{lm}(\theta, \phi) \right) \tag{2.38}$$

In equation 2.38, β_{lm} are the nuclear multipole deformation parameters and Y_{lm} are the spherical harmonics.

Chapter 3

Highly Charged Ions

The study of atomic transitions from highly charged ions (HCI) is the primary interest of this work. A brief description of their properties is presented in this chapter, where the majority of this description is summarized from [Gil01].

3.1 Overview

When many electrons are stripped from an atom, the atom is ionized to a highly charged state. An HCI is defined as having an electronic charge Q $\gg$ 1. Multiply charged ions are classified as having values of Q ranging from 2 - 9, where the re-neutralization energy E_0 (described later in the text), is less than 1000 eV. For very highly charged ions, the electronic charge becomes large, further increasing the E_0 and Q/Z $\approx$ 1. For example, highly charge uranium with Q of 92 has the energy $E_0 \approx$ 750 keV citeGillaspy2001. Highly charged ions are systematically explored either along an 'isoelectronic sequence' or along an 'isonuclear sequence'. Along the isonuclear sequence, the value of the nuclear charge Z is fixed and the electronic number N (N = Z - Q) is varied. Along the isoelectronic sequence, the number of electrons N is fixed and the nuclear charge Z is varied. This sequence begins at the nuclear charge Z = N+1 and goes up with increasing Q.

The increase in Q brings the electron cloud into a tighter bound configuration thus

reducing the size of the atom. For one-electron ions, the Bohr radius of an atom scales as R $\approx$ 1/Z. For an isoelectronic sequence, the spatial extent of the electronic wave function (size) of the one-electron ions scale as R $\approx$ 1/(Q+1) $\approx$ 1/Q. The extent to which the size of a neutral atom shrinks as it gets ionized can be seen by comparing the size of a neutral nickel atom to a hydrogen-like nickel ion as seen in Figure 3.1. A hydrogen-like nickel ion has 27 electrons removed from its core such that the spatial extent of the wave function for this ion will be $\approx$ 27 times smaller than a neutral hydrogen atom. A drastic reduction in the Bohr radius can lead to changes in the physical properties of the HCI compared to that of the corresponding neutral atom.

As the atom changes from its neutral state to a highly charged state, the classical quantum mechanical description of its behavior does not accurately describe the system. In a neutral state, the electrons in an atom orbit the nucleus at large distances from the nucleus. This distance is also larger than the Compton wavelength of the electron (at this wavelength, the photon energy is same as the rest mass energy of the particle) for neutral atoms. For an electron, the Compton wavelength (h/mc) is nearly 2 pm. As the atom gets highly charged, the Bohr radius that scales as R $\approx$ 50/Z pm becomes smaller than the Compton wavelength. At such length scales, effects such as vacuum polarization become significant and quantum field theory becomes apparent in describing the heavily charged systems.

Highly charges ions have a more compressed wave function density than a neutral atom due to their reduced size. An illustration of this can be provided by comparing a neutral U atom to a H-like U ion. The H-like U also known as U^{91+} has nearly 100 times spatially compact wave function compared to the neutral U. Even in heavy neutral atoms, compression of the wave-function occur for inner shell electrons, and the electron experiences the closeness of the nuclear charge. This is evident by comparing the probability density for a valence s-electron in neutral and HCIs, where the probability density scales as Z^3 for neutral atoms and as Z^5 for HCIs [Gil01]. The significant difference in probability density for HCIs allows for parity-violation experiments. Parity violation effect is caused by the

mixing of wave functions with different parities due to the weak interaction of nucleus and the electronic orbitals [ZH12]. The measurements of parity-violation studies with highly charged systems combined with their simplified atomic structure can be used to test the Standard Model that does not explain the parity non-conservation in weak beta decay.

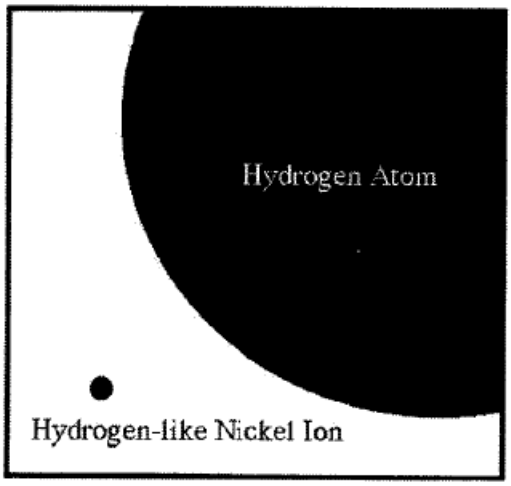

Figure 3.1: Relative spatial extent of wave-function of a hydrogen atom versus hydrogen-like nickel atom. From [Gil01].

HCI's have enhanced kinetic energy, a factor Q times larger than singly charged ions accelerated over a potential difference of V given by $1/2\mathrm{m}v^2 = \mathrm{QV}$. So even at moderate voltages, the kinetic energy of the ions can be much larger for a highly charged system. There are two different notions about potential energy in regards to HCIs: ionization energy and neutralization energy. The ionization energy is the energy required by an atom to lose one electron, and this energy increases as the ion charge increases. The increase of the ionization energy required to remove subsequent electrons naturally occurs as the remaining bound electrons experience more of a binding force from the nucleus. The scaling for the ionization energy with respect to the nuclear charge is Z^2 as $\mathrm{U(Z)} \approx \mathrm{Z/R} \approx \mathrm{Z/(1/Z)} = Z^2$. The neutralization energy E_0 is the energy released while replacing all the missing electrons. This energy is the sum of the ionization energies [Gil01]. As a result, E_0 increases further due to the addition of all the ionization energies that scale as Z^2. This scaling of the

ionization energy and the neutralization energy provides a sense of the enormous potential energy of the ion with the increase in the ion charge. A singly charged Ar (Ar^{1+}) has a potential energy of about 16 eV whereas a fully stripped argon ion (Ar^{18+}) possesses about 14 keV of potential energy.

The scaling of the energy separation between energy states in highly charged ions also depends on Z, hence affecting the photon energy emitted from these ions. The energy separation for states with Δ n =1 (n is the electronic shell) comes from Coulomb potential and scales as Z^2. For fine-structure levels with Δ n = 0, the scaling is given by Z^4 for the electric dipole transitions, termed E1. This scaling law for E1 transitions arises from the relativistic nature of the HCI and is given by the third term in the relativistic energy equation 3.1.

$$E = \sqrt{p^2c^2 + m_0^2c^4} \approx m_0c^2 + \frac{p^2}{2m_0} - \frac{p^4}{8m_0^3c^2} \tag{3.1}$$

As the orbital angular momentum of the electron $l = r \times p$ remains fixed for a given n, momentum p increases with radius r. This leads to the Z^4 dependence in the energy separation. Due to this dependence, the photon energies during transitions shifts towards shorter wavelengths with the increase in the nuclear charge. The extreme increase in photon energies for HCIs is shown in Figure 3.2. Figure 3.2 shows an example of the changing photon wavelengths for the resonance lines ($1s^2$ – 1s2p) and lines from metastable levels (1s2s - 1s2p) of He-like ions. The hyperfine splitting caused by the interaction of electrons and the nuclear magnetic moment is also amplified in HCIs due to the magnetic field generated by the electronic charge at the nucleus. The scaling of Z^3 for the hyperfine interactions arises from the inverse R^3 dependence of the field that follows from the Biot-Savart law. This scaling shifts the photon wavelength in HCIs moving it to the optical regime. This shift allows one to perform spectroscopy with EBITs as well as high-resolution laser spectroscopy and accelerator facilities to accurately determine the hyperfine splitting, unearthing information about the electronic structure of the HCI. Moreover, such precise measurements have opened up possibility of nuclear structure studies. [BOS+98, CBSW96]

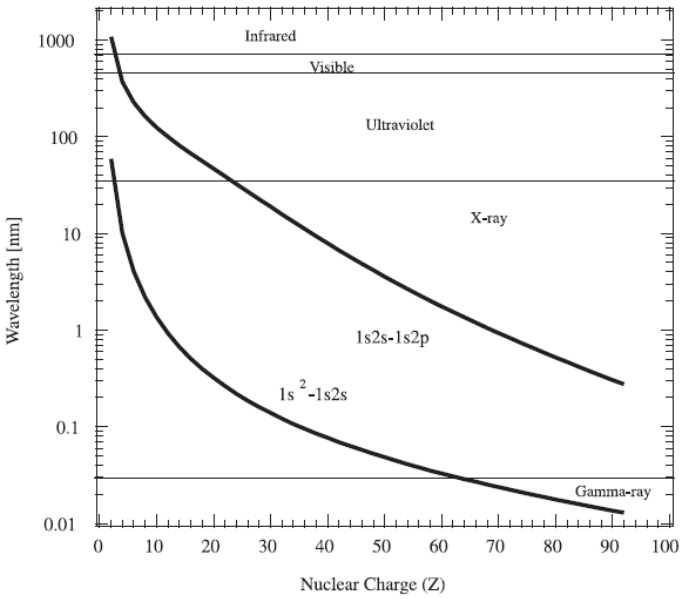

Figure 3.2: Dependence of photon wavelength (nm) with nuclear charge Z for the $1s^2$ – 1s2s (lower) and 1s2s – 1s2p (upper) transitions of He-like ions. From [Gil01].

As the ion loses more electrons, the core electrons experience very strong electric fields that scale as Z^3 [Gil01, Gil10]. This Z^3 scaling of the electric field follows from Coulomb's law and for a one-electron ion such as a hydrogen-like ion, it is given by equation 3.2 [Gil10]:

$$E = \frac{1}{4\pi\epsilon_0}\frac{Ze}{(n^2 a_0/Z)^2} = \frac{(Z\alpha)^3}{n^4}\frac{(mc^2/e)}{(\lambda/2\pi)} = \frac{Z^3}{n^4}(5 * 10^{11})[volts/meter] \tag{3.2}$$

Here, a_0 is the Bohr radius, ϵ_0 is the permittivity of free space, e is electron charge, α is the fine structure constant, m is the electron mass, c is the speed of light in vacuum, and λ is the Compton wavelength of the electron. For a H-like U ion, the electric field is $\approx 10^{17}$ Vm^{-1}, almost 7 orders of magnitude larger than the electric field in neutral H. In general, the Z^3 scaling for the electric field is due to the direct increase of the ion charge with the associated Z and the inverse scaling of the Bohr radius with Z. Properties such as this make HCIs a very good candidate to test strong field quantum electrodynamics effects [GMR85].

For neutral atoms, the outer electron coupling is by electrostatic interactions between the electrons and is described by LS coupling [Cow81]. This coupling description must be modified for HCIs due to the large mixing of states with different quantum numbers. The relativistic effects such as the spin-orbit interaction grow as Z^4, while the electron-electron interactions scale as Z^2. This indicates that the spin-orbit interaction cannot be ignored and and the $j-j$ coupling scheme must be adopted. This is due to the coupling of the spin and orbital angular momentum of the electron. Therefore, the total angular momentum of the electrons j must be used to describe the electron-electron interactions.

While effects like spin-orbit interaction and the hyperfine splitting increase with the nuclear charge, other effects decrease with increasing Z. The Zeeman effect caused by external magnetic fields has no dependence on Z in the first order and $1/Z^2$ dependence in the second order, since the relativistic spin-orbit interaction is much stronger than the external magnetic field. The Stark effect, caused by the external electric field, also decreases with increasing Z. The scaling of the Stark effect comes from the scaling of the electric dipole moment (q $\times$ r) that arise from the polarization of the electron cloud in the presence of external electric field. Since r $\propto$ 1/Z, this effect is inversely proportional to Z in the first order approximation.

An important effect that inversely scales with Z is the lifetime of the excited states, which depends inversely on the line width of the emitted spectra. Since the excited levels in HCIs have shorter lifetimes compared to neutral atoms, the energy distribution of the emitted radiation increases from the Heisenberg uncertainty principle $\Delta E \Delta t \geq \hbar$. The line intensity is also effected by the ionization of atoms. The otherwise forbidden transitions become much stronger in HCIs. The scaling of the probability of magnetic dipole M1 transitions is Z^6 for Δ n =0 transitions. The increase in the intensity of the forbidden transitions is caused by different effects. The spin forbidden transitions is caused by the mixing of wave function of states with different spins. This mixing occurs as a result of the strong spin-orbit interaction that scales as Z^4. Different selection rules become applicable for the forbidden transitions. These selection rules are summarized in Table 2.2.

Highly charged ions can be created by multiple atomic processes such as electron-impact ionization, muon-induced ionization, and photo-ionization. These ions not only interact with the neutral background atoms but also self-interact, producing several collisional and radiative processes. The details of these processes are described in detail in Chapter 4. The importance of HCIs in the study of fundamental and applied atomic physics provided the impetus to develop laboratory devices to investigate these systems in a controlled environment. Perhaps the leading laboratory apparatus to investigate highly charged plasma is the EBIT. The details of the EBIT are described in Chapter 5.

3.2 Na-like Systems

An important class of highly charged ions are the Na-like ions. The ion that has all electrons stripped but eleven of its core electrons gives rise to Na-like ions. Na-like systems have been extensively investigated both theoretically and experimentally [Gil10, GOR+13]. The electronic ground-state configuration of Na-like system is $1s^2 2s^2 2p^6 3s^2 S_{1/2}$. Due to the presence of one valence electron around the Ne-like closed shell, these systems are quasi-hydrogenic in nature. These systems have two very practical benefits: (1) simplified atomic structure that allows for precise atomic-structure calculations and (2) easy to make in EBIT.

An electron in a H-like system experiences a pure Coulomb potential defined by equation 3.3 with a corresponding binding energy given by equation 3.4.

$$V(r) = -\frac{Ze^2}{r} \tag{3.3}$$

$$E_n = -\frac{Z^2}{n^2} R_y \frac{1}{1 + m_e/M}; \tag{3.4}$$

Here, R_y is the Rydberg energy, Z is the nuclear charge, and m_e and M are the electron and nuclear masses, respectively. A simple H-like system can be properly defined by 3.4 where the binding energy depends only on n. The ground state energy of a H atom is

≈ -13.6 eV. This description of a single Coulomb potential produced by the nucleus fails for multi-electron systems as the electric and magnetic interactions between electrons becomes significant. In many-electron systems, the outer electrons experiences an effective Coulomb potential due to the screening by the core electrons. This potential can be approximated by an effective potential, V_{eff}(r) that asymptotically approaches the pure Coulomb potential at distances close to and far from the nucleus as shown in equations 3.5 and 3.6.

$$V_{\text{eff}}(r) \approx -\frac{Ze^2}{r}; r \to 0 \tag{3.5}$$

$$V_{\text{eff}}(r) \approx -\frac{(Z-N+1)e^2}{r} \approx -\frac{Z_{\text{eff}}e^2}{r}; r \to \infty \tag{3.6}$$

An exception to this are the alkali atoms such as Li, Na that have one valence electron around the bound core. Since the n dependence of the binding energy results in degenerate energy levels, this approximation cannot be applied to atoms with more than one electron. To better represent the degeneracy of the energy in alkalis, they can be treated as a simple one-electron system with the energy levels modified from 3.7 by including an additional dependence on the orbital quantum number l, such that:

$$E_{n,l} = -\frac{R_y}{n_{\text{eff}}^2}\frac{1}{1+m_e/M} \tag{3.7}$$

Here, n_{eff} is the effective quantum number given as (n - $\Delta(n,l)$), where $\Delta(n,l)$ is the quantum defect that depends on both n and l. This defect is very large for s electrons and decreases for increasing values of l. The penetration of the orbitals with the core of the Na atom for different l values is shown in Figure 3.3. Here, the n = 1 and n = 2 shells form the core and the overlap of the valence electron in n = 3 shell is shown for the Na atom. The 3s electrons are more bound to the nucleus than the 3p and 3d electrons. Similarly, the valence electron in the Na-like ion outside the Ne-like core has a strong overlap of the s and p orbitals with the nucleus due to the proximity of the electron shells with the nucleus.

The hydrogenic nature of this system makes the atomic structure calculations very precise for such systems. As a result, Na-like systems can be used as a good probe of nuclear properties, such as nuclear charge radius. Gillaspy *et al.* studied transition energies for Na-like ions suggesting that the transition energies of these ions are sensitive to the finite nuclear size [GOR+13].

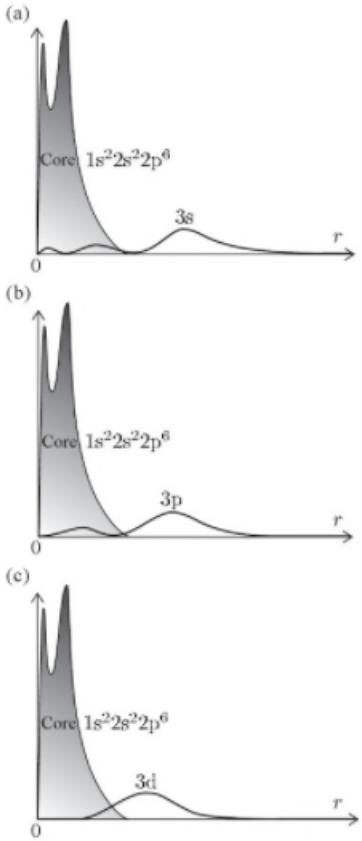

Figure 3.3: Probablity density of electrons in sodium atom for 3s, 3p and 3d configurations. From [Foo05].

The relevance of the study of Na-like gold to perform tests of QED also has been highlighted by Gillaspy *et al.* [Gil10], where they show that the field given by equation 3.2 for n=3 shell of Na-like Au (Z=79) is equal to the electric field strength in a 2 peta watt laser focused to 500 nm diameter spot. At such extreme electric fields, the vacuum polarization effect becomes significant. Access to experiments that can create strong electric

fields can be used to provide tests of QED. An analogy of the field strength in a Na-like Au with that of the intensity of the 2 peta watt laser show that Na-like Au ions can be used to explore quantum vacuum by producing higher or comparable fields to that of powerful lasers available today. The test of QED can be performed by the measurement of the transition energy as the transition energy shifts due to QED effects such as self energy (SE) and vacuum polarization (VP). The advancement in the calculations of QED effects as well as other higher order relativistic effects combined with the experimental precision offered by HCIs allows for such tests. In general, a fractional test of QED is conducted by defining a dimensionless parameter R defined by $R_{QED} = \delta/\text{QED}$ [GOR$^+$13]. Here, δ is the quadrature sum of the experimental and theoretical uncertainty and QED is the theoretical SE and VP values. The higher the experimental precision and the theoretical accuracy, the better is the test. Gillaspy *et al.* [GOR$^+$13] reported a QED test of 0.4 % from the measurement of the transition energies for Na-like Bi ions. The transition energies of the Na-like D transitions have been measured for several elements and measurements as such aim to provide benchmark tests of theoretical calculations [GDR$^+$09, GOR$^+$13].

Chapter 4

Elementary Atomic Processes in High-Temperature Plasmas

4.1 Collisional-Radiative Atomic Processes in Plasmas

The interaction between electrons, ions and radiations can result in multiple atomic processes. These processes are either radiative or collisional in nature. Brief description of different atomic processes that occur in high-temperature plasmas is given below [BS03].

4.1.1 Electron impact excitation

When a free electron collides with an ion X^{q+} and excites the ion to $[X^{q+}]^*$ state, the process is called electron-impact excitation. The energy of the free electron reduces from E1 to E2 and the process is followed by spontaneous decay of the excited ion resulting in a photon emission.

$$X^{q+} + e^- \rightarrow [X^{q+}]^* + e^- \tag{4.1}$$

4.1.2 Electron-impact ionization

When a free electron collides with a ion X^{q+}, it can ionize the ion to $X^{(q+1)+}$ if its energy (E1) is greater than the binding energy (IE) of the bound electron and releases an

additional electron with energy E2. This process is called electron-impact ionization.

$$X^{q+} + e^- \rightarrow X^{(q+1)+} + e^- + e^- \tag{4.2}$$

4.1.3 Three-body recombination

The inverse process of electron-impact ionization occurs when two free electrons combine with the ion X^{q+} resulting in $X^{(q-1)+}$. This process is called three-body recombination and is important in high density and low-temperature plasmas. For EBIT plasmas, this effect is very small and is neglected during calculations.

$$X^{q+} + e^- + e^- \rightarrow X^{(q-1)+} + e^- \tag{4.3}$$

4.1.4 Photo-excitation

Photo-excitation occurs when a photon is absorbed by an ion X^{q+} resulting in an excited ion $[X^{q+}]^*$. The energy of the absorbed photon is equal to the transition energy between the two states. The process is followed by a spontaneous decay where the excited ion decays by releasing a photon.

$$X^{q+} + \hbar\omega \rightarrow [X^{q+}]^* \tag{4.4}$$

4.1.5 Photo-ionization

This process occurs when the photon interacts with an atom $X(q)$ or an ion X^{q+} ionizing it to X^{q+} and $X^{(q+1)+}$, respectively, with an ejection of an electron. For photo-ionization or photo-effect to occur, the energy of the photon needs to be larger than the ionization energy (IE) of the bound electron. The resulting free electron will have an energy equal to $\hbar\omega$ - IE.

$$X^{q+} + \hbar\omega \rightarrow X^{(q+1)+} + e^- \tag{4.5}$$

4.1.6 Radiative recombination

Radiative recombination is a process that occurs when an electron recombines with an ion X^{q+} resulting in a lower charged ion $X^{(q-1)+}$ and emission of a photon. This is the inverse process of photo-ionization. The free electron is captured to a bound state of the ion and the resulting photon will have its energy given by the sum of the binding energy and the energy of the free electron.

$$X^{q+} + e^- \rightarrow X^{(q-1)+} + \hbar\omega \tag{4.6}$$

4.1.7 Dielectronic capture

When an electron is captured by an ion X^{q+} with simultaneous excitation of a bound electron, then the two-step process is called the dielectronic capture. If the doubly-excited state decays by radiative de-excitation of one of the excited electron, it results in dielectronic recombination (DR) as shown in 4.7. When the excess energy from de-excitation of one electron is not released by a photon emission but is instead transferred to the other excited electron such that it becomes free, the process is called auto-ionization (AI) given by equation 4.8. This is a resonant process.

$$X^{q+}(\gamma_0) + e^- \rightarrow [X^{(q-1)+}(\gamma_1, nl)]^{**} \rightarrow X^{(q-1)+}(\gamma_2, nl) + \hbar\omega \tag{4.7}$$

Here, γ_i (i = 0,1,2) shows the electronic core configurations that are involved.

$$X^{q+}(\gamma_0) + e^- \rightarrow [X^{(q-1)+}(\gamma_1, nl)]^{**} \rightarrow X^{q+}(\gamma_2) + e^- \tag{4.8}$$

4.1.8 Resonant scattering

If the dielectronic capture is followed by the auto-ionization process instead of radiative decay, then it leads to resonant scattering.

$$X^{q+}(\gamma_0) + e^- \rightarrow [X^{q+}(\gamma_1, nl)]^{**} \rightarrow [X^{q+}(\gamma_2)]^* + e^- \tag{4.9}$$

4.1.9 Bremsstrahlung

When the electron decelerates in the Coulomb field of an ion, it leads to release of continuous radiation termed as Bremsstrahlung.

$$X^{q+} + e^-(E_0) \rightarrow X^{q+} + e^-(E_1) + \hbar\omega \tag{4.10}$$

4.1.10 Charge exchange

When an atom Y collides with an ion X^{q+} , electron capture or a charge exchange process occurs resulting in another ion $X^{(q-1)+}$ and Y^+.

$$X^{q+} + Y \rightarrow X^{(q-1)+} + Y^+ \tag{4.11}$$

4.2 Collisional-Radiative Modeling in Plasmas

When the velocity distribution of plasma parameters is given by a Maxwell function, the Maxwell-Boltzmann distribution is used to describe the energy level population of the plasmas. Such distribution can well describe high electron density plasmas in local thermodynamic equilibrium (LTE). However, for low electron density plasmas such as fusion plasmas or laboratory plasmas (EBIT plasmas), the Maxwell-Boltzmann distribution is not applicable to determine the plasma ion populations. Rate equations that take into account important physical processes affecting low density plasmas are used to determine the level populations of ions in these plasmas. The processes important in highly charged

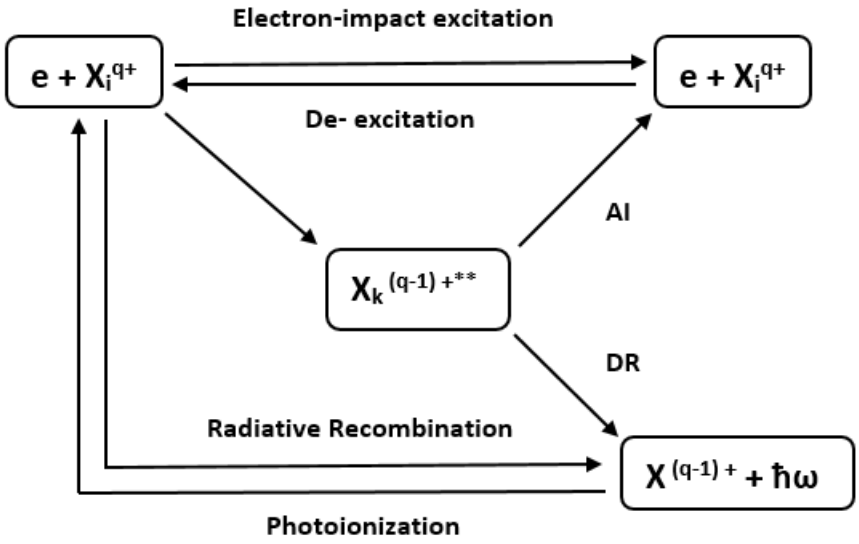

Figure 4.1: Different atomic processes in plasmas. AI and DR stand for autoionization and dielectronic recombination, respectively. Radiative decay is not shown in the diagram. From [BS03].

plasmas are electron impact excitation, deexcitation, electron impact ionization, radiative recombination, dielectronic recombination, autoionization, charge exchange and radiative decay. A collisional-radiative model suitable to the distribution of the plasma is employed in modeling the plasmas. The collisional-radiative modeling for the EBIT plasmas in our work is carried out using the non-Maxwellian collisional-radiative code (NOMAD). NOMAD produces synthetic spectra of the highly charged ions that helps in straightforward identification of the measured spectral lines.

4.2.1 Non-Maxwellian Code (NOMAD)

NOMAD was developed to obtain spectroscopic data for plasmas with an arbitrary electron energy distribution by Yuri V. Ralchenko and Yitzhak Maron [RM01]. The details of the CR model presented below follows from the reference [RDO+11]. To summarize their model, NOMAD is used to solve the inhomogeneous differential rate equations of the form:

$$\frac{d\hat{N}}{dt} = \hat{A}(N_i, N_e, f_e, t)\hat{N}(t) + \hat{S}(t) \tag{4.12}$$

Here, $\hat{A}(N_i, N_e, f_e$,t) is the rate matrix that depend on the ion density N_i, electron density N_e, and the electron-energy distribution function (EEDF) f_e(t). $\hat{N}$(t) is the vector of the atomic state populations and $\hat{S}$(t) is the source function. Electron density is given by the sum of the background electron density N_e^0(t) and the density of the continuum electrons that originate from ionization. The EEDF typically used to model EBIT plasmas is a Gaussian function having a full-width half maximum (FWHM) of 40 eV. The processes taken into account during the modeling include all the excitation, de-excitation, ionization, recombination, charge-exchange processes including the auto-ionization and dielectronic capture process. The time dependent simulation of the EBIT plasma shows that the plasma reach steady state distribution in fraction of secs. The ions are trapped for a few seconds during the measurement. Therefore, a steady-state distribution is assumed to model the EBIT plasma, which results in the rate equation given by:

$$\hat{A}(N_i, N_e, f_e, t)\hat{N}(t) = 0 \tag{4.13}$$

Solution of this rate equation provides the level populations for the atomic states and the intensities of the transitions can be derived from these level populations. The detailed form of equation 4.12 can be written as [RDO$^+$11]:

$$\sum_{j>i} N_{z,j}(A^{rad}_{z,ij} + n_e R^{dx}_{z,ij}) + \sum_{j<i} N_{z,j} n_e R^{ex}_{z,ij} + \sum_k n_e R^{ion}_{z-1,ki} + \sum_k n_e R^{rr}_{z+1,ki} + \delta_{i1} n_0 R^{CX}_{z+1} -$$
$$N_{z,i}\left(\sum_{j<i}(A^{rad}_{z,ji} + n_e R^{dx}_{z,ji}) + \sum_{j>i} n_e R^{ex}_{z,ji} + \sum_k n_e R^{ion}_{z,ki} + \sum_m n_e R^{rr}_{z,mi} + \delta_{i1} n_0 R^{CX}_z \right) = 0.$$

Here, $N_{z,i}$ is the atomic state population of an ion z in state i, n_e is the electron density, n_0 is the neutral density, $A^{rad}_{z,ij}$ is the radiative transition probability, $R^{dx}_{z,ij}$, $R^{ex}_{z,ij}$, $R^{ion}_{z-1,ki}$, $R^{rr}_{z,mi}$, and R^{CX}_z are the rate coefficients for de-excitation, excitation, ionization, radiative

recombination, and charge-exchange between neutrals and ions, respectively. Other recombination processes such as dielectronic recombination and three-body recombination are neglected for the EBIT plasmas.

The atomic data such as the wavelengths, energy levels, transition probabilities, cross sections, etc. required by the CR modeling code were produced by Flexible Atomic Code (FAC). FAC is based on the fully relativistic Dirac equation and is used to model various radiative and collisional atomic processes in plasmas. The detailed description of the atomic theory employed by FAC and the applications of the package have been presented by M. F. Gu [Gu08]. FAC was developed by M.F. Gu using a relativistic configuration interaction (CI) method with independent basis wave-functions derived from a local central field. The atomic structure, radiative rates, oscillator strengths and cross sections for different atomic processes can be calculated using FAC. In the model, the energy levels are determined by diagonalizing the relativistic Dirac-Coulomb Hamiltonian. The electron impact excitation and ionization cross-sections are determined by the use of the relativistic distorted wave (DW) approximation [Gu08].

4.3 Plasma Diagnostics from Line Ratios

To diagnose the plasma parameters such as plasma temperature, plasma density and dynamics, different techniques can be applied. While measuring these plasma properties directly with material probes can be very difficult and in some cases impossible, several spectroscopic methods have been implemented to do so. One of the important methods for plasma diagnostics involves the use of the ratio of allowed and forbidden atomic transitions in the determination of the plasma properties. Spectral line intensity ratios can be used to gather information about the temperature and/or density of the plasma. In cases involving highly charged ions, the ratio of forbidden magnetic-dipole transitions to the allowed electric-dipole transitions has been used to determine the electron density and temperature [RRP$^+$07, RDO$^+$11]. This method is suitable for such systems because the

magnetic-dipole transitions scale with Z^3 for Δ n = 0 transitions and Z^6 for $\Delta n \neq 0$ as seen from Table 1.1.

The basic idea of diagnostic potential comes from the following arguments. The line intensity of a spectral line is given by:

$$I_{ij} = N_j A_{ij} E_{ij} \tag{4.14}$$

where, N_j is the upper level population (cm^{-3}) (depends on plasma properties), A_{ij} is the transition probability (Einstein coefficient) (s^{-1}), and E_{ij} is the photon energy (eV). The collisional excitation rate is given by:

$$R_{ij} = N_p \int v \sigma_{ij}(v) f_p(v) dv \tag{4.15}$$

where, N_p is the projectile density (cm^{-3}), v is the relative velocity (cm/s), and σ_{ij} is the cross-section (cm^2). For electric dipole transitions, the steady state distribution is given by:

$$N_o n_e \sigma v = N_u A_a \tag{4.16}$$

Here, A_a represents the transition probability of allowed transitions, N_u and N_o represents the upper level and lower level population, respectively. From equations 4.14 and 4.16, we can infer that:

$$I_{ij} = N_o n_e < \sigma v > E_{ij} \tag{4.17}$$

Equation 4.17 is valid for both allowed transitions and forbidden transitions at lower densities where radiative decay is the dominant process. This implies that both allowed and forbidden transitions show a linear dependence with n_e, and as a result, their ratio is independent of the electron density. As the electron density increases, levels depopulate both radiatively and through collisions, such that the steady state distribution for forbidden

transition is given by:

$$N_o n_e < \sigma v >= N_u(A_f + n_e < \sigma_u v >) \tag{4.18}$$

$$\frac{I_f}{I_a} = \frac{(A_f + n_e < \sigma_u v >)}{A_a} \tag{4.19}$$

From the relation 4.19, it can be seen that at low densities, $n_e < \sigma_u v >$ can be neglected such that $\frac{I_f}{I_a}$ has no n_e dependence. However, at higher densities, the collisional rates become comparable with the transition probabilities of the forbidden transition A_f, and we can no longer neglect the term $n_e < \sigma_u v >$. Hence, the ratio between the intensities shows dependence on the electron density. The range of sensitivity depend on the transitions involved and it usually spans over one to few orders of magnitude density range.

Chapter 5

Electron Beam Ion Trap

5.1 EBIT Design and Operation

An electron beam ion trap is a small-scale laboratory device used to create and trap highly charged ions. Evgenii Donets and his co-workers [Don83] demonstrated the operation principles of the electron beam ion source (EBIS). The first EBIT was developed by Levine *et al.* [LMH$^+$88] based on similar working principle with modifications for the ion trap part. EBIS/T can be used to store ions for a large amount of time and are able to produce higher charge states of virtually every element in the periodic table. An intense, high-density (on the order of 10^{11} - 10^{12} cm^{-3}) electron beam is accelerated towards the trapping region, which consists of 3 cylindrical drift tubes biased to different voltages. The difference between the potential of the electron gun and the drift tube regions is what causes the electrons to accelerate towards the ion trap. The positive bias of the end drift tubes makes trapping of the ions possible. The trap length is around 1 m for EBIS and about 2-3 cm for EBIT. A magnetic field of a few teslas, generated with the use of a super-conducting magnet, is used to confine the electron beam to a diameter of less than ≈ 100 μm. For example, the NIST EBIT has a trap length of 2 cm and magnetic field of nearly 3 T and the Clemson EBIT has a trap length of 20 cm and magnetic field of 6 T. EBITs are comprised of three sections: the electron gun, trap, and collector region. A schematic diagram of a

generic EBIT is shown in Figure 5.1 [Gil99].

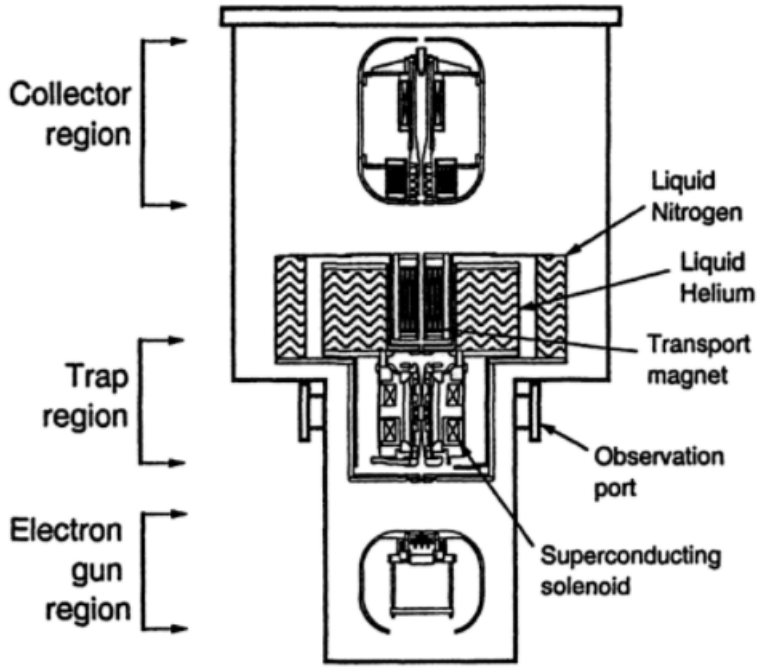

Figure 5.1: Generic EBIT schematic diagram. From [Gil99].

5.1.1 Electron Gun Assembly

Thermionic emission of electrons from a high perveance electron gun with a convex spherical cathode doped with barium oxide results in a high-energy, high-current density electron beam. The electron gun in most EBIT configurations has a potential near the laboratory earth. The cathode is desired to be at zero magnetic field, so that electrons can be directed towards the trap region and high density compression can be achieved. As a result, the cathode is shielded from the superconducting magnet's field by a soft-iron housing that encloses a bucking coil to cancel any residual field present at the gun region. The gun region has focus, anode and snout electrodes that are used to fine-tune the electrostatic field, create the initial field in the cathode and to match the beam to the field outside the gun, respectively. The electron beam current is set by varying the anode

voltage. The minimum attainable radius of the electron beam, if there is zero magnetic field at the cathode is given by 5.1. New EBIS-SC devices such as the Clemson EBIT (CUEBIT) have an electron gun that can be floated to a potential of - 6 kV. The electron gun assembly for this device does not have a coil to cancel the fringe magnetic field.

$$r_h[\mu m] = 260\sqrt{\frac{r_c[cm]}{B[T]}\sqrt{KT_c[eV]}} \tag{5.1}$$

Here, r_h is the 80 % beam radius given by Herrmann theory [Her58], r_c is the cathode radius, KT_c is characteristic electron temperature at the cathode, and B is the magnetic field at the cathode. This gives nearly 33 μm beam radius for the typical EBIT parameters.

5.1.2 Drift Tube Assembly

The trap region consists of 3 sets of cylindrical drift tubes positively biased with respect to the laboratory earth, such that the bias to the central drift tube determines the electron beam energy. The electron beam has some space charge, which results in the decrease of the actual electron beam energy. The trapping of ions in the central drift tube region is allowed by the positive bias of the two outer electrodes with respect to the central drift tube. The trap region is surrounded by the super-conducting magnet of few teslas. The magnet is cooled by different cooling systems (liquid helium in NIST EBIT) to allow for the production of ultra-high vacuum (UHV). UHV is needed in EBIT to maintain the higher charge states of the ions. Clemson EBIT uses a closed cryocooler system that saves money and resources. The magnetic field of the superconducting magnet compresses the electron beam to higher current densities. To allow for UHV, the internal EBIT parts are made from vacuum compatible materials such as copper and stainless steel. The DREEBIT GmBH based CUEBIT has a drift tube that can be floated to up to 20 kV such that the electron beam energy given by the potential difference between the electron gun and drift tube region can be up to 26 kV [TKB$^+$15]. The trap length of the CUEBIT is 20 cm, much longer than the typical 2 - 3 cm trap length of other EBITs. As a result, the CUEBIT can

be used as an efficient ion source, while still having the ability to act as a trap.

5.1.3 Collector Assembly

The collector is maintained at a few kV bias with respect to the cathode. As the electrons pass the trap region towards the collector, they decelerate and expand since the magnetic field is not as intense in this region hitting the collector with an energy of ≈ 3 keV. Transport coils are used to enhance the expansion of the electron beam so that it spreads out to hit the collector. To ensure that the secondary electrons emitted from the collector are trapped and reflected back to the collector, suppressor electrodes are used. These electrodes are negatively biased with respect to the collector and are installed between collector and the collector assembly's entrance. The collector surface heats up by the impact of electrons and therefore the whole assembly is cooled by liquid nitrogen. In CUEBIT, the collector is cooled by de-ionized water. To extract ions for further study, extractor electrodes are used.

5.1.4 Trapping

Neutral atoms as well as singly ionized atoms are injected in the trap region where the electron beam collides with the injected atoms, thus creating higher charge states via electron-impact ionization. The highly charged ions are trapped axially by the electric field applied to the drift tubes and radially by the combination of the axial magnetic field and the space charge of the electron beam. Multiple collisional and radiative processes are encountered in the process of the interaction of electrons, atoms, and ions, resulting in emission of radiation from the EBIT plasmas. This emission can be recorded and studied by the use of spectrometers connected to the accessible viewing ports in between the Helmholtz coils in the trap region. Ions can be extracted by arranging the drift tube potentials and can be operated in either a leaky mode or a pulsed mode. In the leaky mode, ions have enough kinetic energy to escape a moderately deep central trap potential giving rise to a steady current. In the pulsed mode, the ions are confined in the trap, and then expelled with the raise in central drift tube potential.

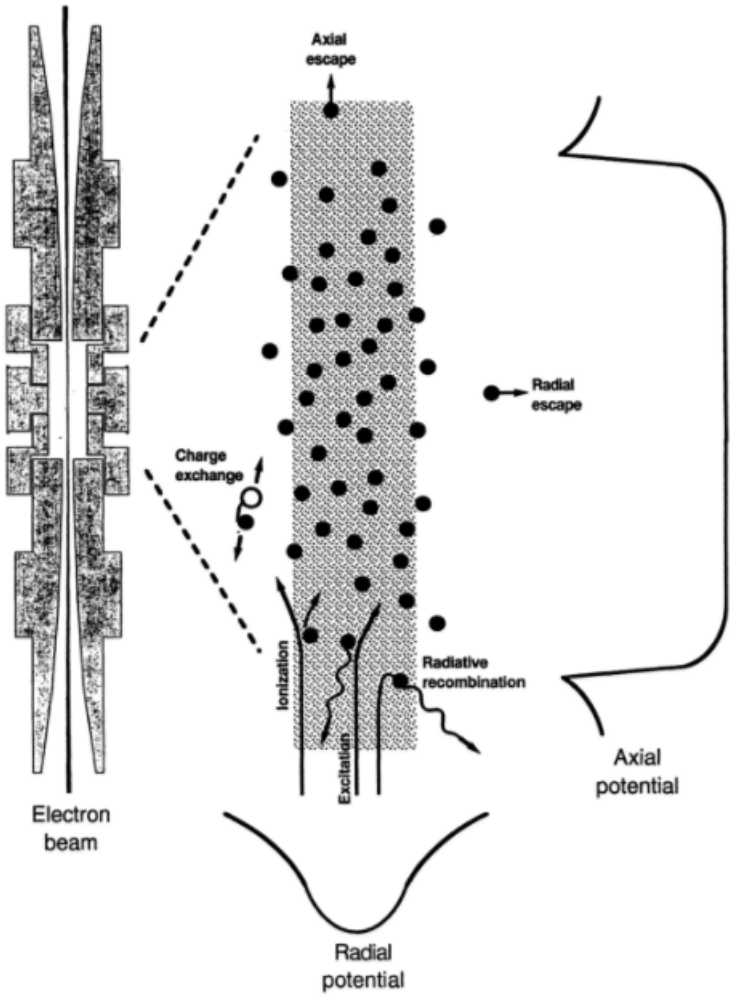

Figure 5.2: Schematic of the trapping in EBIT. From [Gil99].

While the highly charged ions are deeply trapped (V*Q), the Coulomb interactions of ions with electrons through collisions can lead to collisional heating of the ions in the trap. To maintain the trapping of the higher charge states, proper cooling mechanism needs to be provided. An evaporative cooling method has been developed for EBIT [LMH$^+$88] where gases with lower charge states are injected simultaneously with the ions of interest. The ion loss rates for various ions that follow a Boltzmann distribution, is given by [BS03]:

$$R_{loss}(q) = \tau_{comp}^{-1} \exp(\frac{-qeV_{trap}}{T_i}) \tag{5.2}$$

Here, V_{trap} is the effective potential depression in the charge compensated beam, T_i is the common ion temperature, and τ_{comp} is the mean compensation time. It can be seen from 5.2 that low-charged ions are lost first from the trap. This is why low charge gases such as N and Ar are used as coolant for the highly charged systems. The coolant ions come to equilibrium with the rest of the ion cloud quickly by ion-ion collisions and then leave the trap by taking away energy due to their lower charge states and shallower trap depth. This can be further justified from Figure 5.3.

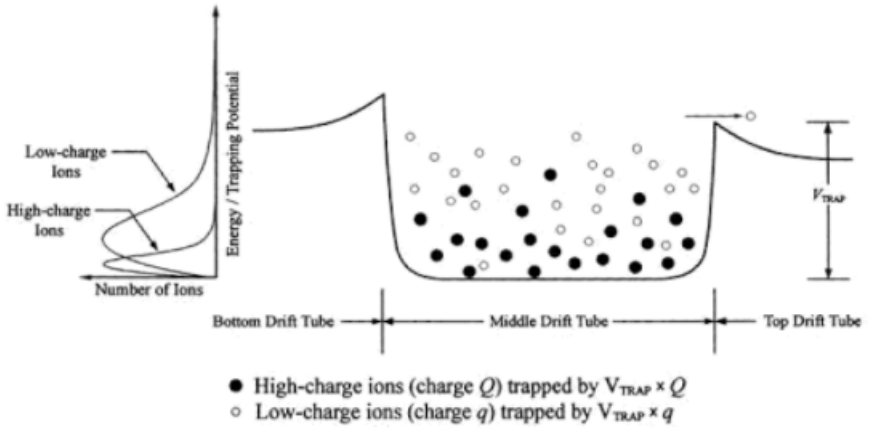

Figure 5.3: Evaporative cooling of highly charged ions (charge Q) by low-charged ions (charge q). From [BS03].

5.2 NIST EBIT

NIST EBIT became operational in 1993 [Gil99]. The schematic of NIST EBIT is given in Figure 5.4. The NIST EBIT also comprises of the electron gun region, drift tube region, and the collector region. The electron gun has a filament heated by nearly 0.5 A current. This results in thermionic emission of electrons that are extracted by biasing the anode electrode positively with respect to the cathode. Usually the anode is biased to around 4.2 kV. The snout electrode remains at around the same bias potential as that of the anode and is used to match the field in the electron gun region to the outside. The transition electrode allows for the travel of these electrons to the drift tube region and is set to around

5 kV. The electron gun region has a bucking coil used to cancel stray magnetic field of the superconducting magnet. The magnet is cooled by a chilled perflourinated liquid.

Once the electrons enter the trap region where they excite and ionize the atoms by electron-impact excitation and ionization, the trapping of the highly charged ions is conducted by the application of electrostatic potential to the drift tubes. The 3 cylindrical drift tubes are shielded by a cylindrical shield electrode, which is set to high voltage of the order of 1 - 30 keV. The drift tubes are floated at this shield potential and usually a voltage of 500 V and 200 V is applied to the lower drift tube and the upper drift tube, respectively. The center drift tube is set to 0 V for trapping and 400 V for dumping the ions from the trap. The axial trapping of ions is accompanied by the potential applied to the drift tubes. The radial trapping of ions is caused by the strong magnetic field and space charge of the electron beam that contribute to an effective radial potential .

The electrons are then attracted towards the collector region set to 2 kV. To make sure that the secondary electrons in the collector do not travel back to the trap region, a suppressor electrode is situated below the collector. The suppressor electrode is usually set to around 650 V. To extract the highly charged ions from the trap, an extractor electrode is situated above the collector and is biased at a negative potential. This electrode also assists in avoiding the secondary electrons created in collector region to escape. Above the collector, a metal injection ion source is placed to allow for the injection of singly charged ions to the trap region. The details of this source is given in Section 5.5. The collector has a magnet to cancel stray magnetic field created by the superconducting magnet in the region cooled by liquid nitrogen.

Since, the EBIT electrodes are kept at very high voltage of the order of a few keV, the high voltage floating systems are kept inside an acrylic box that consists of different power supplies, electronics and fiber-optic systems in a metal shielded room. The drift-tubes, collector magnet and the MEVVA assembly have separate floating systems in the shielded room. The fiber-optic system allows the application of voltages to these assemblies through a control unit separated from the main power supplies. This provides safe handling

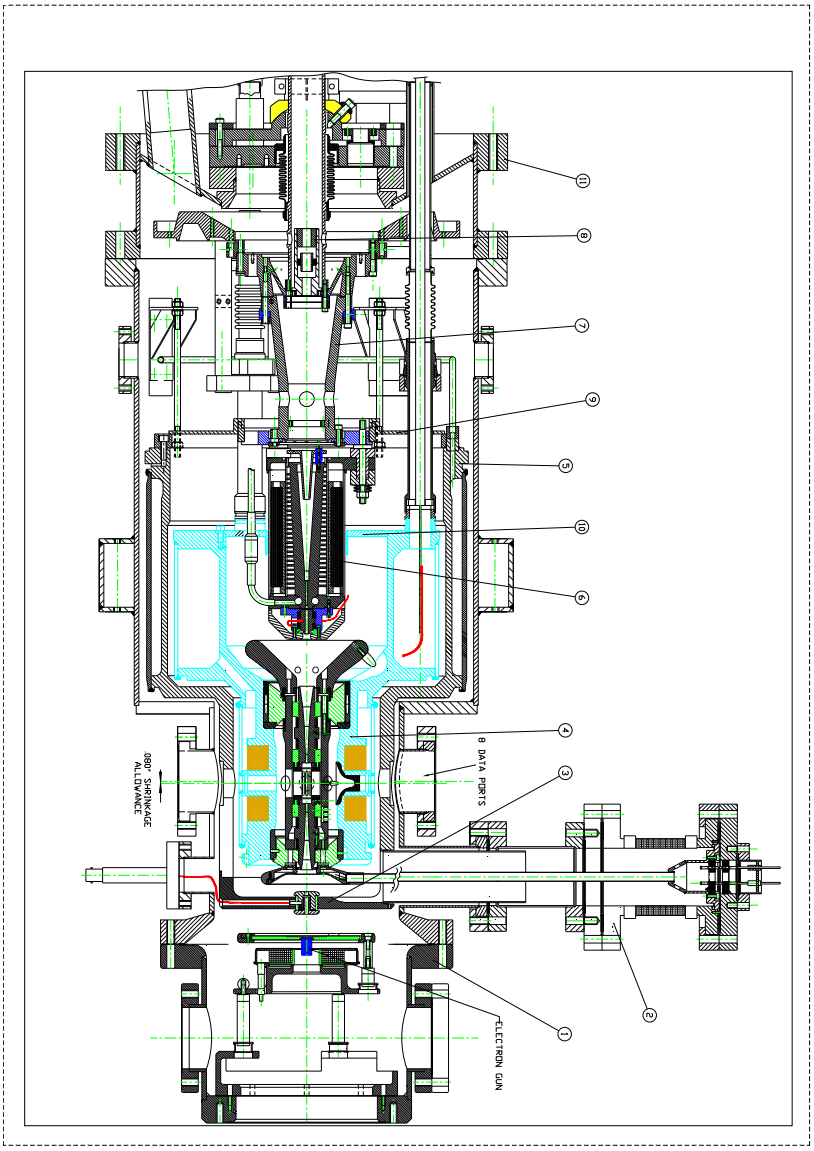

Figure 5.4: A schematic of the NIST EBIT that shows: 1. Electron gun assembly, 2. High voltage feed assembly, 3. Transition components, 4. Drift tubes assembly, 5. Liquid nitrogen vessel support, 6. Collector assembly, 7. Collector suspension assembly, 8. Einzel lens, 9. Liquid nitrogen shield, 10. liquid helium vessel, and 11. helium vessel support assembly. From [RR99].

of the voltage units. The high-vacuum performance of an EBIT is maintained by proper cryogenics assembly. The superconducting magnet needs to be cooled with liquid helium to 4.2 K. As a result, during the measurement, the outer chamber of the EBIT, labeled as 10 in

Figure 5.4 is filled with liquid helium. Liquid helium is inserted to the EBIT with a vacuum insulated transfer line from a 250 liter dewar during the measurement that lasts for nearly four working days with a typical consumption of $\approx$ 3.5 liter per hour during the operation. The collector assembly is cooled with liquid nitrogen to make sure that the region does not over heat by electron impact. The liquid nitrogen shield, 5 in Figure 5.4 is filled constantly through a buffer dewar inside the EBIT room that is fed by a larger tank outside the room. This requires $\approx$ 440 liters of liquid nitrogen per day. The temperature of collector exhaust is monitored during the EBIT operation.

Prior to the operation of EBIT, the device is pre-cooled with liquid nitrogen to make the switching to liquid helium smoother and to avoid excessive boil off of the liquid helium. The temperature of the superconducting magnet is monitored by the resistance of the magnet. At liquid nitrogen temperature, the resistance of the super-conducting magnet, R_{SCM} is 5.5 Ω. Before the transfer of liquid helium to the EBIT during the day of operation, it is necessary for the outer chamber to be free of liquid nitrogen. The timing of the pre-cool is adjusted such that liquid nitrogen boils off right before the transfer of liquid helium and the resistance is higher than, R_{SCM} of 5.8 Ω. At liquid helium temperature, R_{SCM} is 0 Ω. Once the magnet is cooled to liquid helium temperature, it is ramped up to 147.8 A. This results in the magnetic field of 2.7 T. At a maximum field of 3 T, the magnet can be ramped up to 160 A.

Once the SCM magnet is completely ramped, the voltages to other electrodes are applied. The electron filament is slowly ramped to 6.3 V where the current is nearly 0.5 A. The bucking coil is set to nearly 18 A where the voltage is close to 0.5 V. Once all the electrodes are applied with required voltages as given in Table 5.1, the electron beam current is adjusted by applying voltage to the anode electrode. The beam tuning is monitored by the snout electrode, kept below 20 μA. The fine-tuning of the beam is done by adjusting the voltages to different electrodes. Usually, the electron beam tuning responds mostly to the tuning of transition and suppressor electrodes and tuning of the current in the bucking coil. Once the optimum beam current is approached, data acquisition is started. The typical

EBIT parameters during the measurement are given in the table 5.1.

Table 5.1: Typical EBIT voltage settings during operation

Electrodes	**Voltage (V)**
Bucking Coil	0.54475
Focus	-8.57
Snout	4200
Transition	5250
Lower drift tube	500
Middle drift tube (dump)	400
Upper drift tube	260
Suppressor	650
Collector	2000
Extractor	-2300
EBIT Einzel	1500
Collector magnet	5
MEVVA float	9940

The low temperatures also help to attain a base pressure of less than 10^{-10} Torr inside the EBIT. Typical pressure readings in the different parts of the EBIT and the surrounding spectrometers is given in Table 5.2.

Table 5.2: Pressure (in Torr) recorded at different sections of the EBIT setup

EBIT parts	**Pressure (Torr)**
Electron gun	1.6×10^{-10}
Beam Line	1.15×10^{-9}
Gas injection	7×10^{-9}
Deflector region	1.6×10^{-9}
MEVVA	1.9×10^{-8}
EUV ion pump (mirror chamber)	3×10^{-9}
EUV on pump (grating chamber)	1.2×10^{-8}
EUV cold cathode gauge (mirror)	4.3×10^{-9}
EUV cold cathode gauge grating	1×10^{-8}
X-ray crystal spectrometer	2.3×10^{-7}

5.3 Space Charge Correction

The electron beam possesses a net electric charge that gives rise to a space charge. This space charge results in reduction of the actual electron beam energy in the trap region. The space charge potential of the electron beam can be estimated by the potential at the walls of the drift tube due to the electron beam using Gauss's law. The actual electric potential in the trap is the sum of the space charge potential and the potential applied to the drift tubes: V(ρ,z) = V$_{sp}$(ρ) + V$_{dt}$(ρ,z) in cylindrical coordinates (ρ,ϕ,z). This implies that the space charge tends to increase the electrostatic potential at the center drift tube. This results in a shift in the potential energy at the drift tube radius and the actual electron beam energy is reduced by the amount equivalent to this shift, lowering the potential energy. As a result, the space charge effect needs to be corrected. Considering the electron beam to be a cylinder of radius r_e with charge per unit length of λ, the electrostatic field of the charged conductor using Gauss's law is given by:

$$E_{out} = \frac{\lambda}{2\pi r \epsilon_0} : \rho > r_e \tag{5.3}$$

$$E_{in} = \frac{\lambda \rho}{2\pi \epsilon_0 r_e^2} : \rho < r_e \tag{5.4}$$

By integrating the electric field to get the electrostatic potential, we get:

$$V_{out} = V_{0,out} + \frac{\lambda}{2\pi\epsilon_0} ln(\frac{\rho}{r_e}) \tag{5.5}$$

$$V_{in} = V_{0,in} + \frac{\lambda}{4\pi\epsilon_0} (\frac{\rho^2}{r_e^2}) \tag{5.6}$$

V$_{0,in}$ = 0 at ρ = 0, since V$_{in}$ = 0 at the center. At the boundary, where ρ =r_e, V$_{in}$ = V$_{out}$. This results in the potential $V_{0,out} = \frac{\lambda}{4\pi\epsilon_0}$, equal to the total potential of the electron beam.

Equations 5.5 and 5.6 can then be written as:

$$V_{out} = \frac{\lambda}{4\pi\epsilon_0} + \frac{\lambda}{2\pi\epsilon_0} ln(\frac{\rho}{r_e}) : \rho > r_e \tag{5.7}$$

$$V_{in} = \frac{\lambda}{4\pi\epsilon_0} + \frac{\lambda}{4\pi\epsilon_0} (\frac{\rho^2}{r_e^2}) : \rho < r_e \tag{5.8}$$

So, the space charge potential inside and outside the beam can be approximated as:

$$V_{sp,out} = V_{0,out}\left(1 + 2ln(\frac{\rho}{r_e})\right) : \rho > r_e \tag{5.9}$$

$$V_{sp,in} = V_{0,out}(\frac{\rho^2}{r_e^2}) : \rho < r_e \tag{5.10}$$

Plugging in λ as I/v, where v is the electron's velocity given by $\sqrt{2E/m_e}$, we get:

$$V_{sp,out} = \frac{I}{4\pi\epsilon_0\sqrt{2E/m_e}} + \frac{I}{2\pi\epsilon_0\sqrt{2E/m_e}} ln(\frac{\rho}{r_e}) \tag{5.11}$$

The space charge potential is more accurately treated as a Gaussian distribution where $V_{0,out} = 1.08\frac{\lambda}{4\pi\epsilon_0}$ [PKG00] and hence can be written as:

$$V_{sp,out} = \frac{1.08 \times I}{4\pi\epsilon_0\sqrt{2E/m_e}} + \frac{1.08 \times I}{2\pi\epsilon_0\sqrt{2E/m_e}} ln(\frac{\rho}{r_e}) \tag{5.12}$$

If we use a electron beam radius of 35 μm, ρ of 5 mm, the potential at the center drift tube for different electron beam energy given by the central drift tube potential can be used to estimate the space charge potential as shown in Figure 5.5 [Gal17].

5.4 Gas Injection Method

Neutral atoms are not affected by electric or magnetic fields and can be injected into the trap region of the EBIT from any direction. The key for an efficient neutral gas

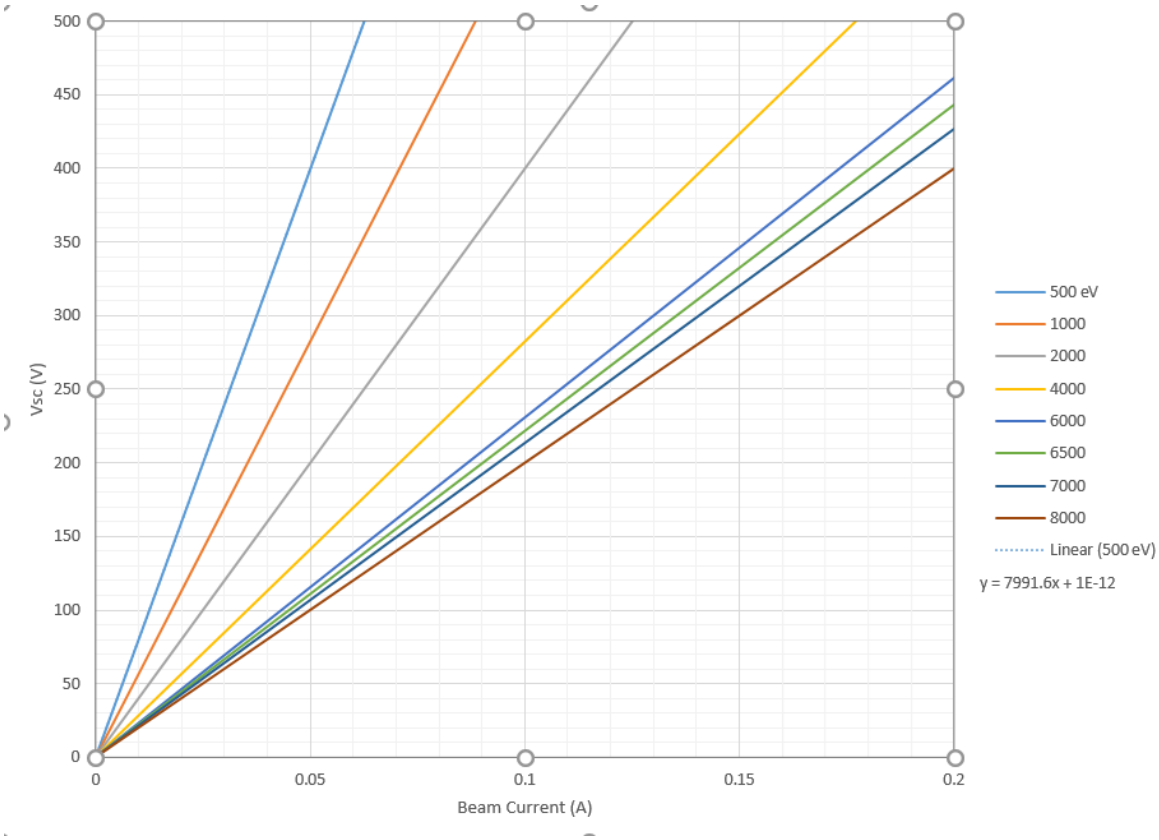

Figure 5.5: The space charge potential calculated at different electron beam voltages and currents. From [Gal17].

injection system is its ability to direct atoms into the center of the trap, where they can be ionized and trapped by the electron beam, and not contribute to the degradation of the overall ultrahigh vacuum conditions in the device. With the current ballistic gas injector setup at NIST, multiple gases can be injected into the EBIT trap region by leaking small amount of neutral gases through a set of apertures and collimator tubes with a leak valve. The schematic of the design of the gas-injection setup is shown in Figure 5.6. The gas injector tube is connected to a manifold that contains 5 gas bottles of Ar, He, Kr, Ne, and CO_2. Neutral atoms can be loaded into the tube before injecting it to the EBIT through the leak valve. With the ballistic setup, neutral atoms that have their velocity vectors in the direction of the injection axis are transported to the EBIT. All other neutral atoms are blocked by the apertures and get pumped away by the consecutive stages of the differential

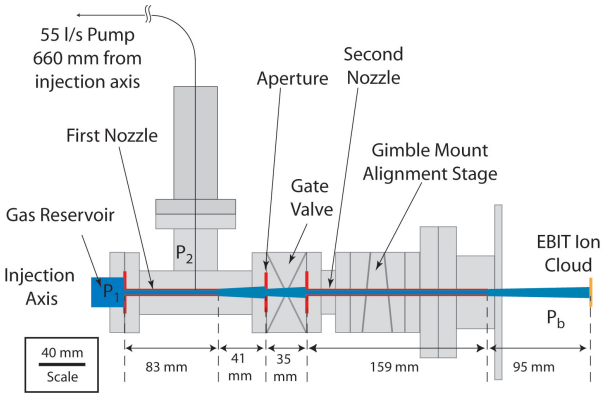

Figure 5.6: Gas injection setup at NIST EBIT. P_1, P_2 are the pressures of the gas reservoir, and P_b is the pressure outside the trap ($< 10^{-9}$ Pa). P_2 is usually two orders of magnitude lower than P_1 where P_1 is around 10^{-6} Pa. From [FSO+07].

pumping system. Once the leak valve is loaded with gas at pressure of the order of 10^{-3} Pa, the section between the leak valve and the gate valve is filled. The gate valve is then opened allowing the flow of the gas through the apertures to the EBIT ion cloud. The pump connected to the gas injector setup allows for the pumping of the gas in the section between the gate valve and the injector axis. Before loading in a new gas, this section is pumped and the valve to the pump is closed during the gas injection. The gas reservoir has 3 leak valves, one of which is connected to the manifold mentioned earlier with 5 different gases. The other two leak valves are connected to separate Xe bottles that contain ^{136}Xe and ^{124}Xe isotopes.

5.5 Metal Vapor Vacuum Arc Ion Source

Besides the gas injection setup that allows for the injection of neutral atoms, NIST EBIT also has a metal injection vapor vacuum arc ion source (MEVVA) designed and installed by Glenn Holland in 2003. The MEVVA is a metal ion source used to inject singly charged ions into the EBIT trap region and is described in detail by Holland *et al.* [HBS+05]. Ionized atoms are affected by the magnetic field of the superconducting magnet surrounding the trap region; therefore they can only be injected into the center along the field lines parallel to the vertical axis of the machine. The MEVVA setup has two

parts: the MEVVA electronics enclosure that houses the high voltage components floated at a bias voltage of 10 kV, and the rf-tight MEVVA head assembly located about 2 m above the center trapping region. The enclosure contains a spark gap switch that receives an electric spark from a trigger generator. The trigger generator is connected to the main EBIT control console through a fiber-optic system and receives a trigger pulse of $\approx$ 26 - 28 kV of nearly 400 nm duration. The spark gap receives the high voltage pulse and conducts charge by means of a high voltage (40 kV), 0.09 μF capacitor. Resistors in series of 150 Ω are used to damp the energy such that the cathode receives 2.4 mC of charge. A Pearson coil is placed in the electronics box to measure the current created by the discharge. The current is $\approx$ 125 A and decays over a period of 50 μs. This current is monitored through an oscilloscope with a 1 MΩ input such that 1 V correspond to 100 A. The signal is attenuated by 10 $\times$ such that the oscilloscope reads a voltage of 1.25 V. The cathodes can be selected by a rotary switch system connected to 10 M Ω resistors for biasing them simultaneously.The cathodes and the anode are connected to the MEVVA head assembly via 9 different 10 m long RG-8 coaxial cables. These cables carry the high voltage pulse created by the spark gap switch to the cathodes in the MEVVA head assembly. The overview of MEVVA system is shown in Figure 5.8. The power rack enclosure includes a rotary selector system that can be placed to the required cathode markers labeled A through F.

The MEVVA head assembly consists of 8 different metal cathodes (1 - 2 mm diameter) separated by a quartz insulator from each other, the central anode and the anode cup. The anode cup sits on top of the insulator and is separated by a gap of 0.5 mm from the cathode. The arrangement of the cathode and anode assembly is shown in Figure 5.7. When an electric trigger is sent to the system, the high voltage pulse approaches the cathode tip via the cables. The high voltage causes an arc discharge in the gap along the surface of the insulator, ionizing the cathode material. An extractor cup is installed past the anode cup and is in electrical contact with the vacuum chamber at ground potential. This allows handling and installation of the cathode and anode assembly outside the vacuum. The cathode and anode assembly are floated at 10 kV positive bias voltage with respect to the extractor

cup. The extractor cup is at ground potential and attracts the arc plasma. The electrons are stopped at the extractor grid and the singly charged ions are successfully transferred to the trap region. The whole MEVVA head assembly is placed above the collector assembly in an inverted mode. The ions are attracted by the extractor grid in the MEVVA assembly and are transported to the central trap region through the collector assembly. The bias voltage at the MEVVA assembly needs to overcome the voltages applied to the electrodes through the center drift tube region where the ions are trapped. The center drift tube is surrounded by a shield electrode and is floated at the shield voltage such that the the trap voltage is the sum of the shield electrode voltage and the center drift tube voltage. To capture the MEVVA ions, the shield voltage is changed to 9.6 kV for a brief amount of time (on the order of 10^{-3} s), while the center drift tube is raised to 0.4 kV, such that the sum matches the MEVVA bias voltage. Once the ions arrive to the center drift tube, the center drift tube power supply voltage is switched to 0 V in order to trap the MEVVA ions. Since, the space charge of the electron beam affects the actual potential at the drift tube, fine-tuning of the shield voltage and the MEVVA bias is necessary for optimum ion capture. The timing sequence of the voltage switching during the operation is shown in section 7.2.

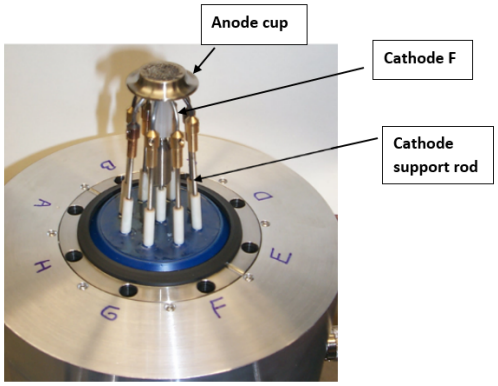

Figure 5.7: MEVVA cathode assembly. From [HBS+05], Patent number: 7672355.

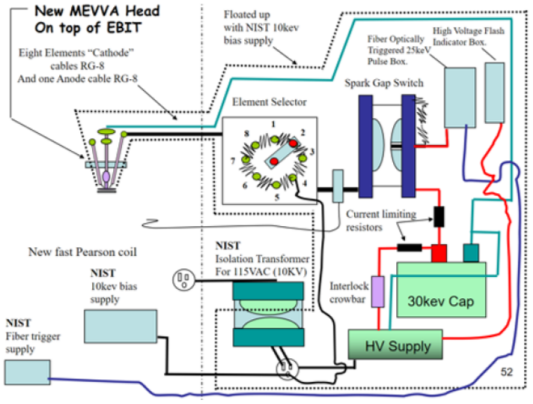

Figure 5.8: MEVVA system overview. From [HBS+05], Patent number: 7672355.

A mesh on a hole through the electrostatic bender is placed in the beam line on the

top of the EBIT to record the ion current in the section. The ion signal and the Pearson coil current signal are simultaneously displayed with respect to the trigger signal on an oscilloscope. An example of such a display screen shot is showed on Figure 5.9 for a Fe cathode. During normal EBIT operation, the MEVVA is triggered at every 5 s. A blue light indicator on top of the MEVVA head assembly provides a visual confirmation of the MEVVA firing. The MEVVA ion pulse monitored at the oscilloscope is usually spread to around 40 μs. To optimize the signal, the delay in the MEVVA trigger pulse can be adjusted along with the trigger frequency and the MEVVA bias voltage. The ions register few volts in the scope corresponding to ion flux of $\approx 10^9$ ions/cm^2.

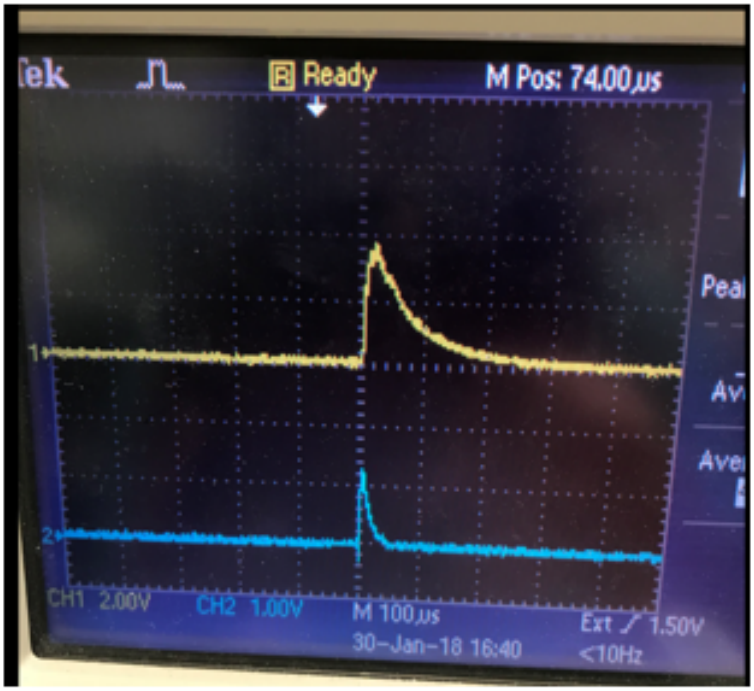

Figure 5.9: The ions detected by the Farday cup (top) and the Pearson coil current (bottom) registered in the oscilloscope for Fe cathode at 9 kV bias voltage triggered at 0.2 Hz.

Usually, the cathodes register up to an ion current resulting in 8 V on the oscilloscope display at the bias voltage of 10 kV. Before the MEVVA operation, few minutes to hours long MEVVA conditioning is performed for the cathodes. Longer conditioning times are needed for the cathodes that have not been fired for a very long time to degas the electrodes.

The cathode of interest can be selected by placing the rotary selector to the corresponding marker. During our measurements, the cathodes installed were: A - W, B - Bi, C - Mo, D - Y, E - Zr, F - Fe, G - Nb, H - Yb. These elements have been recently replaced. The MEVVA head assembly is pumped to nearly 2×10^{-8} Torr pressure with a 20 L/s ion pump. During the MEVVA triggering, the pressure increases to up to an order of 10^{-7} Torr and stabilizes back to the normal pressure within few seconds. Ions originating from the MEVVA initially get trapped within the drift tubes and get further ionized to the desired charge states by the energetic electron beam as described in section 5.1.4. Ions also get excited by the electron beam and emit radiation that can be recorded with different spectrometers attached to the observation ports.

Chapter 6

Spectrometers

Electromagnetic radiation from the EBIT plasma is recorded by multiple wavelength- and energy-dispersive spectrometers in the X-ray and EUV region. The definition of the wavelength regions corresponding to the short-wavelength range is shown in Table 6.1. The distribution of the intensity of the radiation over a wavelength region is conducted by a dispersive element that can be a prism, grating, or a crystal depending on the instrument. For spectroscopy with highly charged ions, grating or crystal based spectrometers are usually used. Different types of dispersion elements are chosen depending on the wavelength range to be measured. For soft X-rays, crystals are used since the wavelength of the X-rays are in the same length scale as the crystal lattice spacing. General schematics of a grating spectrometer is shown in Figure 6.1. The divergent beam of light radiated by some source enters the entrance slit of a focusing mirror resulting in collimated rays that reach the grating element responsible for dispersion. The dispersed rays are then sent to another mirror and imaged by a detector. Usually the photons that are recorded by the detector are converted into electrons carrying electrical charge that is proportional to the photon energy and number. The charge is recorded in digital units making up the intensity of the spectral lines they represent.

Table 6.1: Wavelength regions in short-wavelength range. From [BS03].

Region	Wavelength (nm)
Vacuum ultraviolet (VUV)	30 - 200
Extreme ultraviolet (EUV)	10 -100
XUV	2 - 30
Soft X-rays	0.1 - 4
Hard -rays	0.01 - 0.1
Gamma rays	< 0.01

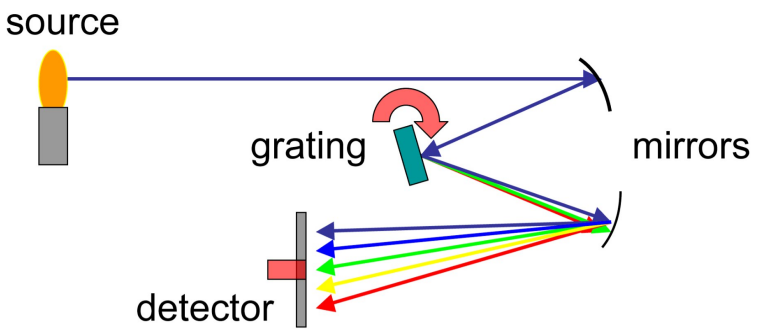

Figure 6.1: Schematic of a grating spectrometer is shown. From [opt].

6.1 Extreme Ultraviolet Spectrometer

The primary spectrometer used in the current work is the flat-field grazing incidence EUV spectrometer. The EUV spectrometer was custom designed for the NIST EBIT and is described in detail by Blagojevic *et al.* [BLF+05]. Since, the wavelength region to be measured is below 30 nm, this requires the use of a grazing incidence geometry. This is because the reflectivity of the material increases with the decrease in the angle of incidence with respect to the grating (grazing angle). The separation of the projection of the grooves gets smaller. The design of the EUV spectrometer is based on the aberration-corrected concave gratings designed by Harada and Kita. [HK80]. The spectrometer consists of three major parts: EUV focusing optics, EUV monochromator, and charge-coupled device (CCD) camera to record the spectral image.

A CCD is a semiconductor based device usually made from p-type Si. Electron-hole pairs are created when the photon interacts with the Si material via photoelectric effect. The charge in the free electrons are stored in an array of light sensitive elements

called pixels. Each pixel contains a couple of p-doped metal-oxide semiconductor (MOS) capacitors where a SiO_2 layer sits on top of a Si substrate that contains an conducting electrode or gates. The electrode is held at a positive potential and attracts the electrons where they are stored. These electrons are transferred pixel by pixel to the measurement electronics during the readout process. The voltage created as the electron packet runs through the readout electronics measured as an electronic number, which is converted into arbitrary digital units and gets registered. The analog to digital units (ADU) can be selected by the gain of the camera controller. Gain in the Princeton Instruments detector used in our experiments is defined as the number of electrons per ADU. The CCD image inherently includes noise that arises during the digitization and readout process, called the readout noise. Another source of noise are the thermally generated electrons in the Si surface. These electrons get excited from the valence band to the conduction band creating thermal current, termed the dark current. Most of the electronic noise can be minimized by cooling the camera. Highly energetic cosmic rays can generate a large amount of charge over a few pixels as well. Cosmic ray filtering for the EUV spectra is done through a program based on removing outliers among different frames of an image of the same set. If the intensity of a pixel in a frame is 5 or more Poisson standard deviations away from the mean of the frames, it is replaced by the average value of the other frames [STD$^+$17].

The EUV focusing optics have a spherical gold coated mirror with radius of curvature R_c of 917.1 cm $\pm$ 2.3 cm to collect light from the slit like EBIT ion cloud. The use of gold as a coating material enhances the reflectance of the mirror in the 5 - 20 nm range. The mirror is placed 48 cm from the EBIT at an angle of incidence of 3° and focuses the light from the EBIT to the entrance slit of the monochromator. The monochromator consists of a bilateral adjustable slit placed 48 cm from the mirror center, and a concave grazing incidence, aberration corrected, flat field diffraction grating as specified in Kita *et al.* [KHNK83] placed at 23.7 cm from the slits. The flat-field allows a flat focal plane contrary to the conventional spectrograph with a cylindrical focal plane where the focal lengths vary. The mounting incidence angle of 87° was used for the concave grating with

R_c of 564.9 cm ± 2.0 cm and a groove number of 1200 grooves/mm. The groove spacing varies based on the relation 6.1 [KHNK83] .

$$\sigma = \frac{\sigma_0}{(1 + \frac{2b_2}{R}w + \frac{3b_3}{R^2}w^2 + \frac{4b_4}{R^3}w^3)} \tag{6.1}$$

where, σ is the groove spacing measured at w from center of grating along the y axis (see Figure 6.2), σ_0 is the nominal groove spacing (1/1200 mm), R is the radius of curvature of the grating surface, and b_2, b_3, b_4 are the varied spacing ruling parameters with b_3 and b_4 defined to correct for aberrations. The values of the parameters are b_2 = -20, b_3 = 455.8 and b_4 = - 11840 for the current setup such that the groove spacing is in between 0.69 μm and 0.99 μm for the wavelength range of 5 to 20 nm.

The grating equation is defined as:

$$sin\alpha + sin\beta = \frac{m\lambda}{\sigma_0} \tag{6.2}$$

where λ is the wavelength, m is the order of diffraction, α is the angle of incidence and β is the angle of diffraction. For gratings with fixed groove spacing of σ_0, the diffraction angle depends only on the incidence angle. For a variable spacing groove, it depends on both α and σ, which is aberration corrected. This implies that the use of the mechanically ruled variable spacing is necessary to exclude effects from aberrations. The schematic of the flat-field grazing incidence spectrometer is shown in Figure 6.2.

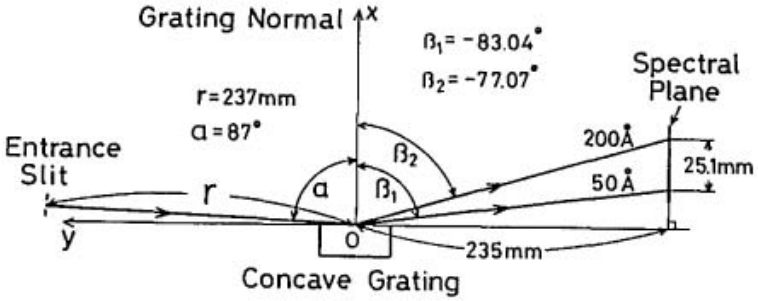

Figure 6.2: Schematic of a flat-field spectrometer. From [KHNK83].

At 23.5 cm from the grating center, a liquid nitrogen cooled, back-illuminated CCD

camera is placed in the focal plane of the grating. The CCD detector consists of a 2048 × 512 pixel array with the pixel sizes of 13.5 μm × 13.5 μm. A 2D linear translation stage was used to position the CCD assembly such that one dimension of the CCD chip sits on the focal plane of the dispersive grating while the other dimension is along the wavelength dispersed by the grating. The quantum efficiency of the detector is shown in Figure 6.3. The CCD position can be registered linearly by means of a micrometer screw gauge to change the wavelength range of interest with the help of the linear translation stage. Table 6.2 shows the wavelength region covered at different micrometer gauge settings. During the data acquisition, the EUV CCD temperature is set to 120°C by using the Winspec software connected to the camera controller that controls the cooling system with a liquid nitrogen bath. The signal readout rate in the Winspec software was maintained at 100 kHz to provide the lowest readout noise. The controller gain was set to 3 in order to measure low-level intensity signals and reduce noise. The spectral images (2048 ×512 pixels), registered with the help of the CCD, were hardware collapsed along the y-axis, so that the resulting image is 1D dataset of 2048 channels. The resolving power of the spectrometer $\lambda/\Delta\lambda$ is nearly 400 for the entrance slit width of 300 μm, comparable to the width of the EBIT light source. The wavelength resolution of the EUV spectrometer is close to 0.02 nm.

Table 6.2: EUV spectral range at different translational CCD positions. + and - refer to the forward and backward direction while rotating the micrometer

Position in ” (Direction with respect to the 0 value)	**Range (nm)**
0.144 (+)	2.7 - 13.3
0.994 (-)	4 - 20
0.675 (-)	7.8 - 25.8

Both the mirror holder and grating holder assembly are placed in two separate ultra high vacuum (UHV) chambers that are set to an optically aligned table along with the CCD camera. The two chambers are pumped by two separate ion pumps with pumping speed of 100 L/s. The pressure is monitored by two cold cathode gauges connected to the chambers. During the data acquisition, the pressure is of the order of 10^{-9} Torr as the system is directly connected to the main vacuum chamber of the EBIT. In order to prevent

the stray light from pumps and gauges to reach the CCD chip, the ion pump for the grating chamber and the cold cathode gauges for both mirror and grating chambers are turned off while taking spectra from the EBIT. The ion pump for the mirror chamber was operated all the time with typical pressure readings of around 3.8×10^{-9} Torr during EBIT runs. The vacuum system of the EUV is separated from the EBIT vacuum by a manual gate valve, which is closed at all times except during data acquisition. Another gate valve between the mirror UHV chamber and grating UHV chamber is open throughout the measurements and only used in case of the separation of the grating and mirror chambers necessary during maintenance work.

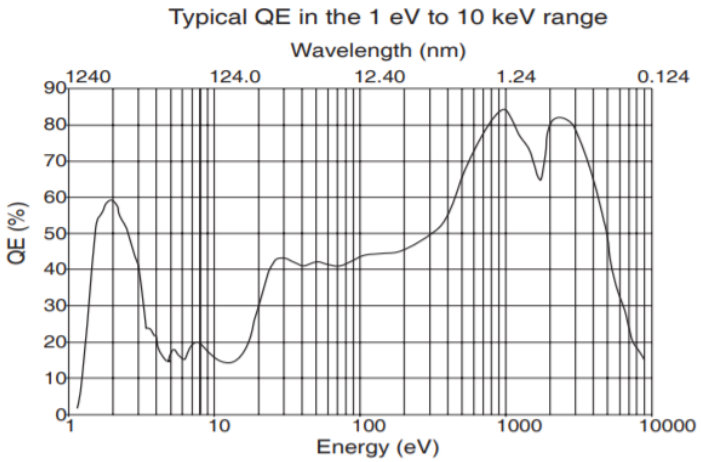

Figure 6.3: The quantum efficiency of the CCD camera in the energy range of 1 - 10000 eV.

The picture of the EUV spectrometer along with the design with dimensions are given in Figs 6.4 and 6.5. The EUV setup also has a zirconium window attached to a separate gate valve between the EBIT observation port and the focusing mirror. This window was not used for our measurements. Its main purpose is to separate the EBIT and spectrometer vacuum chambers in case the two have considerably different vacuum values, but still transmit radiation in the wavelength range of 5 and 25 nm. It also filters the signal from higher or lower wavelengths.

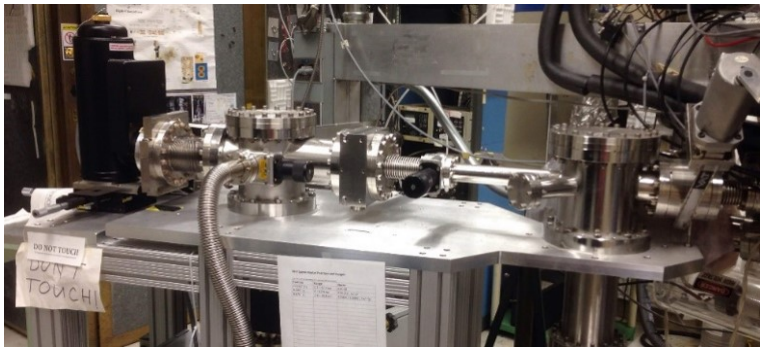

Figure 6.4: EUV spectrometer setup at NIST. Beginning from right: the EUV mirror chamber followed by the slits, the grating chamber and the CCD

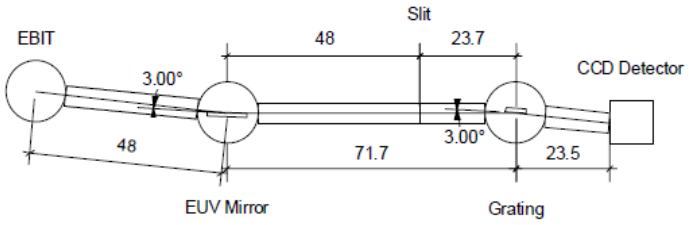

Figure 6.5: Outline of the EUV setup at NIST

6.2 X-ray Spectrometers

In addition to the EUV spectrometer, three X-ray spectrometers are currently installed at NIST EBIT. A moderate-resolution, high counting statistics, energy-dispersive Ge detector and two high-resolution low counting statistics X-ray spectrometers oriented parallel and perpendicular to the EBIT ion cloud are used to record the spectra in the X-ray region. The high resolution X-ray crystal spectrometers [SSR$^+$18] are separated from the EBIT main vacuum chamber by a 230 μm Be windows installed on the EBIT observation ports. The crystal spectrometers are of Johann type with a resolution better than 2 eV at 3 keV X-ray energy but is limited by low photon numbers that is compensated by longer acquisition times. Johann-crystal spectrometers contain a curved crystal bent to a radius R_c, such that an imaginary circle of radius $R_c/2$ termed as the Rowland focusing circle [Joh31] is created. The crystal-detector arm is fixed and the detector sits on the Rowland circle while it scans the X-ray spectra diffracted by the crystal based on Bragg diffraction 2dsin(θ)

= nλ. Here, n is the diffraction order, θ is the diffraction angle and d is the crystal lattice spacing. The CCD camera has 2048 $\times$ 2048 pixels of size 13.5 μm and is cooled with a chilled water setup to -75°C. During data acquisition, the readout of 50 KHz is selected for low readout noise with a 4 $\times$ amplification.

A liquid nitrogen cooled high purity Ge detector is also used simulteneously to record the X-ray data. The detector has a high-counting statistics with a bandwidth up to 20 keV. Low energy photons are also measurable by means of a thin plastic window used in between the EBIT and the spectrometer, instead of a Be window that cuts off low energy photons. Due to the high count rate provided by this spectrometer, the Ge detector is used to optimize the signal in real time.

6.3 Spectral Features and Line shape

The detected distribution of the intensity of the radiation over a wavelength range of a spectral peak gives rise to the spectral line shape. The line shape gives the probability to detect a photon of a given energy. The spectral line shape and width contain information about the atoms and ions. The width is usually used to determine the electron temperature. The electron temperature distribution function due to Doppler broadening is usually taken as a Gaussian with a full width half maximum (FWHM). The spectral line is broadened due to the combination of the instrumental broadening that depends on the instrument function and the intrinsic behavior of the plasma. The intrinsic broadening is caused by combination of natural broadening caused by finite life time of the absorption (emission), Doppler broadening due to the thermal motion of the species, collisional broadening due to interaction with surrounding species, and Stark broadening due to the electric and magnetic fields.

The natural width of a spectral line is given by the lifetime of the transition that is the inverse of the transition probability. The uncertainty in energy that comes from the Heisenberg's principle Δ E Δ t $\geq \hbar$ due to the uncertainty in the lifetime of an excited

state, correspond to the natural width of the line. This width increases for shorter lifetimes and is represented by a Lorentzian profile. The particles in a plasma move with different velocities due to the thermal motion of the ion cloud leading to the Doppler broadening. As the thermal Doppler broadening is dependent on the frequency of the line, the temperature and mass of the ions, it can be used to determine the temperature of the ions. Doppler broadening is represented by a Gaussian profile. In an EBIT, the ions move in all directions and the thermal motion in different directions average out to give a symmetrical Doppler broadening, which is insignificant compared to the instrumental broadening. For the plasmas where the natural line broadening is comparable to the Doppler broadening, the convolution of the Lorentzian and Gaussian profile is used, termed as a Voigt profile.

Other broadening effects are caused by collisional processes in the plasma that can shorten the lifetime of an atomic process increasing the energy uncertainty and hence the width of the spectral line. This broadening is termed as pressure broadening and is larger for denser plasmas and at higher temperatures. A Lorentzian profile is used to characterize this broadening. Another type of pressure broadening arises due to the presence of electric field of the charge particles that interact with the emitting particles resulting in the so called Stark broadening. This broadening is corresponding to the linear Stark effect. The energy broadening is inversely proportional to the square of the distance of the charge particle that interacts.

The broadening in the spectral line radiated by the EBIT plasma is mainly contributed by the instrument broadening. The finite resolution of the spectrometer characterized by the instrument function leads to the broadening of otherwise δ-function like assumed spectral shape. The instrumental broadening is given by the FWHM of a spectral line for the instrument represented by a Gaussian function. In our case, for the EUV spectrometer the FWHM was close to 0.02 nm or 2.5 pixels for a strong transition and the broadening is almost purely a Gaussian distribution.

Chapter 7

Line Identification and Plasma Diagnostics Study of EUV Spectra in Highly Charged Yttrium

7.1 Introduction

EUV measurements of highly charged ions with the NIST EBIT has consistently provided accurate spectroscopic data for various elements in the periodic table, of which we list a few here [PGRR14, FSO+07, ORGR12, GDR+09]. This measurement is a continuation of such spectroscopic efforts by the NIST EBIT group to expand the available atomic data. This work is based on similar measurement of the EUV transitions from highly charged Y plasma. Y is a fifth row element with an atomic number of 39. The study of Y ions was motivated by its relevance in tokamaks [SKIR89, RKS+87, JMD90], laser-produced plasmas [RKS+87, EFSB89], and in astrophysical observations [Ost74]. The elemental abundance of Y in different stars make them astronomically relevant [RC93, ZM91, WCNS09]. A few transitions corresponding to multiply and highly charged states of Y have been reported previously. Further details of these works and references to these measurements are provided in our scientific report [STD+17] attached in Appendix A. Despite these efforts, atomic data

for highly charged Y in the EUV region are limited. Furthermore, very few measurements of the second row isoelectronic sequence of highly charged Y have been reported [SCW$^+$92, MHR$^+$85, DMJ89, MJM$^+$94, Rea82, BBR$^+$86].

The systematic study of the L-shell Y ions (Y XXX - Y XXXVII) was performed with the NIST EBIT along with the identification of a few spectral lines from the M-shell Y ions (Y XXVII - Y XXVIV). The spectral lines from the quasi-hydrogenic Li-like Y charge state originating from 2s – 2p transitions and the Na-like D transitions originating from 3s – 3p transitions were observed and investigated. These measurements represent the first study employing an EBIT to observe such spectral features of Y. Due to the observation of a few diagnostically important, forbidden M1 transitions, the line intensity ratios of the M1 versus E1 transitions were studied as potential plasma diagnostic tool. One of the identified M1 line corresponding to the $2s^2 2p^5$ - $2s2p^6$ transition in F-like Y ions has been extensively investigated previously and is known to be diagnostically relevant [Rea82,AK16,JAG13,KGA$^+$16]. The transition probabilities of M1 lines strongly depend on the spectroscopic charge Z_{sp} and are much stronger in highly charged ions. These transitions originate from long-lived metastable energy levels, which are subject to collisional quenching mechanisms. For plasma with high electron densities, these levels decay mostly by collisions unlike E1 transitions that decay radiatively even at high densities. This results in a density dependence in the line ratio of M1 to E1 transitions.

In the following sections, we describe the observation of highly charged Y spectra. We present the details of the measurement and the spectral analysis of the observed Y spectra. We discuss the systematic study of the spectral lines and the identification of atomic transitions corresponding to the L-shell charge states of Y. The wavelength measurement of the Na-like D transitions and the Li-like resonance lines and comparison with previous works is given. We also discuss the possible applicability of these measurements for plasma diagnostics. Detailed scientific report of this work is published [STD$^+$17].

7.2 Measurement

Singly charged Y ions were injected into the EBIT trapping region from the multi-cathode metal vapor vacuum arc ion source (MEVVA). These ions were further ionized to higher charge states via electron impact ionization. The ions were trapped axially by the electric potentials applied to the three drift tubes, and radially by the axial magnetic field of 2.7 T and the space charge potential due to the electron beam. The drift tubes were set to voltages of 500 V, 0 V and 260 V for the lower, central, and upper drift tubes, respectively. The trap was emptied every 5 s to avoid accumulation of highly charged Xe/Ba impurities by switching the central drift tube potential to 400 V, forcing the ions out. The 500 V applied to the lower drift tube made sure that the ions do not penetrate into the electron gun region. The drift tubes are surrounded by a cylindrically-shaped shield electrode, as described in the experimental section. The shield potential is adjusted to set the electron beam energy needed for the measurement.

The MEVVA is floated at a potential of 10 kV. To capture the singly charged Y ions injected from MEVVA, the shield electrode voltage is raised to 9.6 kV and the central drift tube is simultaneously raised to 0.4 kV. This results in a total potential at the trap region equivalent to the MEVVA potential. Optical switching of the potentials allows for fast matching of the voltages, on time-scales on the order of 1 ms. Subsequently, the central drift tube voltage is lowered to 0 V to trap the ions within the middle drift tube region. The Y charge states of interest were created and the systematic observation of the transitions was recorded with the flat-field grazing incidence spectrometer. Details of the spectrometer is given in chapter 6. The shield potential was changed between 2.3 kV and 6 kV during the measurement to optimize the actual charge state of interest. The sum of the shield potential and the central drift tube potential corrected for the space charge potential produced by the electron beam gives the potential at the trap. The electron beam energy is given by the potential difference in the trap region and the electron gun region, multiplied by the electronic charge. The space charge potential due to the electron beam lowers the actual

electron beam energy as explained in section 5.3.

The timing sequence for the capture of the MEVVA ions and the shield voltage settings used to capture and trap the MEVVA ions are shown in Tables 7.1 and 7.2, respectively. An optical trigger pulse is sent to the function generator after a 1 ms delay in the system cycle that defines the timing sequence set by the LabView VI shown in Table 7.2. A conversion factor of approximately 3 is required to set the voltage setting of the VI. v is the voltage in arbitrary units ($\approx$ V/3) applied to set the shield voltage V (in kV). A visual representation of the timing sequence is given by Figure 7.1.

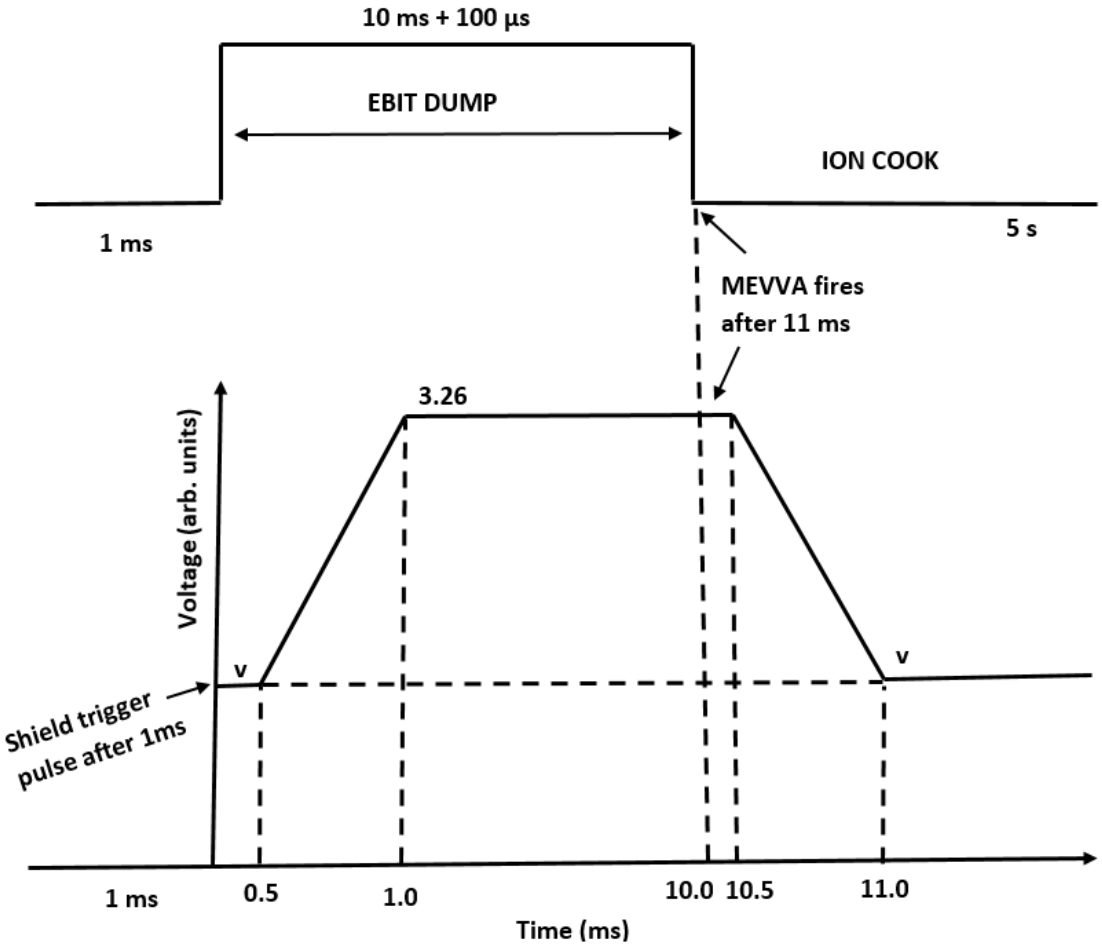

Figure 7.1: The timing sequence during the capture and trapping of MEVVA ions. Figure not drawn to scale.

Table 7.1: Timing sequence for ion cooking and dumping time during MEVVA ions injection.

	Delay(ms)	**Width(ms)**
EBIT Dump	1	10.1
MEVVA	11	1
Shield	1	1

Table 7.2: Values sent to the function generator for shield voltage setup.

Time(arb.un.)	**Time(ms)**	**Voltage(arb.un.)**	**Voltage(kV)**
0	0	v	V
100	0.5	v	V
200	1	3.26	9.51
2100	10.5	3.26	9.51
2200	11	v	V
2300	11.5	v	V

The charge selectivity of an EBIT allows for the production and confinement of the charge states of interest. To create a particular charge state, the electron beam energy during the measurement should be higher than the ionization energy of the corresponding lower charge state. For instance, to create a Be-like Y ion (Y^{35+}), the electron beam energy needs to be higher than the ionization energy of the B-like Y (Y^{34+}). Not all lower charge states will fully turn into higher charge states due to charge exchange. Thus, the resulting spectra will contain transitions from the various charge states present in the plasma. The charge state balance is determined by quantifying the evolution of the ion species within the trapping region with a rate equation. This rate equation involves all of the ionization and recombination processes that occur within the non-Maxwellian EBIT plasma. The charge state distribution is implemented into the CR model NOMAD to generate synthetic spectra. Comparisons with the theoretical spectra helps to properly identify the transitions in the measured spectra. The ionization energies of the charge states of interest for our measurement are listed in Table 7.3. The electron beam energies were varied in between 2.3 keV to 5.98 keV to measure the L-shell transitions and a few M-shell transitions.

Table 7.3: The ionization energies of the Li-like to Al-like Y

Sp. Name.	**Ion charge**	**Iso. Seq.**	**Ground Shells**	**Ground Level**	**Ionized Level**	**Ionization energy (eV)**
Y XXVII	26+	Al	[Ne]$3s^2$3p	$^2\mathrm{P}^o_{1/2}$	$3s^2\ ^1\mathrm{S}_0$	1300
Y XXVIII	27+	Mg	[Ne]$3s^2$	$^1\mathrm{S}_0$	$3s\ ^2\mathrm{S}_{1/2}$	1427.6
Y XXVIV	28+	Na	[Ne]$3s$	$^2\mathrm{S}_{1/2}$	$2p^6\ ^1\mathrm{S}_0$	1483.12
Y XXX	29+	Ne	$1s^22s^22p^6$	$^1S_0$	$2p^5\ ^2\mathrm{P}^o_{3/2}$	3562.9
Y XXXI	30+	F	$1s^22s^22p^5$	$^2\mathrm{P}^o_{3/2}$	$2p^4\ ^3P_2$	3720
Y XXXII	31+	O	$1s^22s^22p^4$	$^3\mathrm{P}_2$	$2p^2_{1/2}\ ^2p_{3/2}\ (0,3/2)\ ^0_{3/2}$	3892
Y XXXIII	32+	N	$1s^22s^22p^3$	$(0,3/2)^0_{3/2}$	$2p^2\ ^3\mathrm{P}_0$	4060
Y XXXIV	33+	C	$1s^22s^22p^2$	$^3\mathrm{P}_0$	$2\mathrm{p}\ ^2\mathrm{P}^0_{1/2}$	4299
Y XXXV	34+	B	$1s^22s^2$2p	$^2\mathrm{P}^0_{1/2}$	$2\mathrm{s}\ ^1\mathrm{S}_0$	4484
Y XXXVI	35+	Be	$1s^22s^2$	$^1\mathrm{S}_0$	$2\mathrm{s}\ ^1\mathrm{S}_{1/2}$	4724
Y XXXVII	36+	Li	$1s^2$2s	$^2\mathrm{S}_{1/2}$	$1\mathrm{s}^2\ ^1S_0$	4875.731

7.3 Wavelength Calibration

The data analysis necessary to identify the yttrium transitions began with a rigorous calibration procedure. Thirty four known spectral lines originating from Ne, Xe, Ba, Fe and O ions were used to calibrate the spectra. Neutral neon and oxygen atoms were injected into the EBIT via the gas injection system. The MeVVA was used to inject singly charged Fe ions into the EBIT. Xe and Ba exist in the EBIT as impurities and are always present within the trapping region during the cooking cycle. Ba atoms are sputtered off of the electron gun cathode that is coated in BaO_2. Trace amounts of Xe have accumulated over time in the EBIT from previous measurements. The goal of calibrating the spectrometer is to convert the detector's channels into values of wavelength in order to identify spectral features.

The following calibration procedure was employed to properly convert the channel numbers into quantities representing wavelength in nm.

1. The calibration lines were fitted with Gaussian functions. The uncertainty associated with the fitting procedure represents the uncertainty associated with spectral line centroid position in channel number. The spectral features that were blended with other features required a weighted multi-peak Gaussian fitting routine where each peak was as-

Table 7.4: List of calibration lines used to calibrate the EUV spectra. The lines are adopted from [ORGR12, KRRN18]

Lines	**Wavelength (nm)**	**Wavelength uncertainty (nm)**	**Channel number**	**Channel uncertainty**
Xe^{41+}	5.2154	0.0025	216.251	0.0187755
Xe^{41+}	6.1622	0.0025	373.066	0.0944335
Xe^{42+}	6.2909	0.0025	394.025	0.00838769
Xe^{43+}	6.6623	0.0007	452.457	0.0135957
Xe^{43+}	12.392	0.003	1229.2	0.0231736
Xe^{42+}	12.5818	0.005	1251.87	0.0452002
Xe^{42+}	12.993	0.003	1301.09	0.052171
Xe^{43+}	13.3246	0.0014	1339.57	0.0463705
Ne^{7+}	6.73832	0.00012	464.14	0.0127339
Ne^{6+}	7.5764	0.0004	590.845	0.0680129
Ne^{7+}	8.80929	0.00014	767.439	0.0238587
Ne^{6+}	9.7502	0.0004	895.317	0.0313637
Ne^{7+}	9.82629	0.00021	905.341	0.215969
Ne^{7+}	10.3084	0.00019	968.783	0.0689785
Ne^{6+}	10.6073	0.0005	1007.55	0.0547047
Ne^{6+}	10.6189	0.0005	1009.11	0.0304425
Ne^{5+}	11.1136	0.0018	1071.9	0.0392911
Ne^{6+}	11.6691	0.0005	1140.96	0.0467289
Ne^{5+}	12.2702	0.00017	1214.27	0.0587002
Ne^{6+}	12.7676	0.0007	1273.88	0.00623614
Ne^{4+}	14.3314	0.0007	1455.04	0.0290278
Ne^{4+}	14.7138	0.0007	1498.11	0.00529119
Ne^{4+}	15.452	0.0007	1579.89	0.0974946
Ne^{7+}	17.6186	0.00028	1810.64	0.0857756
Ne^{6+}	19.5004	0.0008	2002.02	0.0231841
Ne^{7+}	19.6233	0.00042	2014.29	0.0713373
Ne^{7+}	19.6526	0.00042	2017.09	0.0363498
Fe^{22+}	13.2906	0.0005	1335.41	0.0940637
Fe^{23+}	19.2028	0.0005	1972.22	0.0425429
O^{5+}	15.0101	0.0005	1531.14	0.0461736
O^{4+}	17.2169	0.0003	1768.9	0.0622205
O^{5+}	17.3081	0.0005	1778.37	0.036901
Ba^{42+}	4.5788	0.001	103.683	0.0337459
Ba^{43+}	4.761	0.001	136.15	0.0256237
Ba^{43+}	5.5725	0.001	276.309	0.020211

signed a proper weighting factor. These weights was derived by a comparison with the published literature values of these lines. For instance, the line from Ne^{7+} at 9.82629(21) nm in Table 7.4 was determined from the listed values of 9.81166(21) nm, 9.82615(21) nm, and 9.82757(21) nm with weights 55.6, 100.0 and 11.1, respectively. This line contained two resolvable peaks in the observed spectra: the first peak closely overlapping with the first line at 9.81166(21) nm and the second peak being the combination of the lines at 9.82615(21) nm and 9.82757(21) nm. A weighted average of the wavelengths and their weighting factors was used to determine the wavelength of the secondary peak. The weighted average, equation 7.1, assigned the value of 9.82629(21) nm to this peak with a weighting factor of 111.1, nearly double that of 55.6 assigned to the first peak at 9.81166(21) nm.

$$\left(\frac{9.82615 \times 100.0 + 9.82757 \times 11.1}{100.0 + 11.1}\right) \tag{7.1}$$

As a result, the first and second peaks were given a weighting factor of $\frac{55.6}{(55.6+111.1)} = 33.35$ % and $\frac{111.1}{(55.6+111.1)} = 66.65$ %, respectively during the fitting process. The calibration spectra is shown in Figure 7.2.

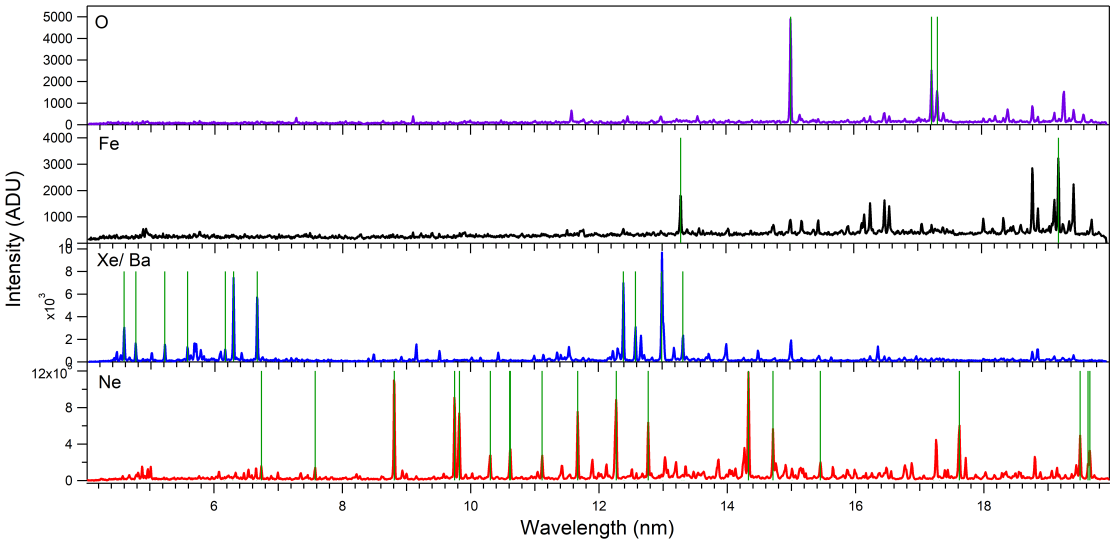

Figure 7.2: EUV spectra of Ne (red), Xe (blue), Fe(black) and O(purple) ions used for calibration purposes. The vertical green lines correspond to the spectral lines used for calibration. ADU stands for analog to digital units of the CCD detector used.

2. The channel number uncertainties are unit less quantities that must be converted to units of nm to produce the total uncertainty. The total uncertainty is given by the quadrature sum of this uncertainty and the uncertainty in the wavelength values from literature. To convert the channel number uncertainty to units in nm, the wavelength versus channel number dataset was first fitted with a third order polynomial.

$$\lambda = K0 + K1 \times x + K2 \times x^2 + K3 \times x^3 \tag{7.2}$$

Here, x is the channel number and λ is the wavelength in nm. The dispersion relation is given by equation 7.3.

$$\frac{\partial \lambda}{\partial x} = K1 + 2 \times K2 \times x + 3 \times K3 \times x^2 \tag{7.3}$$

The uncertainty in the channel number in terms of wavelength is given by 7.4.

$$\Delta\lambda_{eff} = \Delta x \times \frac{\partial \lambda}{\partial x} \tag{7.4}$$

Thus, the total uncertainty in wavelength of the calibration lines is given by 7.5.

$$\Delta\lambda_{total} = \sqrt{(\Delta\lambda_{eff})^2 + (\Delta\lambda^2)} \tag{7.5}$$

A simple picture of the 2D error bars in the wavelength and channel number is shown in 7.3. The analysis software used, Igor Pro, could not accommodate weighted fits in both dimensions. This required combining the uncertainties in a 1D vector as described above.

3. The uncertainty shown by equation 7.5 does not include the systematic uncertainties attributed to experimental limitations. These include individual pixel response of the CCD detector, instrumental vibrations and drifts, and other unidentified sources of error. The systematic uncertainty was estimated by determining a constant offset (in nm) that was added in quadrature to the total $\Delta\lambda_{total}$ until the reduced chi-square of the poly-

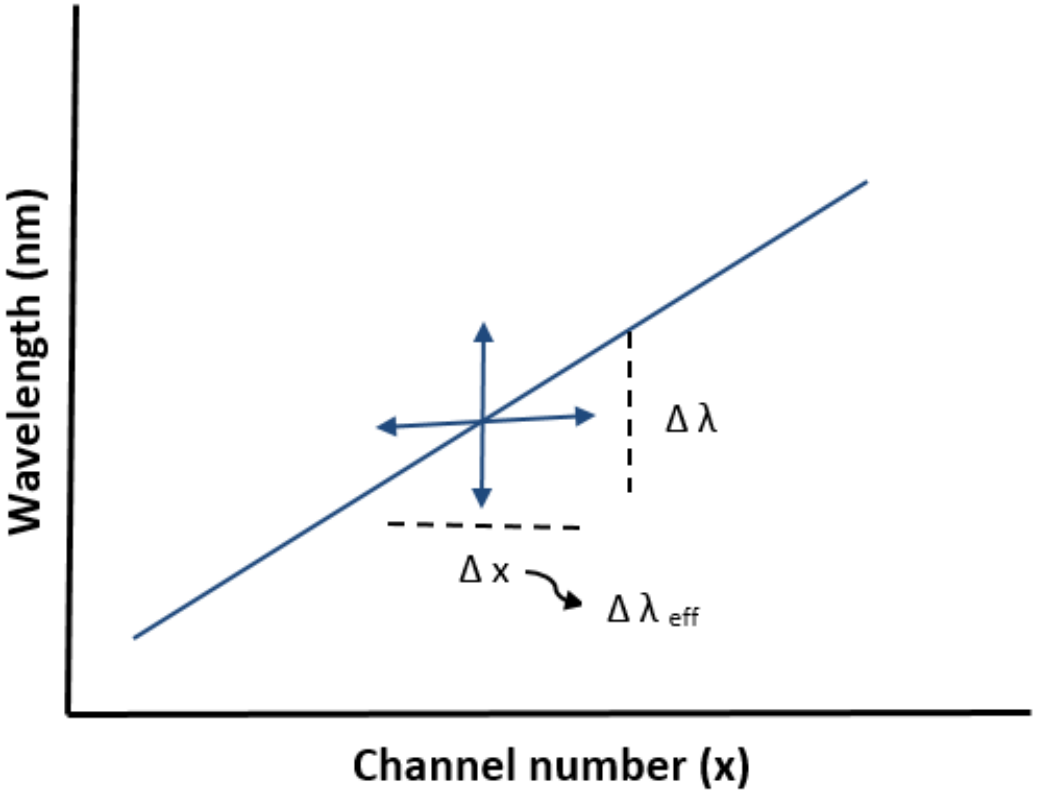

Figure 7.3: A schematic of the wavelength versus channel number. The uncertainties are shown as the 2D error bars.

nomial fitting approach 1. This statistical methodology is a standard procedure in proper data analysis of experimental data [HT10]. The reduced χ^2_{red} is defined as χ^2/n_{dof}. Here, n_{dof} is the number of the degrees of freedom during the fitting process, which equals to the difference of the number of data points N and the number of fitting parameters ν. In this analysis, $\nu = 4$ and N = 35 producing a χ^2 of ≈ 31. With this method, the value for the systematic uncertainty was determined to be 0.0006 nm. Figure 7.4 shows the wavelength versus channel number fit along with the total uncertainty represented as error bars associated with the data points.

4. The residuals between the fitting function and the data points was calculated and falls within the 95 % confidence intervals. This confidence band provides a visual

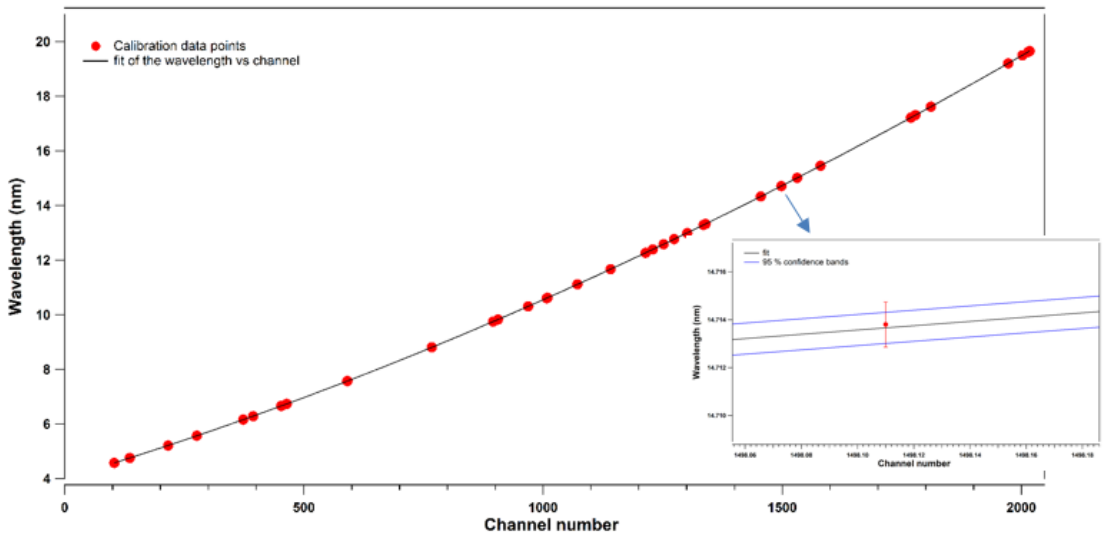

Figure 7.4: The wavelength versus channel number plotted for the calibration data points (red) and a third order polynomial fit (black). A zoomed in view for the data point at 14.7138 nm is shown with the total uncertainty as the error bar and the 95 % confidence band.

representation of the region that should statistically include 95 % of residual data points and represents the two standard deviation (σ) uncertainty about the mean (μ). For a statistically accurate fit, the residuals should fluctuate within the confidence interval about a mean of zero . Figure 7.5 shows the residuals and the 95 % confidence band for the dataset used for our analysis. To determine the residual, the wavelength from the fit was calculated using $fit_{wavelength}$= K0 + K1 $\times$ channel+ K2 $\times$ (channel)^2 + K3 $\times$ (channel)^3. The residual is then given by the difference between the actual wavelength of the lines and the fitted wavelength. Similarly, the confidence bands from the fit function are determined from the fitting routine used.

$$P(\mu - 2\sigma) \leq x \leq P(\mu + 2\sigma) \tag{7.6}$$

5. Once the fitting function is finalized, the channel numbers are converted to values of wavelength in nm using the 3^{rd} order polynomial 7.7. The result of this calibration procedure produced an observable wavelength region of 4.0225 nm to 19.9565 nm. The

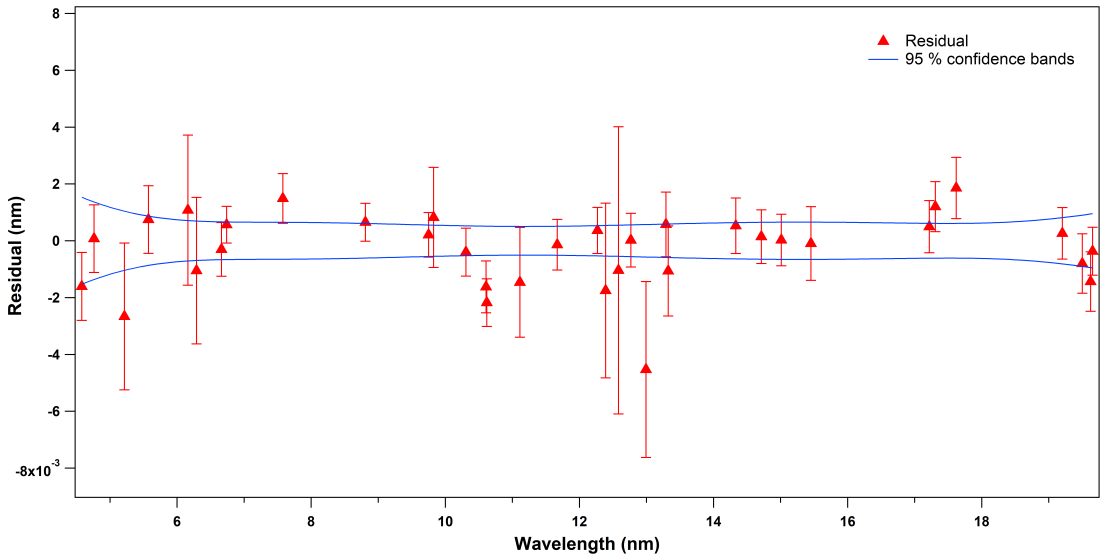

Figure 7.5: Residual of the calibration data points from literature as a function of wavelength (red triangles) and a 95 % confidence band of the calibration fit (blue).

calibration was carried out for the CCD micrometer gauge setting of 0.994" [See 6.2].

$$\lambda = 4.0225 + 0.0052442 \times x + 1.3245E - 06 \times x^2 - 4.1016E - 011 \times x^3 \qquad (7.7)$$

Different gauge settings require separate calibration procedures. The linear translation stage of CCD detector allows for coverage of the wavelength range from 1 nm to 40 nm

7.4 Theory and Line Identification

After calibrating the instrument, the Y spectra was plotted as a function of the calibrated wavelengths in order to identify transitions. The line identification process was aided by comparing the calibrated Y spectra to the synthetic spectra produced by the CR model NOMAD [RM01]. The atomic data necessary for a particular charge state was computed using the FAC atomic structure calculation package [Gu08]. FAC simulations provided the transitional wavelengths, energy levels, transition probabilities, and the cross-sections for excitation, ionization, and recombination processes for the Li-like Y through Al-like Y charge states. These data were used in the NOMAD calculations that included 13 ionization

stages from Si-like to He-like Y ions. The collisional radiative model included 5000 atomic levels and about 1.5 million transitions that describe the atomic processes prominent in EBIT plasma. These include electron impact ionization and excitation, radiative recombination, radiative decays, and charge exchange with neutral atoms. The inclusion of the charge exchange process between highly charged ions and neutral atoms is critical in these models as it effects the ionization balance in the plasma.

The Y plasma was modeled by assuming a steady-state charge state distribution. The electron density of the electron beam is 10^{11} cm^{-3}, sufficiently low allowing for the 3-body recombination process to be neglected. The electron beam energy was modeled as a Gaussian distribution with a FWHM of 40 eV. The ions undergo charge exchange processes with the neutrals, where the rate of charge exchange depends on the charge exchange cross section σ_{CX}, the density of the neutrals N_n, and the effective relative velocity of the particles$\tilde{v_r}$ [RDT$^+$08]. The charge exchange (CX) rate is given by:

$$R_{CX} = N_n \sigma_{CX} \tilde{v_r} \tag{7.8}$$

N_n and $\tilde{v_r}$ are adjustable parameters and can change from one measurement to another. The product of $N_n \tilde{v_r}$ is treated as a free parameter that is varied in the model to match the theoretical to the measured spectra. Another free parameter during the calculation is the electron beam space charge correction. This value is usually adjusted to match the energy dependence of the line intensities of the transitions in the measured and theoretical spectra. There was good agreement between the theoretical and experimental spectra for the spectral line intensities of the transitions with a space charge potential of 150 eV. A measured spectra at 5 keV was in good agreement with the calculated spectra at 5.15 keV. Since the space charge potential depends on the electron beam energy, this parameter changes with beam energy changes as discussed in section 5.3. A convolution of the synthetic spectra with the instrumental energy resolution of the EUV spectrometer allowed for determining the efficiency function of the instrument, needed to accurately generate the theoretical

spectra. The calculated spectra also includes the second and third order transitions to further simplify the line identification process. Figure 7.6 shows the comparison of the calculated spectra at 5 keV with the measured spectra at 5.15 keV. It can be seen from Figure 7.6 that the comparison of modeled spectra with the experimental spectra properly accounts for the ionization balance and helps to identify the transitions.

The output of the modeling for a given charge state is shown in Tables 7.5 and 7.6. Table 7.5 shows the list of the 29 dominant transitions for the Li-like Y ions. Among the 29 transitions listed, we were able to identify the two strongest transitions at theoretical wavelengths of 7.2771 nm and 15.7139 nm. Table 7.6 shows the energy, parity, 2J values and coupling information for ten energy levels for the C-like Y ions. 1*2 represents 2 electrons in the n = 1 shell, 2*4 represents 4 electrons in the n = 2 shell and so on. C-like Y ions have 6 electrons overall (2 in the n =1 shell and 4 in the n = 2 shell). The jj notation for FAC is represented as ($nl \pm n_e$ ($2J_{nl\pm}$) $2J_{total}$). In this notation, n_e is the number of electrons in the nl state, $2J_{nl}$ is 2 times the J value for $nl\pm$ electrons, and $2J_{total}$ is 2 times the total J for all electrons. The electron configuration for energy level 1 is given by $1s^2 2s^2 2p^2$. The notation 2p-2(0)0 for this configuration indicates that there are 2 electrons in the p state with a total J of 0. FAC does not include the sub-shells that couple to a zero total angular momentum in the jj notation. For instance, the NOMAD energy level 16 from the C-like Y in Table 7.6 has a jj notation of $(2p^+)^2$. This is because among the four electrons in the p state, two combine to a 2p+2(0)0 configuration and the remaining two electrons couple to zero angular momentum.

For the electron beam energies lower than 3.75 keV, FAC did not provide good agreement with the observed spectra. To improve the agreement, the M-shell transitions (Na-like through Al-like Y) and the Ne-like Y charge states were calculated with a more accurate RMBPT method [SCS05]. These systems have many electrons therefore complicating the theory. Many body perturbation theory can treat these systems with better accuracy compared to the FAC calculations.

The theoretical data for the energy level populations, transition rates and the tran-

Table 7.5: The output of NOMAD for the strongest transitions in Li-like Y (Y^{37+}). The intensity of the transitions in decreasing order is listed along with the lower and upper level corresponding to the transitions.

Wavelength (nm)	Intensity (arb. un.)	Charge state	Lower level				Upper level			
			Configuration		Energy level	J	Configuration		Energy level	J
7.2771	3.10E-52	37	0	$2s^1$	1	0.5	0	$2p^1$	3	1.5
15.7139	1.84E-52	37	0	$2s^1$	1	0.5	0	$2p^1$	2	0.5
13.5538	3.36E-56	37	0	$2p^1$	2	0.5	0	$2p^1$	3	1.5
5.4404	2.55E-67	37	0	$5g^1$	24	4.5	0	$6h^1$	35	5.5
5.4324	2.07E-67	37	0	$5g^1$	23	3.5	0	$6h^1$	33	4.5
5.4319	1.41E-67	37	0	$5f^1$	22	3.5	0	$6g^1$	34	4.5
5.4178	1.08E-67	37	0	$5f^1$	21	2.5	0	$6g^1$	32	3.5
5.4173	5.68E-68	37	0	$5d^1$	20	2.5	0	$6f^1$	31	3.5
5.3866	3.93E-68	37	0	$5d^1$	19	1.5	0	$6f^1$	30	2.5
5.5422	1.92E-68	37	0	$5p^1$	18	1.5	0	$6s^1$	25	0.5
5.3468	1.74E-68	37	0	$5p^1$	18	1.5	0	$6d^1$	29	2.5
5.1626	1.19E-68	37	0	$5s^1$	16	0.5	0	$6p^1$	27	1.5
5.2394	9.08E-69	37	0	$5p^1$	17	0.5	0	$6d^1$	28	1.5
5.4018	8.66E-69	37	0	$5p^1$	17	0.5	0	$6s^1$	25	0.5
5.2372	7.08E-69	37	0	$5s^1$	16	0.5	0	$6p^1$	26	0.5
5.4804	5.37E-69	37	0	$5d^1$	20	2.5	0	$6p^1$	27	1.5
5.4454	4.68E-69	37	0	$5g^1$	24	4.5	0	$6h^1$	33	4.5
5.4394	3.99E-69	37	0	$5f^1$	22	3.5	0	$6g^1$	32	3.5
5.5193	3.58E-69	37	0	$5d^1$	19	1.5	0	$6p^1$	26	0.5
5.4298	2.82E-69	37	0	$5d^1$	20	2.5	0	$6f^1$	30	2.5
5.3714	1.91E-69	37	0	$5p^1$	18	1.5	0	$6d^1$	28	1.5
5.4523	1.53E-69	37	0	$5f^1$	22	3.5	0	$6d^1$	29	2.5
5.4560	1.07E-69	37	0	$5f^1$	21	2.5	0	$6d^1$	28	1.5
5.4529	8.92E-70	37	0	$5g^1$	24	4.5	0	$6f^1$	31	3.5
5.4525	6.93E-70	37	0	$5g^1$	23	3.5	0	$6f^1$	30	2.5
5.4365	5.69E-70	37	0	$5d^1$	19	1.5	0	$6p^1$	27	1.5
5.4306	7.41E-71	37	0	$5f^1$	21	2.5	0	$6d^1$	29	2.5

Table 7.6: 20 energy levels with increasing energy for C-like Y is listed. The configurations and jj notations for the levels are listed as well.

FAC	1.1.1	
Endian =	0	
TSess =		1392060371
Type =	1	
Verbose =	1	
Y	Z =	39
NBlocks =	2	
E0 =	0,	-5.99E+04
NELE =	6	
NLEV =	656	

NOMAD energy level	FAC energy level	Energy (eV)	P	VNL	2J							
1	0	0	0	201	0	1*2	2*4	$2p^2$	2p-2(0)0			
2	1	72.5	0	201	2	1*2	2*4	$2p^2$	2p-1(1)1	2p+1(3)2		
3	2	84	0	201	4	1*2	2*4	$2p^2$	2p-1(1)1	2p+1(3)4		
4	3	164	0	201	4	1*2	2*4	$2p^2$	2p+2(4)4			
5	4	184	1	201	4	1*2	2*4	$2s$	$2p_3$	2s+1(1)1	2p+1(3)4	
6	5	191	0	201	0	1*2	2*4	$2p^2$	2p+2(0)0			
7	6	231	1	201	2	1*2	2*4	$2s$	$2p^3$	2s+1(1)1	2p+1(3)2	
8	7	261	1	201	4	1*2	2*4	$2s$	$2p^3$	2s+1(1)1	2p-1(1)0	2p+2(4)4
9	8	282	1	201	6	1*2	2*4	$2s$	$2p^3$	2s+1(1)1	2p-1(1)2	2p+2(4)6
10	9	305	1	201	0	1*2	2*4	$2s$	$2p^3$	2s+1(1)1	2p-1(1)0	2p+2(0)0
11	10	313	1	201	2	1*2	2*4	$2s$	$2p^3$	2s+1(1)1	2p-1(1)2	2p+2(4)2
12	11	322	1	201	4	1*2	2*4	$2s$	$2p^3$	2s+1(1)1	2p-1(1)2	2p+2(4)4
13	12	331	1	201	2	1*2	2*4	$2s$	$2p^3$	2s+1(1)1	2p-1(1)2	2p+2(0)2
14	13	386	1	201	4	1*2	2*4	$2s$	$2p^3$	2s+1(1)1	2p+3(3)4	
15	14	424	1	201	2	1*2	2*4	$2s$	$2p^3$	2s+1(1)1	2p+3(3)2	
16	15	456	0	201	4	1*2	2*4	$2p^4$	2p+2(4)4			
17	16	485	0	201	0	1*2	2*4	$2p^4$	2p+2(0)0			
18	17	534	0	201	2	1*2	2*4	$2p^4$	2p-1(1)1	2p+3(3)2		
19	18	548	0	201	4	1*2	2*4	$2p^4$	2p-1(1)1	2p+3(3)4		
20	19	643	0	201	0	1*2	2*4	$2p^4$	2p+4(0)0			

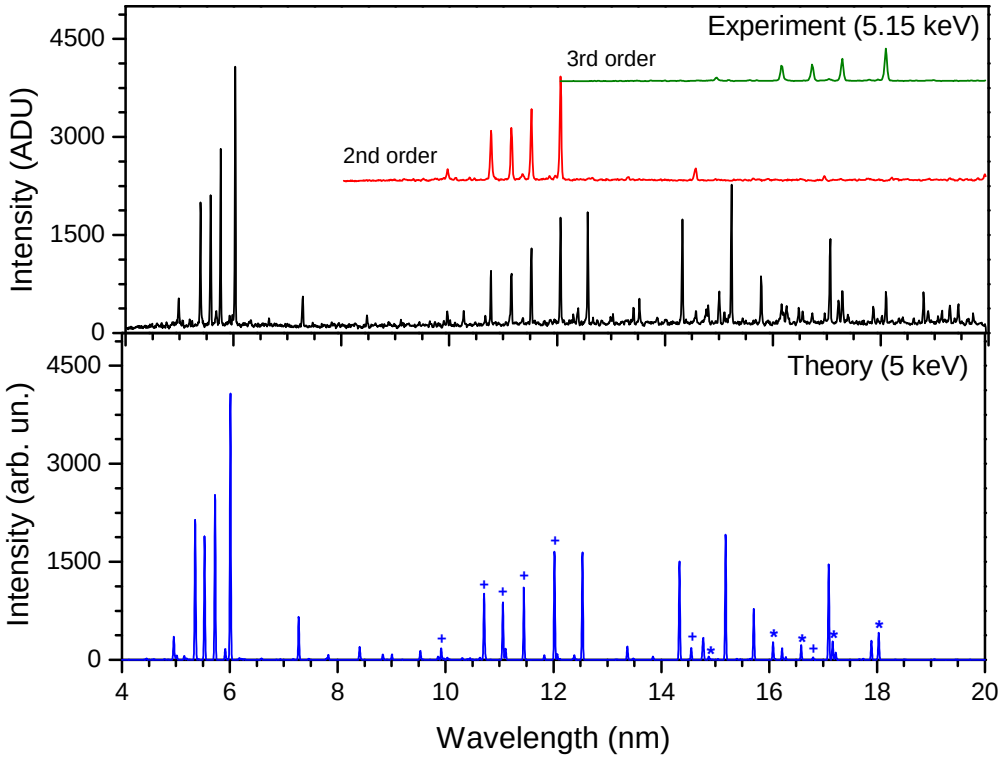

Figure 7.6: Comparison of the measured yttrium spectra at 5.15 keV (black) with the calculated spectra at 5 keV (blue). The second (red) and third (green) order measured spectra along with the second (+) and third (*) lines in the calculated spectra are shown.

sition wavelengths provided enough information to identify most of the strong and isolated lines. Comparison of the line intensities and line positions helped to identify the measured lines without ambiguity in most of the cases. For lines blended with other unknown and unresolved features, the line intensities of the transitions were plotted as a function of electron beam energy. Intensities of lines emitted from the same ionization state usually depend on the electron beam energy in a similar way. This is because the excitation cross sections vary much slower with the electron impact energy than the ionization cross sections near the ionization threshold. These qualitative dependences aided our line identification and is illustrated in Figure 7.7. Transitions corresponding to three charge states, Y XXXIV, Y XXXV and Y XXXVI are shown along with their respective ionization energies.

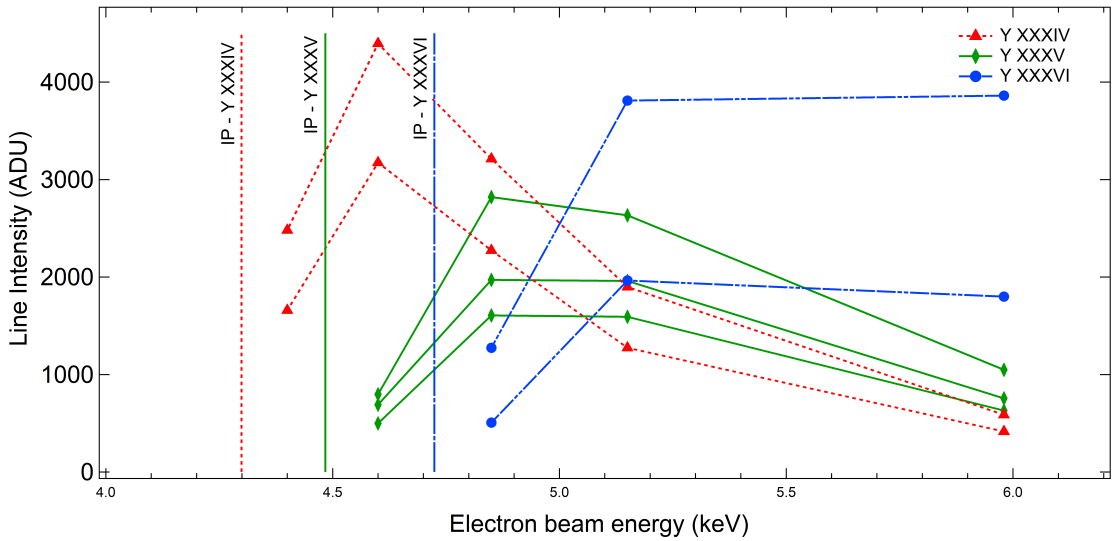

Figure 7.7: Line intensities in units of ADU for the charge states Y XXXIV (red), Y XXXV (green) and Y XXXVI (blue) as a function of electron beam energy in keV. The ionization energies for the respective charge states are labeled as IP. Note: The electron beam energy is not space charge corrected.

To determine the line positions of the Y spectral lines, Gaussian functions were used to fit the Y peaks. For a single unblended strong peak, a single Gaussian function was used to fit the structure. For lines that were blended with other known line features, a multi-peak Gaussian fit was employed to properly account for the structure of the peaks. A particular transition can appear at different beam energies and for such transitions, the wavelength was determined at all energies where the lines were strong and unblended. Similarly, the reflection grating of the EUV spectrometer allows for the observation of multiple diffraction orders from the same transition. For cases where the transitions were observed in second and third order, the obtained wavelength was divided by 2 or 3, respectively to obtain a final combined wavelength in the first order. The observation of the second and third orders of the transitions can also provide an improved visual test of the identified lines. All of the values for a particular transition observed at different beam energies and different orders of diffraction were combined to get a weighted average. Only the transitions that are strong and cleanly separated were selected for the analyses. For lines that were blended with other features, the wavelength corresponding to the energy with the strongest peak was reported.

The reported wavelength for all of the transitions was obtained by using the weighted mean defined as:

$$\bar{x} = \frac{\sum_{i}^{n} w_i x_i}{\sum_{i}^{n} w_i} \tag{7.9}$$

where the weight, w_i of the line at the position x_i is $1/\sigma_i^2$, σ_i being the total uncertainty for each measurement. The uncertainty associated with the transitions were obtained by propagating the individual uncertainties appropriately.

7.4.1 Line identification results

Figure 7.8 and Figure 7.9 show the Y spectra with the identified lines at electron beam energies between 2.3 kV and 6 kV. The charge selectivity offered by the EBIT is utilized to create the charge states of interest by changing the beam energy. The charge state evolution with changing beam energies also provides a clear overview of the created charge states. To create a particular charge state, the applied beam energy has to overcome the ionization energy of the preceding charge states. It is generally difficult to create a pure charge state due to the charge exchange of the ions with neutrals. As a result, multiple charge states are observed in the same spectra and the intensity of transitions corresponding to different charge states change with changing beam energy. The intensity of spectral features from lower charge states decrease with the increases in the beam energy. A clear picture of the charge state evolution for the identified Y transitions can be seen in Figure 7.8 and Figure 7.9. At a beam energy of 2.3 keV, Y transitions from M-shell ions (Al-like Y, Mg-like Y and Na-like Y) were observed. The ionization energies for the Al-like Y, Mg-like Y and Na-like Y ions are 1.3 keV, 1.42 keV and 1.48 keV, respectively. As the beam energy is increased from 2.3 keV to 3 keV, the Al-like and Mg-like charge states disappear, while the Na-like charge state stays with decreased line intensity.

The L-shell ions (Ne-like Y to Li-like Y) were created at beam energies of 3.75 keV and higher. The transitions from Ne-like Y charge states were strong at the beam energy

of 3.75 keV. To create lines from F-like charge states, electron beam energy of 4.1 keV was applied in order to overcome the ionization energy for the Ne-like Y of 3.56 keV. The large shift in the ionization energy of 1.48 keV for the Na-like charge state to 3.56 keV for the Ne-like charge state indicated that more energy is necessary to remove an electron from a closed-shell (Ne-like) ion. The ionization energies did not change significantly until the next closed-shell (He-like Y) charge state, which has an ionization energy of approximately 20 keV. At 4.1 keV, we observed the transitions from F-like and O-like Y charge states that have ionization energies of 3.72 keV and 3.89 keV, respectively. The spectral features from O-like charge state appeared at electron beam energy of 4.25 keV, where we observed a few lines from N-like charge state as well. The line intensities of the transitions from N-like charge state that has an ionization energy of 4.06 keV increased at an electron beam energy of 4.4 keV. A few low intensity lines from C-like charge states appeared at this beam energy.

The ionization energies of C-like and B-like Y ions are 4.29 keV and 4.48 keV, respectively. As we varied the electron beam energies from 4.4 keV to 4.6 keV, the lines from C-like charge states began disappearing and the lines from B-like charge states became stronger. The B-like Y lines were strongest at 4.85 keV beam energy. Further increasing the beam energy to 5.15 keV, the spectral features from Be-like charge states became stronger and the intensity of the B-like Y lines decreased. At this beam energy, the Li-like Y lines started to appear. The Li-like Y charge states were more pronounced at a beam energy of 6 keV. The ionization energies for the B-like Y and Li-like Y charge states are 4.72 keV and 4.87 keV, respectively.

The list of identified transitions and details of these transitions are given in Appendix A. The energy level number, configuration and term symbol for the upper and lower levels are listed for all the transitions. Comparison with theoretical wavelengths and previous observed wavelengths is presented as well. Energy level notations are taken from FAC and are given in jj coupling. The plus sign represents $j = l + 1/2$ and the minus sign represents $j = l - 1/2$, where l is the orbital angular momentum. For example, the Be-like line identified at 6.0322(5) nm has a lower level configuration of $2s^2$ and the jj notation for the energy

term is given by $(2s_+^2)_0$. Each electron in the 2s state have a j value of 1/2 such that the total angular momentum for this configuration is 0. Similarly, the upper level $2s2p$ has the jj notation of $(2s_+, 2p_+)_1$, where one electron is in the s_+ state with a j value of 1/2 and another electron is in the p_+ state with a j value of 3/2. The total angular momentum for the upper level is therefore equal to 1.

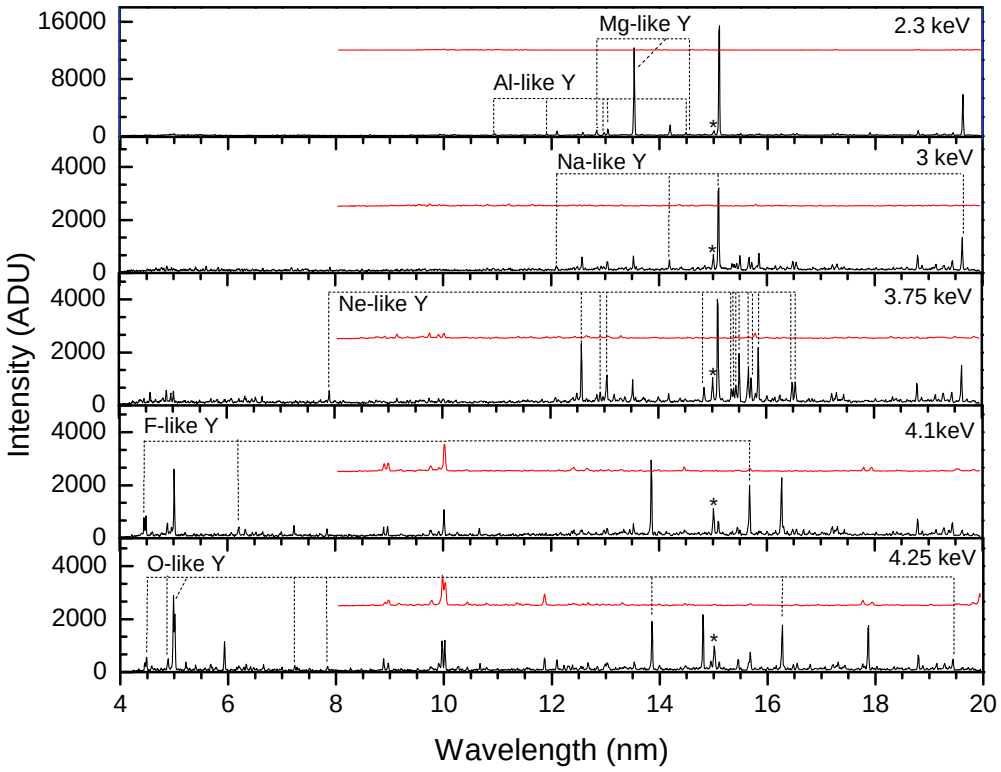

Figure 7.8: Y spectra (black) between energies 2.3 keV and 4.25 keV are shown. The dashed lines (black) correspond to the identified transitions from the O-like Y through Al-like Y charge states. The red spectra offset on top of the black spectra correspond to the second order spectra at different beam energies. The * sign show the impurity line arising from O VI transition. From [STD+17].

Fifty-nine spectral lines were identified corresponding to Δ n = 0 transitions where n = 2 and n = 3. Both electric-dipole and magnetic-dipole transitions were observed and the line intensity ratios of some of the M1 versus E1 lines were seen to have a dependence

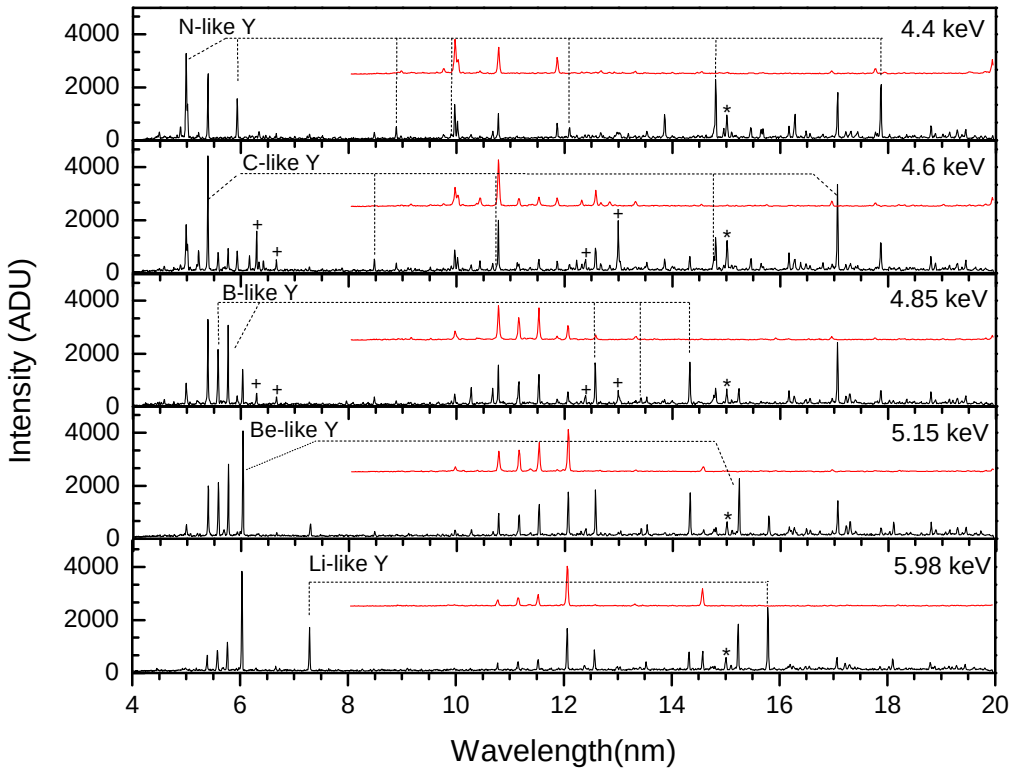

Figure 7.9: Y spectra (black) between energies 4.4 keV and 5.98 keV are shown. The dashed lines (black) correspond to the identified transitions from the N-like Y through Lil-like Y charge states. The red spectra offset on top of the black spectra correspond to the second order spectra at different beam energies. The * sign show the impurity line arising from O VI transition and the + sign show the impurity lines arising from Na-like and Mg-like Xe transitions. From [STD+17]

on the electron density n_e and temperature T. Such dependence can be used to diagnose plasmas by extracting information regarding the plasma parameters, n_e and T from these line intensity ratios. Our measurement led to accurate wavelength determinations of 38 new spectral lines from the Li-like to the Al-like isoelectronic sequences of Y. 21 previously reported transitions were identified and compared with other works. Impurity lines arising from O VI ion at 15.0099(5) nm was present in all the EUV spectra. At the beam energy of 4.6 keV and 4.85 keV, impurity lines originating from Na-like Xe and Mg-like Xe ions were observed. The details of the identified transitions and comparison with previous work

is presented in our scientific report [STD$^+$17]. Our study resulted in line identification of two E1 Be-like Y lines with an increased accuracy in the measurement by Denne *et al.* [DMJ89]. Five transitions from the B-like Y lines were identified with one corresponding to a M1 transition. Three of these transitions were previously reported and agrees with our measured values [MJM$^+$94].

As the number of electrons increase for the C-like, N-like, O-like, F-like charge states, the complication in the calculations increase. The experimental precision is still at the same level as that of one-electron ions. Such measurements therefore provide a direction in further improvement of theoretical work. Through this measurement, we have identified both E1 and M1 transitions corresponding to these charge states. We observed two E1 and a M1 transition from F-like Y charge state. The diagnostic potential of this M1 transition $(2p_+^3)_{3/2}$ - $(2p_+)$ from F-like Y charge state was investigated previously [Rea82, AK16]. Fourteen E1 and one M1 transition in Ne-like Y charge state was identified using RMBPT calculations [SCS05]. The discussion of the measurement of the Li-like resonance lines and Na-like D lines is provided in sections 7.6 and 7.7.

7.5 Error Analysis

Each identified transition had a total uncertainty σ_i, given by the quadrature sum of the following terms:

(1) the statistical uncertainty given by the Gaussian fit of the peak,

(2) the systematic uncertainty derived from the calibration procedure (a constant number of 0.00063 nm), and

(3) the calibration uncertainty of the line position.

The 95 % confidence bands were used to deduce the uncertainty from the calibration (c_i) for a particular wavelength. To do so, the 95 % confidence band (2σ) was fit with a 7^{th} order polynomial given as: $c_i(2\sigma)$ = 0.052966 + (-0.0033082) × Yline + (0.0086963) × Yline^2 + (-0.0012272) × Yline^3 + (0.00010014) × Yline^4 + (-4.723E-06) × Yline^5 + (1.1926E-07)

$\times$ Yline^6 + (-1.2446E-09) $\times$ Yline^7. The calibration uncertainty was then obtained by dividing $c_i(2\sigma)$ by 2. These values provided the same results as the $c_i(1\sigma$ obtained from a 68.3 % confidence band.

The total uncertainty for a wavelength is then weighted by the error propagation method. Applying the error propagation equation to the weighted mean 7.9 results in 7.10.

$$\sigma_\mu^2 = \sum_i \sigma_i^2 (\frac{\partial \bar{x}}{\partial x_i})^2 \tag{7.10}$$

$$\frac{\partial \bar{x}}{\partial x_i} = \frac{\partial}{\partial x_i} \frac{\sum_i (x_i/\sigma_i^2)}{\sum_i (1/\sigma_i^2)} = \frac{1/\sigma_i^2}{\sum_i (1/\sigma_i^2)} \tag{7.11}$$

Combining 7.10 and 7.11, we get:

$$\sigma_\mu^2 = \sum_i \sigma_i^2 \left(\frac{1/\sigma_i^2}{\sum_i (1/\sigma_i^2)} \right)^2 = \frac{1}{\sum_i (1/\sigma_i^2)} \tag{7.12}$$

The total uncertainty for a particular transition is given by 7.13.

$$\sigma_\mu = \sqrt{\frac{1}{\sum_i (1/\sigma_i^2)}} \tag{7.13}$$

7.6 Na-like D transitions

The Na-like D_1 ($3s_{1/2}$ - $3p_{1/2}$) and D_2 ($3s_{1/2}$ - $3p_{3/2}$) transitions are of particular interest in spectroscopy as these transitions are almost 100 $\times$ intense than other Na lines. The Na D-doublet are not separated in the non-relativistic limit as the $3s_{1/2}$ and $3s_{3/2}$ energy levels are degenerate. However, the energy levels split when relativistic effects and QED effects are taken into account. The splitting further increases with increasing ion charge Z [GDR$^+$09, GOR$^+$13]. Figure 7.10 shows the scaling of the relative splitting in Na-like ions as a function of nuclear charge. [Ral17].

First EBIT measurement of the Na-like D transitions of the Y ions was conducted in this work. The Na-like D1 transition (3s - 3p1/2) and the Na-like D2 (3s - 3p3/2) transitions

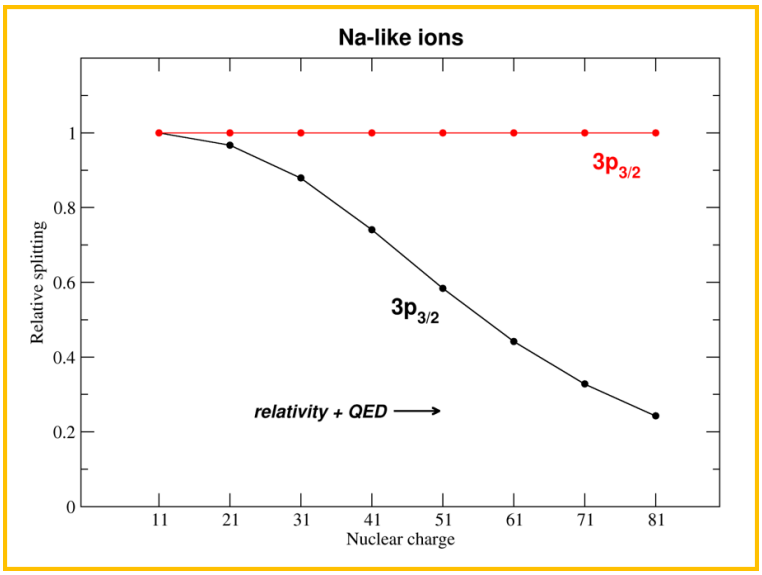

Figure 7.10: Relative splitting of Na-like ions as a function of nuclear charge, Z. From [Ral17].

were measured with an accuracy of 35 ppm and 33 ppm, respectively. The wavelength values were compared with precise RMBPT calculations by Gillaspy *et al.* [GOR$^+$13]. Figure 7.11 shows the Na-like D_1 and D_2 transitions for Y identified at 19.6212(7) nm and 15.1037(5) nm. It can be seen that the line intensities are close to 7000 ADU and 16000 ADU, respectively, for the two D lines that are much more intense than the other Na-like transitions. Our transition wavelength values complements the measurements by Reader *et al.* [RKS$^+$87] and the calculations by Blundell *et al.* [Blu93, GOR$^+$13] and Seely *et al.* [SW90]. The enhanced intensity of the Na-like D transitions leads to spectra with high statistics, making them useful to test the precision of the existing theory.

7.7 Li-like transitions

Two Li-like resonance lines were identified at 7.2874(6) nm for the $2s_{1/2}$ - $2p_{3/2}$ and 15.7862(9) nm for the $2s_{1/2}$ - $2p_{1/2}$ transitions with an accuracy of 82 ppm and 57 ppm, respectively. Li-like systems have a simple quasi-hydrogenic electronic structure with a single electron outside the He-like closed shell. Due to the simplicity in their electronic structure,

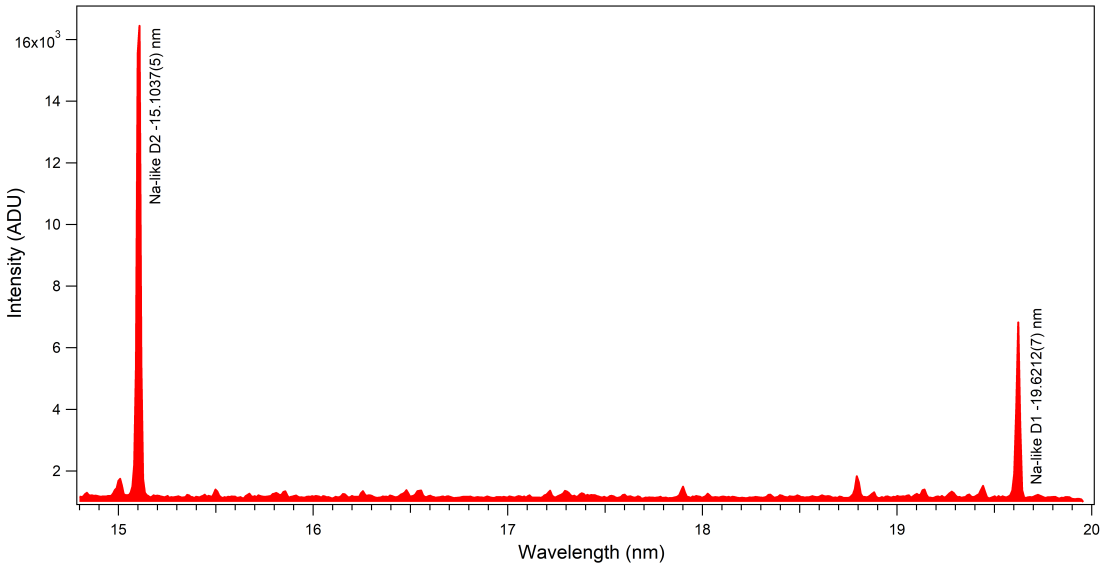

Figure 7.11: The Na-like D_1 (3s - $3p_{1/2}$) and D_2 (3s - $3p_{3/2}$) transitions for Y observed at an electron beam energy of 2.3 keV.

these systems have been investigated theoretically with advanced *ab-initio* methods. Such calculations that include the higher-order QED corrections have been reported for highly charged Li-like ions over the past two decades [Blu93,KBI91,SC11]. For high-Z isoelectronic sequence, the agreement of theory with experiment have been reported [SC08, Bei09]. Our measured value of 15.7862(9) nm for the $2s_{1/2}$ - $2p_{1/2}$ transition agree with the calculations. However, we observed a slight disagreement in the transition wavelength of the $2s_{1/2}$ - $2p_{3/2}$ Li-like transition with that predicted by the theory [KVA$^+$10, SC11]. Both the Li-like spectral lines had a small unresolved blend in their left wing as shown in 7.13. Great care was taken in the estimation of the wavelengths and in the evaluation of the uncertainties of these transitions. The unresolved blends were taken into account by including a second Gaussian function to fit the unknown structure. The comparison of the measured result with the calculations is shown in Figure 6 of Appendix A.

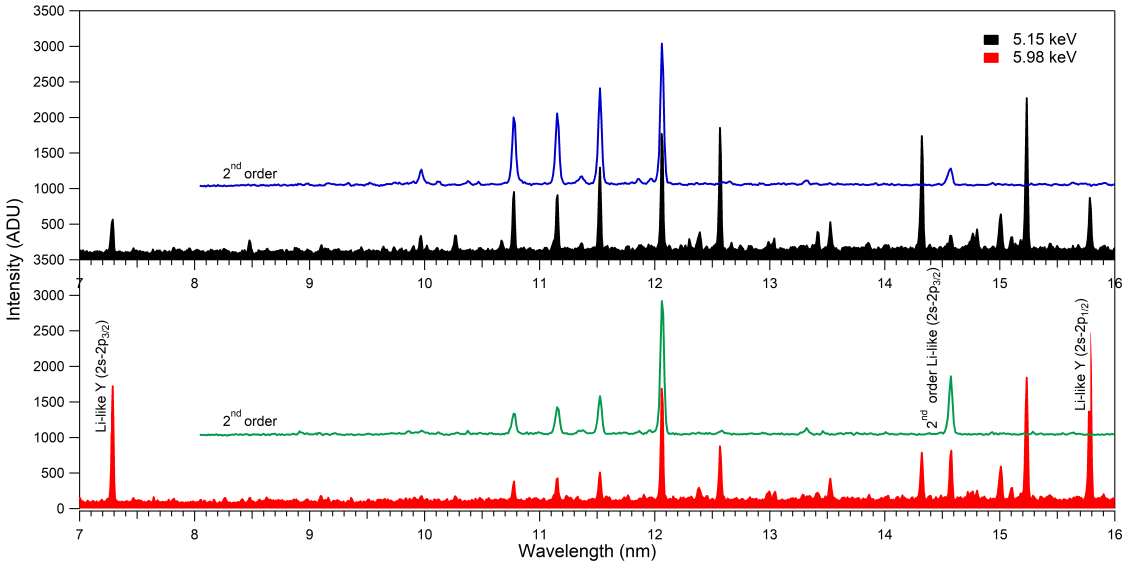

Figure 7.12: The Li-like ($2s_{1/2}$ - $2p_{1/2}$) and ($2s_{1/2}$ - $2p_{3/2}$) transitions for Y observed at an electron beam energy of 5.98 keV (red) and 5.15 keV (black). The second order spectra for 5.98 keV (green) and 5.15 keV (blue) is also shown.

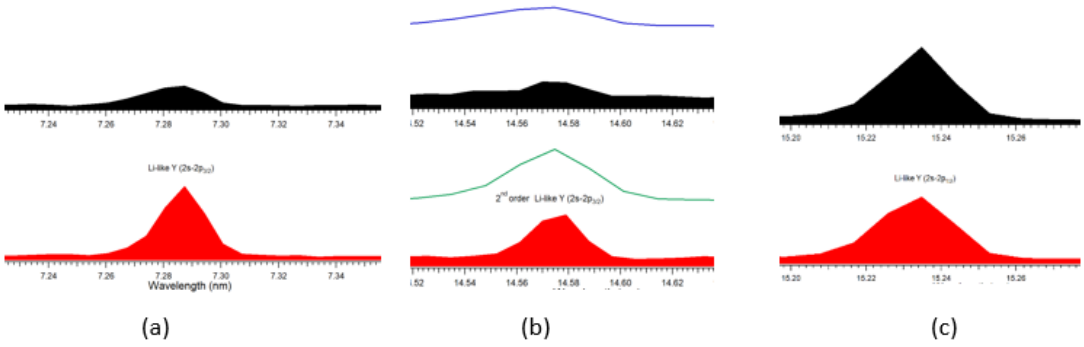

Figure 7.13: Zoomed Li-like Y transitions are shown: (a) First order $2s_{1/2}$ - $2p_{3/2}$, (b) 2^{nd} order $2s_{1/2}$ - $2p_{3/2}$, and (c) $2s_{1/2}$ - $2p_{1/2}$.

7.8 Plasma Diagnostics

10 of the identified transitions originate from the $2s^2 2p^n \rightarrow 2s^2 2p^n$ with n ranging from 1 to 5 corresponding to Δ n =0 M1 transitions. The M1 line at 16.4817(7) nm originated from a transition from an excited configuration $2p^5 3s$ for the Ne-like Y ion.

These transitions carry the potential of plasma diagnostics valuable in hot fusion plasmas as the intensity ratios of some of the spectral lines depend on the electron densities and electron temperatures in these environments. In order to analyze this potential, calculations with NOMAD were performed for a Maxwellian electron energy distribution function with electron densities ranging between 10^{12} cm^{-3} to 10^{20} cm^{-3} and for electron temperatures in the range of 1500 eV to 6000 eV. By using the CR model NOMAD, the Einstein coefficients of the lines were computed with changing electron densities and temperatures. Ratios of the spectral lines that depend on either the density or temperature can be used to extract information on one of the parameters within some range of the other. Figure 7.14 shows the line ratios of some of the identified transitions that show dependence on the electron density for the C-like Y through F-like Y charge states. The most sensitive line-ratios that show density dependence correspond to C-like Y XXXIV, N-like Y XXXIII, O-like Y XXXII, and F-like Y XXXI.

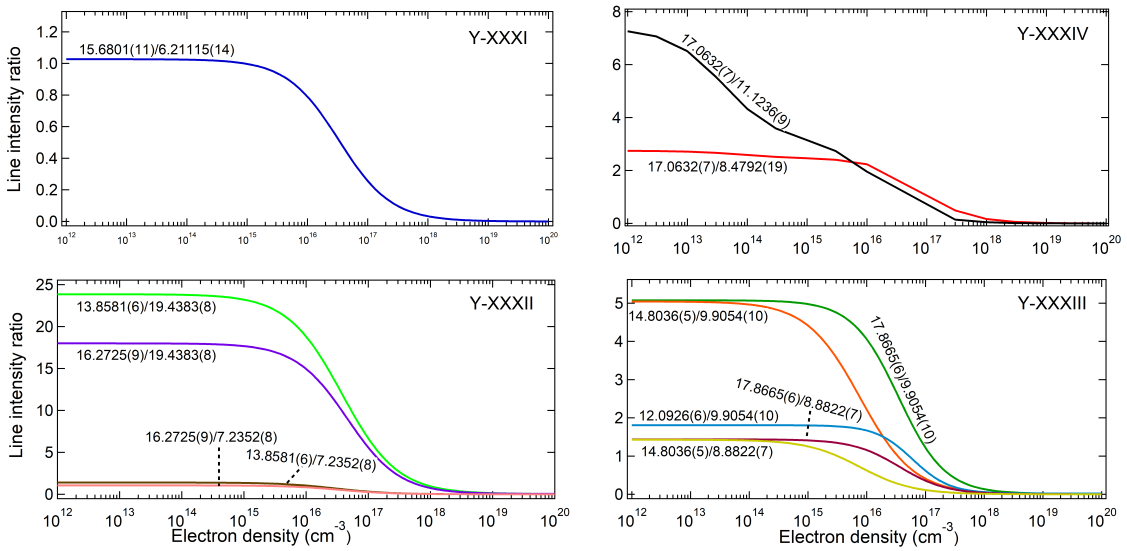

Figure 7.14: The dependence of line intensity ratios with the electron density (cm^{-3}) .

For higher n_e, collisional depopulation becomes comparable to radiative transitions in metastable levels. However, the excited level that leads to an allowed transition decays only by radiation even at higher densities. Thus, the ratio M1/E1 can be sensitive to

Table 7.7: The population and depopulation schemes for the energy levels 3 and 6 from Figure 7.15 are shown with changing electron densities. 3bR, Dxc, Exc, Ion, RaR, and Rad stand for 3 body recombination, de-excitation, excitation, ionization, radiative recombination and radiative decay respectively.

Energy level 3 for N-like Y ion ($2p^3$)						
T=1500 eV	10^{12} cm^{-3}		10^{15} cm^{-3}		10^{18} cm^{-3}	
	In	Out	In	Out	In	Out
3bR	0	0	0	0	0	0
Dxc	0	0	0.06	1.06	1.65	3.87
Exc	28.02	0.04	22.94	25.68	6.22	93.99
Ion	16.05	0	13.11	0.17	3.6	0.63
RaR	0	0	0.07	0.34	0.11	1.25
Rad	55.93	99.96	63.82	72.75	88.42	0.27
Energy level 6 for N-like Y ion ($2s2p^4$)						
T=1500 eV	10^{12} cm^{-3}		10^{15} cm^{-3}		10^{18} cm^{-3}	
	In	Out	In	Out	In	Out
3bR	0	0	0	0	0	0
Dxc	0	0	0	0	0.01	0.23
Exc	82.63	0	82.77	0	85.58	0.16
Ion	6.32	0	6.08	0	2.7	0
RaR	0	0	0	0	0	0.01
Rad	11.05	100	11.15	100	11.71	99.6

the n_e as described in Section 4.3. A justification of this general idea can be provided by comparing the population and depopulation schemes of the upper levels 3 and 6 for a N-like charge state. The transition from the metastable energy level 3, within the ground ($2p^3$) configuration to the lowest level, leads to the M1 transition at 14.8036(5) nm. The transition from excited energy level 6 to the energy level 3 gives rise to the E1 line at 9.9054(10) nm. The upper level 3 corresponds to the excited $2s2p^4$ configuration. Table 7.7 shows how the upper levels 3 and 6 populate and depopulate at different densities. It can be seen from the table that the metastable state $2p^3$ has strong excitation and ionization rates at higher densities and the collisional processes dominate the radiative decay for this level. But for the excited level $2s2p^4$, the levels depopulate mostly by radiative decay even at higher densities.

7.8.1 C-like Y^{33+}

Five lines were identified for C-like Y, with a line occurring at 17.0632(7) nm due to M1 transitions. The ratio of the intensity of this M1 line to the E1 line at 8.4792(19) nm and the E1 line at 11.1236(9) nm varies in the electron density range of 10^{15} cm^{-3} to 10^{18} cm^{-3}. The ratio of the M1 to the line at 11.1236(9) nm also shows some dependence on the electron temperature.

7.8.2 N-like Y^{32+}

Among the seven identified N-like Y lines, 4 lines arise from E1 transitions and 3 from M1 transitions. The ratio of different M1/E1 combinations show a dependence on n_e for the range of 10^{15} cm^{-3} to 10^{18} cm^{-3} by a maximum of two orders of magnitude. The population and de-population scheme for the upper energy levels of some of the transitions for these charge states is shown in Table 7.7. An even better picture of the decay of the upper levels that lead to the observation of different E1 and M1 transitions is illustrated in the Grotrian diagram 7.15. The upper levels correspond to either the ground $2s^2 2p^3$ configuration or the excited $2s2p^4$ configuration. The transitions between the levels in the ground configuration lead to the M1 transitions and the transitions between the levels from the excited configuration to the ground configuration lead to the E1 transitions.

7.8.3 O-like Y^{31+}

Ten O-like Y lines were identified, with two of the lines at 13.8581(6) nm and 16.2725(9) nm originating from M1 transitions. The intensity ratios vary by an order of magnitude or more for these M1/E1 transitions.

7.8.4 F-like Y^{30+}

Among the three identified lines, one line arises from M1 transitions at 15.6801(11) nm and the M1/E1 line ratio of this line with the E1 line at 6.2115(14) nm show a small

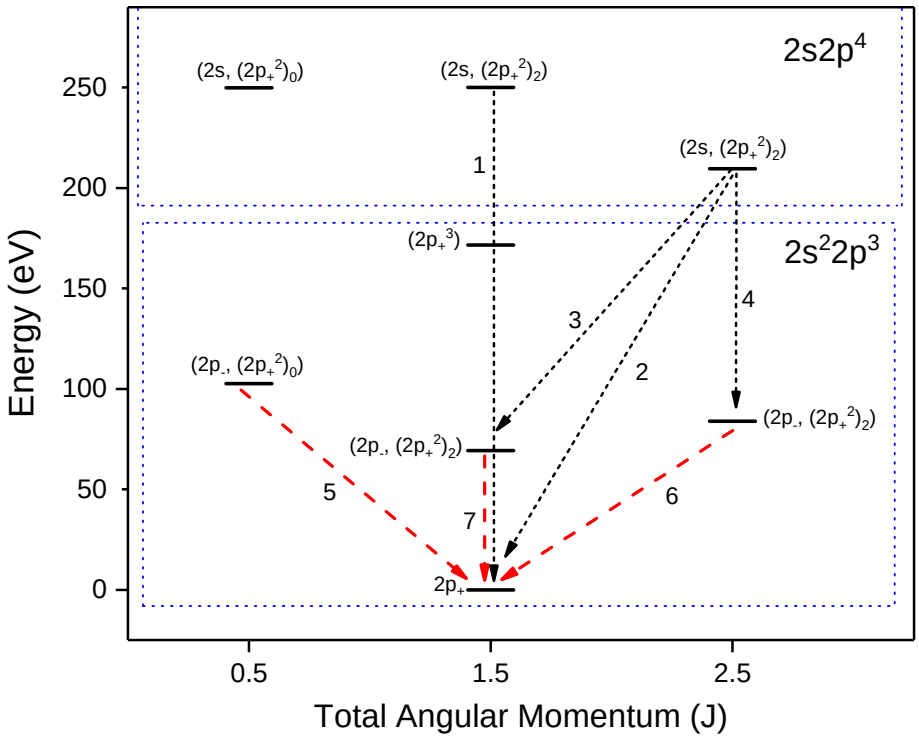

Figure 7.15: 7 transitions corresponding to the N-like Y ions are shown in the Grotrian diagram. The black dotted lines correspond to the 4 E1 transitions and the red dashed lines correspond to 3 M1 transitions. The number labels for lines 1-7 represent the lines at 4.9858(6) nm, 5.9329(4) nm, 8.8822(7) nm, 9.9054(10) nm, 12.0926(6) nm, 14.8036(5) nm, and 17.8665(6) nm.

dependence on electron density of about an order of magnitude. This M1 transition has been previously reported to be significant in plasma diagnostics [Rea82, AK16].

The dependence of the M1/E1 transitions with the changing electron temperatures were studied as well. The ratio of two spectral lines at fixed electron densities can be used to diagnose the temperature of plasmas. Only a few line ratios were seen to show temperature dependence that were not as strong as the density dependence. Figure 7.16 shows a few line ratios that are sensitive to the electron temperature for the B-like Y through the O-like Y charge states.

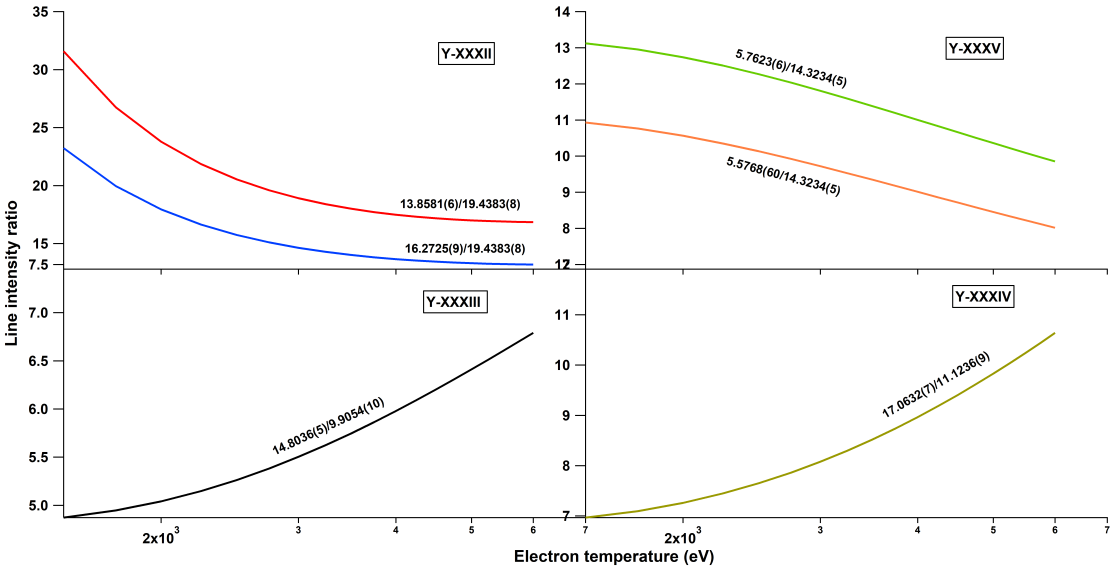

Figure 7.16: The dependence of line intensity ratios with temperature (eV).

With our study of various identified transitions and comparing our results with previous works, we have shown the significance of measuring the EUV spectra from the L-shell ions of Y in providing necessary atomic data to different plasma communities and in testing the existing theoretical framework. Furthermore, the dependence of the line intensity ratios of a few M1 to E1 transitions on electron density and temperature was observed indicating the diagnostics potential of these transitions in high-temperature plasmas.

Chapter 8

New Method to Determine Nuclear Charge Radius Based on EUV Spectroscopy of Na-like Ions

8.1 Introduction

Nuclear mass and nuclear size are fundamental properties of the nucleus that are key to understanding its structure. Atomic transitions, especially in highly charged high-Z systems, are sensitive to these nuclear properties. In particular, the effects of the finite nuclear size scales with increasing Z by a scaling factor of $\approx Z^5$ or Z^6. The nuclear size is four orders of magnitude smaller than the radius of the atomic orbitals. For highly charged systems, the spatial extent of the electronic wave function is reduced and the electronic orbitals are extremely sensitive to interactions with the nucleus. Therefore, observations of transitions can be used to infer information regarding the finite nuclear size. The nuclear size is defined by the nuclear charge radius, which is dependent on the charge distribution of the nucleus. This property is usually parameterized in terms of the root-mean square (RMS) radius $< r^2 >^{1/2}$ because the mean square radius $< r^2 >$, defined by equation 2.35, depends on the nuclear charge distribution ρ_N. A critical evaluation of all the available

experimental data on the RMS charge radii has been provided by Angeli *et al.* [AM13] by including the analysis of all isotopic and isotonic trends.

With the exception of U and Th, the absolute charge radius has not been measured for radioactive isotopes heavier than Bi. There exits only a handful of methods to measure the absolute mean-square radii $< r^2 >$ and the relative mean square charge radii $\delta < r^2 >$. Each method has its own limitations. A review of theoretical and experimental techniques of atomic methods to determine nuclear effects has been compiled by Adrianna Pálffy [Pál10]. Here, we present brief summary of the details of the methods used to determine the absolute and relative mean square charge radii and discuss the motivation for our novel method based on EUV spectroscopy of Na-like ions.

Some of the most reliable measurements of absolute values of RMS radii are conducted through electron scattering [Hof56] and muon spectroscopy [FR53] for stable nuclei. In electron scattering experiments, the differential cross-sections of the interaction between electrons and nuclear target are measured. These measurements are accurate when evaluated in the first order Born approximation for light nuclei. To treat the scattering cross-sections for mid-Z and high-Z nuclei, phase shifts must be included. This method is also limited experimentally to stable isotopes as macroscopic quantities of elements are necessary for the measurement. Recently, the self-confining radioactive isotope (SCRIT) facility developed at RIKEN in Japan conducted the first elastic electron scattering measurements with a minute quantity of the stable ^{132}Xe isotope [TEO$^+$17]. This offers the possibility to perform experiments with radioactive nuclei in the near future.

Muon spectroscopy involves the measurement of the radiation emitted by muons after being captured to a bound orbit. Muons have same charge as that of electrons but are 207 times heavier than the electron. Thus, they form a tighter bound orbital structure with the nucleus. The decay lifetime of the radiation of the 1s muonic orbital is much smaller than the lifetime of the muon. This allows the muonic orbitals to penetrate deep into the nucleus. As a result, the energy of the 1s orbital in a muon can be used as an excellent probe of the nuclear properties. The energies of the transitions scale with the nuclear

excitation energies contributing to large nuclear polarization effects. Since the calculation of nuclear polarization effects is known to have the largest theoretical uncertainties; it limits the accuracy of muon spectroscopic methods. Even so, this method is still one of the most proven techniques to measure absolute RMS radii for stable nuclei. But for non-stable isotopes, this method is not applicable due to the requirement of large sample quantities. The possibility of muon spectroscopy with unstable isotopes using the muon-neutrino facility was first investigated by Jungmann [Jun01].

While the measurement of the absolute RMS nuclear radii is limited to the conventional electron scattering and muonic atom spectroscopy, other spectroscopic methods have been employed to extract the relative RMS nuclear radii $\delta < r^2 >$ between two isotopes. Optical laser spectroscopy (OLS) has been effective in measuring the shift in the frequencies of the optical transitions of interest, termed isotope shift. Two isotopes of a same element have different number of of neutrons, resulting in different mass numbers. This causes the overall charge distribution of the nucleus to vary slightly for the two isotopes, producing the isotope shift between transition frequencies. The first part of the isotope shift is known as the mass shift that arises from the change in the mass of the nuclei of the two isotopes. The second part arises from the change in the nuclear volume and is called the field shift. The details of isotope shift have been provided in Section 2.4. The field shift generally depends on the RMS radii and can be determined by combining the theoretically calculated mass shift with the total isotope shift measured from an experiment. The relative RMS nuclear radii of the two isotopes is deduced from the field shift. Using this technique, the OLS method has been used to detemine $\delta < r^2 >$ for xenon isotopes [BAN$^+$89]. The OLS offers high experimental precision and this method can be applied to stable and unstable isotopic chains. Yet this method is limited by the complex many-electron atomic calculations in neutral atoms and singly-ionized systems can lead to difficulties in interpreting the extracted $\delta < r^2 >$ values.

The specific mass shift (SMS) and the electronic factor (F) defined in Section 2.4 are generally benchmarked by K_α measurements or by King-plot analysis [Kin63]. The

King-plot analysis is a 2-D plot comprised of the comparison of charge radii measurements from different methods on the x and y scale. For the factor F, the shift of the spectral line from a pure configuration with a negligible mass shift is typically shown on the x axis. This analysis is limited, especially for isotopes far from stability, due to the unavailability of data for radioactive isotopes. The evaluation of the charge radius is also dependent on the assumptions taken during the analysis [LRS07]. An example of this is evident in the discrepancy for the Xe isotopic chain, where [LRS07] illustrated the dependence of the results on the method used to determine the electronic factor, F. This dependence is shown in Figure 8.1. The plot shows that the results vary for two different methods used to determine F. This discrepancy suggests the need for more reliable charge radii measurements for the Xe isotopic chain.

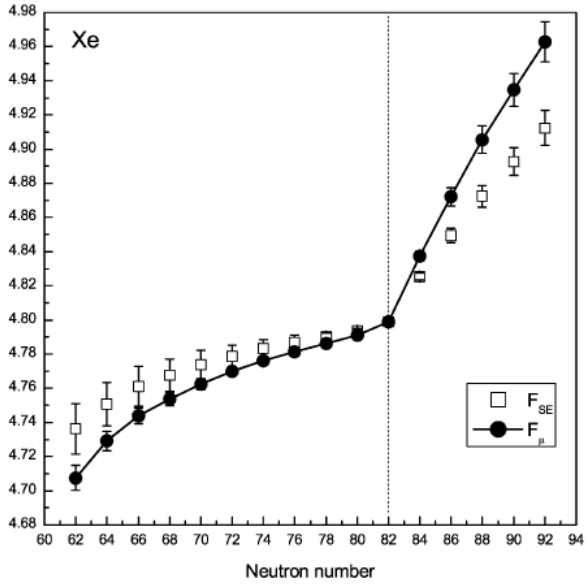

Figure 8.1: Experimental charge radius values for the Xe isotopic chain. F_{SE} correspond to the F factor from semi-empirical calculations and F_{μ} correspond to the King-plot determination of F from muon results. From [LRS07].

Other methods such as K_{α} spectroscopy have been used to measure the isotope shift of X-ray transitions [BBH65]. These few-electron systems do not require as complex atomic structure calculations but are limited practically by experimental precision. The use of

X-ray spectroscopy in combination with highly charged systems to determine $\delta < r^2 >$ was performed with an EBIT by Elliott *et al.* [EBC96]. In their work, the authors highlight the advantage of using highly charged ions in the determination of nuclear charge radii. The few-electron ions, such as the Li-like, Be-like, and B-like U ions pertaining to their study have accurate atomic structure calculations. Furthermore, the highly charged U ions have an enhanced field-shift effect, making these ions suitable to probe the nucleus. But, these systems are difficult to produce experimentally mainly for radioactive isotopes. The nuclear polarization effects dominate in such high-Z systems, complicating the evaluation of $\delta < r^2 >$. The benefit of using highly charged ions in such studies relies on the dependence of the field shift and mass shift on the nuclear charge. The field shift increases with increasing Z and this effect and is amplified for high Z systems as compared to the effect of the mass shift for the same system. Figure 8.2 [LNG$^+$12] shows the dependence of the field shift and mass shift in a Li-like transition on Z.

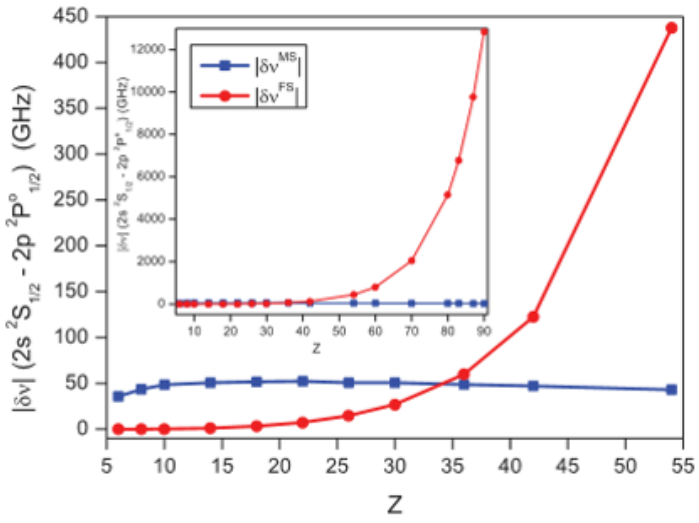

Figure 8.2: Dependence of the mass shift (blue) and field shift (red) as a function of the nuclear charge Z. From [LNG$^+$12].

Another fairly recent method involves DR measurements of Li-like systems [BKM$^+$09] in a storage ring. Measurements of the hyperfine structure of isotopes with different nu-

clear spin were performed by measuring resonant DR features from highly charged ions in an EBIT [SLM$^+$05]. As elements with same Z and different A could have different nuclear spins, the hyperfine interaction can be measured for different isotopes. These processes offer enhanced experimental precision and also have a simplified electronic structure. However, these systems are difficult to create experimentally. The atomic spectroscopic methods described display the relevance of using atomic physics techniques to determine nuclear properties. It has to be noted that the atomic energies by themselves are not sufficient in doing so. Proper inclusion of the electron correlation effects, QED effects, and nuclear polarization effects is necessary to accurately deduce the relative RMS radii.

This work is driven by the need of new methods to investigate the nuclear charge radius. Our work provides a proof-of-principle method to determine $\delta < r^2 >$ using atomic transitions in the EUV region. As discussed earlier in this report, Na-like D (3s - 3p) transitions are good candidates to probe nuclear properties. These systems can be easily created in an EBIT in high numbers and their simple quasi-hydrogenic electronic structure offers enhanced accuracy in the atomic structure calculations. Gillaspy *et al.* [GOR$^+$13] showed that the absolute transition energies of the Na-like D transitions can be calculated with 100 ppm accuracy, given a well-known nuclear charge distribution. In their work, the authors show that the leading uncertainty in the determination of the theoretical transition energy came from the uncertainty of the assumed nuclear size. The ratio of uncertainty of the assumed nuclear size to the total theoretical uncertainty is shown in Figure 8.3. These transitions are sensitive to the nuclear charge due to the strong overlap of 3s orbitals with the nucleus. As a result, such systems are favored to be used to extract information about the nucleus.

The isotope shift between the Na-like D (3s - 3p) transitions and the Mg-like ($3s^2$ - 3s3p) transitions between Xe isotopes ^{124}Xe and ^{136}Xe was measured in this work. The variation in the RMS nuclear radii of Xe isotopes was determined by comparing the measured isotope shift with the calculated shift. RMBPT and MCDHF methods were used to perform highly accurate theoretical calculations that include higher order relativistic ef-

fects, electron correlation effects, QED and Breit interactions. Only a limited amount of experimental data is available for the Xe isotopic chain. Borchers *et al.* [BAN+89] reported a relative mean square radii value of 0.242(0.005)[0.080] fm^2 between ^{124}Xe and ^{136}Xe from an OLS measurement where the uncertainty is dominated by the uncertainty in SMS calculations. The relative RMS charge radius measured by Fricke *et al.* [FBH+95] using muon spectroscopy was 0.3538(0.064) fm^2. Libert *et al.* performed a King-plot analysis by comparing the above-mentioned two methods and reported a value of 0.3499(0.03) fm^2. The value recommended by Angeli *et al.*'s evaluation is 0.2897(0.005) fm^2 [AM13]. The necessity to perform more measurements for the Xe isotopic chain is therefore evident.

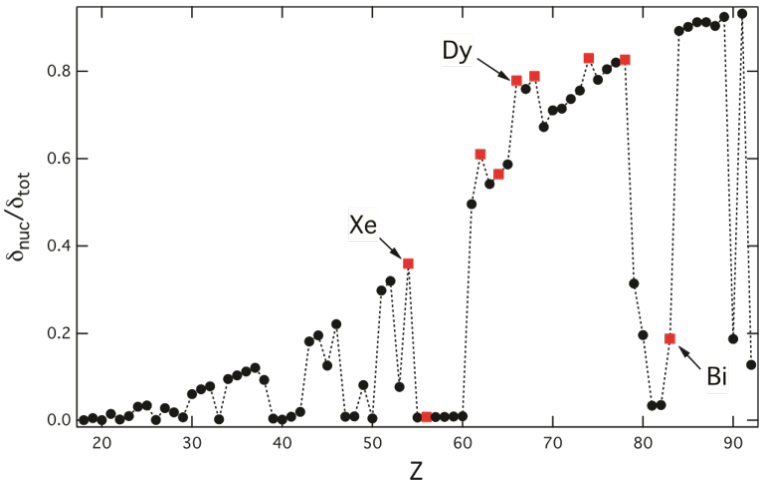

Figure 8.3: Ratio of uncertainty in transition energy due to assumed nuclear size to the total uncertainty in theroy for Na-like D1 transitions. From [GOR+13].

8.2 Measurement

The highly charged Xe ions were produced and trapped with the NIST EBIT facility. ^{136}Xe and ^{124}Xe atoms were loaded through the gas-injection system at an injection pressure of 2×10^{-3} Pa. Once loaded, the atoms were ionized to the charge state of interest via electron impact ionization through collisions with the electron beam. The Xe spectra were measured at the electron beam energy of 6 keV except for a few spectra, where the beam energies were varied. The electron beam current was set to 150 mA during the measurement.

The current and voltage setting was selected to optimize the production of the Na-like and Mg-like charge states. Each spectra were recorded with a flat-field grazing incidence EUV spectrometer [BLF$^+$05] with data acquisition times of 300 s. Spectra in the X-ray region were also recorded with a HpGe detector and a high-resolution crystal spectrometer, simultaneously. Neutral ^{136}Xe and ^{124}Xe atoms were injected alternately and a series of 300 s long acquisitions were taken for each isotope. The reflection grating of the spectrometer allowed for the measurement of different orders of the same transition. Each Xe spectra contains the first and second order of the Na-like D1 3s $^2S_{1/2}$ - 3p $^2P_{1/2}$ transition and the Mg-like $3s^2$ ^{1}S$_0$ - 3s3p ^{3}P$_1$ transition. Similarly, the second and third order of the Na-like D2 3s $^2S_{1/2}$ - 3p $^2P_{3/2}$ transition and the Mg-like $3s^2$ ^{1}S$_0$ - 3s3p ^{1}P$_1$ transition were observed in every collected spectra. Higher orders of the spectral line increases the resolution of the measurement and provides confirmation of the results.

The predicted shift of the Na-like D transitions between the two Xe isotopes was in the order of a 100^{th} of a pixel. To ensure the measurement is not limited by the statistical uncertainty, the measurement was conducted continuously for a period of four days. Overall 686, 5-minute long spectra were collected during the measurement including the background spectra that was used for calibration purposes. Of these spectra, 427 spectra contained xenon data used in the analysis. The rest included calibration spectra, incidental bad data, and major outliers possibly coming from improper cosmic ray removal or other unusual phenomena. ^{136}Xe was injected first for a period of about one hour and then switched to ^{124}Xe isotope and then continued alternately for the course of the measurement. The switching between the isotopes was determined by the automatic liquid nitrogen refill in the buffer dewar (called phase separator) that feeds the liquid nitrogen shield and the collector. This dewar is fed by a larger liquid nitrogen tank outside the EBIT laboratory. The level of liquid nitrogen in the buffer dewar is monitored to maintain the continuous refill. The automatic cycle is adjusted such that refill begins when the level of liquid nitrogen drops to 20 %. This process occurs at every hour or so during which the electron beam anode is turned off. This break in the acquisition was conveniently used as a reference to load the

Table 8.1: General EBIT voltage and current settings during the measurement

EBIT Settings	**6/1/2016**
Focus (V)	-14.483
Suppressor (V)	620
Einzel lens (V)	1270
Extractor (V)	-2290
Transition (V)	5620
Egun filament voltage (V)	6.3
Egun filament current (A)	0.485
Collector exhaust temp. (F)	315
UDT (V)	260
LDT (V)	500
Bucking coil (V)	0.54429
E-gun pressure (torr)	2.70×10^{-10}
Gas injection pressure (torr)	1.50×10^{-5}

isotopes alternatively. Each refill lasted for about 10 minutes and the change between the isotopes was conducted during this time-interval.

The calibration of the spectra was performed with well known spectral lines from highly charged Xe, Ne and Ar ions and provided the full wavelength region of 7.54 nm to 26.25 nm. To systematically study the dependence of the Xe transitions on the electron beam energy, we collected a few spectra by systematically varying the beam energy from 4.2 keV to 15 keV. During a few datasets, Kr or Ne gas was injected together with the Xe isotopes to provide simultaneous measurement of low Z transitions that are unaffected by the field shift effects. The gas injection system installed at the NIST EBIT currently consists of 3 leak valves that allow for the injection of multiple gases simultaneously. One of the leak valves is connected to the gas-injection manifold that contain Ne, Kr, Ar, CO_2, and He gas bottles. The second leak valve is connected to the ^{136}Xe bottle. An additional leak valve connected to the ^{124}Xe bottle was installed to the gas injection setup prior to this measurement. Figure 8.4 shows the layout of the setup for the injection of two Xe isotopes. Table 8.1 shows the general voltage and current settings applied during the measurement.

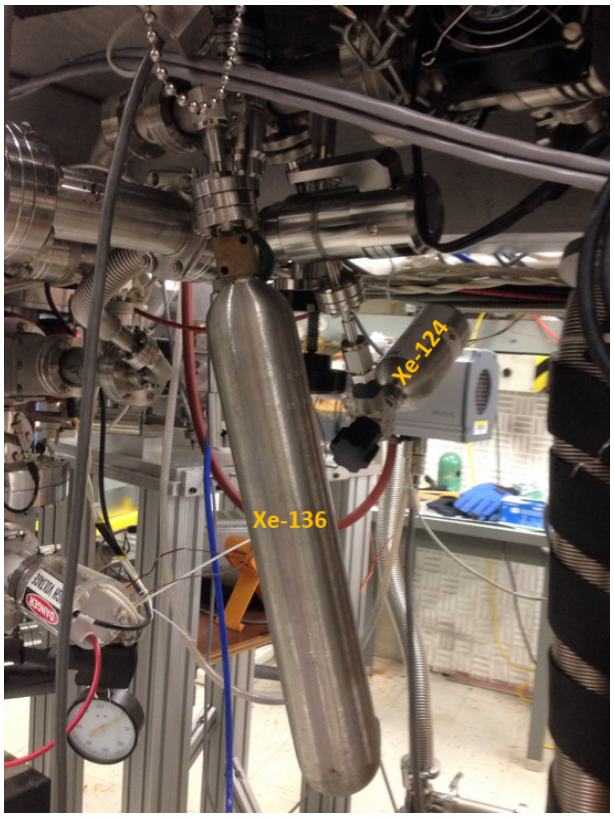

Figure 8.4: ^{136}Xe and ^{124}Xe bottles attached to the NIST EBIT.

8.2.1 EUV ADU to photon conversion

A brief description of how photons are registered in CCD as arbitrary digital units was provided in Section 6.1. The intensity of the line was recorded in analog to digital units (ADU) with the CCD detector attached to the EUV spectrometer. The conversion of this unit to number of photons is provided by the system gain of the EUV controller. The gain of the controller is defined as the number of electrons per ADU. The number of electrons created can be conveniently calculated by ADU $\times$ the system gain. For our EUV spectrometer, the system gain was set to 3, where every 3.6 eV of incoming radiation creates one electron-hole pair in the Si detector. The Xe Na-like D1 line was observed at 12.394 nm equivalent to approximately 100 eV in energy. Since 3.6 eV of radiation produces one electron, a 100 eV radiation produces 100/3.6 or 27.7 electrons. From Figure 8.5, it can be seen that for a 5-minute long exposure, the total number of electrons at the maximum

intensity position of the D1 peak was around 3542 × 3, resulting to a number of photons of (3542 × 3)/27.7 = 383.

For a full width half maximum (FWHM) of 2.446 channels, the number of photons for the whole area of the peak is equal to (3542 × 3 × 2.446)/27.7 or 938. This conversion shows that for an acquisition time of 5 minutes, the number of detected photons is equal to 938. To produce a spectral line with high count rate, many data acquisition cycles must be accumulated. For instance, to record a spectral line with a photon count of 30000, we would need to collect for (30000 × 5)/938 ≈ 159 minutes or 2.65 hours. With the NIST EBIT, Gillaspy *et al.* [GOR$^+$13] measured the transition energy of the Na-like D1 line with a 35 ppm accuracy from a 5-minute long data acquisition time. To get an accuracy of 2 ppm in the measurement of the transition energy, one would need to collect for 25 hours. After one day of acquisition time, the statistical uncertainty can be reduced to less than the expected shift. Our measurement of absolute wavelength position of 12.3935(9) nm for the Na-like D1 transition resulted in a 73 ppm accuracy.

8.2.2 Calibration

The calibration of the EUV spectra was conducted using the same process as discussed in Section 7.3. Known transitions corresponding to Ne, Ar and Xe ions were used to calibrate the spectra. Neutral Ne and Xe atoms were loaded to the EBIT trapping region through the gas injection system. A strong line arising from Ar XXV at 22.115(3) nm was observed in the Ne spectra when the trap was periodically emptied to get rid of the heavy ions. Ar impurity lines are observed as residual Ar lingers around in trace amounts in the ion pumps of the EUV spectrometer vacuum setup. Since spectra were collected over a period of four days, calibration was performed each day. The results from these daily calibrations were compared to check for inconsistencies. All the calibrated regions were within the overall line uncertainties. Figure 8.6 shows the calibration lines corresponding to Ne, Ar and Xe transitions. The residual of the fit and the 95 % confidence bands are shown in Figure 8.7. The spectral lines used for the calibration are listed in Table 8.2. The final

- Location = 642.39 +/- 0.0079731
- Height = 3542.5 +/- 23.594
- Area = 9223.8 +/- 61.479
- FWHM = 2.446 +/- 0.018855

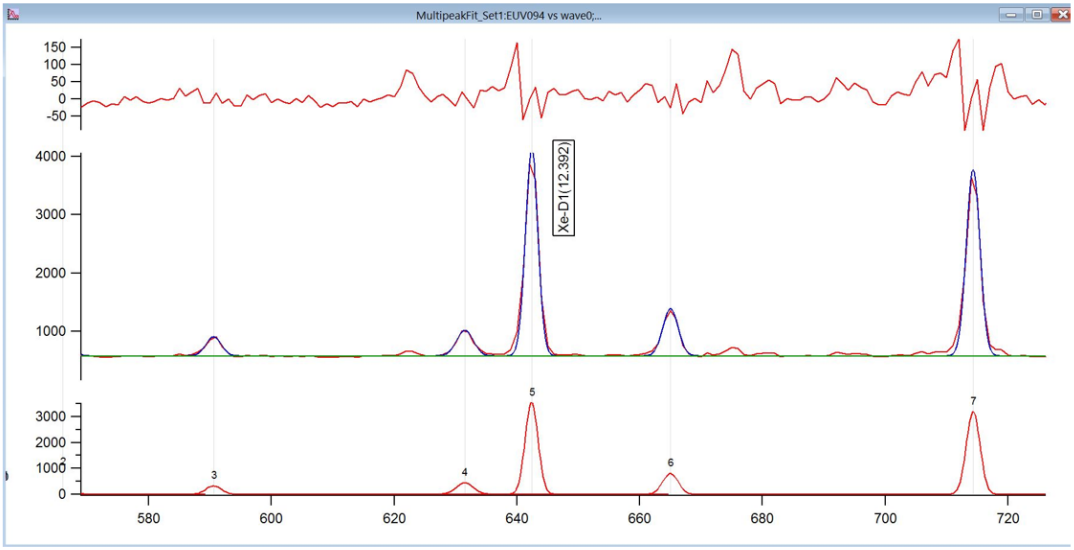

Figure 8.5: ADU to photon conversion in the EUV spectrometer from the Na-D1 spectral line.

calibration polynomial used was given by: λ (nm)= 7.54025 + 0.00675349 $\times$ channel no. + 1.25362 $\times$ 10^{-6} $\times$ (channel no.)^2 - 4.25216 $\times$ 10^{-11} $\times$ (channel no.)^3.

The total uncertainties of each calibration lines were determined from the quadrature sum of the adopted wavelength uncertainty given in the reference tables [KRRN18, ORGR12], the fitting uncertainty of the peaks, and a constant systematic uncertainty of 0.0006 nm, obtained by requiring the chi-square of the fit to be close to 1. The details of the uncertainties have been provided in Section 7.3.

Table 8.2: Lines from Ne, Xe and Ar ions used for the calibration of the Xe spectra. Lines in bold correspond to the second order lines.

Lines	**Wavelength (nm)**	**Uncertainty (nm)**	**Channel number**	**Uncertainty**
Ne^{7+}	8.80929	0.00014	181.83	0.0324
Ne^{6+}	9.7502	0.0004	309.674	0.0182
Ne^{7+}	9.82629	0.00021	319.629	0.0207
Ne^{6+}	10.6189	0.0005	423.034	0.1217
Ne^{5+}	11.1136	0.0018	486.131	0.0177
Ne^{6+}	11.6691	0.0005	555.264	0.0389
Ne^{6+}	12.7676	0.0007	688.224	0.0468
Ne^{4+}	14.3314	0.0007	869.35	0.0228
Ne^{4+}	14.7138	0.0007	912.419	0.0329
Ne^{7+}	17.6186	0.00028	1225.12	0.0401
Ne^{6+}	19.5004	0.0008	1416.47	0.0204
Ne^{7+}	**19.6526**	**0.00042**	**1431.65**	**0.0297**
Ne^{6+}	**23.3382**	**0.001**	**1784.04**	**0.0380**
Ne^{5+}	**24.5404**	**0.00034**	**1894.16**	**0.0197**
Ne^{6+}	**25.5352**	**0.0014**	**1983.06**	**0.0844**
Ar^{14+}	22.115	0.003	1669.64	0.0169
Xe^{43+}	12.392	0.003	643.557	0.0144
Xe^{42+}	12.993	0.003	715.409	0.0336
Xe^{43+}	13.3246	0.0014	753.797	0.0481
Xe^{43+}	**24.784**	**0.006**	**1916.16**	**0.0632**
Xe^{24+}	16.4412	0.0005	1101.2	0.0639
Xe^{25+}	17.3938	0.0005	1201.83	0.0645
Xe^{40+}	15.4564	0.0025	994.636	0.0865
Xe^{41+}	12.2278	0.0025	623.6	0.0288
Xe^{41+}	15.0111	0.0025	945.96	0.0197

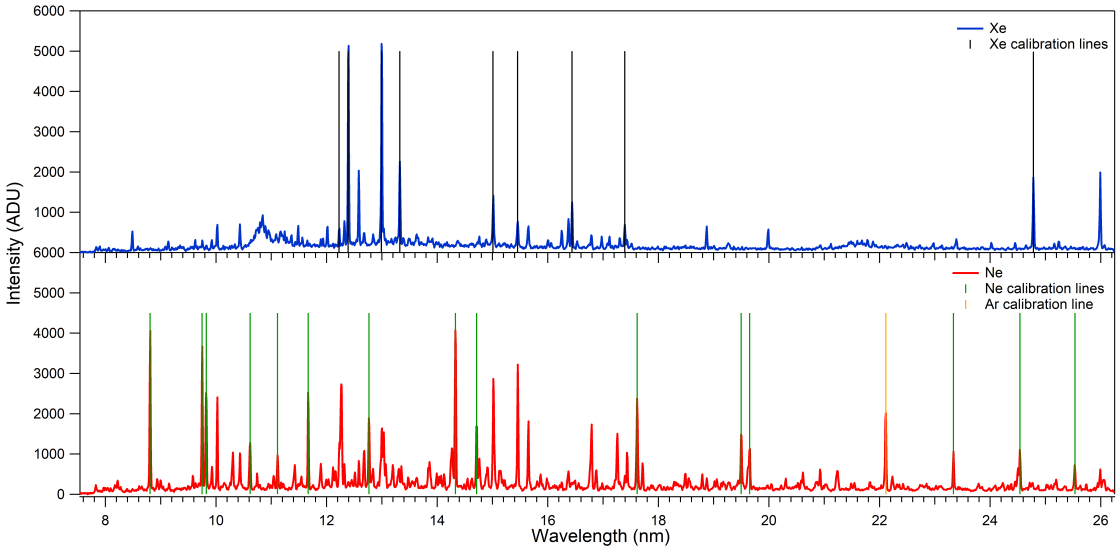

Figure 8.6: The calibration lines from Xe (black), Ar(orange) and Ne (green) ions. The bottom spectra (red) correspond to the Ne spectra and the top spectra(blue) correspond to the Xe spectra.

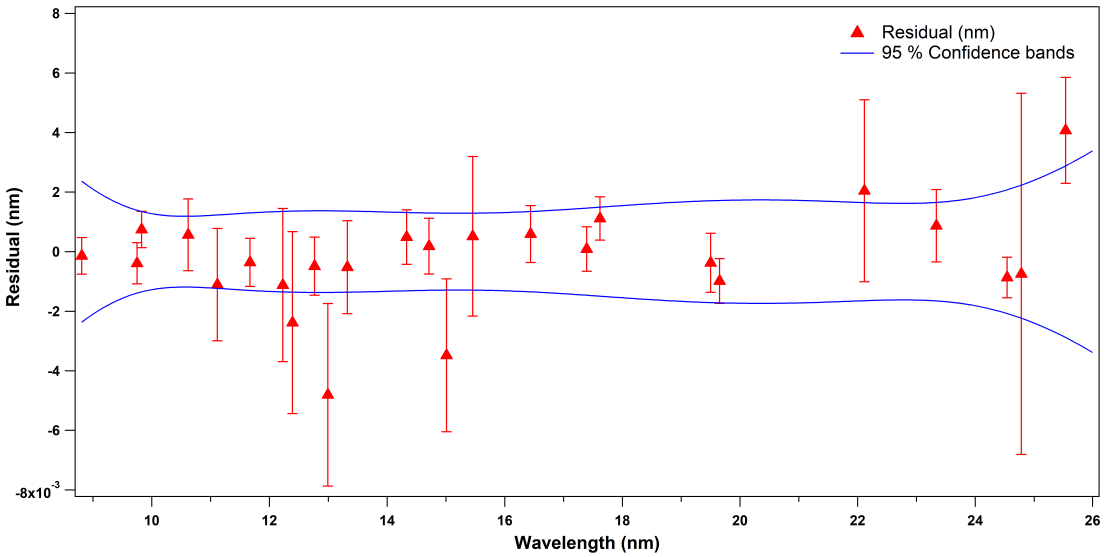

Figure 8.7: Residual of the calibration lines with the total uncertainties as the error bars.

8.3 Determination of Isotope Shift between ^{124}Xe and ^{136}Xe

The transitions that are most sensitive to the isotope shift and have large field shift effects were chosen for the measurement of isotope shift. Table 8.3 and Figure 8.8 show the transitions that were selected during the data analysis. The Na-like 3s – 3p transitions and

Table 8.3: Highly charged Xe transitions selected for the analysis of isotope shift measurement. The cells highlighted in green correspond to the Na-like D1 3s - $3p_{1/2}$ transitions, blue correspond to the Na-like D2 3s -$3p_{3/2}$ transitions, yellow correspond to the Mg-like $3s^2$ -3s3p $^1P_1$ and orange correspond to the Mg $3s^2$ -3s3p $^3P_1$ transitions.

Wavelength	Charge state	Stage	Sq	Transition	Type	Order
8.4870(25)	Xe XLIV	43+	Na	3p $^2P_{3/2}$ - 3d $^2D_{5/2}$	E1	1
5.0100(25)	Xe XLI	40+	Si	$3p_2$ $^1S_0$ - 3p3d $(1/2,5/2)_1$	E1	2
5.2154(25)	Xe XLII	41+	Al	3p $^2P_{1/2}$ - 3d $^2D_{3/2}$	E1	2
12.0133(3)	Xe IX	8+	Pd	4d $^{101}S_0$ - $4d^9$4f $^1P^0$	E1	1
12.2278(25)	Xe XLII	41+	Al	$3s^2$3p $^2P_{1/2}$ -3s3p_2 $^2S_{1/2}$	E1	1
6.1622(25)	Xe XLII	41+	Al	$3s^2$3p $^2P_{1/2}$ -3s3p^2 $(1,3/2)_{1/2}$	E1	2
12.394(1)	Xe XLIV	43+	Na	3s $^2S_{1/2}$ - 3p $^2P_{1/2}$	E1	1
6.2875(12)	Xe XLIII	42+	Mg	$3s^2$ $^1S_0$ - 3s3p $^1P_1$	E1	2
12.993(3)	Xe XLIII	42+	Mg	$3s^2$ $^1S_0$ - 3s3p $^3P_1$	E1	1
6.6628(5)	Xe XLIV	43+	Na	3s $^2S_{1/2}$ - 3p $^2P_{3/2}$	E1	2
15.0111(25)	Xe XLII	41+	Al	3p $^2P_{1/2}$ - 3p $^2P_{3/2}$	M1	1
15.4564(25)	Xe XLI	40+	Si	$3p^2$ $^1S_0$ - $3p^2$ $(1/2,3/2)_2$	E2	1
15.6447(25)	Xe XL	39+	P	$3p^3$ $^2P_{3/2}$ - $3p^3$ $(1/2,2)_{5/2}$	M1	1
16.3727(25)	Xe XXXIX	38+	S	$3p^4$ $(3/2,3/2)_2$ - $3p^4$ $(1/2,3/2)_1$	M1	1
16.4412(5)	Xe XXV	24+	Zn	$4s^2$ $^1S_0$ - 4s4p $^1P_1$	E1	1
17.3938(5)	Xe XXVI	25+	Cu	4s $^2S_{1/2}$ - 4p $^2P_{3/2}$	E1	1
6.2875(12)	Xe XLIII	42+	Mg	$3s^2$ $^1S_0$ - 3s3p $^1P_1$	E1	3
6.6628(5)	Xe XLIV	43+	Na	3s $^2S_{1/2}$ - 3p $^2P_{3/2}$	E1	3
12.394(1)	Xe XLIV	43+	Na	3s $^2S_{1/2}$ - 3p $^2P_{1/2}$	E1	2
12.993(3)	Xe XLIII	42+	Mg	$3s^2$ $^1S_0$ - 3s3p $^3P_1$	E1	2

the Mg-like $3s^2$ – 3s3p transitions have large field shifts due to the strong overlap of the 3s orbitals with the nucleus. However, the field shift coefficients for the 3p – 3d transitions from Al-like Xe are smaller. This is due to the decreased overlap of the p and d orbitals with the nucleus relative to the s orbitals. Table 8.3 provides the list of strong transitions in the observed EUV spectra. Most of the transitions correspond to higher charge states from S-like Xe through Na-like Xe ions (Xe XXXIX - Xe XLIV). Few lower charge states arising from Zn-like Xe (Xe XXV) and Cu-like Xe (Xe XXVI) ions were present as well due to charge exchange. A line at 12.0133(3) nm appears from an even lower charge state of Xe IX, corresponding to a 4d – 4f transition. This transition has a very high reported intensity [CRTBW02] and is present at a beam energy of 6 keV.

The strength of the field shift and mass shift effects was determined from atomic structure calculations. The values of the calculated field shift coefficients for the Na-like,

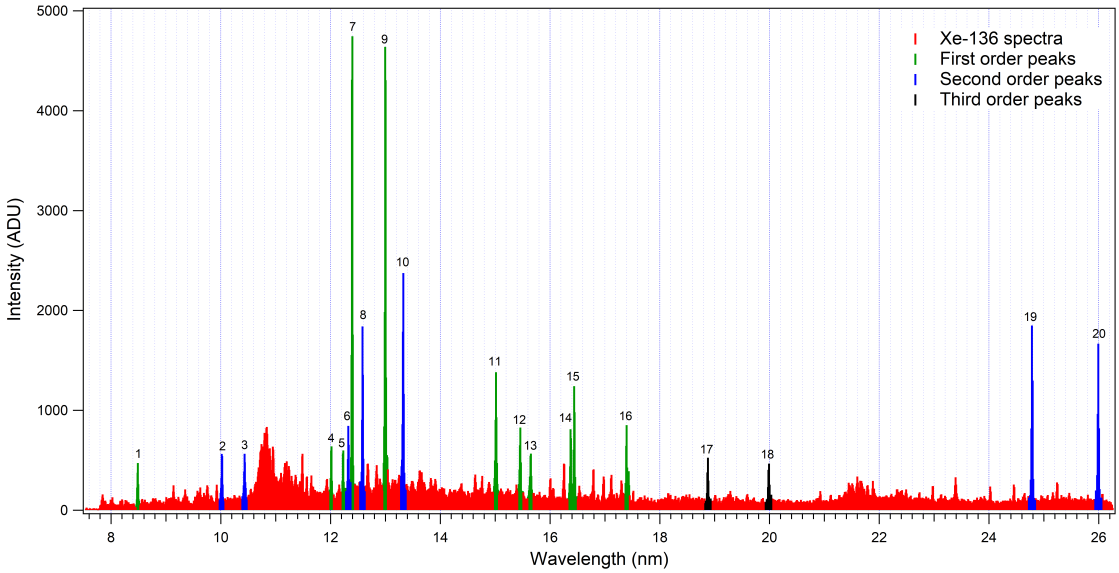

Figure 8.8: 20 lines chosen for analysis of the isotope shift. First, second and third order lines are highlighted in green, blue and black, respectively. The lines are labeled by numbers 1-20 and are listed in the same order in Table 8.3.

Mg-like, and Al-like transitions are given in Table 8.4. The table shows that the field shift coefficients for the Na-like D transitions and the Mg-like transitions are large compared to the Al-like transitions. Calculations were performed using the Relativistic Many-Body Perturbation Theory (RMBPT) and Multi-configuration Dirac-Hartree-Fock (MCDHF) methods. The Na-like D1 3s $^2S_{1/2}$ - 3p $^2P_{1/2}$ transition was observed in first and second order, labeled as 7 and 19 in Figure 8.8. The Na-like D2 3s $^2S_{1/2}$ - 3p $^2P_{3/2}$ transition was observed in second and third order, labeled as 10 and 18 in Figure 8.8. Similarly, we observed the Mg-like transition $3s^2$ ^{1}S$_0$ - 3s3p ^{1}P$_1$ in second and third order (8 and 18 in Figure 8.8) and $3s^2$ ^{1}S$_0$ - 3s3p ^{3}P$_1$ in first and second order (9 and 20 in Figure 8.8).

8.3.1 Determination of the line centroids

To avoid any model-dependent errors, a peak fitting function was not used to determine the wavelength centroid for the peaks. A weighted average method was employed

Table 8.4: The field shift (FS) coefficients in units of GHz/fm^2 and mass shift (MS) coefficients in units of THz amu for the Na-like, Mg-like and Al-like transitions. The normal mass shift coefficients are labeled as NMS and specific mass shift coefficients are labeled as SMS.

		Na-like Xe^{43+}			Mg-like Xe^{42+}		Al-like Xe^{41+}
		3s - $3p_{1/2}$ (D1)	3s - $3p_{3/2}$ (D2)	$3p_{3/2}$ - $3d_{5/2}$	3s - 3s3p $^3P_1$	3s - 3s3p $^1P_1$	$3p_{1/2}$ - $3p_{3/2}$
FS coeff.	RMBPT	-963.7	-990.7	13.7	-940.2	-975.9	-31.9
(GHz/fm^2)	MCDHF	-959.67	-984.91	16.72	-935.21	-969.10	-33.78
NMS coeff.	RMBPT	-13.3	-23.2	-18.0	-12.4	-24.9	-9.50
(THz amu)	MCDHF	-13.17	-23.32	-18.18	-13.3	-24.12	-9.50
SMS coeff.	RMBPT	-170.2	-169.6	-91.6	-168.4	-163.7	-3.5
(THz amu)	MCDHF	-170.7	-169.96	-92.14	-164.3	-162.69	-4.68

to calculate the centroid positions of the lines of interest given by 8.1.

$$x_{cm} = \frac{\sum_i x_i \times I_i}{\sum_i I_i} \tag{8.1}$$

where x_i is the channel number, I_i is the intensity for the respective channel, and x_{cm} is the centroid position of the peak. To determine the centroid, a constant overall background of 500 ADU was subtracted from all data sets. The centroid was determined by using different number of channels ranging from 5 to 11. The best representation of the peaks were given by choosing 7 channels around the mean of the centroid positions. Therefore, we used 7 channels to obtain the final centroid position. A systematic study was performed later to check the final results, including a Gaussian fit using 5 channels around the maximum position. Details of the systematic study of the shift with the channel number is presented in Section 8.4.

The anticipated isotope shift between the D1 lines of the two Xe isotopes was less than 10^{-4} nm (about $1/100^{\,th}$ of a pixel). Hundreds of EUV spectra were therefore recorded over a period of 4 days to minimize the statistical uncertainty. Due to the large number of datasets, a python computer code was written to compute the wavelength centroid. The source code is provided in Appendix D. Figures 8.10 and 8.9 present the comparison of the Na-like D1 peak for the ^{124}Xe and ^{136}Xe isotopes in terms of channel numbers and wavelength (in nm), respectively. A clear visual representation of the shift is not expected

as the shift is anticipated to be very small. A demonstration of the statistical variation of the shift in the line position is shown on Figures 8.10 (b) and 8.10(c). Even though there seems to be a visible shift between the two lines after the first 5 minutes of data acquisition, the difference gradually disappears with a higher number of photons under the peak. Due to the large number of photons required to determine a statistically significant isotope shift, the experiment was a multi-day effort and the variation in line positions with time was expected due to possible thermal and electronic systematic drifts.

Note that Figure 8.10(c) is not normalized in intensity and the lower intensity for ^{124}Xe is due to a smaller number of spectra for the ^{124}Xe isotope. The figures hint that longer acquisition for better statistics is not enough to determine a shift on the order of 10 ppm, as there are other systematic uncertainties that need to be properly accounted for.

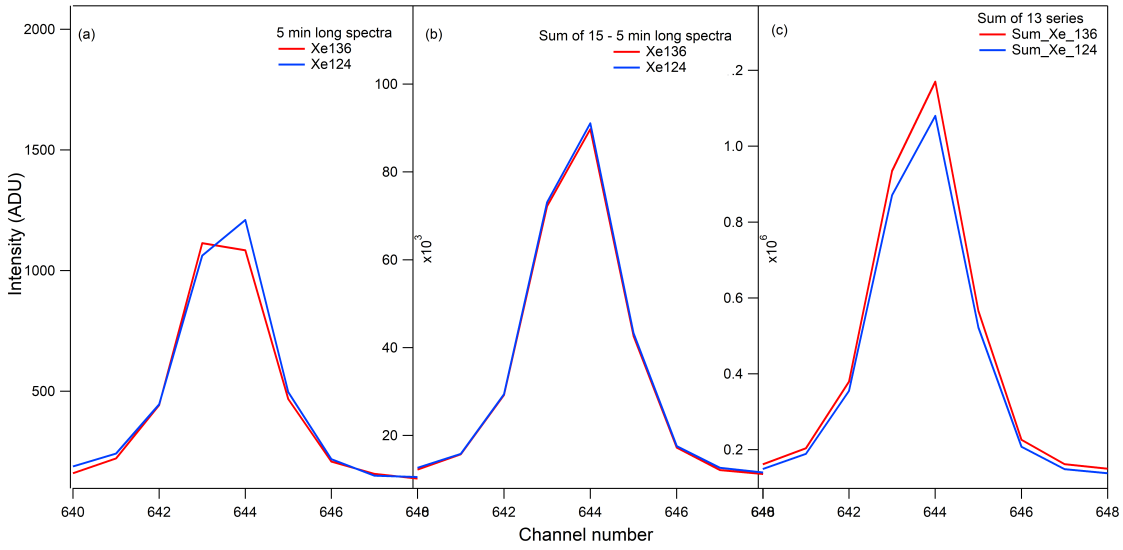

Figure 8.9: The Na-like D1 transition for ^{136}Xe (red) and ^{124}Xe (blue) as a function of channel number for (a) 5-minute collection, (b) sum of 15 5-minute collections and (c) sum of 13 series of about 10-15 spectra for each isotopes. The intensities are not normalized.

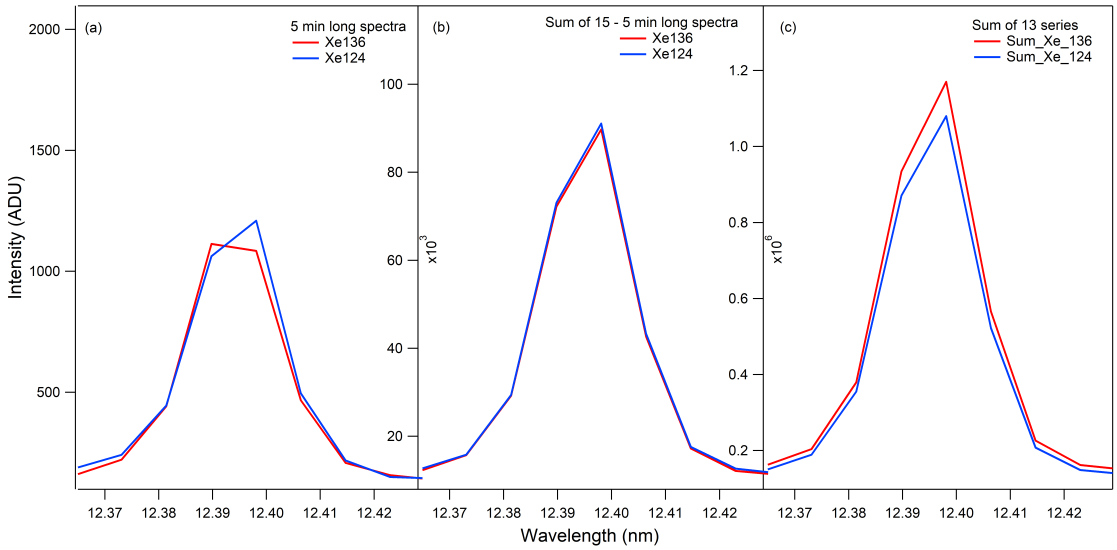

Figure 8.10: The Na-like D1 transition for ^{136}Xe (red) and ^{124}Xe (blue) shown as a function of wavelength (nm) for (a) 5-minute collection, (b) sum of 15 5-minute collections and (c) sum of 13 series of about 10-15 spectra for each isotopes. The intensities are not normalized.

8.3.2 Systematic drifts in the line position

To identify possible systematic drifts during the data acquisition, a time-ordered sequence of the line positions was created for both isotopes. The line positions were plotted as a function of the file number (number of measurements), which is dependent on time. The scatter plot of the line position versus the file number after removing possible outliers is shown in Figures 8.11 and 8.12 for first and second order Na-like D1 (3s -3p$_{1/2}$) transitions, respectively. A considerable amount of time-dependent, systematic drifts in the line position were observed over the course of the measurement. These systematic drifts arise due to thermal and electronic shifts in the CCD detector during the measurement. Significant jumps were observed at two positions that correspond to the times when the EUV CCD was refilled with liquid nitrogen. The scatter of the centroid positions was therefore separated into three regions in between these fill times. The largest jump was observed before the third region. This was associated with the combination of liquid nitrogen refill of the CCD dewar and the replacement of liquid helium tank on the EBIT on the third day of the experiment.

The three regions that were separately analyzed are shown in the scatter plots Figures 8.11 and 8.12. The red circles and blue squares correspond to ^{136}Xe and ^{124}Xe isotopes, respectively. Each circle and square represent the line position determined from a 5-minute collection. The line positions were determined from the weighted centroid method mentioned earlier. The missing data points depict the removed significant outliers and series where different events affected the acquisition. The removed data points correspond to the files with disrupted settings, such as sudden changes in the gas injection pressure, disruption in the collector magnet and bucking coil current values, and failure to open the gate valve to the gas injection.

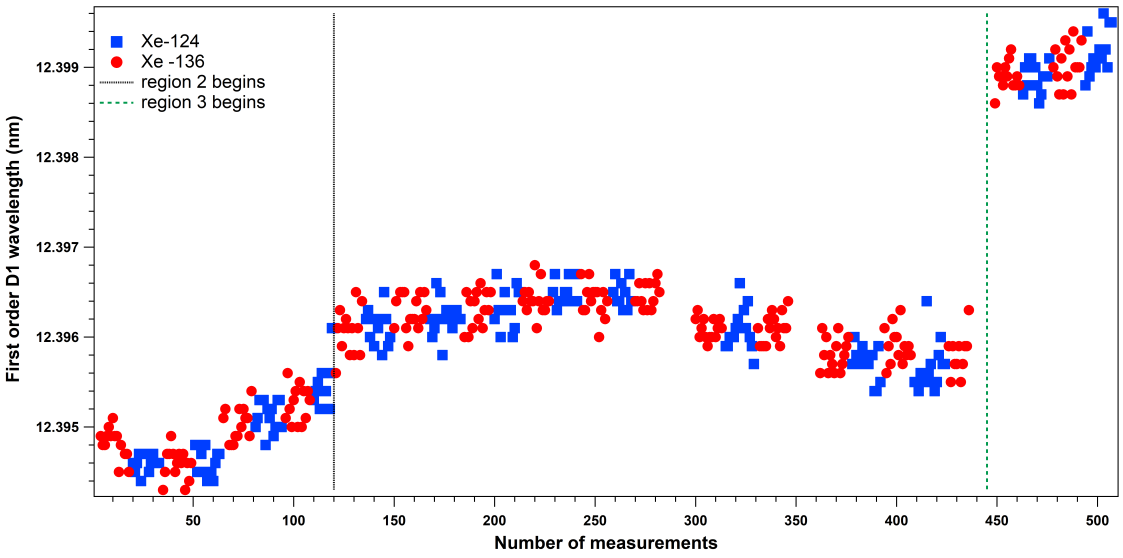

Figure 8.11: Line centroids of the first order Na-like D1 transition for^{136}Xe (red) and ^{124}Xe (blue) plotted as a function of the number of measurements.

The absolute uncertainty of the line position of the Na-like D1 transition was determined from the calibration procedure to be 0.0009 nm. This uncertainty is about two orders of magnitude larger than the anticipated isotope shift. The goal of the measurement is to determine the relative change in the line position between the two isotopes. The absolute uncertainty of the line positions does not limit the determination of the shift because the uncertainty in the dispersion function is much smaller. The following sections describe the different methods adopted to determine the relative shift in the line positions. The Na-like

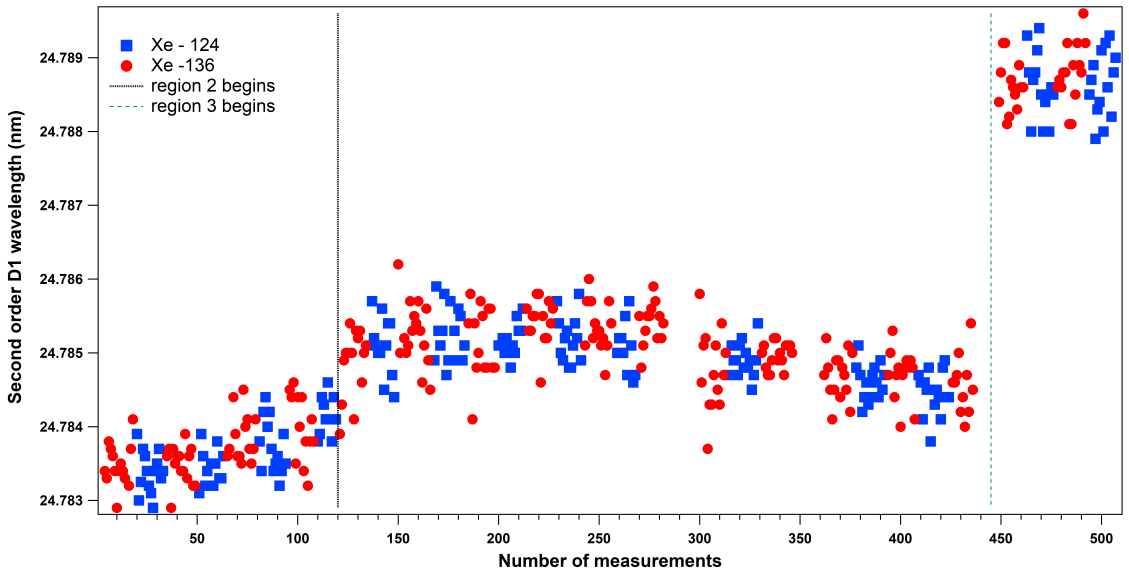

Figure 8.12: Line centroids of the second order Na-like D1 transition for ^{136}Xe (red) and ^{124}Xe (blue) plotted as a function of the number of measurements.

D1 transition is chosen for the primary analysis of the shift as this transition is clean and strong in the spectrum, not affected by blends or excess background in the neighborhood of the line.

8.3.3 Isotope Shift Analysis: Method I

The first method implemented in the determination of the shift between the line positions of the two isotopes is based on reference lines that do not show such a shift. The lines of interest, such as the Na-like D1 line, is strongly affected by large field shift effects. Conversely, lines arising from lower charge states of Xe have negligible sensitivity to nuclear effects. As a result, the difference in the line positions of the line of interest and the reference line can be evaluated to determine the isotope shift. The line at 12.0133(3) nm corresponding to the Xe IX line results from a 4d – 4f transition. Since the electronic orbitals of a 4d – 4f transition do not penetrate the nucleus, this line was used as a reference. The time-dependent systematic drift should affect all the spectral lines. As a result, the difference in the line positions between the lines of interest and the reference line should have no time-dependent drifts. This cancellation of the time dependent systematic drifts

implies that the difference in line positions could be used to determine the isotope shift.

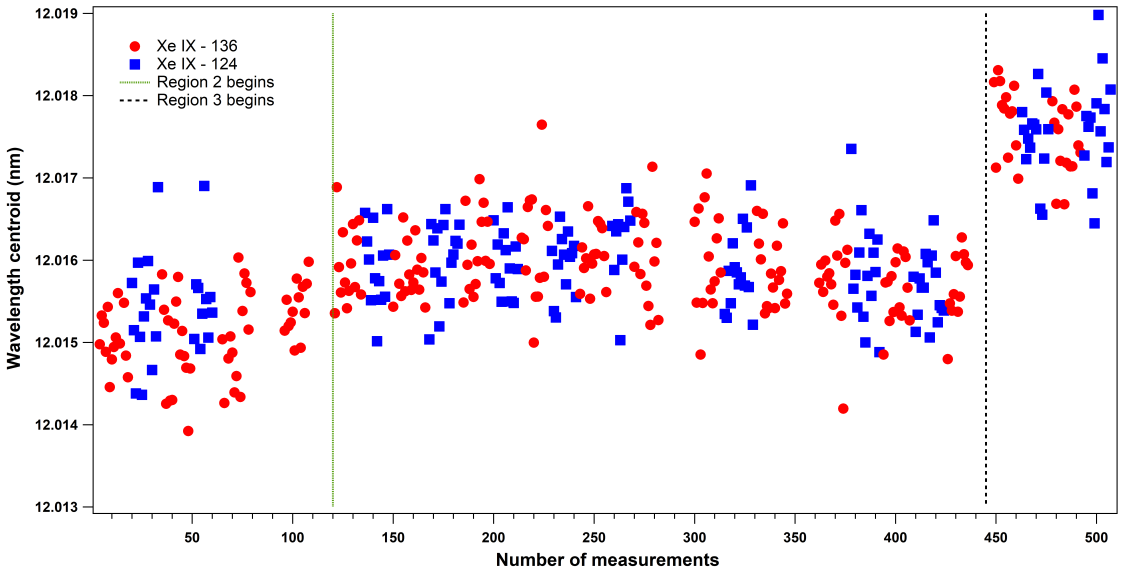

Figure 8.13: Scatter plot of the line positions for Xe lX line plotted as a function of the number of measurements

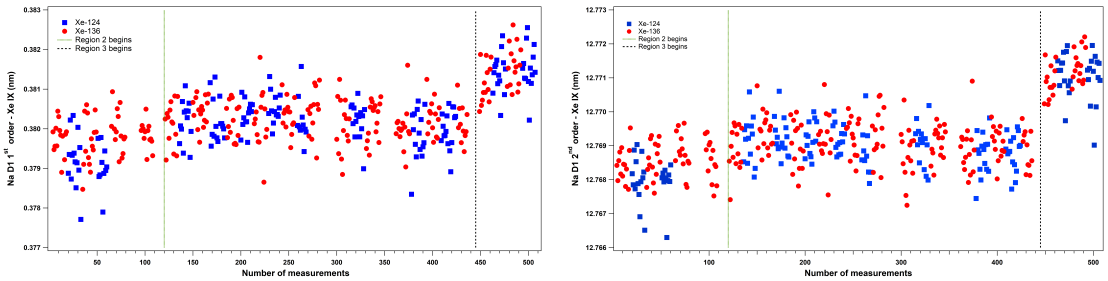

Figure 8.14: Scatter plot of the difference in the line position of Xe lX line and the first order Na-like D1 line (left) and the second order Na-like D1 line (right) plotted as a function of the number of measurements

We observed that the difference in the line positions of the Xe IX 4d – 4f transition and the two orders of Na-like D1 3s - 3p transition do not completely cancel the time-dependent systematic drifts. This can be seen in Figure 8.14. This observation suggests that the time-dependent drift is not consistent throughout all the CCD pixels. Different pixels in the CCD camera respond differently to various environmental effects such as temperature and mechanical vibrations. A similar trend can be observed by plotting the difference in the line positions obtained by using Gaussian fit to determine the line centroids. This is shown

in Figure 8.15. Additional lines were chosen as reference lines to evaluate the isotope shift from the difference between the reference lines and the lines of interest. The differences in the line positions from other references showed similar trends as well.

Since the reference lines originate from the transitions in highly charged Xe ions, some of these transitions might have slight nuclear effects. These effects arise from the Z dependence of the field shift. As an alternative approach, the low charge-states transitions of ionized Ne and Kr were also chosen as reference lines during the data analysis. This was possible since a few spectra contain both Xe and Ne or Kr lines when they were injected simultaneously. Ne or Kr lines were used as the reference lines and the wavelength difference between the Xe transitions and these reference lines were determined. This difference displayed similar dependence to the non-uniform time-dependent shifts. Furthermore, the lines selected for reference were comparatively weaker than the lines of interest. The uncertainties in the centroid positions of the reference lines dominated the overall uncertainties of the differences. Once the difference in the line positions were determined for all the datasets, the mean value of these differences was calculated for both isotopes separately. The standard error from the mean provided the uncertainty of the differences. The difference between the mean for the two isotopes represented the isotope shift. The uncertainty in the shift was determined from the quadrature sum of the individual uncertainties for the two isotopes. For some of the selected reference lines, the uncertainties were of the same order as the shift or larger than the shift. This method was not used in the final data analysis for the determination of the shift.

8.3.4 Isotope Shift Analysis: Method II

Since the transitions at different pixel positions varied differently over time, an alternative method to find the shift was used. The full time ordered sequence of 428 centroid positions separated by the liquid nitrogen refill was used to determine the shift. The systematic time-dependent drift was taken into account by fitting the scatter of the centroid positions independently for each of the three regions with third order polynomial fits that

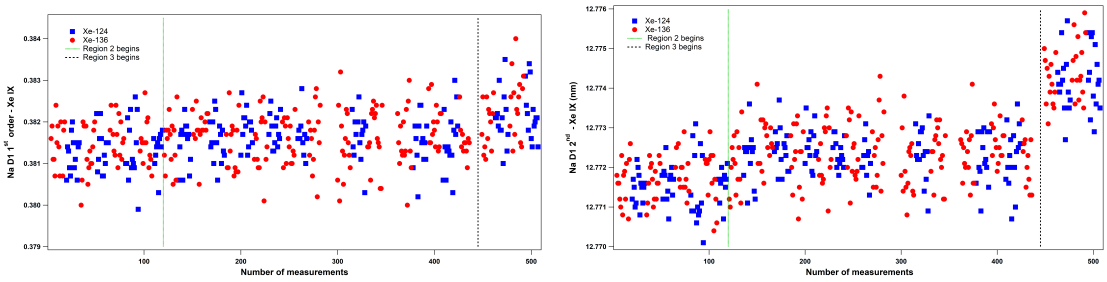

Figure 8.15: Scatter plots of the difference in the Gaussian line centroid of Xe lX line and the first order Na-like D1 line (left) and the second order Na-like D1 line (right) as a function of the number of measurements

best describe the variation. The shift was determined for the lines listed in Table 8.3. Among these transitions the ones that correspond to the strongest isotope shifts given in Table 8.4 were used to evaluate the variation in the charge radius. These transitions for the two isotopes of Xe are shown in 8.16.

The scatter of the distribution was subtracted from the third order polynomial fit separately for the three regions. This resulted in a randomly scattered residual distribution, which no longer included the systematic drift. The polynomial fit applied to the scatter and the residual between the fit and dataset are shown in Figures 8.17, 8.18, 8.19, and 8.20 for the first and second order Na-like D1 transitions.

The randomly scattered residuals for both isotopes were binned independently around their respective mean, adjusted by an offset to account for the nominal wavelength. The binned residual distribution resulted in a normally distributed Gaussian peak. This peak was fitted with a Gaussian function given by equation 8.2.

$$f(x) = A \exp \frac{(x-\mu)^2}{2\sigma^2} \tag{8.2}$$

The binned distribution was fit independently for the two isotopes to get the centroid position μ_k^A and the width σ_k^A. Stronger lines resulted in narrower distributions as expected. This is because stronger peaks with same mean μ_k^A have small σ_k^A due to the increase in statistics. The isotopic shift between the transitions for ^{124}Xe and ^{136}Xe was then computed

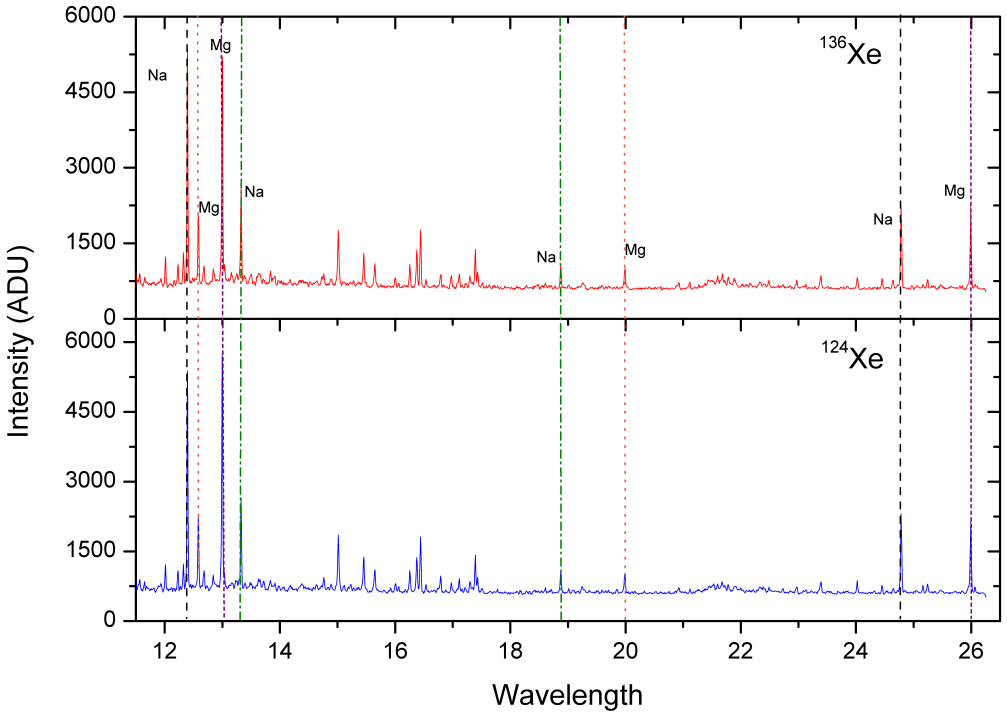

Figure 8.16: Xenon spectra for isotopes 136 (red) and 124 (blue). The lines represent the Na-like D1 (dash, black), Na-like D2 (dash dot, green), Mg-like (dot, orange) and Mg-like (short-dash, purple) transitions.

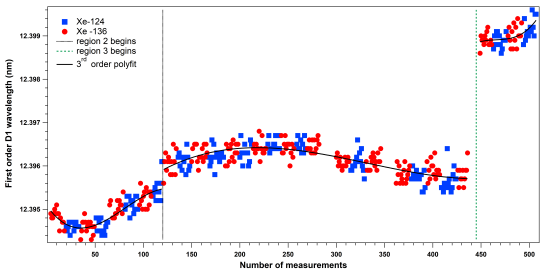

Figure 8.17: Third order polynomial fit (black) applied to the three regions of the scatter plot for the first order Na-like D1 line plotted as a function of the number of measurements

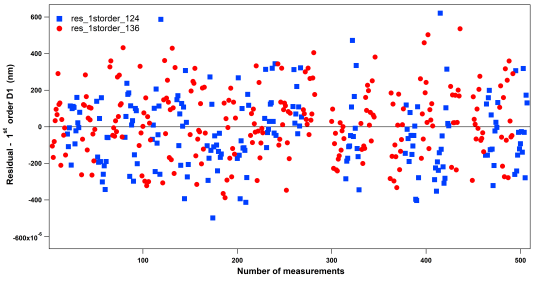

Figure 8.18: Residual of the first order Na-like D1 line after removal of the time-dependent systematic drifts

as the difference between their centroid positions given by equation 8.3.

$$\delta\lambda_k^{A,A'} = \mu_k^A - \mu_k^{A'} \tag{8.3}$$

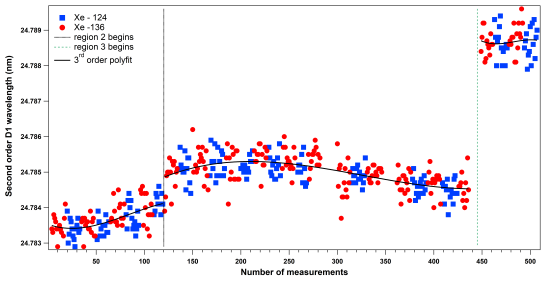

Figure 8.19: Third order polynomial fit (black) applied to the three regions of the scatter plot for the second order Na-like D1 line plotted as a function of the number of measurements

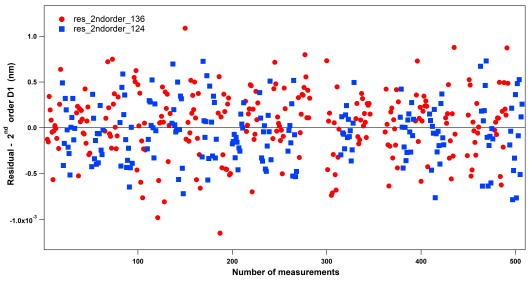

Figure 8.20: Residual of the second order Na-like D1 line after removal of the time-dependent systematic drifts

The uncertainty in the shift was calculated as the quadrature sum of the independent uncertainties of the two isotopes, estimated from the width of the bell curve, $\sqrt{2}\sigma$.

$$\alpha_k^{A,A'} = \sqrt{\alpha_k^{A\,2} + \alpha_k^{A'\,2}} \tag{8.4}$$

where $\alpha_k^A = \sigma_k^A/\sqrt{N}$. N represents the number of data points for the two isotopes. For current analysis, $N_{136} = 239$ and $N_{124} = 189$. The isotope shift was determined accordingly for the different orders of the isotopes for the transitions of interest. The shift and the corresponding uncertainty obtained in second and third order were divided by 2 and 3, respectively, to produce the shift and uncertainty in first order. The final shift corresponding to a particular transition was given by the weighted average of the shifts in different orders. The uncertainties were propagated to get the final uncertainty. The shifts in the two orders were found to lie within their respective individual uncertainties. The shift for the D1 transition was obtained by using equation 8.5 and the uncertainty was obtained by using equation 8.6.

$$D1 = \frac{\frac{D1_{1st}}{D1^2_{1sterror}} + \frac{D1_{2nd}}{D1^2_{2nderror}}}{\frac{1}{D1^2_{1sterror}} + \frac{1}{D1^2_{2nderror}}} \tag{8.5}$$

$$D1_{error} = \sqrt{\frac{1}{\frac{1}{D1^2_{1sterror}} + \frac{1}{D1^2_{2nderror}}}} \tag{8.6}$$

Table 8.5 lists the shift and uncertainties obtained from the Gaussian fit of the residual distributions. Figures 8.21 and 8.22 show the Gaussian distribution for Xe-124 and Xe-136 isotopes for the first and second order Na-like D1 transition, respectively, and the shift between the centroids. The gray area represents the error in the centroid position corresponding to the individual isotopes and the green line represent the error in the absolute position of the Na-D1 line. It can be seen that the absolute uncertainty is much larger than the isotope shift.

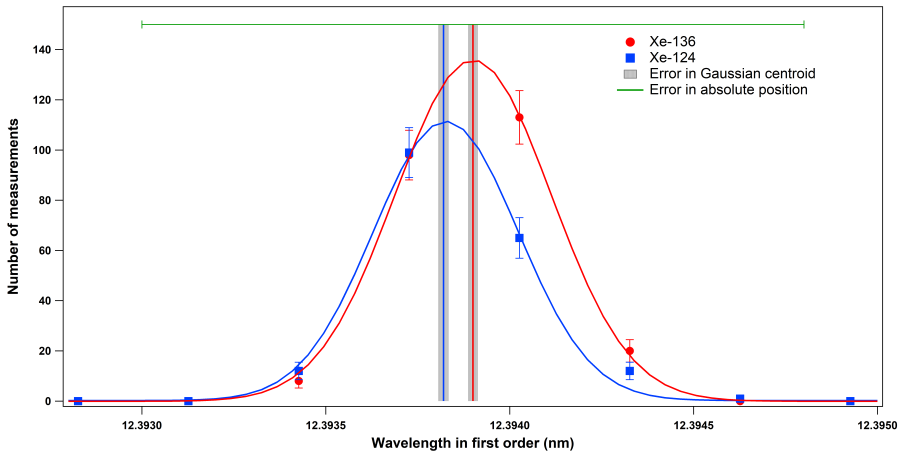

Figure 8.21: Shift in the line position of the first order Na-like D1 line between Xe isotopes 124 (blue) and 136 (red). The green line correspond to the absolute uncertainty in line position and the gray area correspond to the error in the Gaussian centroid.

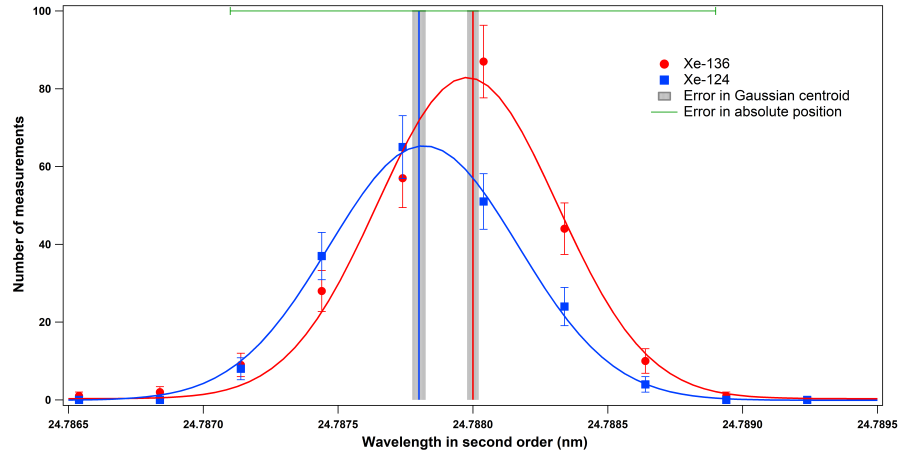

Figure 8.22: Shift in the line position of the second order Na-like D1 line between Xe isotopes 124 (blue) and 136 (red). The green line correspond to the absolute uncertainty in line position and the gray area correspond to the error in the Gaussian centroid.

Table 8.5: Isotope shift (^{124}Xe - ^{136} Xe) and the respective uncertainty in units of nm is listed for the Na-like 3s - 3p and Mg-like $3s^2$ - 3s3p transitions

Transitions	**Shift (nm)**	**Uncertainty (nm)**
Xe^{43+} (3s - $3p_{1/2}$)	-7.81 $\times$ 10^{-5}	1.28 $\times$ 10^{-5}
Xe^{43+} (3s - $3p_{3/2}$)	-4.84 $\times$ 10^{-5}	1.22 $\times$ 10^{-5}
Xe^{42+} $3s^2$ - 3s3p $^3P_1$)	-6.73 $\times$ 10^{-5}	1.33 $\times$ 10^{-5}
Xe^{42+} $3s^2$ - 3s3p $^1P_1$)	-1.02 $\times$ 10^{-5}	1.12 $\times$ 10^{-5}

Different systematic tests were conducted to evaluate the isotope shift obtained with this method. The dependence of the measured shift with changing number of channel numbers used to calculate the wavelength centroid was evaluated. The dependence of the shift with the change in the bin width used while binning the residual distributions was studied as well. The details of these systematic tests are given in Section 8.4. From these tests, it was confirmed that the results with different channel numbers and bin sizes were within the uncertainties.

Another test of consistency in the shift was performed by fitting the residual distribution with a constant function instead of binning the distribution. The scatter of the residual was fitted separately for the two isotopes with a constant, where the difference in these values gave the isotope shift. The shift obtained with this fit should agree with the shift obtained from the histogram of the residuals fitted with the Gaussian function, given no error is introduced by binning the data. Figures 8.23 and 8.24 show the residual fitted with a constant and the resulting shift determined from the difference in the constant.

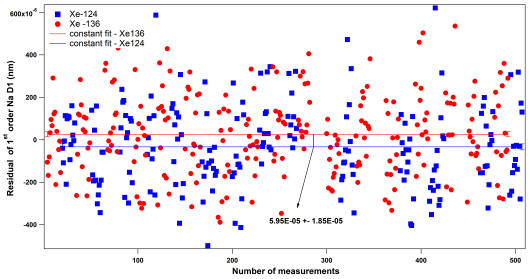

Figure 8.23: Residual distribution of the first order Na-like D1 line and constant fitted to the individual isotopes: blue represents ^{124}Xe and red represents ^{136}Xe

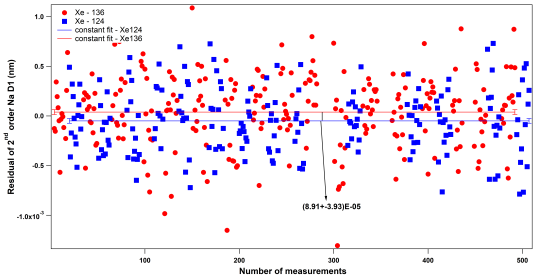

Figure 8.24: Residual distribution of the second order Na-like D1 line and constant fitted to the individual isotopes: blue represents ^{124}Xe and red represents ^{136}Xe

The wavelength shift for the first order Na-like D1 line was determined to be $5.95(1.85)\times10^{-5}$ nm. This value was is in agreement with the value of $7.45(1.98)\times10^{-5}$ nm for the same transition obtained using the second method. However, for the second order Na-like D1 line, the shift was obtained to be $4.46(1.68)\times10^{-5}$ nm. This was determined by dividing the shift between the two isotopes $8.91(3.93)\times10^{-5}$ nm by 2. This value does not agree within the uncertainty of the value of $8.06(1.67)\times10^{-5}$ nm obtained with the second method. The combined shift from the constant fit procedure was $5.13(1.24)\times10^{-5}$ nm. This shift falls just outside the shift listed in Table 8.5. To analyze this problem in detail, a more rigorous data analysis procedure was formulated. The details of this new method is given in section 8.3.5.

8.3.5 Isotope Shift Analysis: Method III

In the second method, the shift was determined by binning the residual distribution followed by fitting the distribution with a Gaussian function. However, a disagreement in the shift of the second order D1 transition was observed when the residual distribution was fit with a constant. This disagreement is either due to the assumption of a normal distribution for the residuals or due to some systematic dependence of the second order Na-like D1 transition on the electron beam energy. For further evaluation of the result, an alternative method was developed. The three parts described below follow the same reasoning. Part III was chosen for the final data analysis and the final reported values of the shift is determined with this method.

8.3.5.1 Analysis: Part I

In this method, a third order polynomial function with an added constant term was used to fit the long-term variation of the centroid positions. The function used to fit the variation of the wavelength centroid positions was defined as: f(x) = $K_0 + K_1 \times x + K_2 \times x^2 + K_3 \times x^3$ + C. The first four terms correspond to a third order polynomial as before and the last term corresponds to the added constant term. This function was used to fit the

scatter of the centroid separately for each regions for the two isotopes such that the difference in the constant term gives the isotope shift. The initial guess for the fitting coefficients, K_0, K_1, K_2 and K_4 were provided by the previous analysis in the second method. These coefficients were constrained to have no uncertainty such that the uncertainty in the constant term (C) contains the uncertainty in the fit. The uncertainty in the shift was given by the quadrature sum of the individual uncertainties in the constant term for the two isotopes.

This method was applied to all three regions and the combined shift was obtained by the weighted average of the individual shifts as defined in equation 7.9. The combined uncertainty was determined by propagating the individual uncertainties. Table 8.6 lists the shift obtained with this method for three different regions and the combined final shift along with their uncertainties. The shift obtained with this method for the Na-like D1 line was $5.01(1.23)\times10^{-5}$ nm. Figures 8.25 and 8.26 show the different regions fitted with a polynomial plus a constant function for the two orders of the Na-like D1 transition.

Table 8.6: Shift obtained using the polynomial fit plus a constant for the first and second order Na-like D1 transitions

	Region	Shift (x_i)	(σ_i)	$W_i = 1/\sigma_i^2$	$x_i.W_i$	Shift (nm)	Uncertainty (nm)
1^{st} order Na-like D1 transition	1	-4.09× 10^{-5}	3.43× 10^{-5}	8.50× 10^{8}	-3.48× 10^{4}	-5.86× 10^{-5}	1.86× 10^{-5}
	2	-6.72× 10^{-5}	2.49× 10^{-5}	1.61× 10^{9}	-1.08E× 10^{5}		
	3	-6.11× 10^{-5}	4.81× 10^{-5}	4.32× 10^{8}	-2.64E× 10^{4}		
2^{nd} order Na-like D1 transition	1	-5.14× 10^{-5}	3.07× 10^{-5}	1.06× 10^{9}	-5.45E× 10^{4}	-4.50× 10^{-5}	1.66× 10^{-5}
	2	-4.17× 10^{-5}	2.12× 10^{-5}	2.22× 10^{9}	-9.28× 10^{4}		
	3	-4.65× 10^{-5}	5.34× 10^{-5}	3.51× 10^{8}	-1.63× 10^{4}		

8.3.5.2 Analysis: Part II

The procedure in part I required an initial guess for the fitting coefficients. Furthermore, the coefficients were constrained to have no uncertainty. A better way to follow this procedure would require fitting a polynomial plus a constant function by using a multivariate fitting routine. In this routine, a third variable was defined that takes the value zero for one isotope and one for the other. The function was then defined as: f(x,z) = K_0 + $K_1 \times x + K_2 \times x^2 + K_3 \times x^3$ + C × z. Here, z is the new variable that was set to 0 for one isotope and 1 for the other, such that the coefficient C is the shift between the

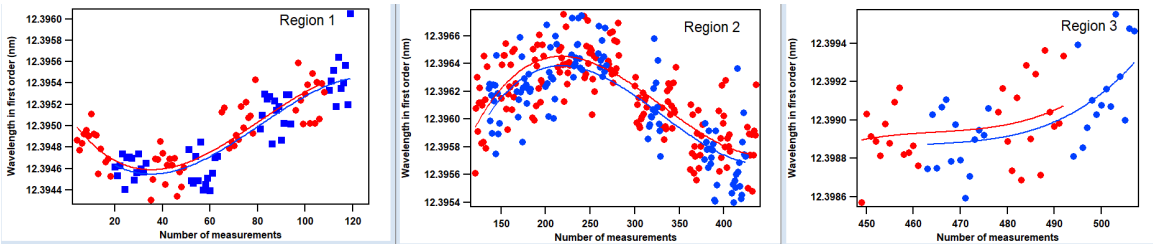

Figure 8.25: Polynomial plus a constant fit for the first order of the three regions of the Na-like D1 transition.

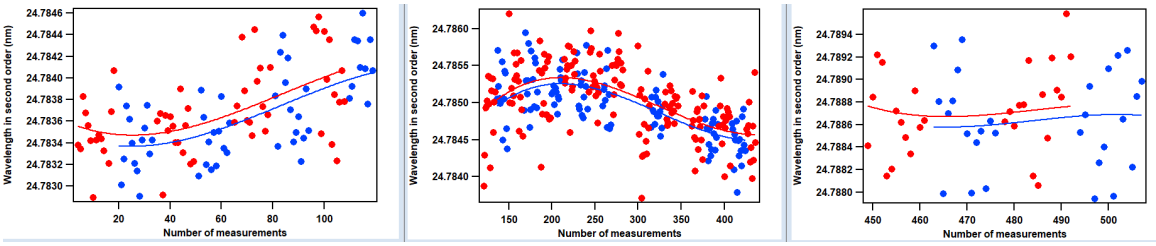

Figure 8.26: Polynomial plus a constant fit for the second order of the three regions of the Na-like D1 transition.

isotopes. This fitting function allowed us to fit the data set for the two isotopes at the same time to evaluate the shift properly. The fitting routine was determined for the three regions separately and the combined shift was obtained by the weighted average of the individual shifts defined as equation 7.9. The combined uncertainty was determined by propagating the individual errors. Table 8.7 lists the shifts for different regions for the first and second order of Na-like D1 line obtained with a multi-variate fitting function. The combined shift for the Na-like D1 line was obtained to be $5.6(1.34)\times10^{-5}$ nm.

Table 8.7: Shift obtained using the multi-variate polynomial fit for the first and second order Na-like D1 transitions

	Region	Shift (x_i)	(σ_i)	$W_i = 1/\sigma_i^2$	$x_i.W_i$	Shift (nm)	Uncertainty (nm)
1^{st} order Na-like D1 transition	1	-4.17× 10^{-5}	3.74× 10^{-5}	7.15× 10^{8}	-2.98× 10^{4}	-6.15× 10^{-5}	2.00× 10^{-5}
	2	-6.90× 10^{-5}	2.56× 10^{-5}	1.53× 10^{9}	-1.05× 10^{-5}		
	3	-7.21× 10^{-5}	6.07× 10^{-5}	2.71× 10^{8}	-1.96× 10^{4}		
2^{nd} order Na-like D1 transition	1	-6.60× 10^{-5}	3.30× 10^{-5}	9.21× 10^{8}	-6.08× 10^{4}	-5.15× 10^{-5}	1.80× 10^{-5}
	2	-4.36× 10^{-5}	2.28× 10^{-5}	1.92× 10^{9}	-8.38× 10^{4}		
	3	-5.91× 10^{-5}	6.50× 10^{-5}	2.37× 10^{8}	-1.40× 10^{4}		

Comparison of the shift in the first and second order Na-like D1 transition is given in Table 8.8 and Figure 8.27.

It can be seen from Figure 8.27 that the shift in the first order Na-like D1 agrees

Table 8.8: The shift (^{124}Xe - ^{136}Xe for the first and second order Na-like D1 transitions using different methods.

	First order Na-like D1		Second order Na-like D1	
	Shift (nm)	Uncertainty (nm)	Shift (nm)	Uncertainty (nm)
Residual Gaussian fit	-7.45× 10^{-5}	1.98× 10^{-5}	-8.06× 10^{-5}	1.67× 10^{-5}
Residual constant fit	-5.95× 10^{-5}	1.85× 10^{-5}	-4.46× 10^{-5}	1.68× 10^{-5}
Polynomial + constant fit	-5.86× 10^{-5}	1.86× 10^{-5}	-4.50× 10^{-5}	1.66× 10^{-5}
Multi-variate polynomial fit	-6.15× 10^{-5}	2.00× 10^{-5}	-5.15× 10^{-5}	1.80× 10^{-5}

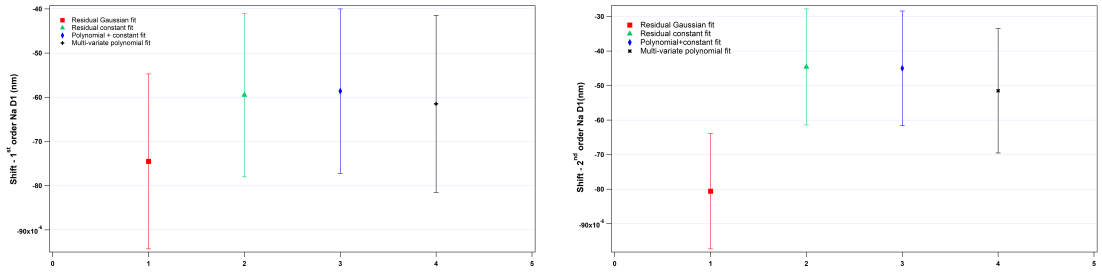

Figure 8.27: The shift (^{124}Xe - ^{136}Xe) for the first order (left) and second order (right) Na-like D1 line using different methods

within the uncertainty with the different methods of analysis. However, the shift in the second order Na-like D1 transition determined from the Gaussian fit of the binned residual distribution does not agree with the other methods. On further analysis of the second order D1 line, it was seen that the centroid of this transition changes with changing number of channels around the peak. This deviation in the wavelength centroid was larger in the third region of the scatter plot. The systematic dependence of the second order D1 transition suggest the possibility of blend with unknown features. The inconsistencies with the shift measured for the second order D1 line was attributed to these blends. The wavelength centroids of the Na-like D1 transition in the first and second order is shown in Figure 8.28.

8.3.5.3 Analysis: Part III

In the above mentioned methods, the shift was determined separately for the three different regions and then combined together to find the final shift. The systematic investigation of the second order Na-like D1 transition indicated the presence of blends with unknown features. As a result, the final analysis of the shift was conducted by using the

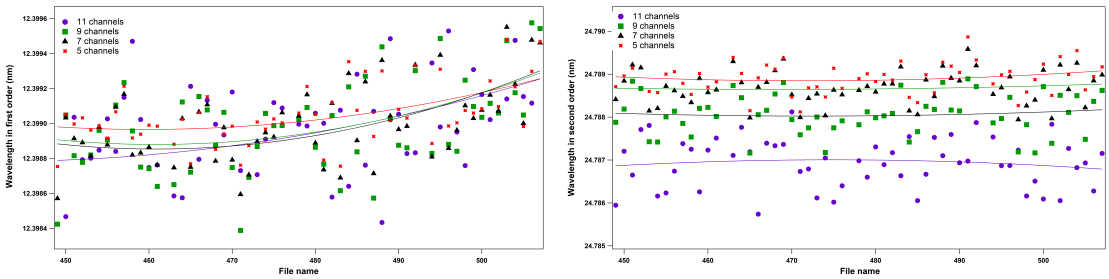

Figure 8.28: Wavelength centroids of the first order (left) and second order (right) Na-like D1 transitions for datasets in the third region of the scatter plot with changing number of channels

first order Na-like D1 transition only. For the final analysis, a python routine was constructed to analyze the time-ordered sequence of the D1 line centroid positions such that the whole dataset were fitted with a multi-variate polynomial together for the three regions. The same polynomial functions were used for the two isotopes with the inclusion of a six piece function that depends on the isotope and the region other than an overall constant free term, representing the final shift. Different sets of coefficients were used for datasets in the different regions. The shift for the Na-like D1 transition obtained from this method was $6.55(2.03)\times10^{-5}$ nm. An alternative analysis was implemented with the model to get the shift in channel number by fitting the channel centroids instead of the wavelength centroids. The shift in channel number was then converted to the shift in wavelength in units of nm by applying the dispersion (dE/dx) obtained from the calibration process. The shift corresponding to this method was obtained to be $6.26(1.69)\times10^{-5}$ nm. The slightly larger uncertainty in the shift with the use of the wavelength centroids instead of the channel centroids correspond to the additional uncertainty that arises from the calibration.

Figure 8.29 shows the partial series of the centroid values plotted for the data set with alternating isotope sequences along with the polynomial fit. The residuals were binned separately for the two isotopes and the resulting normally distributed data was fitted with a pure Gaussian function as shown in Figure 8.30. The centroid of the Gaussian for the two isotopes are in excellent agreement by more than order of magnitude of the uncertainty reported for the shift. This provided confidence in the analysis procedure developed to

treat the data. The uncertainty in the shift included contributions from both statistical and systematic uncertainties. A systematic investigation of the shift was performed by conducting different tests. Systematic studies of the shift were performed by varying the bin sizes used in the residual distributions, by changing the order of the polynomial used to fit the scatter of the centroid positions, and by using different number of channels while calculating the line centroid to verify the consistency of the results.

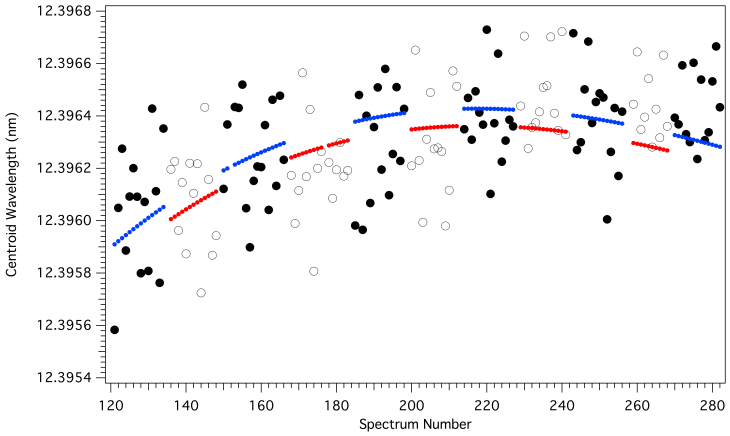

Figure 8.29: Partial series of the centroid values of the centroid positions of the Na-like D1 transition in first order for the ^{124}Xe (open circles) and ^{136}Xe (full circles) isotopes.

8.4 Systematics Study of the Isotope Shift

A number of systematic tests were conducted to evaluate the measured shift and the accuracy of method used. Since the weighted average centroid was used to find the line positions of several peaks, it was necessary to check for deviation in the result with the number of channels chosen to calculate the wavelength centroid. Figure 8.31 shows how the shift changes with changing number of channels chosen to compute the weighted average. It was noted that the best representation of the peaks were given by selecting a pixel size of 7. We present the final values corresponding to the respective analysis.

Similarly, another systematic test of the isotopic shift was done by changing the bin width of the scattered distribution of the residuals. This test was performed to verify that

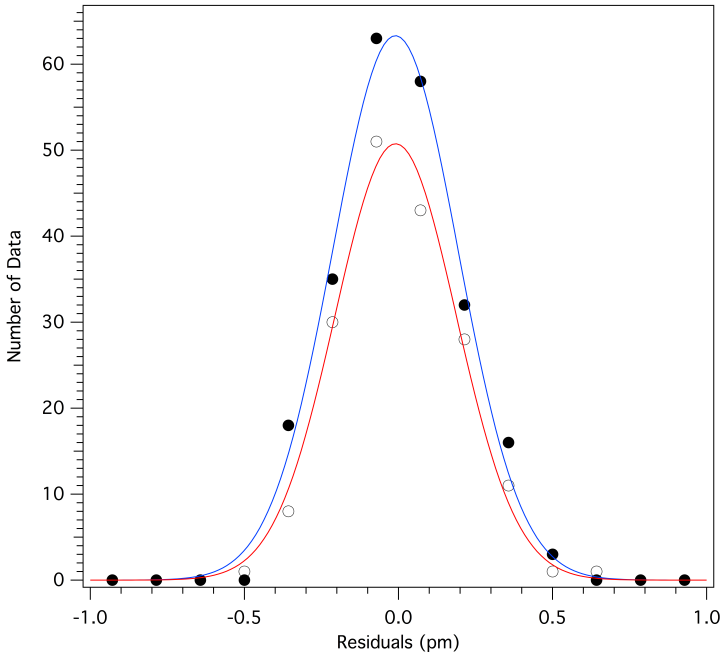

Figure 8.30: Statistical distributions of the residuals ^{124}Xe (open circles) and ^{136}Xe (full circles) isotopes fitted with pure Gaussian functions.

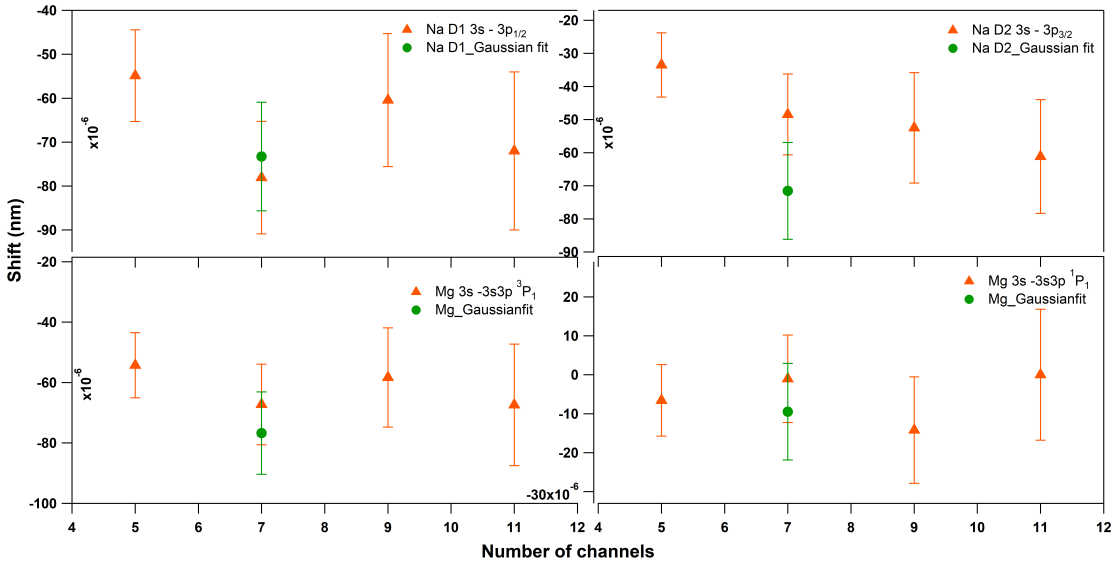

Figure 8.31: Isotope shift (orange) between ^{124}Xe and ^{136}Xe plotted with changing number of channels used to determine the wavelength centroid. The green data points correspond to the Gaussian fitting with 7 channels around a peak.

the binning process does not introduce additional uncertainties or changes to the final shift value. This test was performed for the shift obtained using the second method of analysis described in Section 8.3.4. The values for the isotopic shift with different bin widths is shown in Figure 8.32 along with their associated uncertainties. It can be seen that all the values lie within the measurement uncertainty. Since a bin width of 0.0003 nm gave enough data points around the Gaussian peak of the binned residual distribution, we chose this bin width for the analysis.

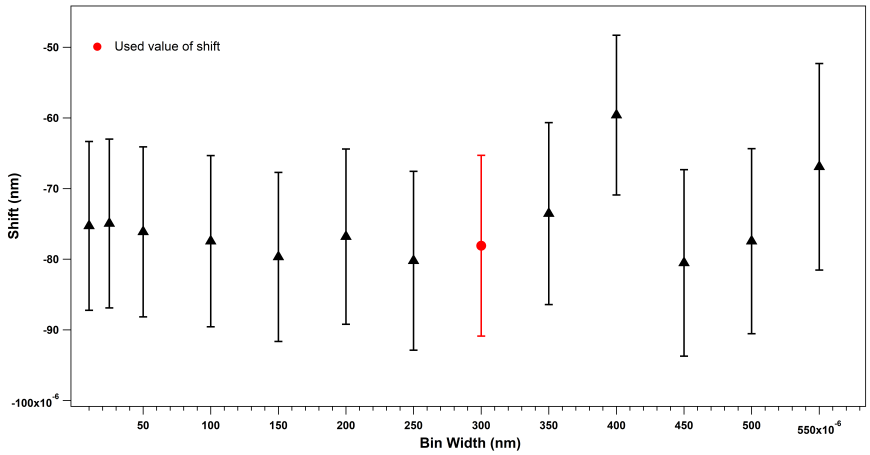

Figure 8.32: Isotope shift (^{124}Xe - ^{136}Xe) for Na-like D1 transition (black) for different bin sizes while binning the scattered residual. The red circle corresponding to the bin width of 0.0003 nm was used for the final analysis.

8.5 Theory

The isotope shift of the transitions of interest were calculated using the RMBPT and MCDHF methods using the GRASP2K package [JAG13]. Brief details about the methods have been provided in Section 2.3.2. The RMBPT calculations specific to the measurement were performed by collaborator Dr. Steven Blundell and the MCDHF calculations were performed by Dr. Dipti Goyal.

For the MCDHF method, a two-parameter Fermi model defined by equation 2.36 was used to get the nuclear potential experienced by the bound electrons. The atomic

state function (ASF) for single configuration Dirac-Fock solution was calculated for ^{136}Xe. The agreement in the isotope shift of the Na-like D1 transition with the wave-function of ^{136}Xe compared to the wave-function of ^{124} was within 0.12 %. The correlation effects were included in the calculation by expanding the configuration state functions (CSFs) with the inclusion of single excitations, double excitations from the occupied orbitals to n = 6 or 7, or triple excitations within n = 3 shells. The relativistic configuration interaction (RCI) calculations were implemented to take into account the Breit interactions and the QED effects up tothe n = 4 or 5 shells. The relativistic isotope shift module (RIS3) was then implemented to obtain the mass shift and the field shift coefficients. The resulting values for the coefficients for the different transitions are listed in Table 8.4 and labeled as MCDHF. The field shift is calculated from the electronic factor F_k using the definition 8.7, where F_k calculated using the equation 8.8.

$$\delta\nu_{k,FS}^{A,A'} = F_k \delta < r^2 >^{A,A'} \tag{8.7}$$

where,

$$F_k = \frac{Z}{3\hbar}\left(\frac{e^2}{4\pi\epsilon_0}\right)\Delta \mid \psi(0)^2 \mid \tag{8.8}$$

These calculations do not include effects from the higher nuclear moments in the field shift.

To evaluate the contributions from the higher nuclear moments, the field shift was estimated explicitly from the difference in the transition energies between the ^{124}Xe and ^{136}Xe isotopes that were obtained separately by solving the MCDHF+RCI equations. The difference in the results obtained with these two methods provided an estimate of the contribution of the higher order nuclear moments. This difference was $\approx$ 4 % for the 3s - 3p transitions, $\approx$ 11 % for the 3p - 3d transitions, and $\approx$ 0 % for the 3p - 3p transition. The 0 % contribution from higher moments for transitions within the same orbital might correspond to the cancellation of the different orders of moments, resulting in a net effect of zero. The field shift coefficient obtained with the second method has been labeled as GRASP HNM in Table 8.4.

Another method employed in calculating the mass shift and field shift coefficients used the RMBPT method performed up to second order [AJP$^+$92] for the Mg-like transitions and up to third order [JBS88b, JBS88a] for the Na-like transitions. The transition energy was calculated separately for the two isotopes with the assumption of different nuclear charge distributions for the different isotopes. The shift in the transition energy was then determined in each order from the RMBPT simulations. The RMBPT method were found to converge rapidly with the third-order contributions to the Na-D lines. The field-shift coefficient F_k, was determined from equation 8.7. $\delta < r^2 >^{A,A'}$ is determined from the difference in the mean-square radius of the two nuclear charge distribution assumed in the calculation. Different nuclear charge distributions were used for the isotopes and the process was repeated using different pairs of nuclear charge distributions. The values of F_k obtained with different pairs changed within 1 % to 2 % and was taken as the error due to the dependence in the nuclear model. Higher order correlations effects and QED corrections were estimated from GRASP2k and was found to have an error of less than 0.1 %. The dominant error comes from the assumption that F_k is proportional to $\delta < r^2 >$, which is termed as the parametrization error or the error due to nuclear dependence. For a transition involving a valence s electron, the field shift is more accurately proportional to the Seltzer moment λ [BBP$^+$87] given as,

$$\lambda = \delta < r^2 > + S_4 * \delta < r^4 > + S_6 * \delta < r^6 > \tag{8.9}$$

Values for the coefficients S_4 and S_6 from [BBP$^+$87] suggest that for Xe, the higher-order moments are about 4 % of $\delta < r^2 >$. A similar conclusion was obtained with the GRASP2k package. The nuclear-model dependence of F thus corresponds to the typical fluctuations in the quantity $1+(S_4 * \delta < r^4 > + S_6 * \delta < r^6 >)/\delta < r^2 >$ with the nuclear model. The mass shift coefficient was calculated with the inclusion of nuclear recoil corrections to an order of $(Z\alpha)^2$ beyond the non-relativistic mass shift [Pal87]. Since the non-relativistic nuclear-recoil effect is on the order of $(Z\alpha)^2$ as well, the overall recoil correction of the order

of $(Z\alpha)^4$ was used in the calculation. The calculations were performed twice, including and not including the nuclear recoil effects, such that the difference in the two methods results in the required mass-shit coefficient. The error in the mass shift coefficient is mainly due to the omitted higher-order $(Z\alpha)^5$ relativistic corrections in the nuclear-recoil formalism. This contributed about 6 % of the total mass shift coefficient. Excellent agreement was found between the results obtained using the two methods.

Table 8.9 lists the values of the FS and MS coefficients for different transitions in units of (10^{-6} nm) for the Na-like D1 transition. These values are listed in Table 8.4, where the units of field-shift coefficient is GHz/fm^2 and mass shift coefficient is THz amu. Conversion factor used are given below:

1 cm^{-1} = 299979.3 MHz

M^{124} = 123.9058942 amu

M^{136} = 135.907214 amu

Table 8.9: The mass shift and field shift from theory and measurement along with the uncertainties are listed for the Na-like D1 in units of 10^{-6} nm.

	RMBPT		**GRASP2K (HO included)**		**CIDF [Tup]**
	$\delta\lambda$	$\Delta\delta\lambda$	$\delta\lambda$	$\Delta\delta\lambda$	$\delta\lambda$
Normal mass shift	-4.8		-4.8		-4.84
Specific mass shift	-62.2		-62.3		-62.7
Total mass shift	-67.0	3.4	-67.1	3.4	-67.5
Field shift	143.0	2.86	142.0	2.84	143.3
Theory	76.1	4.4	75.3	4.4	75.8
Experiment	65.5(20.3)				

Disagreement in the isotope shift was observed in between the theoretical and experimental shift of the Na-like D2 line. A systematic dependence of the transition wavelength with the electron beam energy was observed for this transition. A similar trend in the Na-like D2 line has been reported by Gillaspy *et al* in their work [Gil10] that was referred to unresolved blend with a P-like Xe transition from Vilkas *et al.*'s [VIT06]calculations. Since,

the Na-like D1 line in first order indicated no signs of blends, the shift and the relative charge radius was obtained using this transition.

8.6 Determination of Relative Nuclear Charge Radius

Once the measured and calculated isotope shift was determined, the change in the mean-square charge radii $\delta < r^2 >$ was estimated by comparing the two values. To do so, the mass shift coefficient obtained from the calculation was subtracted from the total measured isotope shift. From the definition of the isotope shift 2.23, the total shift can be written as:

$$\delta\nu = F \times \delta < r^2 > +(NMS + SMS)\frac{M^A - M^{A'}}{M^A \times M^{A'}} \tag{8.10}$$

The mass shift coefficients and the field shift coefficient was calculated using the two theoretical methods.

From the measured shift, we get the term $F \times \delta < r^2 >$ using equation 8.11.

$$F \times \delta < r^2 >= \delta\nu_{exp} - MS \tag{8.11}$$

We can then estimate the parameter $\delta < r^2 >$ by using equation 8.12.

$$\delta < r^2 >= \frac{F \times \delta < r^2 >}{F} \tag{8.12}$$

The nominator represent the measured field shift determined from equation 8.11 and the denominator is provided from the calculations. Combing these values, we can determine the nuclear parameter, $\delta < r^2 >$.

For the Na-like D1 transition, the estimation of $\delta < r^2 >$ from the measured and calculated values is explained here. The measured isotope shift is equal to 6.55×10^{-5} nm, with the uncertainty of 2.03×10^{-5} nm. The transition frequency is given by:

$$\delta\nu = \frac{c \times \delta\lambda}{\lambda^2} \tag{8.13}$$

Here, c is the speed of light in vacuum = 2.997E17 nm. $\delta\lambda$ is the shift in the wavelength = 6.55$\times$ 10^{-5} nm and λ is the transition wavelength = 12.394 nm. This results in a frequency shift of -127.83 GHz.

The value of the MS coefficient from RMBPT calculation for this transition is -183.5 THz amu. The conversion of this value to frequency shift is given by:

$$MS(THzamu) \times \frac{M_A - M'_A}{M_A \times M'_A} = -183.5 \times \frac{123.9059 - 135.9072}{123.9059 * 135.9072} = 0.13077THz = 130.77GHz$$

The term $F \times \delta < r^2 >$ is then given by difference in the total shift and the mass shift, which equals -258.61 GHz. From the RMBPT calculations, F = -963.7 GHz/fm^2. This results in the $\delta < r^2 >$ = 0.2683 fm^2 using equation 8.12. Similarly, if we use the value of the mass shift and field shift obtained from the MCDHF calculations, the value of $\delta < r^2 >$ is determined to be 0.2697 fm^2. The result obtained with the two methods agree within 0.1 % with each other.

The final value of $\delta < r^2 >$ for the Na-like D1 transition was computed from the average of the two values determined with the RMBPT method and GRASP2K method. This resulted in a value of 0.269 fm^2 for the relative change in the mean square radii between ^{124}Xe and ^{136}Xe isotopes. To obtain the uncertainty in the value of the $\delta < r^2 >$, the uncertainty of the measured value of 2.03$\times$$10^{-5}$ nm was used along with the uncertainty of the calculations. The details of the error evaluation is given in the Section 8.7.

Separate evaluation of the Mg-like and the Al-like transitions is to be continued. With the measured isotope shift of -6.73(1.34)$\times$$10^{-5}$ nm obtained by using the second method. Table 8.5 for the Mg-like 3s^2 – 3s3p ^{3}P$_1$ transition, the variation in the mean-square radius was obtained to be 0.279(0.032) fm^2.

8.7 Error Analysis

The field shift is usually approximated as $\delta\nu_{FS}$ = F $\times$ δ $< r^2 >$, F being the electronic factor. The proper definition of F is given by:

$$F = \frac{\delta\nu_{FS}}{\lambda} \tag{8.14}$$

The error in the calculation of F was close to 1% – 2 % and the error in the calculation of mass shift coefficient was nearly 5 %. If we include the error in the higher order nuclear moments in the definition of F, the error in $\delta < r^2 >$ can be approximated as,

$$\Delta\delta < r^2 >= \sqrt{(\Delta\delta\nu_{FS}/F)^2 + (\Delta F * \delta\nu_{FS}/F^2) + (\Delta S_{HO})^2} \tag{8.15}$$

Here, S_{HO} corresponds to the error due to the higher order nuclear terms $S_4 * \delta < r^4 > + S_6 * \delta < r^6 >$ and can be considered negligible since the higher order nuclear moments are already included in the calculations. The total uncertainties in the theory propagated to an error of 3.3 % in the extracted value of $\delta < r^2 >$.

The error in the value of the measured field shift is given by the quadrature sum of the error in the mass shift estimated from the calculations and the error in the total measured shift.

$$\Delta\delta\nu_{FS} = \sqrt{(\Delta\delta\nu_{exp})^2 + (\Delta\delta\nu_{MS})^2} \tag{8.16}$$

For the Na-like D1 transition, $\Delta\delta\nu_{exp}$ = 2.03$\times$ 10^{-5} nm = 39.62 GHz. The error in MS, $\Delta\delta\nu_{MS}$ = 5 % of MS = 6.55 GHz. So, the error in the field shift from equation 8.16 = 39.618 GHz. Similarly, the second term in equation 8.15 using 2 % for the error in F is equal to 0.0008 GHz. Using these values along with equation 8.15, the error in $\delta < r^2 >$ is 0.042 fm^2. Since F already includes the contributions from higher order terms, the contribution from S_{HO} can be neglected. A similar result is obtained using the error in the mass shift from the GRASP2k calculation. Thus, the variation in the mean square radius for the Na-like D1 transition is equal to 0.269(0.042) fm^2.

The relative theoretical uncertainty was determined to be 3.3 % and the relative total uncertainty was obtained to be ≈ 16 %. This error in the extracted value of $\delta < r^2 >$ was dominated by the measurement uncertainty. With the advancement in the theoretical models in recent years, advancements in the experimental precision can further improve the reported accuracy in the values of the relative mean square radii.

8.8 Comparison with Previous Work

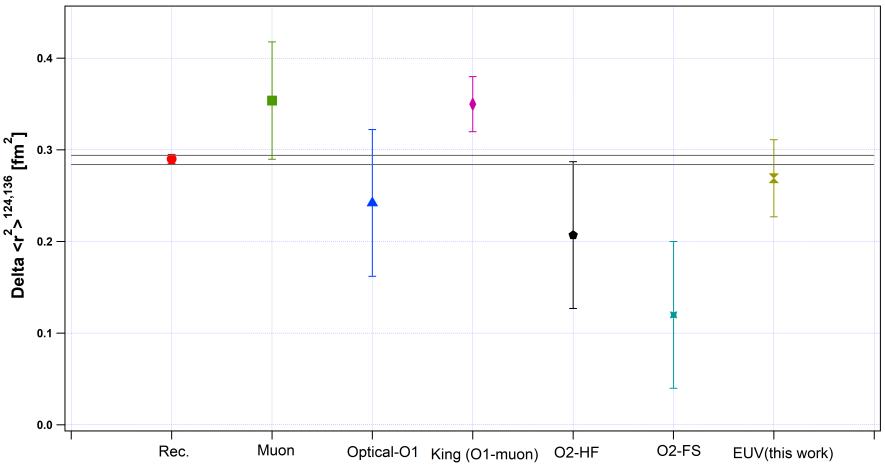

Figure 8.33: Comparison of the variation in charge radius between Xe isotopes 124 and 136 obtained with different methods.

Figure 8.33 shows the comparison of our result with the previous experimental and theoretical works. The difference in mean-square nuclear charge radius between ^{136}Xe and ^{124}Xe, $\delta < r^2 >^{136,124}$ from our work resulted in a value of 0.269(0.042) fm^2. It can be seen from the Figure 8.33 that this value agrees with the recommended value (Rec.) [AM13] and the values from the previous measurements using muon spectroscopy (Muon) [FBH$^+$95] and optical laser spectroscopy (optical-O1) [BAN$^+$89]. Our result also agrees with the result of the King plot analysis obtained from the combined optical measurements and the muonic-atom results (king)1-muon) [LRS07]. The calculated value based on the Hartree-Fock method (O2-HF) agrees with our result as well. Slight disagreement of our result with the value obtained from the Fermi-Segre calculations (O2-FS) [FHKS74] was observed.

The satisfactory agreement of our work based on the EUV spectroscopy of the Na-like D1 transition with other methods provides further confidence in this method. Only two measurements of the relative charge radius of Xe isotopes are available. Our measurement based on this new technique provides additional experimental data that can help in further evaluation of the existing nuclear charge radii values, such as the results of Angeli [AM13]. Furthermore, this method complements the optical measurement by providing additional data set to calibrate the atomic structure calculations. This method has an advantage of precise atomic structure calculations of the mass shift and the field shift. RMBPT method converges as 1/Z for multiply charged ions for each successive order, which is otherwise non-perturbative for neutral atoms. This method can be used as a new tool in the determination of the nuclear charge radii for radioactive isotopes that are short-lived since small quantities of the isotopes are required. With the existing and upcoming isotope beam facilities around the world, our method provides a new scope for conducting measurements of the isotope shift. g

Chapter 9

Conclusions and Discussion

9.1 Highly Charged Ions at the Interface of Atomic-, Plasma-, and Nuclear Physics Research

The extreme ultraviolet spectra of highly charged Y and Xe ions were measured using an electron beam ion trap. The study was focused on understanding the atomic transitions corresponding to these plasmas, which was used to (i) identify the unknown line features, (ii) diagnose plasmas using line intensity ratios, and (iii) determine the nuclear charge radius. The identification of atomic data relevant to different research communities can provide benchmark tests of the atomic theory. Elements in medium-Z region are important because accurate wavelength determinations is possible in this region with an EBIT. Such measurements can provide further understanding of many-electron systems. We measured EUV spectra of the L-shell ions of highly charged yttrium, (Y^{26+} – Y^{36+}) in the wavelength range of 4 nm to 20 nm. The transitions were identified with wavelength uncertainties ranging between 0.0004 nm for the strong lines and 0.0020 nm for the weak lines. The line identification was aided by the collisional-radiative non-Maxwellian code NOMAD to treat the steady-state EBIT plasma. Several spectral lines corresponding to the electric-dipole E1 and magnetic-dipole M1 transitions were observed. To analyze the potential suitability of the M1 transitions to plasma diagnostics, CR modeling was performed on Maxwellian

plasmas for electron densities of 10^{12} cm^{-3} to 10^{20} cm^{-3} and temperatures of 1500 to 6000 eV. The line ratios of some of the identified M1 and E1 transitions were found to show dependence on the electron density and temperature. Such dependence suggests these line ratios could be employed to diagnose fusion plasmas.

The Al-like Y through L-like Y transitions were selectively produced by increasing the electron beam energy from 2.3 keV to 6 keV. A total of 59 spectral lines were identified in this work from the Li-like to the Al-like isoelectronic sequence. Of these, 39 lines were newly identified and 21 lines correspond to previously identified transitions. The identification of transition wavelengths for Be-like to Ne-like charge states of Y helps to constrain the theoretical studies. The theoretical calculations for these systems are complicated due to the large number of electron-electron correlations in the many-electron systems, reducing the level of accuracy of the simulations. However, the experimental accuracy of these systems is comparable to that of the one-electron ions. The Li-like 2s -2p resonance lines and the Na-like D 3s - 3p lines are of significant interest. These lines can be accurately calculated with *ab-initio* methods because of their simple atomic structure. In this work, the Li-like resonance lines (2s -2$p_{1/2}$) and (2s -2$p_{3/2}$) were identified with an accuracy of 57 ppm and 82 ppm, respectively, at the beam energy of 6 keV. The resonance line arising from the (2s -2$p_{3/2}$) transition exhibits a slight disagreement with previous calculations. This discrepancy demands the existing theoretical framework be further developed.

The identification of the strong Na-like D transitions for highly charged Y agreed with both the previous measurements and the theoretical calculations, where we report smaller uncertainty in the transition wavelengths. This is the first measurement reported for these transitions with the use of an EBIT. The Na-like D1 (3s - 3$p_{1/2}$) and the Na-like D2 (3s - 3$p_{3/2}$) transitions were measured with an accuracy of 35 ppm and 33 ppm, respectively. The study of the D transitions by [GOR$^+$13] showed that the accuracy in the transition energies along the isoelectronic sequence is limited by the theoretical accuracy. The dominant uncertainty in their calculations originated from the uncertainty in the value of the nuclear charge radius. The authors suggested that the Na-like D transitions are

sensitive to the nuclear size. With the combination of the high precision spectroscopy of these transitions and accurate atomic structure calculations, these transitions can be used to probe the nuclear charge radius. Such transitions are, therefore, important to the research at the interface of atomic and nuclear physics. In addition, the need for the measurements of charge radii of radioactive isotopes is evident from the limited number of methods capable of doing so. As such, these provides motivation for the second part of the work.

The second part of this work was focused on the determination of variation in the nuclear charge radii from EUV spectroscopy of Na-like D transitions of highly charged Xe ions. The isotope shift of the transition wavelength of the Na-like D1 transition between ^{124}Xe and ^{136}Xe was measured to be $6.55(2.03) \times 10^{-5}$ nm. Using this shift in combination with the calculated mass shift and field shift, the difference in the charge radii, $\delta < r^2 >$ was determined to be 0.269(0.042) fm^2. This value agrees well with the previous measurements and with the recommended value provided by Angeli *et al.* [AM13]. Their result was based on the compilation and assessment of the available experimental data along the isotopic and isotonic sequences. This agreement provided confidence in the new EUV based method to determine the nuclear size. Furthermore, this method complements the optical laser spectroscopy measurements by providing more data to test and calibrate complex calculations of neutral and singly ionized atoms used in OLS. This technique does not need macroscopic quantities of the isotopes, offering an advantage over the conventional electron scattering and muon spectroscopy methods. Our method offers the possibility of measuring the isotope shift in short-lived radioactive isotopes at rare-isotope beam facilities. Some of the facilities where such measurements can be conducted are the Isotope Separator and Accelerator (ISAC) facility at TRIUMF and the upcoming Facility for Rare Isotope Beam (FRIB) at Michigan State University.

Moreover, the simplicity of the quasi-hydrogenic Na-like systems can overcome the accuracy of that of neutral and singly ionized systems. For the neutral atoms, the many-body problem is non-perturbative but for multiply charged systems, RMBPT converges as 1/Z for each successive order. The highly charged ions also have suppressed mass shift

effects such that this shift can be directly subtracted to evaluate the field shift. Our calculations performed by the RMBPT and MCDHF method resulted in an overall uncertainty in the theory of less than 4 %. The field shift effects are amplified in highly charged ions. This allows for the measurement of the shift even with the moderate resolution EUV spectrometer.

9.2 Theoretical Implications and Recommendations for Further Research

Atomic spectroscopy provides reliable atomic data accessible to many research communities. The reliability of these data depends on both the precise measurements and the accurate calculations. The experimental and theoretical studies go hand in hand, complementing each other. In this work, a collisional-radiative code was employed for a non-Maxwellian EBIT plasma at different electron beam energies to identify the evolution of several charge states of yttrium and xenon. The use of CR modeling served in straightforward identification of new and previously identified transitions.

In these results, the transition wavelengths were measured with an accuracy of 100 ppm or less. Some of the identified transitions showed disagreement with the available theoretical results. This necessitates further assessment of the calculations. Since the calculations for the few electron ions are more complicated than one-electron ions, the measurement of transitions in such systems provides a reference in treating the calculations. Our wavelength measurement of the Li-like Y resonance line ($2s_{1/2}$ - $2p_{3/2}$ showed a slight disagreement with the theoretical results [KVA$^+$10,SC11]. Further work in the measurement of this transition and other newly identified transitions in mid-Z elements can provide confirmation of our results and tests of the theoretical results.

The proof of principle method to determine the relative change in the mean square charge radii for Xe ions can also be applied to radioactive elements. By employing this technique at the rare isotope beam facilities, measurements of short-lived radioactive iso-

topes can be conducted. Such measurements will provide more datasets that are required to properly calibrate the electronic factor and specific mass shift calculations in neutral atoms. The uncertainty in our result of the relative change in charge radius of Xe isotopes is dominated by the experimental uncertainty. Our experimental uncertainty of 20.3 fm in the isotope shift value of 65.5 fm comprises a 30 % relative measurement uncertainty. By comparing this result with the mass shift and the field shift calculations, we derived the combined uncertainty in the value of $\delta < r^2 >$ to be $\approx$ 16 %. The experimental precision can increase with improvements in the detector capabilities and the use of higher resolution grating of the EUV spectrometer. CCD detectors with larger pixel arrays and smaller pixel size can further improve the measurement accuracy.

Our method is based on the measurement of the shifts in transition energy of the Na-like D transitions between two isotopes. As a result, this method was not limited by the uncertainties of the absolute wavelengths. Neutral Xe atoms were continuously injected into the EBIT trapping region, which produced sample sizes of a million or less ions that were necessary to reach the current statistical accuracy. Continuous injection of Xe atoms results in the creation of lower charge states. Transitions from these charge states can blend with the spectral features of interest. We were restricted to the first order Na-like D1 (3s – $3p_{1/2}$) transition due to the observed systematic dependencies of other spectral features. The clean and isolated Na D1 transition was enough to test our method. Nevertheless, a further optimization of the gas injection procedure is required to limit the production of the lower charge states. This will permit the use of multiple transitions in such analysis. The metal ion source (MEVVA) at the NIST EBIT allows for similar measurements of other isotopes by installing the cathodes relevant to the element of interest. We have recently installed Ir and Os cathodes in this setup with a goal of conducting similar measurement. By measuring the shift in the transition energy between the Na-like ^{193}Ir and ^{192}Os isotopes, we intend to measure the relative charge radius between the two isotopes.

Appendices

Appendix A Identification and Plasma Diagnostics Study of Extreme Ultraviolet Transitions in Highly Charged Yttrium

atoms

MDPI

Article

Identification and Plasma Diagnostics Study of Extreme Ultraviolet Transitions in Highly Charged Yttrium

Roshani Silwal [1,2,*], Endre Takacs [1,2], Joan M. Dreiling [2], John D. Gillaspy [2,3] and Yuri Ralchenko [2]

1 Department of Physics and Astronomy, Clemson University, Clemson, SC 29634, USA; etakacs@clemson.edu
2 National Institute of Standards and Technology, Gaithersburg, MD 20899, USA; joan.dreiling@nist.gov (J.M.D.); jgillasp@nsf.gov (J.D.G.); yuri.ralchenko@nist.gov (Y.R.)
3 National Science Foundation, Arlington, VA 22230, USA
* Correspondence: rsilwal@clemson.edu

Academic Editor: Joseph Reader
Received: 17 July 2017; Accepted: 12 September 2017; Published: 18 September 2017

Abstract: Extreme ultraviolet spectra of the L-shell ions of highly charged yttrium (Y^{26+}–Y^{36+}) were observed in the electron beam ion trap of the National Institute of Standards and Technology using a flat-field grazing-incidence spectrometer in the wavelength range of 4 nm-20 nm. The electron beam energy was systematically varied from 2.3 keV–6.0 keV to selectively produce different ionization stages. Fifty-nine spectral lines corresponding to $\Delta n = 0$ transitions within the $n = 2$ and $n = 3$ shells have been identified using detailed collisional-radiative (CR) modeling of the non-Maxwellian plasma. The uncertainties of the wavelength determinations ranged between 0.0004 nm and 0.0020 nm. Li-like resonance lines, $2s$–$2p_{1/2}$ and $2s$–$2p_{3/2}$, and the Na-like D lines, $3s$–$3p_{1/2}$ and $3s$–$3p_{3/2}$, have been measured and compared with previous measurements and calculations. Forbidden magnetic dipole (M1) transitions were identified and analyzed for their potential applicability in plasma diagnostics using large-scale CR calculations including approximately 1.5 million transitions. Several line ratios were found to show strong dependence on electron density and, hence, may be implemented in the diagnostics of hot plasmas, in particular in fusion devices.

Keywords: highly charged ions; yttrium; spectroscopy; extreme ultraviolet; Li-like; Na-like; magnetic dipole; plasma diagnostics; electron beam ion trap; non-Maxwellian plasma

1. Introduction

Multi-electron ions are under intense theoretical study as state-of-the-art calculations rival highly accurate measurements sensitive to higher order terms of quantum electrodynamics (QED) corrections to atomic energy levels [1]. While elements with a high-Z atomic number have these effects amplified, ions in the medium-Z region have special importance because they allow for more accurate experiments and provide constraints to theoretical trends. In the past few years, the electron beam ion trap (EBIT) research program at the National Institute of Standards and Technology (NIST) has reported accurate measurements in the extreme ultraviolet (EUV) region that focus on systematic observations of transitions in L-shell, M-shell and N-shell ions [2–14]. The work reported here extends these results to a range of previously unobserved transitions of a fifth row element, yttrium.

Yttrium was chosen for the current investigation because of its relevance as a possible diagnostic impurity in tokamak fusion plasmas. For instance, together with strontium, zirconium, niobium and molybdenum, yttrium has been injected into the Texas Experimental Tokamak (TEXT) [15,16], the Joint European Torus (JET) tokamak [17] and the Princeton tokamaks [18–20] and has also been

observed in laser-produced linear plasmas [16,21]. L-shell ions of high-Z elements, especially Be-like to Ne-like [22–26], and a few M-shell ions such as Na-like, Mg-like and Al-like [15,16,27–30] were used to diagnose these hot plasmas for decades. The elemental abundance of yttrium in stars also makes it astronomically important. Its relevance in nuclear astrophysics, weak interaction physics and nuclear structure physics has been discussed [31–34].

Among the various transitions in these elements, special interest is devoted to forbidden transitions that originate from long-lived metastable energy levels. The importance of the forbidden transitions in medium-Z and high-Z elements has been demonstrated by different researchers for astrophysical [35] and fusion [18,36] plasmas. For example, charge states near closed shells include potentially useful forbidden transitions such as those between the $2s^2 2p^5$–$2s 2p^6$ configurations of F-like ions and the magnetic dipole transition $2s^2 2p^5\ ^2P_{3/2}$–$^2P_{1/2}$ in the same ion. These have been extensively investigated in earlier studies [37–40].

There have been a few EUV measurements of highly charged yttrium over the past couple of decades. Alexander et al. observed the EUV spectra of Y IX–XIII in the wavelength range of 4.5 nm–35 nm using vacuum spark [41]. Ekberg et al. performed a series of measurements for the identification of transitions in Si-like Y XXVI [42], Al-like Y XXVII [43] and Mg-like Y XXVIII [21,28] in the EUV spectra emitted from line-focus laser-produced plasmas as part of the X-ray laser research program. Reader et al. have reported observations of F-like Y XXXI [37], Mg-like Y XXVIII [44] and Na-like Y XXVIV [16,45] using laser-produced and tokamak plasmas in a series of systematic spectroscopic studies. Similar experiments for moderate charge states also reported observations of multiply-charged yttrium spectra (Y II–XI); see, e.g., [46–50]. Despite these experiments, the second row isoelectronic sequences of yttrium have largely been unexplored in the EUV region to date.

In this paper, we report the systematic study and identification of atomic spectral lines of the L-shell charge states of yttrium ranging from Li-like to Ne-like ions (Y XXX–Y XXXVII) created and trapped in the NIST EBIT [51,52]. We also present the most pronounced spectral lines of the Na-like, Mg-like and Al-like yttrium charge states, as these can provide benchmark experimental results for precise multi-electron atomic theory calculations. Na-like D1 and D2 lines originate from quasi-hydrogenic ions and have been used as a probe of QED contributions due to their high intensities and the available precise ab initio calculations [6,53–55]. We report the first data for the wavelengths of the Na-like D1 and D2 yttrium lines measured with an EBIT to provide accurate experimental results that complement the previously reported measurements of Reader et al. [45] in laser-produced and tokamak plasmas.

In addition to the spectral analysis, we also discuss the forbidden magnetic dipole (M1) transitions of highly charged yttrium ions that are potentially important for plasma diagnostics. The spectroscopy of forbidden magnetic dipole lines can help deduce important plasma parameters such as the density and temperature of plasmas. These parameters are obtained in practice from intensity ratios of various atomic spectral lines rather than direct measurements, which are difficult or even impossible in fusion, laboratory and astrophysical plasmas [56]. The availability of accurate collisional-radiative models makes this technique a reliable tool for plasma diagnostics [57–59].

M1 transition probabilities strongly depend on the spectroscopic charge Z_{sp}, and for highly ionized ions, these transitions become prominent. At low electron densities, the radiative decay rates are substantially larger than collisional depopulation from both metastable and allowed excited levels. At higher densities, however, the metastable levels decay both by collision and radiation, whereas allowed transitions still take place mostly by radiative decay. This makes the ratio of the allowed versus forbidden transitions dependent on the electron density.

The following sections describe the experimental method, the theoretical calculations that aided in line identifications, the list of the observed transitions and their uncertainties and a discussion of the diagnostic capabilities of some of the M1 transitions.

2. Experiment

The NIST EBIT and a multi-cathode metal vapor vacuum arc ion source (MEVVA) were used to produce highly charged yttrium ions, and the ion spectra were recorded with a custom-made EUV flat field grazing incidence spectrometer [60]. Both the MEVVA and the NIST EBIT are discussed in detail elsewhere [51,61], but we will now briefly review the most important details.

The MEVVA, which produces singly-charged ions by sparking a high voltage across metal cathodes, is located $\approx$ 2 m above the central trapping region of the EBIT. The ions are created at a potential of about 10 kV above ground and are accelerated towards the center of the EBIT through several electrodes at lower voltages. The trapping region, consisting of the drift tubes (upper, middle and lower), is floated on top of the voltage of the cylindrically-shaped shield electrode. To capture the ions in the trap, the shield electrode voltage is very briefly (on the order of 10^{-3} s) switched to a potential of about 9.6 kV, and the middle drift tube voltage is simultaneously raised by an additional 0.4 kV. Then, precisely at the arrival of the ions, the middle drift tube is pulsed down to the shield voltage in order to trap and confine the plasma in the trap. During the entire timing sequence, the lower and upper drift tubes are kept at constant potentials with respect to the shield (0.5 kV and 0.26 kV, respectively) to create axial trapping. Radial confinement is accomplished by a combination of the axial 2.7 T magnetic field and the space charge of the intense electron beam, which is directed through the drift tubes to further ionize the ions. The electron beam energy can then be set as required for the experiment by adjusting the shield electrode voltage. The beam energy in the EBIT is determined by the voltage difference between the electron gun and the middle drift tube, taking into account the space charge of the electron beam in the interaction region [62]. The latter depends on the density of the electron beam and therefore scales with the beam energy and current in addition to the ion cloud neutralization factor, which is generally difficult to quantify. In our experiment, the modeling of the observed spectral line intensities showed that the space charge correction was approximately 150 eV. Electron beam currents were varied between 66 mA and 147 mA during the measurement. To control the charge-state distribution of the yttrium ions, the energy of the electron beam was systematically varied from 2.3 keV–6.0 keV.

The flat field EUV grazing incidence spectrometer [60] is equipped with a liquid-nitrogen-cooled charged-coupled device (CCD) detector with 2048 $\times$ 512 active pixels of 13.5 µm $\times$ 13.5 µm size each. The spectrometer consists of a gold-coated spherical focusing mirror that focuses light radiated from the EBIT plasma onto a slit, followed by a gold-coated concave reflection grating with a groove spacing of approximately 1200 lines mm^{-1}. The instrument has a resolving power of $\lambda/\mathrm{d}\lambda \approx 400$. The 2D images recorded by the CCD were hardware collapsed along the vertical axis, so that the resulting image was a 1D (2048 $\times$ 1) spectrum. Ten 60 s frames of yttrium spectra were collected in a set, giving a total acquisition time of 600 s for each energy. The spectra were filtered of cosmic rays using a program that identifies outlier intensities among different frames within the same set. If the intensity of a channel in a certain frame is five or more Poisson standard deviations away from the mean of all of the frames, it is replaced by the average value of the other frames before the frames are summed together to form the overall spectrum.

3. Wavelength Calibration

Spectra emitted by yttrium ions were acquired in the approximate wavelength region of 4 nm to 20 nm. Wavelength calibration was performed using highly charged neon lines (Ne V–VIII), xenon lines (Xe XLI–XLII), barium lines (Ba XLIII–XLIV), oxygen lines (O V–VI) and iron lines (Fe XXIII–XXIV) [5,7,11,63,64], as described in this section. Neon and carbon dioxide gases were injected into the EBIT as neutral atoms from the gas injection setup described by Fahy et al. [2], with the injection pressure normally on the order of 10^{-3} Pa. Iron ions were loaded from the MEVVA ion source. Small amounts of barium and xenon ions are always present in the trap as heavy ion contaminants from the electron gun and the ion pumps. In order to prevent long-term accumulation of these ions, the EBIT trap was emptied and reloaded every 10 s.

The calibration lines were fitted using unweighted Gaussian profiles, and the locations of the peaks were noted in terms of the channel (pixel) numbers corresponding to the respective lines. The literature-recommended wavelengths [5,11,64] were plotted as a function of channel number weighted with the uncertainty in these wavelengths. A third order polynomial from the fit was used to convert the uncertainties in channel number to the uncertainties in wavelength. The statistical uncertainties of the calibration lines were then determined from the quadrature sum of these uncertainties with the adopted wavelength uncertainties from the literature.

The final calibration function was a third order polynomial that describes the wavelength versus channel as a fit weighted by the inverse square of the total uncertainties of the lines. The latter was calculated as the quadrature sum of the overall statistical uncertainty and the systematic uncertainty. The systematic uncertainty was estimated to be 0.0006 nm by requiring the reduced chi-square of the fit to be 1 according to the standard statistical procedure [65]. Systematic uncertainty may arise from several factors during the experiment such as small device vibrations or uneven pixel response. The residual of the literature values of the calibration lines with respect to their calibrated wavelength provided an assessment of the quality of the calibration. Including their uncertainties, 95% of the residual should lie within two standard deviation (σ) of their mean (μ): $P(\mu - 2\sigma \leq x \leq \mu + 2\sigma) \approx 0.9545$. Figure 1 shows the calibration data points and 95% confidence band of the fit.

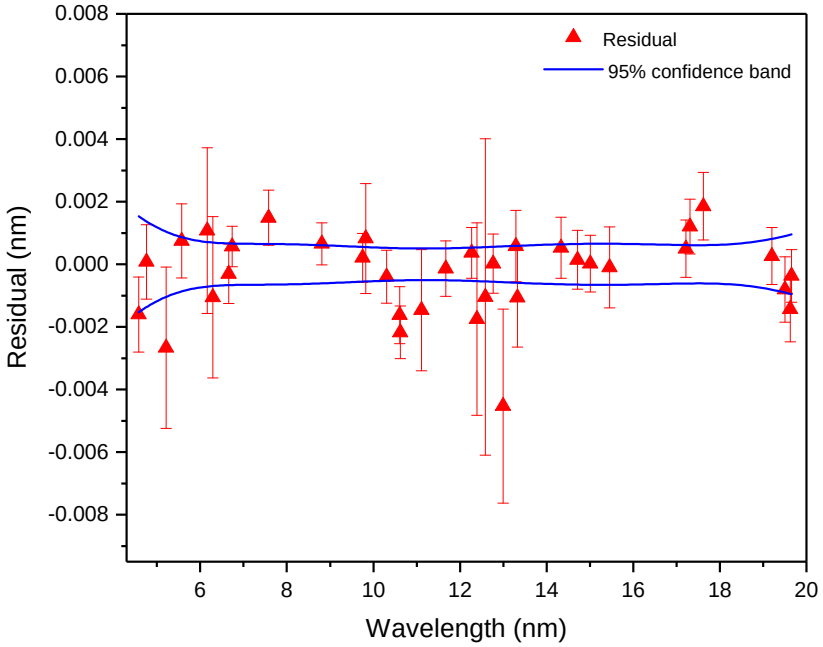

Figure 1. Residual of the adopted wavelength of the calibration lines with respect to their calibrated wavelength. The individual uncertainties of the data points are as described in the text. The solid (blue) line corresponds to the 95% confidence band of the calibration fit.

In calculating the overall calibration uncertainty contributing to the total uncertainty at a given wavelength for the identified yttrium lines, we have used the 95% confidence band at the position of the line. The calibration uncertainties reported are equal to the vertical width of the confidence band divided by four (equivalent to one standard deviation). The calibration uncertainty calculated from the 68.3% confidence band corresponding to one standard deviation gives comparable results, as expected.

4. Theoretical Modeling

The spectral modeling for the non-Maxwellian EBIT plasma was performed with the collisional-radiative code NOMAD [66] that has been extensively used in EBIT spectroscopy. The yttrium plasma was assumed

to be in the steady state, optically thin and uniform with electron density of 10^{11} cm^{-3}. The electron beam energy distribution was modeled by a Gaussian function with the full width at half maximum of 40 eV.

A detailed collisional-radiative (CR) model would generally require a large amount of atomic data, such as energy levels, wavelengths, transition probabilities and cross-sections. For the present analysis, we make use of the Flexible Atomic Code (FAC) [67], which is based on a fully-relativistic model potential and can consistently generate all required data. In total, our CR model included 13 ionization stages from Si-like to He-like ions of yttrium, about 5000 atomic levels and nearly 1.5 million transitions describing spontaneous radiative decays, electron-impact ionization and excitation, as well as radiative recombination. NOMAD also takes into account the charge exchange of ions with neutral atoms present in the trap, which shifts the ionization balance to lower charge states. Within the model, the density of neutral atoms is a free parameter and adjusted such that the theoretical and experimental spectra closely agree. The neutral densities obtained from the spectra of the current experiment are consistent with previous values under similar EBIT conditions.

Another adjustable parameter (although less important due to the lower sensitivity of the results to its variations) is the space charge correction to the electron beam energy as described in the experimental section. A generally good match between the observed and calculated line intensity ratios was obtained with a 150 eV correction to the values calculated from the applied voltages.

The CR model used these data to build and solve a system of rate equations to determine level populations and line intensities for EBIT plasmas of given electron energies. With this approach, NOMAD was used to simulate the yttrium emission as the electron beam energy was systematically changed during the experiment. The calculated spectra were convoluted with the spectrometer energy resolution and corrected for the efficiency of the grazing incidence instrument to obtain the theoretical result.

5. Line Identification

Yttrium spectra were taken as a function of the calibrated wavelength and fitted with unweighted Gaussians to determine the line positions. The uncertainty associated with the identified lines was then calculated from the quadrature sum of the uncertainty of the line fit that corresponds to the statistical uncertainty, the calibration uncertainty, the systematic uncertainty (estimated using the calibration data as discussed above) and uncertainty assigned for a possible small systematic line asymmetry (discussed below), which might be due to line blends or instrument asymmetries. In order to reach the desired ionization stages, the beam energy was systematically varied from 2.3 keV–6.0 keV. By matching theoretical and experimental spectra, we were able to conveniently identify most of the yttrium lines, as shown in Figure 2.

Some of the yttrium lines were also observed in the second and third orders of diffraction, in addition to the first order. Second order and third order yttrium spectra were plotted simultaneously as a visual aid to better identify the observed lines. They were obtained by dividing the line intensities of the first order experimental spectra by 2.5 and eight and multiplying the wavelength by two and three, respectively. Since we observed the same yttrium lines at several different beam energies, our reported wavelengths are the weighted averages of the positions of these lines using the formula for the best combined estimate of N measurements of the same quantity, $x_{CE} = \frac{\sum w_i \times x_i}{\sum w_i}$, x_i being the line position at different energies. The weight w_i is given by $w_i = \frac{1}{s_i^2}$, where s_i is the total uncertainty corresponding to each measurement. A few lines were blended with unresolved features, making it difficult to precisely determine their positions. In such cases, the spectra at energies that gave the cleanest and strongest signals were solely used. As a test for unanticipated systematics, the difference in the individual wavelengths at different energies with their weighted average was calculated. This difference was binned to get a histogram that represents a normal distribution about their mean, which should be zero. The distribution was fitted with a Gaussian function, and the mean value of 0.0003 nm was assigned to be the uncertainty due to unknown line asymmetries. As mentioned earlier, this uncertainty was added in quadrature to the rest of the uncertainties to get the total line uncertainty.

For the lines that we observed in second and third order, the wavelengths and the corresponding uncertainties were divided by two and three, respectively, and the weighted average was calculated accordingly. The total uncertainty for each of the identified lines was computed using the error propagation method $s = \sqrt{\frac{1}{\sum \frac{1}{s_i^2}}}$.

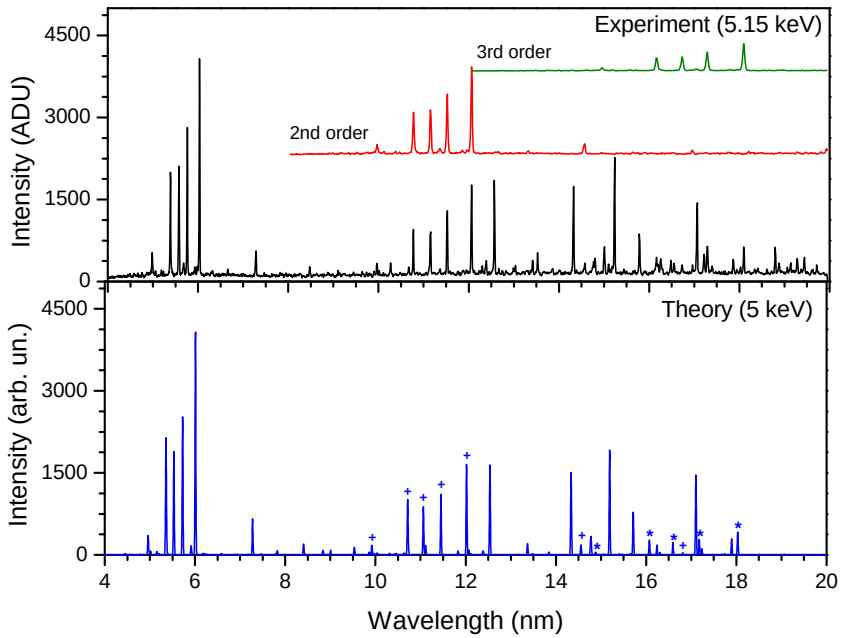

Figure 2. Comparison of the experimental spectrum (**top**) of yttrium with the theoretical spectrum (**bottom**). The intensity is given in analog to digital units (ADU) for the measured spectra. The second and third order spectra for the experimental data are also shown (red and green insets, respectively). The theoretical spectrum includes the second (+) and third (∗) order spectra and is calculated at an energy of 5 keV for the electron beam energy of 5.15 keV, to account for the space-charge correction in the experiment.

The most prominent observed lines were unambiguously identified through comparison with theory. For instance, the Be-like lines $2s^2\ {}^1S_0$–$2s2p\ {}^1P_1$ and $2s^2\ {}^1S_0$–$2s2p\ {}^3P_1$ were identified at 6.0322(5) nm and 15.2336(7) nm experimentally compared to the calculated values of 6.0098 nm and 15.1907 nm. The measured wavelengths of the Li-like, B-like, C-like and N-like yttrium lines are within 1.3% of our theoretical values, sufficient for line identification purposes. We note that for electron beam energies below 3.75 keV, where M-shell yttrium ion charge states become prominent, a more accurate relativistic many-body perturbation theory (RMBPT) calculation had to be invoked to match theoretical and experimental data. These calculations were performed by Safronova et al. [68] for the lines of the Ne-like, Na-like, Mg-like and Al-like charge states of yttrium lines.

In order to help with the identification of lines that were close in wavelength, we considered the evolution of charge states with electron beam energy by plotting the line intensities as a function of the beam energy. The ionization energies of the different charge states determine the minimum beam energy required for the emergence of a particular charge state. For instance, the ionization energy of Y XXXIV is 4.299 keV [64]; hence, a beam energy of 4.299 keV or higher is required to observe spectral lines from Be-like Y XXXV. This gives an idea of the range of charge states one is supposed to observe at a particular beam energy. In addition, lines emitted from the same ionization state usually depend in a similar way on the beam energy. These qualitative dependencies aided the line identification as illustrated in Figure 3. In order to verify these qualitative assumptions, we have used our detailed CR model calculations to make a final assignment based on the line intensity dependences.

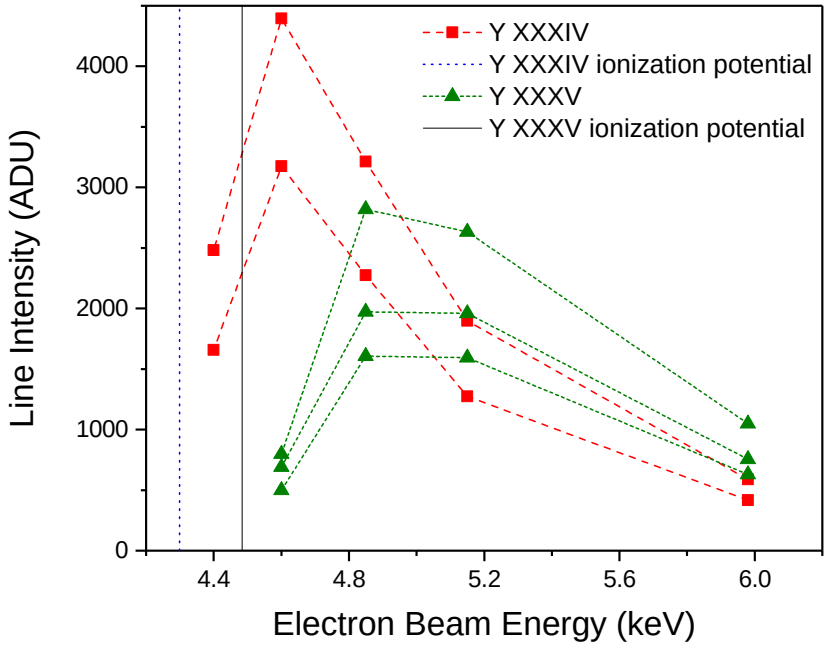

Figure 3. Line intensity plotted as a function of electron beam energy for three Y XXXV lines (green triangles) and two Y XXXIV lines (red squares). The solid (black) and dotted (blue) vertical lines depict the ionization potential of Y XXXV and Y XXXIV, respectively.

6. Results and Discussions

Table 1 presents the yttrium lines identified in our experiment for the charge state range between Y XXVII and Y XXXVII. We focused on lines that originate from $\Delta n = 0$ transitions within the $n = 2$ and $n = 3$ principal quantum number states. Most of the lines are electric dipole (E1) transitions, while a few lines are magnetic dipole (M1) transitions. All M1 lines correspond to transitions within the $2s^2 2p^m$ ground state configurations of different charge states ($m = 1, 2, 3, 4, 5$), with the exception of the line at 16.4817(7) nm, which originates from within the excited configuration $2p^5 3s$ of Ne-like yttrium ion. The energy levels within the ground configuration are close and result in longer wavelength forbidden lines, while the energy levels contributing to the allowed (E1) transitions are further separated and give rise to shorter wavelength lines. Level notations are taken from FAC and are given in *jj*-coupling. The plus sign stands for the j value of $l + 1/2$, and the minus sign represents the j value of $l - 1/2$, where l is the orbital angular momentum. As an example, the line at 5.9329(4) nm connects the $2s^2 2p^3$ upper level with a total angular momentum of $J = 5/2$ to the $2s2p^4$ of $J = 3/2$. It should be noted that in FAC, the subshells that couple to zero angular momentum are omitted in the notation. As an illustration of this, the $2p^5$ configuration is noted as $2p^3_+$ when both electrons on the $2p_-$ subshell are present and couple to zero joint angular momentum. Yttrium spectra recorded at different energies are shown in Figures 4 and 5, with the identified lines labeled by their isoelectronic sequence.

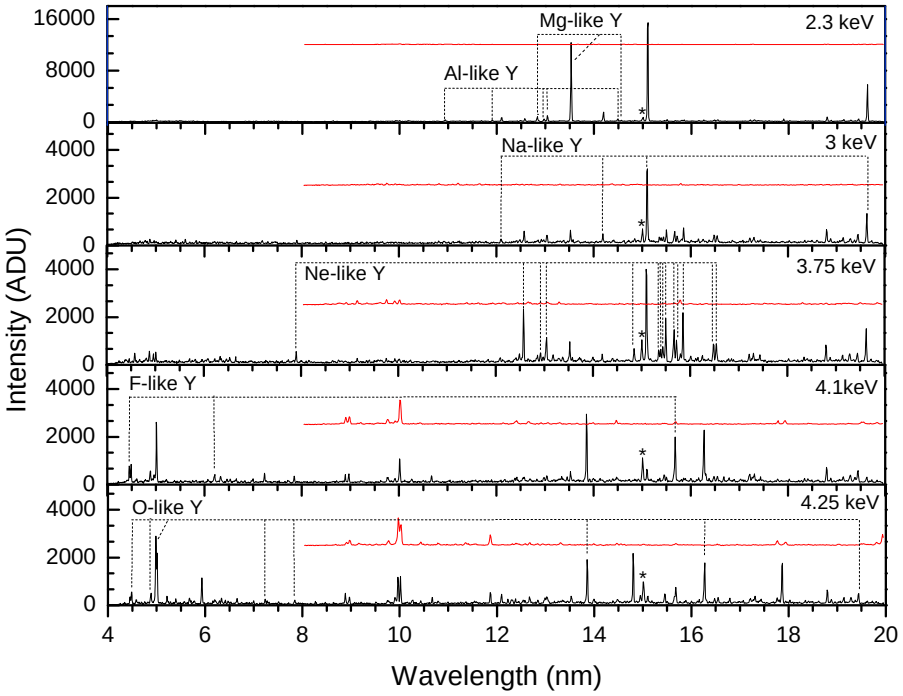

Figure 4. Yttrium spectra at beam energies from 2.30 keV–4.25 keV. The black and red (shifted) spectra correspond to the first and second order Y spectra, respectively. The ∗ marks the impurity coming from oxygen at 15.0099(5) nm.

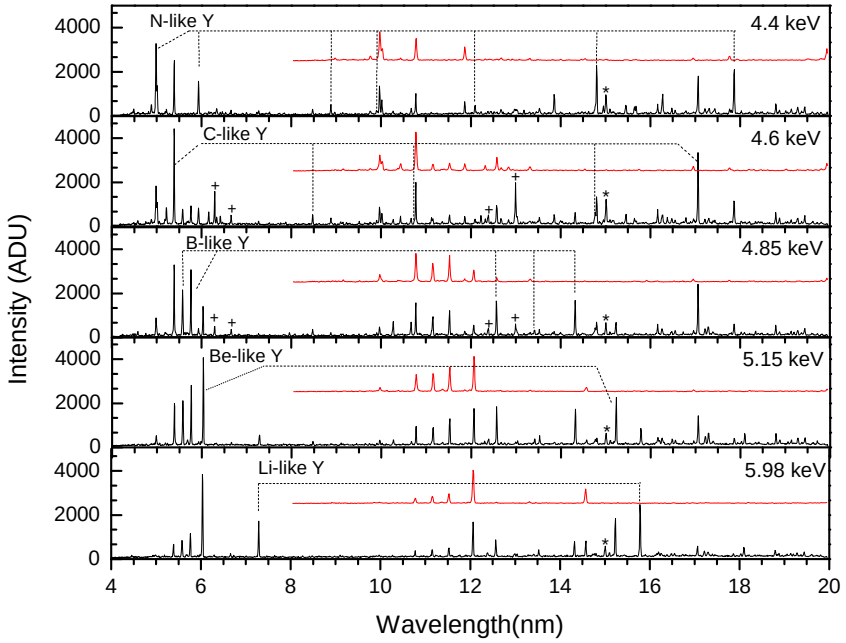

Figure 5. Yttrium spectra at beam energies from 4.40 keV–5.98 keV. The black and red (shifted) spectra correspond to the first and second order Y spectra, respectively. The + marks the Na-like and Mg-like xenon impurities at beam energies of 4.6 keV and 4.85 keV and the ∗ marks the impurity coming from oxygen at 15.0099(5) nm.

Table 1. The table below presents the list of the yttrium lines identified Y^{26+}–Y^{36+}. Previous measurements and calculations are reported as well. Isoelectronic sequence is abbreviated as Seq., configuration is abbreviated as Config., and the level number is abbreviated as No.

Ion Charge	Seq.	Type	Lower Level			Upper Level			Experimental Wavelength (nm)		Theoretical Wavelength (nm)	
			No.	Config.	Term$_J$	No.	Config.	Term$_J$	This Work	Previous Work	This Work	Previous Work
36	Li	E1	1	$2s$	$2s_+$	2	$2p$	$2p_+$	7.2874(6)		7.2771	7.2893 [69] 7.2887(1) [70] 7.2892 [71] 7.2890(1) [72] 7.2888 [73]
36	Li	E1	1	$2s$	$2s_+$	3	$2p$	$2p_-$	15.7862(9)		15.7139	15.7878 [69] 15.7868(5) [70] 15.7865 [71] 15.7874(4) [72] 15.7867 [73]
35	Be	E1	1	$2s^2$	$(2s_+^2)_0$	6	$2s2p$	$(2s_+, 2p_+)_1$	6.0322(5)		6.0098	6.0337(20) [f] [24] 6.0283 [74]
35	Be	E1	1	$2s^2$	$(2s_+^2)_0$	3	$2s2p$	$(2s_+, 2p_-)_1$	15.2336(7)		15.1907	15.2345(20) [f] [24] 15.2302 [74]
34	B	E1	1	$2p$	$2p_-$	7	$2s2p^2$	$((2s_+, 2p_-)_1, 2p_+)_{1/2}$	5.5768(6)		5.5310	5.5771 [f] [25]
34	B	E1	1	$2p$	$2p_-$	6	$2s2p^2$	$((2s_+, 2p_-)_1, 2p_+)_{3/2}$	5.7623(6)		5.7254	5.7629 [f] [25]
34	B	E1	1	$2p$	$2p_-$	3	$2s2p^2$	$2s_+$	12.5693(6)		12.5372	
34	B	E1	2	$2p$	$2p_+$	5	$2s2p^2$	$((2s_+, 2p_-)_1, 2p_+)_{5/2}$	13.4185(8)		13.3700	
34	B	M1	1	$2p$	$2p_-$	2	$2p$	$2p_+$	14.3234(5)		14.3363	14.321 [75] 14.322 [f] [25]
33	C	E1	1	$2p^2$	$(2p_-^2)_0$	7	$2s2p^3$	$(2s_+, 2p_+)_1$	5.3878(5)		5.3571	
33	C	E1	3	$2p^2$	$(2p_-, 2p_+)_2$	7	$2s2p^3$	$(2s_+, 2p_+)_1$	8.4792(19) [b]		8.4071	
33	C	E1	2	$2p^2$	$(2p_-, 2p_+)_1$	5	$2s2p^3$	$(2s_+, 2p_+)_2$	11.1236(9) [b]		11.1132	
33	C	M1	1	$2p^2$	$(2p_-^2)_0$	3	$2p^2$	$(2p_-, 2p_+)_2$	14.7700(10)		14.7668	
33	C	M1	1	$2p^2$	$(2p_-^2)_0$	2	$2p^2$	$(2p_-, 2p_+)_1$	17.0632(7)		17.1036	17.0625 [76] 17.0558 [76]

Table 1. *Cont.*

Ion Charge	Seq.	Type	Lower Level			Upper Level			Experimental Wavelength (nm)		Theoretical Wavelength (nm)	
			No.	Config.	Term$_J$	No.	Config.	Term$_J$	This Work	Previous Work	This Work	Previous Work
32	N	E1	1	$2p^3$	$2p_+$	8	$2s2p^4$	$(2s_+,(2p_+^2)_2)_{3/2}$	4.9858(6)		4.9593	
32	N	E1	1	$2p^3$	$2p_+$	6	$2s2p^4$	$(2s_+,(2p_+^2)_2)_{5/2}$	5.9329(4)		5.9151	
32	N	E1	2	$2p^3$	$(2p_-,(2p_+^2)_2)_{3/2}$	6	$2s2p^4$	$(2s_+,(2p_+^2)_2)_{5/2}$	8.8822(7)		8.8358	
32	N	E1	3	$2p^3$	$(2p_-,(2p_+^2)_2)_{5/2}$	6	$2s2p^4$	$(2s_+,(2p_+^2)_2)_{5/2}$	9.9054(10)		9.8612	
32	N	M1	1	$2p^3$	$2p_+$	4	$2p^3$	$(2p_-,(2p_+^2)_0)_{1/2}$	12.0926(6)		12.0717	
32	N	M1	1	$2p^3$	$2p_+$	3	$2p^3$	$(2p_-,(2p_+^2)_2)_{5/2}$	14.8036(5)		14.7819	
32	N	M1	1	$2p^3$	$2p_+$	2	$2p^3$	$(2p_-,(2p_+^2)_2)_{3/2}$	17.8665(6)		17.8947	
31	O	E1	1	$2p^4$	$(2p_+^2)_2$	7	$2s2p^5$	$(2s_+,(2p_+^3)_{3/2})_1$	4.4854(8)	4.4857(15) [77]	4.4567	
31	O	E1	2	$2p^4$	$(2p_+^2)_0$	7	$2s2p^5$	$(2s_+,(2p_+^3)_{3/2})_1$	4.8871(12)	4.8882(15) [77]	4.8569	
31	O	E1	1	$2p^4$	$(2p_+^2)_2$	6	$2s2p^5$	$(2s_+,(2p_+^3)_{3/2})_2$	5.0103(5)	5.0085(15) [77]	4.9828	
31	O	E1	3	$2p^4$	$(2p_-,(2p_+^3)_{3/2})_1$	6	$2s2p^5$	$(2s_+,(2p_+^3)_{3/2})_2$	7.2352(8)	7.2356(15) [77]	7.1754	
31	O	E1	4	$2p^4$	$(2p_-,(2p_+^3)_{3/2})_2$	6	$2s2p^5$	$(2s_+,(2p_+^3)_{3/2})_2$	7.8430(8)		7.7848	
31	O	M1	1	$2p^4$	$(2p_+^2)_2$	4	$2p^4$	$(2p_-,(2p_+^3)_{3/2})_2$	13.8581(6)		13.8442	13.89(2) [77]
31	O	M1	1	$2p^4$	$(2p_+^2)_2$	3	$2p^4$	$(2p_-,(2p_+^3)_{3/2})_1$	16.2725(9)		16.307	16.28(2) [77]
31	O	E1	16	$2p^33p$	$(2p_+,3p_+)_3$	32	$2p^33d$	$(2p_+,3d_+)_4$	19.4383(8)		19.4639	
30	F	E1	1	$2p^5$	$(2p_+^3)_{3/2}$	3	$2s$	$2s_+$	4.4500(7)	4.4496(15) [37]	4.417	4.4083 [26] 4.4486 [f] [26] 4.4492 [39]
30	F	E1	2	$2p^5$	$2p_-$	3	$2s$	$2s_+$	6.2115(14) [b]	6.2107(15) [37]	6.1454	6.1299 [26] 6.2109 [f] [26]
30	F	M1	1	$2p^5$	$(2p_+^3)_{3/2}$	2	$2p^5$	$2p_-$	15.6801(11)		15.7043	15.681(12) [f] [37] 15.654(5) [f] [78] 15.678 [f] [26] 15.678(12) [79] 15.71 [38] 15.6826 [39]

Table 1. *Cont.*

Ion Charge	Seq.	Type	Lower Level			Upper Level			Experimental Wavelength (nm)		Theoretical Wavelength (nm)	
			No.	Config.	Term$_J$	No.	Config.	Term$_J$	This Work	Previous Work	This Work	Previous Work
												15.685 [f] [80]
29	Ne	E1	3	$2p^5 3s$	$((2p_+^3)_{3/2}, 3s_+)_1$	20	$2p^5 3p$	$(2p_-, 3p_-)_0$	7.8983(8)		7.9003 [a]	7.914 [f] [81]
29	Ne	E1	3	$2p^5 3s$	$((2p_+^3)_{3/2}, 3s_+)_1$	11	$2p^5 3p$	$((2p_+^3)_{3/2}, 3p_+)_0$	12.5743(7)		12.5696 [a]	12.576 [f] [81]
29	Ne	E1	12	$2p^5 3p$	$(2p_-, 3p_-)_1$	24	$2p^5 3d$	$(2p_-, 3d_-)_2$	12.9238(8)		12.9267 [a]	
29	Ne	E1	5	$2p^5 3p$	$((2p_+^3)_{3/2}, 3p_-)_2$	15	$2p^5 3d$	$((2p_+^3)_{3/2}, 3d_-)_3$	13.0471(8)		13.0550 [a]	
29	Ne	E1	2	$2p^5 3s$	$((2p_+^3)_{3/2}, 3s_+)_2$	10	$2p^5 3p$	$((2p_+^3)_{3/2}, 3p_+)_2$	14.8480(7)		14.8389 [a]	
29	Ne	E1	10	$2p^5 3p$	$((2p_+^3)_{3/2}, 3p_+)_2$	22	$2p^5 3d$	$((2p_+^3)_{3/2}, 3d_+)_3$	15.3559(10)		15.3587 [a]	
29	Ne	E1	19	$2p^5 3p$	$(2p_-, 3p_+)_2$	26	$2p^5 3d$	$(2p_-, 3d_+)_3$	15.3945(10)		15.3972 [a]	
29	Ne	E1	18	$2p^5 3p$	$(2p_-, 3p_+)_1$	25	$2p^5 3d$	$(2p_-, 3d_+)_2$	15.4387(10)		15.4444 [a]	
29	Ne	E1	3	$2p^5 3s$	$((2p_+^3)_{3/2}, 3s_+)_1$	10	$2p^5 3p$	$((2p_+^3)_{3/2}, 3p+)_2$	15.4902(18) [b]	15.497(15) [82] 15.50 [83]	15.4882 [a]	15.503 [f] [81] 15.50 [84]
29	Ne	E1	9	$2p^5 3s$	$(2p_-, 3s_+)_1$	20	$2p^5 3p$	$(2p_-, 3p_-)_0$	15.5024(8) [b]		15.4904 [a]	15.498 [f] [81]
29	Ne	E1	6	$2p^5 3p$	$((2p_+^3)_{3/2}, 3p_+)_3$	17	$2p^5 3d$	$((2p_+^3)_{3/2}, 3d_+)_4$	15.6711(10)		15.6769 [a]	
29	Ne	E1	9	$2p^5 3s$	$(2p_-, 3s_+)_1$	19	$2p^5 3p$	$(2p_-, 3p_+)_2$	15.7208(7)	15.714(15) [82] 15.71 [83]	15.7085 [a]	15.723 [f] [81] 15.71 [84]
29	Ne	E1	2	$2p^5 3s$	$((2p_+^3)_{3/2}, 3s_+)_2$	6	$2p^5 3p$	$((2p_+^3)_{3/2}, 3p_+)_3$	15.8537(7)		15.8455 [a]	
29	Ne	M1	3	$2p^5 3s$	$((2p_+^3)_{3/2}, 3s_+)_1$	8	$2p^5 3s$	$(2p_-, 3s_+)_0$	16.4817(7)		16.4843 [a]	
29	Ne	E1	3	$2p^5 3s$	$((2p_+^3)_{3/2}, 3s_+)_1$	7	$2p^5 3p$	$((2p_+^3)_{3/2}, 3p_+)_1$	16.5411(8)	16.537(15) [82]	16.5488 [a]	16.542 [f] [81] 16.463 [85] 16.484 [85]
28	Na	E1	2	$3p$	$3p_-$	4	$3d$	$3d_-$	12.0979(8)	12.098(20) [16]	12.1353	12.09248 [86] 12.0993(7) [f] [45]
28	Na	E1	3	$3p$	$3p_+$	5	$3d$	$3d_+$	14.1938(7)	14.1938(6) [16]	14.2458	14.1873 [86] 14.1959(7) [f] [45]

Table 1. *Cont.*

Ion Charge	Seq.	Type	Lower Level			Upper Level			Experimental Wavelength (nm)		Theoretical Wavelength (nm)	
			No.	Config.	Term$_J$	No.	Config.	Term$_J$	This Work	Previous Work	This Work	Previous Work
28	Na	E1	1	$3s^2$	$3s_+$	3	$3p$	$3p_+$	15.1037(5)	15.1035(10) [16]	15.0542	15.1038 [55] 15.10402(40) [7] 15.1033 [f] [29] 15.1038(7) [f] [45] 15.0658 [86]
28	Na	E1	1	$3s^2$	$3s_+$	2	$3p$	$3p_-$	19.6212(7)	19.6215(10) [16]	19.5175	19.6199 [55] 19.6209(7) [7] 19.6219 [f] [29] 19.6213(7) [45]
27	Mg	E1	5	3s3p	$(3s_+, 3p_+)_1$	14	3s3d	$(3s_+, 3d_+)_2$	12.8333(9)	12.8352(10) [21] 12.8349(5) [15] 12.8301(15) [44]	12.7875	
27	Mg	E1	1	$3s^2$	$(3s_+^2)_0$	5	3s3p	$(3s_+, 3p_+)_1$	13.5276(5)	13.5279(10) [21] 13.5283(5) [15] 13.5216(15) [44]	13.4437	13.5276 [87] 13.5213 [88]
27	Mg	E1	3	3s3p	$(3s_+, 3p_-)_1$	7	$3p^2$	$(3p_-, 3p_+)_2$	14.5650(20) [b]	14.5603(10) [21]	14.528	
26	Al	E1	1	$3p$	$3p_-$	10	3s3p^2	$(3s_+, (3p_+^2)_0)_{3/2}$	10.9388(15) [w,b]	10.9391(20) [30] 10.9413(10) [43]	10.8578	
26	Al	E1	2	$3p$	$3p_+$	11	3s3d	$3d_-$	11.9072(12) [w,b]	11.9131(20) [30] 11.9110(10) [43]	11.8248	
26	Al	E1	2	$3p$	$3p_+$	10	3s3p^2	$(3s_+, (3p_+^2)_2)_3$	12.9717(11) [w]	12.9729(20) [30] 12.9745(10) [43]	12.852	
26	Al	E1	1	$3p$	$3p_-$	8	3s3p^2	$((3s_+, 3p_-)_1), 3p_+)_{1/2}$	13.0401(8)	13.0416(20) [30] 13.0417(10) [43]	12.9265	
26	Al	E1	1	$3p$	$3p_-$	6	3s3p^2	$((3s_+, 3p_-)_1), 3p_+)_{3/2}$	14.4883(8) [w]	14.4914(20) [30] 14.4910(10) [43]	14.4675	

[a] Wavelength from Safronova et al.'s calculation [68]; [b] blended with other line feature; [w] weak lines; and [f] fitted values.

A total of 59 spectral lines were identified in this work from the Li-like to the Al-like isoelectronic sequences. Of these lines, 38 are new and 21 correspond to previously measured transitions in O-like, F-like, Na-like, Mg-like and Al-like charge states [15,16,21,24–26,29,30,37,43–45,77]. The previously measured transitions are also listed in Table 1 together with their currently measured wavelengths. We observed an O VI line at 15.0099(5) nm in all of the spectra due to impurities in the trap. At 4.60 keV and 4.85 keV drift tube voltages, we also observed impurity lines due to xenon, including a Xe XLII line at 15.0116(7) nm blended with the above-mentioned O VI line. Mg-like Xe XLIII lines were observed at 6.2903(6) nm and 12.9969(9) nm wavelengths, and two Na-like Xe XLIV lines were found at 6.6628(7) nm and 12.3939(7) nm. These lines are listed in the NIST Atomic Spectra Database [7,64] at 6.288(3) nm, 12.993(3) nm, 6.6628(5) nm and 12.394(1) nm, respectively.

Two Li-like yttrium lines were identified at 7.2874(6) nm/170.134(15) eV and 15.7862(9) nm/78.5395(44) eV, corresponding to the $(2s_+)$–$(2p_+)$ and $(2s_+)$–$(2p_-)$ electric dipole transitions, respectively. The Li-like isoelectronic sequence has been extensively studied both theoretically and experimentally due to its simple electronic structure. Highly accurate ab initio calculations agree with precise experimental results at the high-Z end of the isoelectronic sequence [1,89]. Although recent results are sensitive to higher order QED terms, further developments are expected, especially in the moderately high-Z region where experiments can provide accurate data due to the wavelength range available to grazing incidence EUV spectrometers. Our current relative uncertainty of 57×10^{-6} for the wavelength of the $(2s_+)$–$(2p_-)$ transition shows good agreement with previous high precision calculations [70–72]; however, the $(2s_+)$–$(2p_+)$ theoretical results [70,72] are slightly outside our relative uncertainty of 82×10^{-6} as shown in Figure 6. Upon close examination, a small feature of unidentified origin was found in the low wavelength wings of both Li-like lines. They were taken into account with the inclusion of a second small Gaussian peak in the fits. The reported results and uncertainties reflect the inclusion of these features, and we therefore believe that they are not responsible for the slight disagreement between the theoretical values and our results for the $(2s_+)$–$(2p_+)$ line.

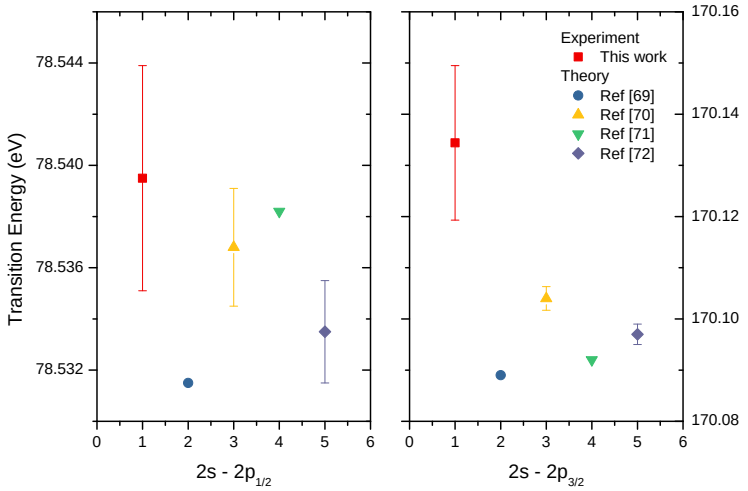

Figure 6. Comparison of measured and calculated Li-like yttrium lines.

The two electric dipole Be-like yttrium lines in the measured spectra at 6.0322(5) nm and 15.2336(7) nm correspond to the transitions of $(2s_+^2)_0$–$(2s_+, 2p_+)_1$ and $(2s_+^2)_0$–$(2s_+, 2p_-)_1$, respectively. Be-like ions are quasi two-electron systems. Therefore, calculations at the level of the precision of the measurement are difficult. Denne et al. [24] predicted these wavelengths in yttrium by fitting the difference between the theoretical and experimental wave numbers and then extrapolating to attain the fine-structure separation. Their predictions of 6.0337(20) nm and 15.2345(20) nm had uncertainties

much larger than our measurements. Thus, we provide a considerable increase in the accuracy of the wavelengths.

A similar approach was used by Mrynas et al. [25] for the predictions of the wavelengths of B-like yttrium $(2p_-)$–$((2s_+, 2p_-)_1, 2p_+)_{1/2}$, $(2p_-)$–$((2s_+, 2p_-)_1, 2p_+)_{3/2}$ and $(2p_-)$–$(2p_+)$ lines. The obtained respective values were 5.5771 nm, 5.7629 nm and 14.322 nm, but no uncertainties were provided for the fitted wavelength predictions. These results are in a generally good agreement with our observed values of 5.5768(6) nm, 5.7623(6) nm and 14.3234(5) nm. Beyond these three transitions, two additional lines have been identified for B-like yttrium, as shown in Table 1. Out of the five reported transitions, four are E1, and one is an M1 transition.

With an increasing number of electrons, the electronic structure of open shell ions becomes more difficult for theory. However, the experimental wavelength determinations are as accurate as for their simpler structure counterparts. Accurate wavelength results in these ions can provide guidance for further theoretical work for the better understanding of the electron-electron interactions in these systems. Here, we report E1 and M1 transitions for both C-like and N-like yttrium ions.

Behring et al. [77] observed O-like yttrium transitions by irradiating a solid yttrium target with 24 frequency-tripled laser beams. We identified six E1 transitions and two M1 transitions in the same system and provide wavelength values for these in Table 1. The observations of Behring et al. are consistent with our measurements with the exception of the M1 transition $(2p_+^2)_2$–$(2p_-, (2p_+^3)_{3/2})_2$. Our measurement of 13.8581(6) nm for this M1 line is at a shorter wavelength than their predicted wavelength of 13.89(2) nm. The M1 transition at 16.2725(9) nm agrees with their predicted wavelength of 16.28(2) nm [77].

Wavelengths of F-like yttrium lines were measured by Reader et al. [37] using laser produced plasmas. The $(2p_+^3)_{3/2}$–$(2s_+)$ and $(2p_-)$–$(2s_+)$ transitions in these ions were measured to be 4.4496(15) nm and 6.2107(15) nm, respectively. Our results for the same transitions indicated 4.4500(7) nm and 6.2115(14) nm wavelengths and are in good agreement with the previously observed values. Calculations by Feldman et al. [26] reported values of 4.4083 nm and 6.1299 nm that are further away from these measurements than our FAC calculated wavelengths values of 4.417 nm and 6.1454 nm.

The M1 transition $(2p_+^3)_{3/2}$–$(2p_-)$ in F-like Y is interesting due to its potential for plasma diagnostics [37,38]. Reader et al. [37] predicted the wavelength by comparing the observed fine-structure intervals with Dirac–Fock calculations and obtained 15.681(12) nm. This is in agreement with our measured value of 15.6801(11) nm.

The ground state of Ne-like ions is a closed shell. However, the low lying excited states have interesting features that have been exploited in many experiments and observations [90]. The level structure has been investigated for use in the diagnosis of astrophysical and laboratory plasmas [91,92] and has been used in soft X-ray laser schemes [93]. We report fourteen E1 and one M1 transitions in Ne-like Y. The Ne-like yttrium lines were identified using the theoretical values from highly accurate RMBPT calculations [68].

In our spectra, we were able to identify four E1 transitions of Na-like yttrium ions. The two most prominent ones are the well-known Na-like D_1 $(3s_+)$–$(3p_+)$ and D_2 $(3s_+)$–$(3p_-)$ lines. Our measured wavelength values of 15.1037(5) nm and 19.6212(7) nm, respectively, lie within the uncertainty of the 15.1035(10) nm and 19.6215(10) nm measurements by Reader et al. in tokamak plasmas and laser-produced plasmas [16]. Seely et al. [29] reported calculated values of 15.0961 nm and 15.0310 nm for the D_1 line and 19.6047 nm and 19.4851 nm for the D_2 line with and without QED corrections, respectively. This illustrates the importance of QED corrections at this level of experimental accuracy. Their fitted values of 15.1033 nm and 19.6219 nm for these transitions are within our experimental uncertainty. Our measured wavelengths also agree well with Blundell's calculated values of 15.10402(40) nm and 19.6209(7) nm for the D_1 and D_2 lines [7]. Gillaspy et al. [7] have pointed out that the accuracy of the measurements in medium-Z to high-Z systems is sensitive to the finite

nuclear size correction in the otherwise calculable QED terms. This illustrates the importance of these transitions in studies at the interface of atomic and nuclear physics.

Our goal in these studies was the identification of lines in the L-shell ion states of yttrium in the EUV region. The few M-shell charge states we report here appeared at the low energy end of our systematic scans. The highest isoelectronic sequences investigated here were those for Mg and Al. In Mg-like yttrium, we report the observation of three E1 lines that have been previously measured by Ekberg et al. [21], Sugar et al. [15] and Reader et al. [44]. Similarly, the five Al-like yttrium E1 lines that we identified were previously measured by Ekberg et al. [43] and Sugar et al. [30]. The slight disagreement with some of the previous measurements might be due to weak lines and blends with other line features.

7. Diagnostically Important M1 Transitions

Among the 59 identified yttrium lines listed in Table 1, 10 lines are due to forbidden M1 transitions. States that decay via M1 transitions have a different dependence on collisional depopulation from states with E1 transitions. Thus, the corresponding intensity ratios of M1 to E1 lines are sensitive to the electron densities and temperatures, thereby making them potential candidates for plasma diagnostics. To analyze the feasibility of this, calculations with the CR modeling code NOMAD were performed for Maxwellian electron energy distribution plasmas with electron densities ranging from 10^{12} cm^{-3}–10^{20} cm^{-3} and temperatures from 1500 eV–6000 eV, which provide the largest abundance of the ions.

The most sensitive intensity ratios for the spectral lines of Y^{30+}–Y^{33+} ions are presented in Figure 7. The figure provides examples for sensitivity to the electron density (n_e) in the range of 10^{12} cm^{-3}–10^{19} cm^{-3}. At low densities, radiative rates for both forbidden and allowed transitions are much stronger than the collisional rates, and therefore, no dependence on electron density arises. However, at higher densities, collisional quenching dominates radiative decay for forbidden lines, and the line intensity ratios become sensitive to n_e.

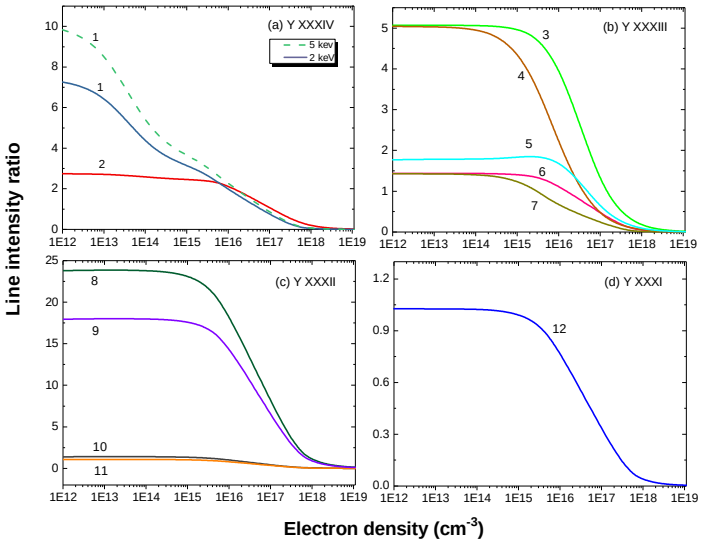

Figure 7. Density-sensitive line ratios for (**a**) C-like Y XXXIV, (**b**) N-like Y XXXIII, (**c**) O-like Y XXXII and (**d**) F-like Y XXXI. The number labels correspond to the line ratios: (1) 17.0632(7) nm/11.1236(9) nm at 5-keV electron energy (dash) and 2-keV electron energy (solid), (2) 17.0632(7) nm/8.4792(19) nm, (3) 17.8665(6) nm/9.9054(10) nm, (4) 14.8036(5) nm/9.9054(10) nm, (5) 12.0926(6) nm/9.9054(10) nm, (6) 17.8665(6) nm/8.8822(7) nm, (7) 14.8036(5) nm/8.8822(7) nm, (8) 13.8581(6) nm/19.4383(8) nm, (9) 16.2725(9) nm/19.4383(8) nm, (10) 16.2725(9) nm/7.2352(8) nm, (11) 13.8581(6) nm/7.2352(8) nm and (12) 15.6801(11) nm/6.21115(14) nm.

The five C-like yttrium lines listed in Table 1 include an M1 transition at a 17.0632(7) nm wavelength. The ratio of this M1 line to the E1 line at 8.4792(19) nm varies by a factor of 45 or less in the electron density range of 10^{15} cm^{-3}–10^{18} cm^{-3}. The line intensity ratio I(17.0632(7))/I(11.1236(9)) varies by more than two orders of magnitude for the same range of electron density. This line ratio also shows dependence on the electron temperature at lower densities as illustrated in Figure 7a. The line ratio of the M1 line at 17.0632(7) nm to another line at the FAC wavelength of 12.3869 nm shows a similar dependence on electron density and temperature because both of the E1 transitions at 11.1236(9) nm and 12.3869 nm arise from the same upper level decaying to the second and third energy levels, respectively. The line at 12.3869 nm, which is about half of the intensity of line at 11.1236(9) nm, could not be resolved due to strong blend with a Na-like Xe line at 12.3939(7) nm. However, at other plasma conditions with no Xe, this line should be easily resolved.

Among the seven identified N-like yttrium lines, four of the lines arise from E1 transitions, and three arise from M1 transitions. The ratios of the M1/E1 intensity show a dependence on n_e between 10^{15} cm^{-3} and 10^{18} cm^{-3} of a maximum of two orders of magnitude. According to our FAC calculations, the transition probability of the M1 line at 14.8036(5) nm is 6.75×10^5 s^{-1} compared to the transition probability of 3.9×10^6 s^{-1} for the M1 line at 12.0926(6) nm and 3.7×10^6 s^{-1} for the M1 line at 17.8665(6) nm. This explains why the ratios I(14.8036(5))/I(9.9054(10)) and I(14.8036(5))/I(8.8822(7)) start decreasing at densities of 10^{15} cm^{-3}, whereas the intensity ratios of the M1 line at 12.0926(6) nm to the E1 lines and the M1 line at 17.8665(6) nm to the E1 lines only start to fall off at densities of 10^{16} cm^{-3} and higher. These transitions are illustrated in the Grotrian diagram shown in Figure 8.

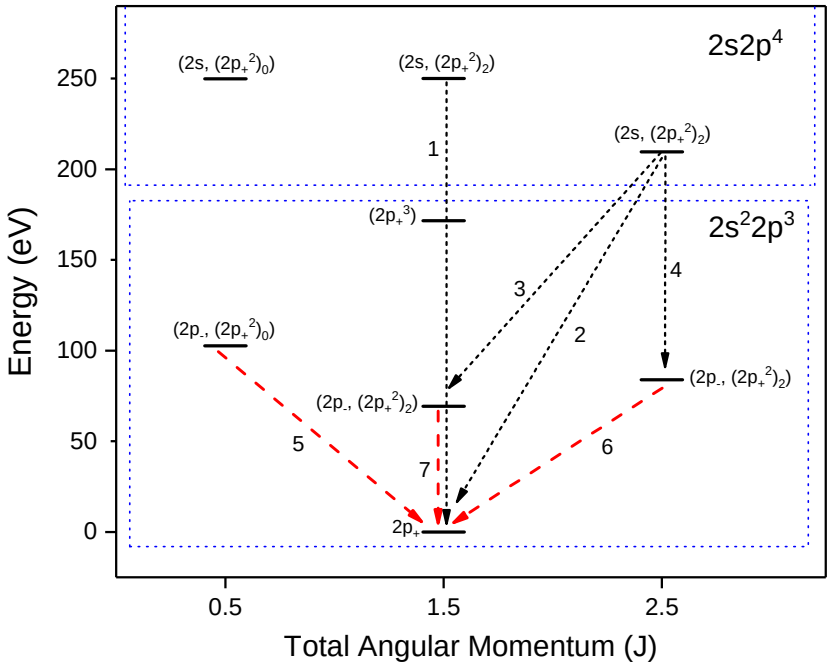

Figure 8. Partial Grotrian diagram of the ground state and first lowest excited configurations of N-like yttrium. The number labels in increasing order from 1–7 correspond to the lines at 4.9858(6) nm, 5.9329(4) nm, 8.8822(7) nm, 9.9054(10) nm, 12.0926(6) nm, 14.8036(5) nm and 17.8665(6) nm, respectively. Only three of the energy levels for the $2s2p^4$ configuration are shown. The dashed red lines correspond to magnetic dipole (M1) transitions, and the dotted black lines correspond to electric dipole (E1) transitions.

A closer look at the the density dependence of M1/E1 ratios in N-like ions gives an insight into the population scheme of allowed and metastable upper levels. For instance, let us take the population

and depopulation channels of the metastable level in the ground state configuration $2p^3$ that is the upper level of the 17.8665(6) nm M1 transition and a $2s2p^4$ excited state level that is the origin of three E1 transitions (5.9329(4) nm, 8.8822(7) nm and 9.9054(10) nm wavelengths). At a temperature of 1500 eV, the metastable level $2p^3$ at a lower density of 10^{12} cm^{-3} is depopulated by radiative decay with 99.96% probability. At a higher density of 10^{16} cm^{-3}, the depopulation is 73% by collisional excitation to higher levels, 3% by collisional deexcitation to a lower ground state level, and only a 21% probability remains for radiative decay. At an even more elevated electron density of 10^{18} cm^{-3}, the level is depopulated mostly by collisional excitation with nearly 94% probability, leaving 4% to collisional deexcitation, 1% to radiative recombination and a negligible probability (0.27%) to radiation. The $2s2p^4$ excited level is depopulated 100% by radiative decay at 10^{12} cm^{-3} and 10^{16} cm^{-3}, and the probability only slightly lowers to 99.6% at 10^{18} cm^{-3}. This means that the ratio of the intensity of the $2s2p^4$ E1 transitions to that of the $2p^3$ M1 transition shows a strong variation with the electron density.

Out of the eight O-like yttrium lines, we observed two that originate from M1 transitions at 13.8581(6) nm and 16.2725(9) nm. The intensity ratios between the M1 and E1 transitions vary by more than an order of magnitude in the density ranges we investigated. For instance, the intensity ratio I(13.8581(6))/I(19.4383(8)) changes by a factor of 67 for densities ranging from 10^{15} cm^{-3}–10^{18} cm^{-3}.

For the one M1 and two E1 lines in F-like Y, an order of magnitude variation is seen for the intensity ratio of M1 line at 15.6801(11) nm to the E1 line at 6.2115(14) nm.

8. Conclusions

New and previously-measured EUV lines in L-shell ions along with transitions in a few M-shell ions of highly charged yttrium were observed. The measurements were performed with an electron beam ion trap, and spectral lines were recorded in the wavelength region of 4 nm–20 nm. The experimental uncertainties were combinations of statistical and systematic uncertainties that included sources with calibration origins and uncertainties from unresolved blends. The total uncertainties ranged between 0.0004 nm and 0.0020 nm. Line identifications were inferred from comparisons with spectra simulated from the collisional-radiative model NOMAD based on a non-Maxwellian distribution designed for EBIT-like environments. For Ne-like Y ions, a better agreement between theory and experiment was found using relativistic many-body perturbation theory (RMBPT) [68]. Several of the identified forbidden M1 transitions were found to be potentially useful for density diagnostics of laboratory, fusion and astrophysical plasmas.

Acknowledgments: This work was funded by the Measurement Science and Engineering (MSE) Research Grant Programs of the Department of Commerce at the National Institute of Standards and Technology (NIST). We would like to thank the Department of Physics and Astronomy at Clemson University for their support. We are grateful to M. Safronova for providing the theory for Ne-like Y ions. J.M.D. acknowledges support from a National Research Council Associateship award at NIST.

Author Contributions: E.T. and J.D.G. contributed to the design and construction of the apparatus. R.S., E.T., Y.R. and J.M.D. conceived of and designed the experiments. R.S., J.M.D., E.T. and J.D.G. performed the experiments. Y.R. performed the calculations. R.S. analyzed the data. All authors contributed to writing the paper.

Conflicts of Interest: The authors declare no conflict of interest.

References

1. Sapirstein, J.; Cheng, K.T. Tests of Quantum Electrodynamics with EBIT. *Can. J. Phys.* **2008**, *86*, 25–31.
2. Fahy, K.; Sokell, E.; O'Sullivan, G.; Aguilar, A.; Pomeroy, J.M.; Tan, J.N.; Gillaspy, J.D. Extreme-Ultraviolet Spectroscopy of Highly Charged Xenon Ions Created Using an Electron-Beam Ion Trap. *Phys. Rev. A* **2007**, *75*, 032520.
3. Podpaly, Y.A.; Gillaspy, J.D.; Reader, J.; Ralchenko, Y. EUV Measurements of Kr XXI–Kr XXXIV and the Effect of a Magnetic-Dipole Line on Allowed Transitions. *J. Phys. B At. Mol. Opt. Phys.* **2014**, *47*, 095702.
4. Podpaly, Y.A.; Gillaspy, J.D.; Reader, J.; Ralchenko, Y. Measurements and Identifications of Extreme Ultraviolet Spectra of Highly-Charged Sm and Er. *J. Phys. B At. Mol. Opt. Phys.* **2015**, *48*, 025002.

5. Reader, J.; Gillaspy, J.D.; Osin, D.; Ralchenko, Y. Extreme Ultraviolet Spectra and Analysis of $\Delta n = 0$ Transitions in Highly Charged Barium. *J. Phys. B At. Mol. Opt. Phys.* **2014**, *47*, 145003.
6. Gillaspy, J.D.; Draganić, I.N.; Ralchenko, Y.; Reader, J.; Tan, J.N.; Pomeroy, J.M.; Brewer, S.M. Measurement of the D-Line Doublet in High-Z Highly Charged Sodiumlike Ions. *Phys. Rev. A* **2009**, *80*, 010501.
7. Gillaspy, J.D.; Osin, D.; Ralchenko, Y.; Reader, J.; Blundell, S.A. Transition Energies of the *D* lines in Na-like ions. *Phys. Rev. A* **2013**, *87*, 062503.
8. Kilbane, D.; O'Sullivan, G.; Podpaly, Y.A.; Gillaspy, J.D.; Reader, J.; Ralchenko, Y. EUV Spectra of Rb-like to Ni-like Dysprosium Ions in an Electron Beam Ion Trap. *Eur. Phys. J. D* **2014**, *68*, 222.
9. Kilbane, D.; O'Sullivan, G.; Gillaspy, J.D.; Ralchenko, Y.; Reader, J. EUV Spectra of Rb-like to Cu-like Gadolinium Ions in an Electron-Beam Ion Trap. *Phys. Rev. A* **2012**, *86*, 042503.
10. Kilbane, D.; Gillaspy, J.D.; Ralchenko, Y.; Reader, J.; O'Sullivan, G. Extreme Ultraviolet Spectra from *N*-Shell Ions of Gd, Dy and W. *Phys. Scr.* **2013**, *T156*, 014012.
11. Osin, D.; Reader, J.; Gillaspy, J.D.; Ralchenko, Y. Extreme Ultraviolet Spectra of Highly Charged Xenon Observed with an Electron Beam Ion Trap. *J. Phys. B At. Mol. Opt. Phys.* **2012**, *45*, 245001.
12. Osin, D.; Gillaspy, J.D.; Reader, J.; Ralchenko, Y. EUV Magnetic-Dipole Lines from Highly-Charged High-Z Ions with an Open 3D Shell. *Eur. Phys. J. D* **2012**, *66*, 286.
13. Ralchenko, Y.; Reader, J.; Pomeroy, J.M.; Tan, J.N.; Gillaspy, J.D. Spectra of W^{39+}–W^{47+} in the 12–20 nm Region Observed with an EBIT Light Source. *J. Phys. B At. Mol. Opt. Phys.* **2007**, *40*, 3861–3875.
14. Ralchenko, Y.; Draganic, I.N.; Tan, J.N.; Gillaspy, J.D.; Pomeroy, J.M.; Reader, J.; Feldman, U.; Holland, G.E. EUV Spectra of Highly-Charged Ions W^{54+}–W^{63+} Relevant to ITER Diagnostics. *J. Phys. B At. Mol. Opt. Phys.* **2008**, *41*, 021003.
15. Sugar, J.; Kaufman, V.; Indelicato, P.; Rowan, W.L. Analysis of Magnesiumlike Spectra from Cu XVIII to Mo XXXI. *J. Opt. Soc. Am. B* **1989**, *6*, 1437–1443.
16. Reader, J.; Kaufman, V.; Sugar, J.; Ekberg, J.O.; Feldman, U.; Brown, C.M.; Seely, J.F.; Rowan, W.L. $3s$–$3p$, $3p$–$3d$, and $3d$–$4f$ Transitions of Sodiumlike Ions. *J. Opt. Soc. Am. B* **1987**, *4*, 1821–1828.
17. Jupén, C.; Denne, B.; Martinson, I. Transitions in Al-like, Mg-like and Na-like Kr and Mo, Observed in the JET Tokamak. *Phys. Scr.* **1990**, *41*, 669–674.
18. Hinnov, E. Highly Ionized Atoms in Tokamak Discharges. *Phys. Rev. A* **1976**, *14*, 1533–1541.
19. Hinnov, E.; Boody, F.; Cohen, S.; Feldman, U.; Hosea, J.; Sato, K.; Schwob, J.L.; Suckewer, S.; Wouters, A. Spectrum Lines of Highly Ionized, Zinc, Germanium, Zirconium, Molybdenum, and Silver Injected into Princeton Large Torus and Tokamak Fusion Test Reactor Tokamak Discharges. *J. Opt. Soc. Am. B* **1986**, *3*, 1288–1294.
20. Suckewer, S.; Hinnov, E.; Cohen, S.; Finkenthal, M.; Sato, K. Identification of Magnetic Dipole Lines above 2000 Å in Several Highly Ionized Mo and Zr Ions on the PLT Tokamak. *Phys. Rev. A* **1982**, *26*, 1161–1163.
21. Ekberg, J.O.; Feldman, U.; Seely, J.F.; Brown, C.M. Transitions and Energy Levels in Mg-like Ge XXI–Zr XXIX Observed in Laser-Produced Linear Plasmas. *Phys. Scr.* **1989**, *40*, 643–651.
22. Nilsen, J.; Beiersdorfer, P.; Widmann, K.; Decaux, V.; Elliott, S.R. Energies of Neon-like $n = 4$ to $n = 2$ Resonance Lines. *Phys. Scr.* **1996**, *54*, 183–187.
23. Fischer, C.F. Multiconfiguration Hartree-Fock Breit-Pauli Results for $2p_{1/2}$–$2p_{3/2}$ Transitions in the Boron Sequence. *J. Phys. B At. Mol. Phys.* **1983**, *16*, 157–165.
24. Denne, B.; Magyar, G.; Jacquinot, J. Berylliumlike Mo XXXIX and Lithiumlike Mo XL Observed in the Joint European Torus Tokamak. *Phys. Rev. A* **1989**, *40*, 3702–3705.
25. Myrnäs, R.; Jupén, C.; Miecznik, G.; Martinson, I.; Denne-Hinnov, B. Transitions in Boronlike Ni XXIV, Ge XXVIII, Kr XXXII and Mo XXXVIII and Fluorinelike Zr XXXII and Mo XXXIV, Observed in the JET Tokamak. *Phys. Scr.* **1994**, *49*, 429–435.
26. Feldman, U.; Ekberg, J.O.; Seely, J.F.; Brown, C.M.; Kania, D.R.; MacGowan, B.J.; Keane, C.J.; Behring, W.E. Transitions of the Type $2s$–$2p$ in Highly Charged Flourinelike and Oxygenlike Mo, Cd, In, and Sn. *J. Opt. Soc. Am. B* **1991**, *8*, 531–537.
27. Curtis, L.J.; Ramanujam, P.S. Isoelectronic Wavelength Predictions for Magnetic-Dipole, Electric-Quadrupole, and Intercombination Transitions in the Mg Sequence. *J. Opt. Soc. Am.* **1983**, *73*, 979–984.
28. Ekberg, J.O.; Feldman, U.; Seely, J.F.; Brown, C.M.; MacGowan, B.J.; Kania, D.R.; Keane, C.J. Analysis of Magnesiumlike Spectra from Mo XXXI to Cs XLIV. *Phys. Scr.* **1991**, *43*, 19–32.

29. Seely, J.F.; Wagner, R.A. QED Contributions to the $3s$–$3p$ Transitions in Highly Charged Na-like Ions. *Phys. Rev. A* **1990**, *41*, 5246–5249.
30. Sugar, J.; Kaufman, V.; Rowan, W.L. Aluminiumlike Spectra of Copper Through Molybdenum. *J. Opt. Soc. Am. B* **1988**, *5*, 2183–2189.
31. Zhao, G.; Magain, P. Abundances of Neutron Capture Elements in Metal-Poor Dwarfs I. Yttrium and Zirconium. *Astron. Astrophys.* **1991**, *244*, 425–432.
32. Redfors, A.; Cowley, C.R. Elemental Abundances of Yttrium and Zirconium in the Mercury-Manganese Stars ϕ Herculis, κ Cancri and ι Coronae Borealis. *Astron. Astrophys.* **1993**, *271*, 273–275.
33. Kessler, T.; Moore, I.D.; Kudryavtsev, Y.; Peräjärvi, K.; Popov, A.; Ronkanen, P.; Sonoda, T.; Tordoff, B.; Wendt, K.D.A.; Äystö, J. Off-line Studies of the Laser Ionization of Yttrium at the IGISOL Facility. *Nucl. Instrum. Methods Phys. Res. Sect. B* **2008**, *266*, 681–700.
34. Wahlgren, G.M.; Carpenter, K.G.; Norris, R.P. Heavy Elements and Cool Stars. *AIP Conf. Proc. Astron.* **2008**, doi:10.1063/1.3099261.
35. Osterbrock, D.E. *Astrophysics of Gaseous Nebulae*; W. H. Freeman & Co Ltd.: San Francisco, CA, USA, 1974.
36. Denne, B.; Hinnov, E. Spectral Lines of Highly-Ionized Atoms for the Diagnostics of Fusion Plasmas. *Phys. Scr.* **1987**, *35*, 811–818.
37. Reader, J. $2s^22p^5$–$2s2p^6$ Transitions in the Flourinelike Ions Sr^{29+} and Y^{30+}. *Phys. Rev. A* **1982**, *26*, 501–503.
38. Aggarwal, K.M.; Keenan, F.P. Radiative Rates for E1, E2, M1, and M2 Transitions in F-like ions with $37 \leq Z \leq 53$. *At. Data Nucl. Data Tables* **2016**, *109–110*, 205–338.
39. Jönsson, P.; Alkauskas, A.; Gaigalas, G. Energies and E1, M1, E2 Transition Rates for States of the $2s^22p^5$ and $2s2p^6$ Configurations in Fluorine-like Ions Between Si VI and W LXVI. *At. Data Nucl. Data Tables* **2013**, *99*, 431–446.
40. Khatri, I.; Goyal, A.; Aggarwal, S.; Singh, A.K.; Mohan, M. Extreme Ultraviolet and Soft X-ray Spectral Lines in Rb XXIX. *Chin. Phys. B* **2016**, *25*, 033201.
41. Alexander, E.; Even-Zohar, M.; Fraenkel, B.S.; Goldsmith, S. Classification of Transitions in the EUV Spectra of Y IX–XIII, Zr X–XIV, Nb XI–XV, and Mo XII–XVI. *J. Opt. Soc. Am.* **1971**, *61*, 508–514.
42. Ekberg, J.O.; Jupén, C.; Brown, C.M.; Feldman, U.; Seely, J.F. Classification of Resonance Transitions in Ge XIX, Se XXI, Sr XXV, Y XXVI and Zr XXVll. *Phys. Scr.* **1992**, *46*, 120–126.
43. Ekberg, J.O.; Redfors, A.; Brown, C.M.; Feldman, U.; Seely, J.F. Transitions and Energy Levels in Al-like Ge XX, Se XXII, Sr XXVI, Y XXVII and Zr XXVIII. *Phys. Scr.* **1991**, *44*, 539–547.
44. Reader, J. $3s^2$–$3s3p$ and $3s3p$–$3s3d$ Transitions in Magnesiumlike Ions from Sr^{26+} to Rh^{33+}. *J. Opt. Soc. Am.* **1983**, *73*, 796–799.
45. Reader, J.; Ekberg, J.O.; Feldman, U.; Brown, C.M.; Seely, J.F. Spectra and Energy Levels of Sodiumlike Ions from Y^{28+} to Sn^{39+}. *J. Opt. Soc. Am. B* **1990**, *7*, 1176–1181.
46. Ateqad, N.; Chaghtai, M.S.Z.; Rahimullah, K. Addition to the Analysis of Y VII, VIII and Mo X. *J. Phys. B At. Mol. Phys.* **1984**, *17*, 4617–4622.
47. Litzén, U.; Hansson, A. Additions to the Spectra and Energy Levels of the Zinc-like Ions Y X–Cd XIX. *Phys. Scr.* **1989**, *40*, 468–471.
48. Nilsson, A.E.; Johansson, S.; Kurucz, R.L. The Spectrum of Singly Ionized Yttrium, Y II. *Phys. Scr.* **1991**, *44*, 226–257.
49. Epstein, G.L.; Reader, J. Spectrum and Energy Levels of Triply Ionized Yttrium (Y IV). *J. Opt. Soc. Am.* **1982**, *72*, 476–492.
50. Reader, J.; Acquista, N. Spectrum and Energy Levels of Ten-Times Ionized Yttrium (Y XI). *J. Opt. Soc. Am.* **1979**, *69*, 1285–1288.
51. Gillaspy, J.D. First Results from the EBIT at NIST. *Phys. Scr.* **1997**, *T71*, 99.
52. Gillaspy, J.D.; Aglitskiy, Y.; Bell, E.W.; Brown, C.M.; Chandler, C.T.; Deslattes, R.D.; Feldman, U.; Hudson, L.T.; Laming, J.M.; Meyer, E.S.; et al. Overview of the Electron Beam Ion Trap Program at NIST. *Phys. Scr.* **1995**, *T59*, 392–395.
53. Gillaspy, J.D. Testing QED in Sodium-like Gold and Xenon: Using Atomic Spectroscopy and an EBIT to Probe the Quantum Vacuum. *J. Instrum.* **2010**, *5*, C10005.
54. Gillaspy, J.D. Precision Spectroscopy of Trapped Highly Charged Heavy Elements: Pushing the Limits of Theory and Experiment. *Phys. Scr.* **2014**, *89*, 114004.

55. Sapirstein, J.; Cheng, K.T. S-Matrix Calculations of Energy Levels of Sodiumlike Ions. *Phys. Rev. A* **2015**, *91*, 062508.
56. Griem, H.R. *Principles of Plasma Spectroscopy*; Cambridge University Press: Cambridge, UK, 1997.
57. Ralchenko, Y.; Gillaspy, J.D.; Reader, J.; Osin, D.; Curry, J.J.; Podpaly, Y.A. Magnetic-Dipole Lines in $3d^n$ Ions of High-Z Elements: Identification, Diagnostic Potential and Dielectronic Resonances. *Phys. Scr.* **2013**, *T156*, 014082.
58. Ralchenko, Y.; Draganić, I.N.; Osin, D.; Gillaspy, J.D.; Reader, J. Spectroscopy of Diagnostically Important Magnetic-Dipole Lines in Highly Charged $3d^n$ Ions of Tungsten. *Phys. Rev. A* **2011**, *83*, 032517.
59. Ralchenko, Yu. Density Dependence of the Forbidden Lines in Ni-like Tungsten. *J. Phys. B At. Mol. Opt. Phys.* **2007**, *40*, F175–F180.
60. Blagojević, B.; Le Bigot, E.-O.; Fahy, K.; Aguilar, A.; Makonyi, K.; Takács, E.; Tan, J.N.; Pomeory, J.M.; Burnett, J.H.; Gillaspy, J.D.; et al. A High Efficiency Ultrahigh Vacuum Compatible Flat Field Spectrometer for Extreme Ultraviolet Wavelengths. *Rev. Sci. Instrum.* **2005**, *76*, 083102.
61. Holland, G.E.; Boyer, C.N.; Seely, J.F.; Tan, J.N.; Pomeroy, J.M.; Gillaspy, J.D. Low Jitter Metal Vapor Vacuum Arc Ion Source for Electron Beam Ion Trap Injections. *Rev. Sci. Instrum.* **2005**, *76*, 073304.
62. Gillaspy, J.D. Highly Charged Ions. *J. Phys. B At. Mol. Opt. Phys.* **2001**, *34*, R93–R130.
63. Kramida, A.; Brown, C.M.; Feldman, U.; Reader, J. Extension and New Level Optimization of the Ne IV Spectrum. *Phys. Scr.* **2012**, *85*, 025303.
64. Ralchenko, Y.; Kramida, A.; Reader, J.; The NIST ASD Team. NIST Atomic Spectra Database (Version 5), 2011. Available online: http://physics.nist.gov/asd (accessed on 15 January 2017).
65. Hughes, I.G.; Hase, T.P.A. *Measurements and Their Uncertainties*; Oxford University Press: Oxford, UK, 2010.
66. Ralchenko, Y.; Maron, Y. Accelerated Recombination Due to Resonant Deexcitation of Metastable States. *J. Quant. Spectosc. Radiat. Transf.* **2001**, *71*, 609–621.
67. Gu, M.F. The Flexible Atomic Code. *Can. J. Phys.* **2008**, *86*, 675–689.
68. Safronova, U.I.; Cowan, T.E.; Safronova, M.S. Relativistic Many-Body Calculations of Electric-Dipole Lifetimes, Transition Rates and Oscillator Strengths for $2l^{-1}$–$3l'$ States in Ne-like Ions. *J. Phys. B At. Mol. Opt. Phys.* **2005**, *38*, 2741–2763.
69. Kim,Y.-K.; Baik, D.H.; Indelicato, P.; Desclaux, J.P. Resonance Transition Energies of Li-, Na-, and Cu-like Ions. *Phys. Rev. A* **1991**, *44*, 148–166.
70. Kozhedub, Y.S.; Volotka, A.V.; Artemyev, A.N.; Glazov, D.A.; Plunien, G.; Shabaev, V.M.; Tupitsyn, I.I.; Stöhlker, T. Relativistic Recoil, Electron-Correlation, and QED Effects on the $2p_j$–$2s$ Transition Energies in Li-like Ions. *Phys. Rev. A* **2010**, *81*, 042513.
71. Blundell, S.A. Calculations of the Screened Self-Energy and Vacuum Polarization in Li-like, Na-like, and Cu-like Ions. *Phys. Rev. A* **1993**, *47*, 1790–1803.
72. Sapirstein, J.; Cheng, K.T. S-Matrix Calculations of Energy Levels of the Lithium Isoelectronic Sequence. *Phys. Rev. A* **2011**, *83*, 012504.
73. Seely, J.F. QED Contributions to the $2p$–$2s$ Transitions in Highly Charged Li-like Ions. *Phys. Rev. A* **1989**, *39*, 3682–3685.
74. Verdebout, S.; Nazé, C.; Jönsson, P.; Rynkun, P.; Godefroid, M.; Gaigalas, G. Hyperfine Structures and Landé g_J- Factors for $n = 2$ States in Beryllium-, Boron-, Carbon-, and Nitrogen-like Ions from Relativisitc Configuration Interaction Calculations. *At. Data Nucl. Data Tables* **2014**, *100*, 1111–1155.
75. Huang, K.-N.; Kim, Y.-K.; Cheng, K.T.; Desclaux, J.P. Correlation and Relativistic Effects in Spin-Orbit Splitting. *Phys. Rev. Lett.* **1982**, *48*, 1245.
76. Liu, H.; Jiang, G.; Hu, F.; Wang, C.-K.; Wang, Z.-B.; Yang, J.-M. Intercombination Transitions of the Carbon-like Isoelectronic Sequence. *Chin. Phys. B* **2013**, *22*, 073202.
77. Behring, W.E.; Brown, C.M.; Feldman, U.; Seely, J.F.; Reader, J.; Richardson, M.C. Transitions of the Type $2s$–$2p$ in Oxygenlike Y, Zr, and Nb. *J. Opt. Soc. Am. B* **1986**, *3*, 1113–1115.
78. Edlén, B. The 2_p Interval of $2s^2 2p^5$ and $2s^2 2p$. *Opt. Pura Apl.* **1977**, *10*, 123–129.
79. Kaufman, V.; Sugar, J. Forbidden Lines in $ns^2 np^k$ Ground Configurations and $nsnp$ Excited Configurations of Beryllium through Molybdenum Atoms and Ions. *J. Phys. Chem. Ref. Data* **1986**, *15*, 321–426.
80. Curtis, L.J.; Ramanujam, P.S. Ground-State Fine Sturcture for the B and F Isoelectronic Sequence Using the Extended Regular Doublet Law. *Phys. Rev. A* **1982**, *26*, 3672–3675.

81. Nilsen, J.; Scofield, J.H. Wavelengths of Neon-like $3p \rightarrow 3s$ X-ray Laser Transitions. *Phys. Scr.* **1994**, *49*, 588–591.
82. Shimkaveg, G.M.; Carter, M.R.; Walling, R.S.; Ticehurst, J.M.; Mrowka, S.; Trebes, J.E.; MacGowan, B.J.; Dasilva, L.B.; Matthews, D.L.; London, R.A.; et al. X-ray Laser Coherence Experiments in Neon-like Yttrium. In Proceedings of the International Conference on Lasers '91, San Diego, CA, USA, 9–13 December 1992; pp. 84–92.
83. Matthews, D.L.; Hagelstein, P.L.; Rosen, M.D.; Eckart, M.J.; Ceglio, N.M.; Hazi, A.U.; Medecki, H.; Macgowan, B.J.; Trebes, J.E.; Whitten, B.L.; et al. Demonstration of a Soft X-Ray Amplifier. *Phys. Rev. Lett.* **1985**, *54*, 110.
84. Cogordan, J.A.; Lunell, S. Energies of $2p^5 3s$, 3p, and 3d Levels of Neon-like Ions from Relativistic MCDF Calculations, $20 \leq Z \leq 54$. *Phys. Scr.* **1985**, *33*, 406–411.
85. Biersdorfer, P.; Obst, M.; Safronova, U.I. Radiative Decay Probabilities of the $(2s^2 2p_{1/2}^5 3s_{1/2})_{J=0}$ Level in Neonlike Ions. *Phys. Rev. A* **2011**, *83*, 012514.
86. Fontes, C.J.; Zhang, H.L. Relativistic Distorted-Wave Collision Strengths for $\Delta n = 0$ Transitions in the 67 Li-like, F-like and Na-like Ions with $26 \leq Z \leq 92$. *At. Data Nucl. Data Tables* **2017**, *113*, 293–315.
87. Santana, J.A. Relativistic MR-MP Energy Levels: Low-Lying States in the Mg Isoelectronic Sequence. *At. Data Nucl. Data Tables* **2016**, *111–112*, 87–186.
88. Safronova, U.I.; Jonson, W.R.; Berry, H.G. Excitation Energies and Transition Rates in Magensiumlike Ions. *Phys. Rev. A* **2000**, *61*, 052503.
89. Beiersdorfer, P. Precision Energy-Level Measurements and QED of Highly Charged Ions. *Can. J. Phys.* **2009**, *87*, 9–14.
90. Andersson, M.; Grumer, J.; Brage, T.; Zou, Y.-M.; Hutton, R. Analysis of the Competition Between Forbidden and Hyperfine-Induced Transitions in Ne-like Ions. *Phys. Rev. A* **2016**, *93*, 032506.
91. Beiersdorfer, P.; von Goeler, S.; Bitter, M.; Thorn, D.B. Measurement of the 3D $\rightarrow 2p$ Resonance to Intercombination Line-Intensity Ratio in Neonlike Fe XVII, Ge XXIII, and Se XXV. *Phys. Rev. A* **2001**, *64*, 032705.
92. Mauche, C.W.; Liedahl, D.A.; Fournier, K.B. First Application of the Fe XVII I(17.10 Å)/I(17.05 Å) Line Ratio to Constrain the Plasma Density of a Cosmic X-Ray Source. *Astrophys. J.* **2001**, *560*, 992–996.
93. Tallents, G.J. The Physics of Soft X-ray Lasers Pumped by Electron Collisions in Laser Plasmas. *J. Phys. D* **2003**, *36*, R259–R276.

Appendix B Manuscript for the paper titled "Measuring the Variation in Nuclear Charge Radius of Xe Isotopes by EUV Spectroscopy of Highly-Charged Na-like Ions"

Measuring the Nuclear Charge Radius Variation of Xe Isotopes by EUV Spectroscopy of Highly-Charged Na-like Ions

R. Silwal[a,b], A. Lapierre[c], J.D. Gillaspy[b,d], J.M. Dreiling[b] , S.A. Blundell[e] , Dipti[b], A. Borovik, Jr[b,f], G. Gwinner[g], A.C.C. Villari[c], Yu. Ralchenko[b], and E. Takacs[a,b]

[a]Department of Physics and Astronomy, Clemson University, SC, 29634
[b]National Institute of Standards and Technology (NIST), Gaithersburg, MD, 20899
[c]National Superconducting Cyclotron Laboratory, Michigan State University, East Lansing, MI, 48824
[d]National Science Foundation, Arlington, VA, 22314
[e]Univ. Grenoble Alpes, CEA, CNRS, INAC-SyMMES, 38000 Grenoble, France
[f]Physikalisches Institut Justus-Liebig Universitat Giessen, Giessen, 35392 Germany
[g] Department of Physics and Astronomy, University of Manitoba, Winnipeg, MB R3T 2N2, Canada

The variation in mean-square nuclear charge radius of xenon isotopes was measured utilizing a new method based on extreme ultraviolet spectroscopy of transitions in Na-like highly charged ions. The isotope shift of the Na-like D1 ($3s\ ^2S_{1/2}$ - $3p\ ^2P_{1/2}$) transition between the ^{124}Xe and ^{136}Xe isotopes was experimentally determined using the electron beam ion trap at the National Institute of Standards and Technology. This variation was inferred by comparison of the measured isotope shift with atomic-structure calculations in which the field shift and mass shift contributions were calculated with enhanced precision using the relativistic many-body perturbation theory and the multi-configuration Dirac-Hartree-Fock method. The mean-square nuclear charge radius difference was determined to be $\delta\langle r^2\rangle^{136,\ 124} = 0.269(0.042)$ fm^2. Our result agrees with previous experimental results and shows agreement with a recommended value obtained from a detailed compilation and evaluation of experimental nuclear charge radii [I. Angeli and K. P. Marinova, At. Data and Nucl. Data Tables 99, 69-95 (2013)].

The charge radius and the mass of the nucleus are its most fundamental properties. Studies of nuclear charge radii essential to understanding nuclear structure have revealed unusual properties such as nuclear halos [Sanchez2006], contribute to precision tests of the Standard Model [Mané2011], and enter in determinations of stellar element abundances [Aoki2001].

Only a few complementary techniques for the determination of the absolute mean-square nuclear charge radius $\langle r^2\rangle$ and its isotope variation $\delta\langle r^2\rangle$ exist. Muonic-atom spectroscopy [Fricke1995] and electron scattering [Hofstadter1956] offer direct measurements of the absolute $\langle r^2\rangle$. X-ray spectroscopy of inner shell K_α lines and valence electron optical isotope shifts allow for $\delta\langle r^2\rangle$ measurements between isotopes [Brockmeier1965].

Each method has its own difficulties that can limit its accuracy. In muonic-atom spectroscopy as the muon orbit is comparable to the nuclear size large nuclear polarization effects have to be considered. For electron scattering on heavy nuclei careful analysis of the experimental cross-sections must be conducted beyond the first Born approximation taking into account the phase shift. Moreover, these methods require considerable amounts of target material and are thus generally applied to stable nuclei. A recent report of the first elastic electron scattering experiment at the self-confining radioactive-isotope ion target (SCRIT) facility [Tsukada2017] promises the potential of future measurements for unstable nuclei as well.

The laser spectroscopy measurements of optical isotope shifts in neutral atoms and singly charged ions offer utmost experimental precision and can be applied to long chains of stable and unstable isotopes. The difficulty of this technique lies in the calculation of the electronic structure of many-electron atomic systems that can contribute to systematic offsets in the inferred $\delta\langle r^2\rangle$ [Libert2007]. Electron screening or correlation effects in heavy elements, such as bismuth or uranium, can be particularly difficult to calculate theoretically. These calculations are sometimes benchmarked to non-optical methods such as K_α

measurements [Anatassov1992] or King plot analysis [Cheal2012].

In search for new methods for the measurement of nuclear radii highly ionized atoms offer certain advantages. Particular charge states can have simpler electronic structure and higher sensitivity to the nuclear charge distribution compared to the neutral form of the same element. Electron probability distributions generally compressed closer to the nucleus when part of the electron cloud is missing resulting in amplified isotope shifts of energy levels.

In previous work relativistic normal and specific mass shifts (nuclear recoil) were explored by magnetic-dipole transitions of Be-like and B-like argon isotopes in the visible range [Orts], but the experimental precision was insufficient to probe the charge distribution. Precision x-ray spectroscopy [Elliott] and dielectronic recombination measurements [Schuch2005, Brandau2008] of isotope shifts in heavy, few-electron ions have proven to be applicable to determine $\delta\langle r^2\rangle$ in a variety of nuclei because the electronic structure of these ions can be calculated with high accuracy. However, the systems studied are generally difficult to produce experimentally, in particular for radioactive isotopes.

Driven by the improved accuracy of theoretical calculations for low-lying energy levels of Na-like systems over the past decades, Gillaspy *et al*. [Gillaspy2013] suggested that spectroscopic measurements of extreme ultraviolet (EUV) transitions in Na-like ions might be sensitive enough to determine nuclear charge distribution. The simple 3s electronic configuration penetrates the Ne-like closed shell to probe the nucleus in a way that can be accurately addressed by theory. Moreover, these ions can be produced in large abundance in small laboratory scale devices in comparison with few-electron ions.

In this letter, we present a $\delta\langle r^2\rangle^{A,A'}$ measurement for Xe isotopes with mass numbers of A=136 and A′=124. $\delta\langle r^2\rangle^{A,A'}$ was inferred by combining accurate theoretical calculations with precise measurement of the isotope shift in the transition frequency of the 3s $^2S_{1/2}$ - 3p $^2P_{1/2}$ (D1) transition in highly charged Na-like $^{136}Xe^{43+}$ and $^{124}Xe^{43+}$ ions. This experiment is the first to determine the difference between the $\langle r^2\rangle$ values of two isotopes by measuring the shift in their Na-like D1 transition energy. Benchmarks for this isotope pair are the previous optical isotope shift measurement of the same quantity that reported a value of 0.242 (0.080) fm^2 [Borchers1989] and the recommended value of (0.290 ±0.005) fm^2 suggested by interconnected trends across the nuclear radii surface in a compilation by [Angeli2013]. The new technique uses an electron-beam ion trap (EBIT) that can be also employed for unstable nuclei as demonstrated by Elliott *et al.* [Elliott1988].

The $\delta\nu$ isotope-dependent frequency shift has two components:

$$\delta\nu = \delta\nu_{FS} + \delta\nu_{MS} \, . \tag{1}$$

$\delta\nu_{MS}$ is the mass shift due to the finite mass of the nucleus and $\delta\nu_{FS}$ is the field shift associated with the nuclear volume. It is notable that the field shift scales with the nuclear charge as approximately $Z^{8/3}$ and it dominates the mass shift in heavy systems. As an approximation, $\delta\nu_{FS}$ can be considered to be proportional to the difference between the mean square nuclear charge radii of the two isotopes:

$$\delta\nu_{FS} = F\,\delta\langle r^2\rangle, \tag{2}$$

where $\delta\langle r^2\rangle$ is defined as [Angeli2013]:

$$\delta\langle r^2\rangle^{A,A'} = \langle r^2\rangle^{A} - \langle r^2\rangle^{A'} \tag{3}$$

Both the F field shift coefficient and the $\delta\nu_{MS}$ mass shift can be obtained from highly accurate atomic-structure calculations allowing for the experimental determination of $\delta\langle r^2\rangle^{A,A'}$ from the measured $\delta\nu$ shift.

In this experiment, EUV spectra were collected for Na-like $^{136}Xe^{43+}$ and $^{124}Xe^{43+}$ ions produced in the EBIT at the National Institute of Standards and Technology (NIST). Details of the measurements of EUV emission from Xe ions are similar to that in previous experiments in this wavelength region [Gillaspy2013]. Thorough description, along with the analysis of other transitions found in the same spectra, will be given in an upcoming publication.

Briefly, over the course of the experimental campaign, isotopically pure ^{136}Xe and ^{124}Xe neutral gases were alternately injected into the EBIT for approximately one-hour periods at a time, during which 10 to 12 spectra were collected using a liquid-nitrogen-cooled back-illuminated charge-coupled-device (CCD) camera attached to a flat-field EUV grating spectrometer [Blagojevic2005]. Each spectrum was collected for 300 s and contained 5 individual frames, which were acquired as a standard data taking procedure to allow for the post-processing removal of cosmic ray streaks randomly striking the detector during the experiment [Silwal2017].

The EBIT was operated at 6.0 keV electron beam energy and 150 mA electron beam current to optimize the production of the Na-like Xe charge state. The Na-like D1 spectral line was selected because it fits the procedure for the determination of $\delta\langle r^2\rangle^{A,A'}$ due to the high theoretical accuracy of the calculations for this line. It also has a further experimental advantage, as thorough analyses showed that this line is cleanly separated from other spectral features in the EUV spectrum. Systematic test of the Na-like D1 line as a function of the electron excitation energy showed no blends with other charge states, unlike the case of the other major Na-like candidate the $3s\ ^2S_{1/2}$ - $3p\ ^2P_{3/2}$ (D2) line [Gillaspy2010]. Further systematic investigation of the D1 transition in the second order of diffraction in the present study revealed that it also suffers from contributions from unknown features, therefore the current analysis was restricted to the strong and clean first order D1 line. Fig. 1 shows the full spectral range detected by the CCD camera, including emission from Na-like Xe and nearby charge states.

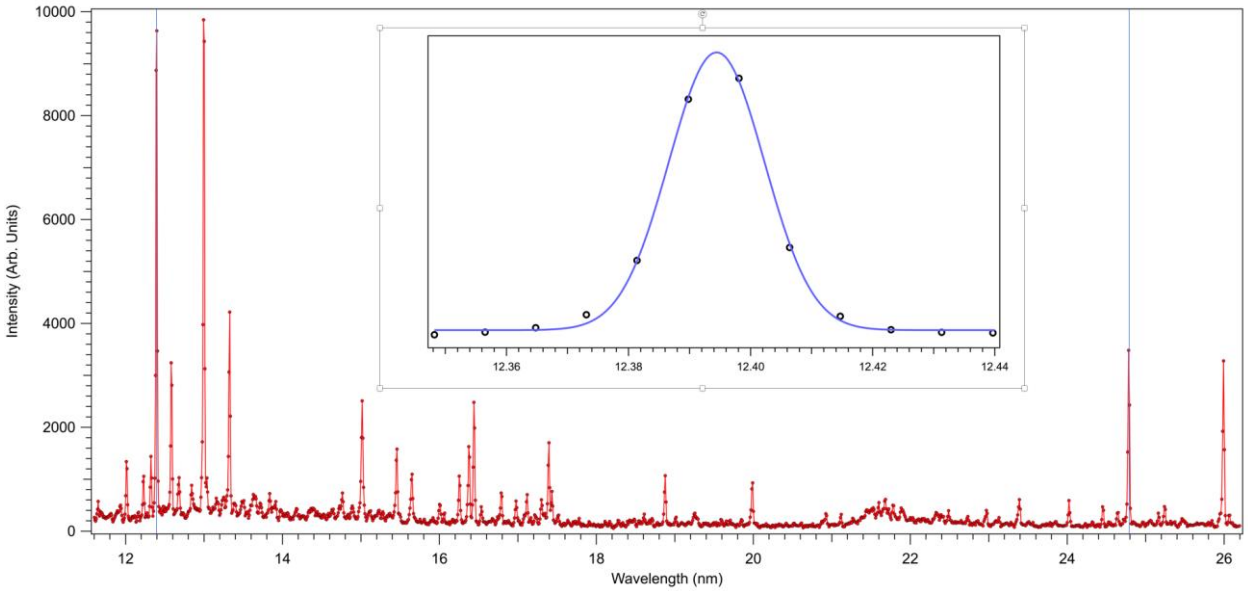

Fig. 1: Xenon EUV spectrum indicating the Na-like D1 line in first and second order by vertical lines. In the insert shows the first order line with a Gaussian fit.

Absolute wavelength calibration used well-known transitions of Ne, Xe and Ar [Kramida2017] collected several times during the data-taking epoch. Measurement of the isotope shift of the D1 transition in this experimental arrangement entails the determination of a spatial displacement that is well within the uncertainty of the absolute position. The uncertainty of the calibration that resulted an absolute wavelength of 12.3935(0.0009) nm for the D1 line in first diffraction order is not a limiting factor in the determination of the wavelength shift as the dispersion function it establishes has a much smaller uncertainty.

Because of the less than 10^{-4} nm anticipated shift between the D1 lines of the two Xe isotopes, a large number of EUV photons were required to achieve the necessary statistical uncertainty. Owing to the count rate of the D1 line emission the experiment was a multi-day acquisition effort during which long term thermal and electronic systematic drifts could be expected. We adopted a data analysis procedure that allowed us to eliminate the long-term variation of the line position by determining the centroid positions of the D1 line in each individual 300 s spectrum and creating a time-ordered sequence of the data that included both isotopes. The centroid positions were determined as a weighted average of the wavelength values associated with each channel to avoid any model-dependent errors. The number of channels around the mean of the centroid positions was varied to check for systematic dependences and in the final analysis 7 channels were used.

The full sequence of D1 line wavelength positions, including 428 centroid values, was fitted to a set of third order polynomial functions that described the long-term variation of the absolute position of the spectral line. Different sets of coefficients were allowed for datasets in between liquid nitrogen refills of the CCD camera at which times more thermal variations were expected. The polynomial functions for the two isotopes were kept to be the same except for an overall constant free parameter representing the isotope shift. Fig. 2 a shows a partial series of the centroid values with the alternating isotope sequences and the polynomial fit with the shift. Residuals were binned for each isotope individually, providing statistical distributions, which were fit with pure Gaussian functions as shown in Fig. 2 b. The agreement between the centroid positions is more than order of magnitude better than the uncertainty reported for the shift, giving us confidence in the evaluation procedure.

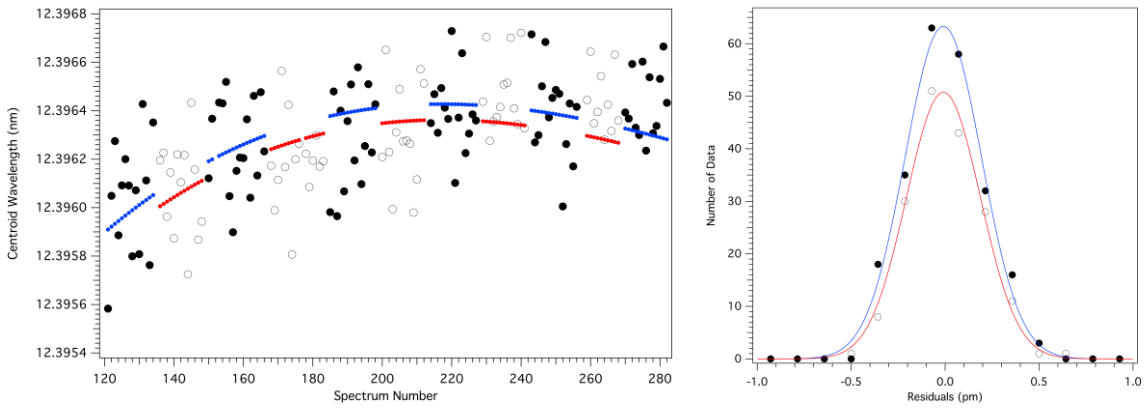

Fig. 2: a) Partial series of the centroid positions of the Na-like D1 transition in first order for the ^{124}Xe (open circles) and ^{136}Xe (full circles) isotopes and their fitted values described in the text. b) Statistical distributions of the residuals ^{124}Xe (open circles) and ^{136}Xe (full circles) isotopes fitted with pure Gaussian functions.

To verify the consistency of the experimental results, a series of systematic tests were performed throughout data analysis. These included different polynomial orders for the systematic drift, varying the number of channels in calculating the centroid positions, and changing bin sizes for the residual

distributions. The isotope shift values from these tests were within the uncertainty of the isotope shift reported here. The wavelength difference between the two isotopes was converted into the δν difference in frequency to allow for the determination of $\delta\langle r^2\rangle$ based on the theoretical procedure below.

In this work, the mass shift (MS) and field shift (FS) for the Na-like D1 ($3s\ ^2S_{1/2}$ - $3p\ ^2P_{1/2}$) transition were calculated using two different theoretical methods: the relativistic many-body perturbation theory (RMBPT) [Johnson1988A, Johnson1988B] and the multi-configuration Dirac-Hartree-Fock (MCDHF) theory of the GRASP2K code [Jonsson2013].

RMBPT was performed up to third order including both the Coulomb and Breit interactions in each order. A relativistic configuration interaction (RCI) module was used in the GRASP2K code to consider perturbatively the Breit interaction as well as leading quantum electrodynamics (QED) contributions (vacuum polarization as well as self-energy corrections). It was found that the two theories were in an overall excellent agreement. Table 1 shows the experimental and calculated isotope shifts from the current investigation along with the calculations from the large-scale configuration-interaction Dirac-Fock (CIDF) method of Tupitsyn *et al*., which solves the Dirac-Coulomb-Breit equation to calculate the energies and isotope shifts. [Tupitsyn2003].

Table 1: Measured and calculated values of the isotope shift along with their uncertainties for the Na-like D1 transition $3s\ ^2S_{1/2} – 3p\ ^2P_{1/2}$ for the isotope pair $^{136}Xe – ^{124}Xe$.

Theory						**Experiment**	
	RMBPT		GRASP2K		CIDF [Tupitsyn 2003]		
Coefficients	δλ (fm)	Δ δλ (fm)	δλ (fm)	Δ δλ (fm)	δλ (fm)	δλ (fm)	Δ δλ (fm)
NMS	-4.8		-4.8		-4.8		
SMS	-62.2		-62.3		-62.7		
Total MS	-67.0	3.4	-67.1	3.4	-67.5		
FS	143.0	2.86	142.0	2.84	143.0		
Total	**76.1**	**4.4**	**75.3**	**4.4**	**75.8**	**65.5**	**20.3E**

To obtain the field shift from the experimental frequency shift δν, the mass shift was accounted for through theoretical calculations. In RMBPT theory, the relativistic nuclear recoil corrections were calculated up to order $(Z\alpha)^2$ beyond the nonrelativistic mass shift by using the Palmer operator [Palmer1987]. This operator gives the one- and two-body nuclear-recoil terms in the relativistic

Hamiltonian corresponding to the normal (NMS) and specific (SMS) mass shifts, respectively. The nonrelativistic nuclear-recoil effect is itself of the order of $(Z\alpha)^2$, therefore the leading relativistic correction considered here is of the order of $(Z\alpha)^4$. The mass shift in each order of RMBPT was found by taking the difference of two calculations, one including nuclear recoil throughout, and the other excluding nuclear recoil, and then carefully testing this difference for numerical significance. In this way, it was possible to infer the NMS and the SMS coefficients, R and S, respectively, which are defined such that for two different isotopes with nuclear masses M_A and $M_{A'}$, the NMS and SMS frequency shifts ($\delta\nu_{NMS}$ and $\delta\nu_{SMS}$, respectively) are given by

$$\delta\nu_{NMS}(A,A') = R\,(1/M_A - 1/M_{A'}) \qquad (4)$$

and

$$\delta\nu_{SMS}(A,A') = S\,(1/M_A - 1/M_{A'}), \qquad (5)$$

where

$$\delta\nu_{MS} = \delta\nu_{NMS} + \delta\nu_{SMS}. \qquad (6)$$

Third-order RMBPT contributions to the mass shift coefficients for the D1 transition were found to be on the order 0.1% or less of the total mass shift. The dominant theoretical uncertainty in the mass shift is likely to be associated with the omitted higher-order relativistic terms, which start at the order of $(Z\alpha)^5$ [Erickson1965]. It could be on the order of several percent of the total mass shift for the D1 transition observed. We have assumed 5% for the relative theoretical uncertainty of the total mass shift throughout the calculations, although this number might be an overestimate considering the agreement between the different theoretical results in Table 1.

In order to calculate the field shift coefficient F in RMBPT, the transition frequency $\delta\nu$ was calculated assuming different nuclear charge distributions for isotopes A = 136 and A=124 and the difference $\delta\nu_{FS} = \delta\nu_{136} - \delta\nu_{124}$ was formed in each order. For the present calculations a two-parameter (c, a) Fermi model was assumed to obtain the nuclear potential experienced by the electrons. Parameter c is the half density radius [Parpia1992] and a is related to the t surface thickness of the charge distribution through the relation a= t/4ln3. The RMBPT calculations for the field shift were found to converge rapidly, with the third-order contributions to the D1 transition accounting for less than 0.1% of the total $\delta\nu_{FS}$. Self-energy and vacuum polarization QED corrections would enter at the 0.1% level as estimated by the GRASP2K calculations below. The field-shift coefficient is obtained as $F = \delta\nu_{FS}/\delta\langle r^2\rangle$, where $\delta\langle r^2\rangle$ is the change in mean-square radius of the two nuclear charge distributions assumed in the calculation.

The dominant theoretical uncertainty in the calculation of F comes from the unknown charge distribution of the nucleus. To estimate this nuclear-model dependence, the whole calculation procedure was repeated for several pairs of nuclear charge distributions, which involved changes of the charge density both on the surface and in the bulk volume regions of the nucleus. Through all of these changes, F was found to fluctuate at the 2% level, which was assumed to be the likely level of nuclear-model dependence.

In the MCDHF approach, the atomic state function (ASF) was expanded in the configuration state functions of the same parity, total angular momentum (J) and its projection (M_J). The reference configurations were $1s^22s^22p^63s$ and $1s^22s^22p^63p$ for the ground state and excited state, respectively. To begin with, the ASF's for the single configuration Dirac-Fock solution for the reference configurations were calculated for the ^{136}Xe isotope. The 1s, 2s and 2p orbitals were treated as core while the 3s and 3p

orbitals were treated as valence orbitals. We have limited the excitation from the 1s orbital to single excitations to the active sets. The configuration state function space was expanded by means of single (S), double (D) excitations from the occupied orbitals to active sets of up to n=6 and also triple (T) excitations within the n = 3 states to consider the valence-valence (VV), core-valence (CV), core-core (CC) correlation effects. These calculations were carried out by adding the virtual orbitals layer by layer to monitor the convergence of energies and oscillator strengths. The Breit interactions and the leading QED effects up to n= 5 were also included during RCI calculations. Self-energy and vacuum polarization QED corrections were estimated phenomenologically and were found to enter at the 0.1% level.

After obtaining the wave function, the relativistic isotope shift (RIS3) module [Naze2013] was used to calculate the mass shift. Similar to RMBPT, GRASP2K also includes nuclear recoil corrections of the order of $(Z\alpha)^4$ for mass shift calculations. The field shift was calculated explicitly from the difference between transition energies that are obtained by solving the MCDHF + Breit equations for isotopes A and A' separately, keeping the nuclear surface thickness 2.30 fm for both.

To estimate the effect of higher-order nuclear moments, we considered that for a transition involving a valence s electron, Eq. (2) can be more accurately replaced by

$$\delta\nu_{FS} = F\,\lambda, \qquad (7)$$

where λ is the Seltzer moment of the nucleus [Blundell1987]:

$$\lambda = \delta\langle r^2\rangle + S_4\,\delta\langle r^4\rangle + S_6\,\delta\langle r^6\rangle = [1 + S_{HO}/\delta\langle r^2\rangle]\,\delta\langle r^2\rangle \qquad (8)$$

with $S_{HO} = S_4\,\delta\langle r^4\rangle + S_6\,\delta\langle r^6\rangle$ representing the higher nuclear moment terms. The values of the S_4 and S_6 coefficients [Blundell1987] suggest that the contribution of higher-order moments to the field shift $\delta\nu_{FS}$ is about 4% in our case.

Similar conclusion can be obtained from the GRASP2K code using the procedure described by Li *et al.* [Li2012] which uses the probability density of the electron wave function at the origin to calculate the field shift, effectively selecting the term $\delta\langle r^2\rangle$ in λ. The field shift obtained this way was found to be 4% larger than the result implicitly containing higher-order nuclear moments described above.

Using the calculated values of the mass shift and *F*, along with the experimentally obtained frequency shift, $\delta\nu$, the difference between the mean-square nuclear charge radii of ^{136}Xe and ^{124}Xe was determined to be $\delta\langle r^2\rangle^{136,124} = 0.269(0.042)$ fm^2.

The overall uncertainty in the determination of $\delta\langle r^2\rangle$ includes $\Delta\delta\nu_{FS}$ from the experiment and the mass shift correction, ΔF from the field shift, and ΔS_{HO} from higher order nuclear moments:

$$\Delta\delta\langle r^2\rangle \approx \sqrt{\left(\frac{\Delta\delta\nu_{FS}}{F}\right)^2 + \left(\frac{\Delta F\,\delta\nu_{FS}}{F^2}\right)^2 + (\Delta S_{HO})^2} \qquad (9)$$

The 16% relative total uncertainty of the current determination of $\delta\langle r^2\rangle$ between ^{136}Xe and ^{124}Xe isotopes is dominated by the experimental uncertainty over the theoretical uncertainty that amounts to about 3% including the mass-shift. Detailed list of the values of the different quantities that contribute to the evaluation of $\delta\langle r^2\rangle$ together with their measured or estimated uncertainties are listed in Table 1.

As shown in Fig. 3, the value from the current experiment is within the uncertainty of that of $\delta\langle r^2\rangle^{136,124} = 0.242(0.080)$ fm^2 obtained from the most recent optical (laser spectroscopy) isotope shift measurement by Borchers *et al.* [Borchers1989]. Their combined 0.080 fm^2 uncertainty is the quadrature sum of the experimental uncertainty of 0.005 fm^2 and theoretical uncertainty of 0.080 fm^2. The latter is an

order of magnitude larger than the reported experimental uncertainty, due to the lack of precise theoretical calculations for the neutral system. Our result is in satisfactory agreement with a value of 0.350(0.030) fm^2 [Libert2007] obtained through a King plot analysis of optical isotope shifts [Borchers1989] versus muonic-atom spectroscopy measurements [Fricke1995]. Our result also agrees with the recommended value of 0.290(0.005) fm^2 [Angeli2013] obtained by detailed analysis of published experimental nuclear charge-radius data.

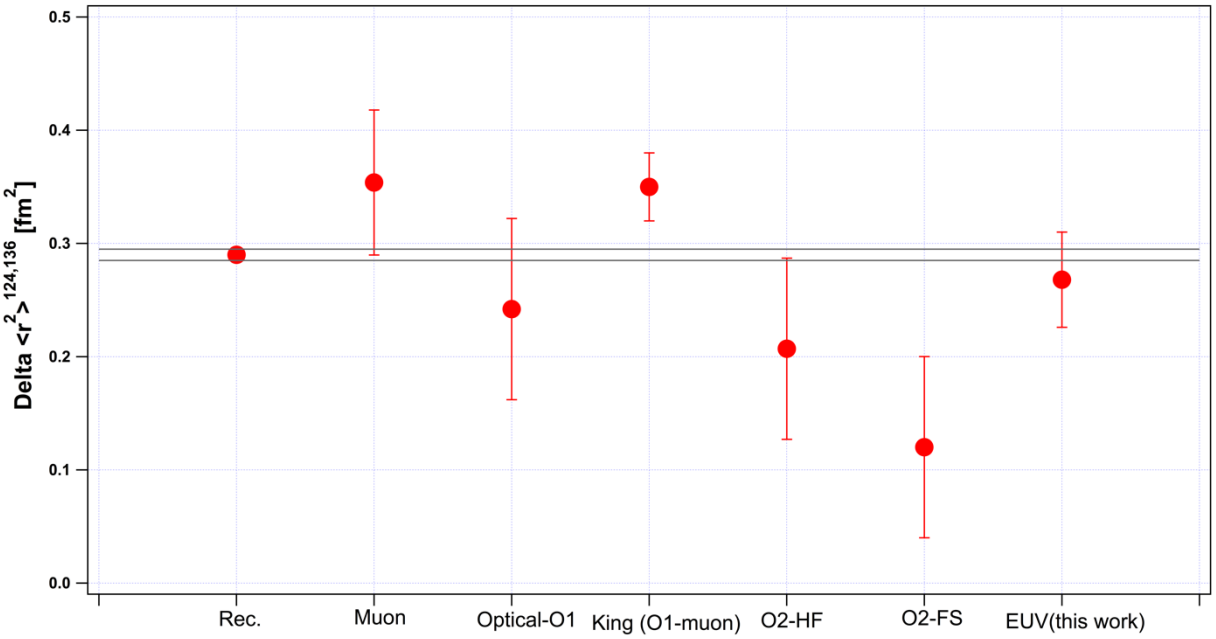

Fig. 3: Change in mean-square nuclear charge radius between ^{136}Xe and ^{124}Xe ($\delta\langle r^2\rangle^{136,124}$) measured by Na-like D1 EUV spectroscopy compared with previous measurements and analyses. Rec.: recommended value [Angeli2013]; Muon: muonic-atom spectroscopy [Angeli1995]; Optical-O1: optical shift by laser-spectroscopy [Borchers1989]; King (O1-Mu): King plot analysis combining the optical measurements with the muonic-atom results [Libert2007]; O2-HF and O2-FS: optical (interferometer) shift based on the Hartree-Fock method and Fermi-Segre calculations [Fischer1974] EUV: this work. The two horizontal lines represent the uncertainty listed for the recommended value [Angeli2013].

The agreement of our measurement with the recommended value, previous measurements, and a King plot analysis of optical versus muonic-atom measurements illustrates the relevance of EUV spectroscopy of Na-like ions for nuclear-size measurements. The new method for determining the difference in the mean square nuclear charge radius between isotope pairs based upon the isotope shift of the Na-like D1 transition takes advantage of the simple electronic structure of multiply charged ions. Atomic-structure calculations for these systems can reach accuracies higher than those for neutral atoms and singly charged ions used in optical isotope shift measurements. In multiply charged ions, RMBPT converges as 1/Z (Z being the atomic number) for each successive order, while for neutral atoms, the atomic many-body problem is essentially non-perturbative. MCDHF and RCI calculations are much more accurate for these systems as well. Moreover, the precise calculation of the mass shift, which is suppressed at high-Z, allows this shift to be subtracted directly.

In optical measurements of neutral atoms and singly charged ions, the calculations have to often include electron correlation effects, difficult to calculate, sometimes adding large uncertainties to the inferred charge radius differences. Measurements of complex multi-electron systems occasionally rely on

King plots of the studied transitions against optical, muonic-atom, or Kα transitions of the same isotopes. The new method complements the optical method by adding to the set of transitions that can be used to calibrate and test atomic-structure calculations.

The method uses an ion trap and can be applied to small sample sizes of only a million ions or less. It can offer the possibility of conducting isotope shift measurements on radioactive isotopes at existing rare-isotope beam facilities like the Isotope Separator and Accelerator (ISAC) facility at TRIUMF, and next-generation facilities as the Facility for Rare Isotope Beams (FRIB) at Michigan State University. These facilities are expected to increase production rates by several orders of magnitude.

This work was partially funded by the NIST Grant Award #70NANB16H204 of the Measurement Science and Engineering (MSE) Research Grant Programs. AL and ACCV acknowledges support by the National Science Foundation under Grant No. PHY-1565546. JMD acknowledges funding from the National Research Council Research Associateship Award at NIST. GG acknowledges support by NSERC (Canada). We would like to thank David Takacs for his help with the initial data analysis.

[Sanchez2006] R. Sánchez, W. Nörtershäuser, G. Ewald, D. Albers, J. Behr, P. Bricault, B. A. Bushaw, A. Dax, J. Dilling, M. Dombsky, G. W. F. Drake, S. Götte, R. Kirchner, H.-J. Kluge, Th. Kühl, J. Lassen, C. D. P. Levy, M. R. Pearson, E. J. Prime, V. Ryjkov, A. Wojtaszek, Z.-C. Yan, and C. Zimmermann, Phys. Rev. Lett., 96, 033002 (2006)

[Mané2011] E. Mané, A. Voss, J. A. Behr, J. Billowes, T. Brunner, F. Buchinger, J. E. Crawford, J. Dilling, S. Ettenauer, C. D. P. Levy, O. Shelbaya, and M. R. Pearson, Phys. Rev. Lett., 107, 212502 (2011)

[Aoki2001] W. Aoki, S. G. Ryan, J. E. Norris, T. C. Beers, H. Ando, N. Iwamoto, T. Kajino, G. J. Mathews, M. Fujimoto, Astrophys. J., 561, 346 (2001)

[Renton1988] P.B. Renton, Europhy. News. J.A. **19**, 11-12 (1988).

[Frankfurt2012] L. Frankfurt and M. Straikman, Int. J. Mod. Phys. E **21**, 1230002 (2012).

[Hofstadter1956] R. Hofstadter, Rev. Mod. Phys. **28**, 214–254 (1956).

[Fricke1995] G. Fricke, C. Bernhardt, K. Heilig, L. A. Schaller, L. Schellenberg, E. B. Shera, and C. W. Dejager, At. Data and Nucl. Data Tables **60**, 177 (1995).

[Tsukada2017] K. Tsukada *et al*,. Phys. Rev. Lett. **118**, 262501 (2017).

[Libert2007] J. Libert, B. Roussière, and J. Sauvage, Nucl. Phys. A 786, **47** (2007).

[Anatassov1992] A. Anatassov, Yu.P. Gangrsky, K.P. Marinova, B.N. Markov, B.K. Kul'djanov, and S.G. Zemlyanoi, Hyperfine Interactions, 74, 31 (1992)

[Cheal2012] B. Cheal, T. E. Cocolios, and S. Fritzsche, Phys. Rev. A 86, 042501 (2012).

[Orts2006] R. S. Orts *et al*,. Phys. Rev. Lett. **97**, 103002 (2006).

[Brockmeier1965] R. T. Brockmeier, F. Boehm, E. N. Hatch, Phys. Rev. Lett. **15**, 132 (1965).

[Elliott1988] S. R. Elliott, P. Beiersdorfer, M. H. Chen, V. Decaux, and D. A. Knapp, Phys. Rev. C **57**, 583 (1998).

[Schuch2005] R. Schuch, E. Lindroth, S. Madzunkov, M. Fogle, T. Mohamed, and P. Indelicato, Phys. Rev. Lett. **95**, 183003 (2005).

[Brandau2008] C. Brandau *et al*,. Phys. Rev. Lett. **100**, 073201 (2008).

[Angeli2013] I.Angeli and K.P. Marinova, At. Data and Nucl. DataTables **99**, 69-95 (2013).

[Elliott1996] S. R. Elliott, P. Beiersdorfer, and M. H. Chen, Phys. Rev. Lett. **76**, 1031 (1996).

[Gillaspy2013] J. D. Gillaspy, D. Osin, Yu. Ralchenko, J. Reader, and S. A. Blundell, Phys. Rev. A **87**, 062503 (2013).

[Fahy2007] K. Fahy, E. Sokell, G. O'Sullivan, A. Aguilar, J. M. Pomeroy, J. N. Tan, and J. D. Gillaspy, *et al,* Phys. Rev. A **75**, 032520 (2007).

[Blagojevic2005] B. Blagojević *et al*,. Rev. Sci. Instrum. **76**, 083102 (2005).

[Silwal2017] R. Silwal, E. Takacs, J.M. Dreiling, J.D. Gillaspy, and Y. Ralchenko, Atoms **5**, 30 (2017).

[Gillaspy2010] J.D. Gillaspy, J. Instrumentation **5**, p. C10005 (2010).

[Kramida2017] A. Kramida, Yu. Ralchenko, J. Reader, and NIST ASD Team (20l7), NIST Atomic Spectra Database (version 5.5.1), [Online]. Available: https://physics.nist.gov/asd.

[Osin2012] D. Osin, J. Reader, J. D. Gillaspy and Yu Ralchenko, J. Phys. B: At. Mol. Opt. Phys. **45**, 245001 (2012).

[Jonsson2013] P. Jönsson, G. Gaigalas, J. Bierońc, C. Froese Fischer, I. P. Grant, Comput. Phys. Commun. **184**, 2197 (2013).

[Johnson1988A] W.R. Johnson, S. A. Blundell, and J. Sapirstein. Phys. Rev. A **37**, 2764 (1988).

[Johnson1988B] W.R. Johnson, S. A. Blundell, and J. Sapirstein. Phys. Rev. A **38**, 2699 (1988).

[Blundell1987] S. A. Blundell, P E G Baird, C W P Palmer, D N Stacey and G K Woodgate,. J. Phys. B: At. Mol. Phys. **20**, 3663 (1987).

[Li2012] J. Li, C. Nazé, M. Godefroid, S. Fritzsche, G. Gaigalas, P. Indelicato, and P. Jönsson, Phys. Rev. A **86**, 022518 (2012).

[Naze2013] C. Naze, E. Gaidamauskas, G. Gaigalas, M. Godefroid, P. Jönsson, Comput. Phys. Commun. **184**, 2187 (2013).

[Palmer1987] C.W.P. Palmer, J. Phys. B: At. Mol. Phys. **20**, 5987 (1987).

[Erickson1965] G.W. Erickson and D.R. Yennie, Ann. Phys. (NY) **35**, 271 (1965).

[Tupitsyn2003] I.I. Tupitsyn, V. M. Shabaev, J. R. Crespo López-Urrutia, I. Draganić, R. Soria Orts, and J. Ullrich, Phys. Rev. A **68**, 022511 (2003).

[Borchers1989] W. Borchers, E. Arnold, W. Neu, R. Neugart, K. Wendt, G. Ulm, ISOLDE Collaboration, Phys. Lett. B **216**, 7 (1989).

[Parpia1992] F.A. Parpia, and A.K. Mohanty, Phys. Rev. A **46,** 3735 (1992).

[Angeli1995] I. Angeli, Table of nuclear root mean square charge radii, International atomic energy agency, Nuclear data section, Vienna (1995).

[Fischer1974] W. Fischer, H. Hühnermann, G. Krömer, H. J. Schäfer, Z. Physik **270**, 113 - 120 (1974).

Appendix C Abstracts from Presentations at Conferences

48th Annual APS Division of Atomic, Molecular and Optical Physics

June 5-9, 2017

Sacramento, CA

Isotopic shift measurement of Na-like Xe ions as a new method to measure absolute and relative charge radii of rare isotopes

R. Silwal[a,b], A. Lapierre[c], J. Gillaspy[b,e] , A.C.C. Villari[c], G. Gwinner[d], S. A. Blundell[f], J. M. Dreiling[b] , B. H. Rudramadevi[a], A. Borovik Jr[g], Y. Ralchenko[b], and E. Takacs[a,b]

[a]Department of Physics and Astronomy, Clemson University, SC 29634 USA

[b]National Institute of Standards and Technology, Gaithersburg, MD 20878 USA

[c]Michigan State University, East Lansing, MI 48824 USA

[d]University of Manitoba, Manitoba, Canada

[e]National Science Foundation, Arlington, VA 22230 USA

[f]INAC/SYMMES, CEA-Grenoble/Université Grenoble Alpes, France

[g]I. Physikalisches Institut, Justus-Liebig Universit¨at Gießen, Giessen, Germany

Except for U and Th, the absolute charge radius of unstable (radioactive) isotopes is unavailable for elements heavier than Bi because current measurement techniques, such as electron scattering and muonic x-ray spectroscopy, require macroscopic amounts of the elements. Relative shifts in charge radii along isotopic chains, obtained from optical frequency shifts, strongly depend on semi-empirical approaches thereby adding further uncertainties. Transition energies of Na-like ions are sensitive to nuclear size, and because of their simple electronic structure, ab-initio atomic structure calculations can reach high accuracy. For heavy elements, it has even been noted that the precision of such calculations is limited by the large uncertainty in charge radii [1]. This suggests a new method for charge radius measurements using Na-like ions. As a proof-of-principle, we have measured the energy shift associated with the D_1 and D_2 3s-3p transitions for Na-like Xe-124 and Xe-136. The relative shift in charge radius of these isotopes is inferred by comparing experimental and theoretical energy shifts from high-precision calculations. We present preliminary results obtained from EUV and x-ray spectra observed in an electron beam ion trap.

1. Gillaspy et al., *Phys. Rev. A* **87**, 062503 (2013)

Precision Physics, Quantum Electrodynamics and Fundamental Interactions
April 30, 2017 - May 5, 2017
IESC Cargese, France

Determination of the relative nuclear radii of xenon isotopes by the precision measurement of the isotopic shift of Na-like spectral lines

R. Silwal[1,2], A. Lapierre[3], J.D. Gillaspy[2,4], A.C.C. Villari[3], G. Gwinner[5], S.A. Blundell[6], J.M. Dreiling[2], B.H. Rudramadevi[1], A. Borovik Jr[7], Yu. Ralchenko[2], and E. Takacs[1,2]

1. Department of Physics and Astronomy, Clemson University, SC, USA
2. National Institute of Standards and Technology, MD, USA 2
3. National Superconducting Cyclotron Laboratory, Michigan State University, East Lansing, MI, USA 2
4. National Science Foundation, Arlington, VA, USA 4
5. University of Manitoba, Manitoba, Canada 5
6. INAC/SYMMES, CEA-Grenoble/Université Grenoble, France 6
7. I. Physikalisches Institut, Justus-Liebig Universität Giessen, Giessen, Germany 7

The atomic properties of quasi-hydrogenic Na-like ions can be calculated to high precision using *ab intio* methods. For instance, assuming a known charge distribution, the absolute transition energies of the D lines of Na-like ions can be theoretically calculated to an accuracy of about 100 ppm[1]. The strong overlap between the 3s valence electron and the nucleus makes the Na-like transition energies sensitive to nuclear size effects. In particular, the Na-like 3s-3p D_1 and D_2 transitions offer a large calculable field-shift, making these spectral lines potentially useful for extracting information about the nuclear charge radius, a key nuclear physics parameter [2].

In heavy elements, especially in rare (radioactive) isotopes, the values of the nuclear radii in the literature have large uncertainties due to limitations of the available experimental techniques. The combination of measurements and calculations of the Na-like D lines offers a new method for improving the determinaton of the nuclear radii, which has the potential to rival optical isotope shift measurements [3].

Extreme ultraviolet (EUV) spectroscopy of highly charged Na-like ions can achieve the desired accuracy. We have performed a proof-of-principle experiment for the measurement of relative change in charge radius of Xe isotopes using the electron beam ion trap (EBIT) at the National Institute of Standards and Technology (NIST) [4]. We have measured the Na-like D spectral lines of the Xe-124 and Xe-136 isotopes and determined the difference between their nuclear radii by evaluating the shift in the line positions. The expected field shift is approximately 11 ppm of the transition energy, and the shift in the line positions can be determined to the similar level of experimental accuracy.

Details of the experiment and theoretical calculations will be presented, and the potential of the technique for the determination of nuclear radii will be discussed.

References

[1]J.D. Gillaspy, D. Osin, Yu. Ralchenko, J. Reader, and S.A. Blundell, Phys. Rev. A **87**, 062503 (2013).
[2] I. Angeli and K.P. Marinova Journal of Physics G: Nuclear and Particle Physics **61** 42(5) (2015)
[3] J. Libert, B. Roussiére and J. Sauvage, Nuclear Physics A **786**, 47 (2007).
[4] J. D. Gillaspy, Phys. Scr. **71**, 99 (1997).

2017 Joint ICTP-IAEA School on Atomic Processes in Plasmas

27 February - 3 March 2017

ICTP - Miramare, Trieste, Italy.

EUV measurements of Y XXVII - Y XXXVII with an EBIT and magnetic dipole transitions suitable for plasma diagnostics

R. Silwal [a,b], E. Takacs [a,b], , J. M. Dreiling [b] , J. D. Gillaspy [b,c], and Yu. Ralchenko [b]

[a] Department of Physics and Astronomy, Clemson University, Clemson, S.C. 29634-0978, USA

[b] National Institute of Standards and Technology, Gaithersburg, MD 20899, USA

[c] National Science Foundation, Arlington, VA 22230, USA

Email:rsilwal@g.clemson.edu, roshani.silwal@nist.gov

Abstract:

Extreme-ultraviolet spectra of the L-shell ions of highly charged yttrium (Y^{26+}-Y^{36+}) were observed in the electron beam ion trap (EBIT) at the National Institute of Standards and Technology (NIST) using a flat-field grazing-incidence spectrometer in the wavelength range of about 4 nm to 20 nm. In order to reach the desired ionization stages, the beam energy was systematically varied from 2.3 keV to 6 keV during the experiment. The wavelength calibration was provided by the previously measured lines of neon, xenon, oxygen and iron. Fifty-nine spectral lines corresponding to $\Delta n = 0$ transitions within n=2 and n=3 have been identified using detailed collisional-radiative modeling of the non-Maxwellian EBIT plasma with uncertainties between 0.0003 nm and 0.0018 nm. Few of the identified lines were due to the forbidden magnetic dipole (M1) transitions within $2p^n$ configurations. To analyze the potential applicability of these lines to plasma diagnostics, large-scale collisional-radiative (CR) calculations was performed to generate Y spectra in Maxwellian plasmas with electron temperatures on the order of several keV; such high temperatures correspond to the maximal abundance of the L-shell ions of Y. It was found that several line ratios show strong dependence on electron density and/or electron temperature and hence may be implemented in diagnostics of hot plasmas, in particular, in fusion devices.

47th Annual Meeting of the APS Division of Atomic, Molecular and Optical Physics

May 23-27, 2016

Providence, RI

PRECISION WAVELENGTH MEASUREMENTS AND IDENTIFICATIONS OF EUV LINES FROM HIGHLY CHARGED L-SHELL YTTRIUM IONS

R. Silwal[a,b], J. M. Dreiling[b], J. D. Gillaspy[b,c], E. Takacs[a,b], and Yu. Ralchenko[b]

[a] Department of Physics and Astronomy, Clemson University, Clemson, S.C. 29634-0978, USA

[b] National Institute of Standards and Technology, Gaithersburg, MD 20899, USA

[c] National Science Foundation, Arlington, VA 22230, USA

Email: rsilwal@g.clemson.edu, roshani.silwal@nist.gov

We present the measurements of extreme-ultraviolet spectra of the L-shell ions of highly charged yttrium (Y^{29+}-Y^{36+}) created and trapped in the electron beam ion trap (EBIT) of the National Institute of Standards and Technology. Few Na-like, Mg-like and Al-like yttrium lines (Y^{26+}-Y^{28+}) are reported as well. In order to reach the desired ionization stages, the beam energy was systematically varied from 2.3 keV to 6 keV during the experiment. A flat-field grazing-incidence spectrometer was used to record the spectra in the wavelength range of 4.022 nm to 19.957 nm. The wavelength calibration was provided by the previously measured lines of neon, xenon, oxygen and iron. A total of 63 new spectral lines (allowed and forbidden) corresponding to the $\Delta n=0$ transitions within n=2 and 3 have been identified using collisional-radiative simulations of the non-Maxwellian EBIT plasma. The total uncertainties assigned to the measured wavelengths vary between 0.001 nm to 0.003 nm and include contributions from calibration uncertainties, statistical uncertainties from the line fits, and estimated systematic uncertainties.

19th International Conference on Atomic Processes in Plasmas

4-8 April 2016

Paris, France

PLASMA DIAGNOSTICS WITH EUV SPECTRA FROM HIGHLY CHARGED IONS OF YTTRIUM

Roshani Silwal[*, #, 1], Joan M Dreiling[*], John D Gillaspy[*, $], Endre Takacs[*, #] and Yuri Ralchenko[*]

*National Institute of Standards and Technology, Gaithersburg, MD 20899, USA

[#]Department of Physics and Astronomy, Clemson University, Clemson, SC 29634-0978, USA

[$]National Science Foundation, Arlington, VA 22230, USA

Extreme-ultraviolet spectra of the L-shell ions of highly-charged yttrium (Y^{29+}-Y^{36+}) were observed in the electron beam ion trap (EBIT) at the National Institute of Standards and Technology [1] using a flat-field grazing-incidence spectrometer [2] in the wavelength range of about 4 nm to 20 nm. Neon, xenon, iron and oxygen lines [3] were used for the wavelength calibration. Detailed collisional-radiative (CR) modeling [4] for the non-Maxwellian EBIT plasma was used to simulate the spectra and classify previously unknown lines. Among the 63 newly identified yttrium lines, measured with uncertainties between 0.001 nm and 0.003 nm, several lines are due to the forbidden magnetic dipole (M1) transitions within $2p^n$ configurations. To analyze the potential applicability of these lines to plasma diagnostics, we performed large-scale CR calculations of yttrium spectra in Maxwellian plasmas with electron temperatures on the order of several keV; such high temperatures correspond to the maximal abundance of the L-shell ions of yttrium. It was found that several line ratios show strong dependence on electron density and/or electron temperature and hence may be implemented in diagnostics of hot plasmas and, in particular, fusion devices.

References

1. J. D. Gillaspy, *Phys. Scr. T* **71**, 99 (1997).
2. B. Blagojevic *et al*., Rev. Sci. Instrum.**76**, 083102 (2005).
3. Yu. Ralchenko, A. Kramida, J. Reader, and the NIST ASD Team, NIST Atomic Spectra Database (version 5), http://physics.nist.gov/asd.
4. Yu. Ralchenko and Y. Maron, *J. Quant. Spectosc. Radiat. Transfer* **71**, 609 (2001).

[1]Email: rsilwal@g.clemson.edu, roshani.silwal@nist.gov

46th Annual Meeting of the APS Division of Atomic, Molecular and Optical Physics

June 8-12, 2015

Columbus, OH

X-RAY DIAGNOSTICS OF CUEBIT HIGHLY CHARGED ION PLASMA

Roshani Silwal, Amy C. Gall, Endre Takacs, James E. Harriss, Chad E. Sosolik
Department of Physics and Astronomy, Clemson University, Clemson, SC, 29634

The CUEBIT, Clemson University Electron Beam Ion Trap is one of the few EBIT facilities around the globe that produces highly charged ions by successive electron impact ionization. Ions are confined in the machine by the space charge of the electron beam, a 6 T magnetic field generated by a superconducting magnet, and the voltages applied to axial electrodes. The device is a small laboratory scale instrument used for the study of the structure and emission of highly charged ions and the collisions of these ions with external targets. Along with the introduction of the facility including its structure and capabilities, we present an overview of various spectroscopic and imaging tools that allow the diagnosis of the high temperature ion cloud of the CUEBIT. Instruments include a crystal spectrometer, solid-state detectors, and pin-hole imaging setup equipped with an x-ray CCD camera. Measurements of x-ray radiation from CUEBIT are used to investigate the fundamental properties of the highly charged ions and their interaction with the energetic electron beam.

Appendix D Data Analysis Source Code

#Compute the centroid of spectral lines as a function of channel number and wavelength (nm).

```
import xlrd
# This excel file contains the list of lines and ranges
ExcelLines = xlrd.open_workbook('C:\Isotope
shift\Final_try\Lines_7pixels.xlsx')
StrongSheet = ExcelLines.sheet_by_index(0)

# Loading the lower and higher limits. MidCh is the estimated line
position.
LowCh = []
HighCh = []
MidCh = []
for i in range(1,StrongSheet.nrows-5):
    LowCh.append(StrongSheet.cell(i,0).value)
    HighCh.append(StrongSheet.cell(i,1).value)
    MidCh.append(StrongSheet.cell(i,2).value)
print HighCh
# This excel file includes all the data
AllData = xlrd.open_workbook('C:\Isotope
shift\Final_try\XenonAllEUVdata.xlsx')
AllSheet = AllData.sheet_by_index(2)

# Loading the channel and wavelength columns. The first element is empty,
the second is a label.
WaveLength = []
Channel = []
for i in range(0,AllSheet.nrows):
    Channel.append(AllSheet.cell(i,0).value)
    WaveLength.append(AllSheet.cell(i,1).value)

# Loading each spectra. The first element is the isotope (136 or 124),
the second is the file name (EUV###).
# Spectrum[k][i] is the intensity of channel i-2 of spectrum k-2
# Spectrum[k][1] is the file name of spectrum k-2, Spectrum[k][0] is the
isotope of spectrum k-2
Spectrum = []
i = 0
while i < AllSheet.ncols:
    ithrow = []
    j = 0
    while j < AllSheet.nrows:
        ithrow.append(AllSheet.cell(j,i).value)
        j += 1
    Spectrum.append(ithrow)
    i +=1

#Calculating centroids
CentroidsAll=[]
CentroidsWavelengthAll=[]
DiffAll=[]
k = 2
while k < AllSheet.ncols:
```

```
#CentroidsInColumn[i] is the centroid of peak i
    CentroidsChannelInColumn = []
    CentroidsWavelengthInColumn = []
    for j in range(0, len(MidCh)):
        NominChannel = 0
        NominWavelength = 0
        Denomin = 0
        for i in range(int(LowCh[j]), int(HighCh[j])+1):
            NominChannel += Spectrum[0][i+2]*Spectrum[k][i+2]
            NominWavelength += Spectrum[1][i+2]*Spectrum[k][i+2]
            Denomin += Spectrum[k][i+2]
            #print Spectrum[1][i+2]
        PeakjCentroidCh = NominChannel/Denomin
        PeakjCentroidW = NominWavelength/Denomin
        CentroidsChannelInColumn.append(PeakjCentroidCh)
        CentroidsWavelengthInColumn.append(PeakjCentroidW)

#CentroidsAll[k] is a list of the centroids of all peaks in column k
#CentroidsAll[k][i] is the centroid of peak i in column k (starts with
column 0 and peak 0)
    CentroidsAll.append(CentroidsChannelInColumn)
    CentroidsWavelengthAll.append(CentroidsWavelengthInColumn)

#Diff[i] is the difference in channels between the centroid of peak i and
MidCh[i]
    Diff=[]
    for i in range(0,len(MidCh)):
        Diffi = int(MidCh[i] - CentroidsChannelInColumn[i])
        Diff.append(Diffi)

#DiffAll[k] is the difference of all peaks in column k
#DiffAll[k][i] is the difference of peak i in column k  (starts with
column 0 and peak 0)
    DiffAll.append(Diff)
    k+=1

# Output into file the centroid positions of all the peaks in nm.
# The first column is the isotope, the second is the file number,
followed by centroids of the peaks
file = open('C:\Isotope
shift\Final_try\WavelengthCentroids_alldata.txt','w')

for k in range(0,AllSheet.ncols-2):
    Isotope=int(str(Spectrum[k+2][0])[0:3])
    SpectrumNumber=int(str(Spectrum[k+2][1])[3:6])
    Centroids=''
    for i in range(0,len(MidCh)):
        Centroids+=' '+str(CentroidsWavelengthAll[k][i])
    file.write(str(Isotope)+' '+str(SpectrumNumber)+Centroids+'\n')

file.close()

# Output into file the centroid positions of all the peaks in channels.
```

```
# The first column is the isotope, the second is the file number,
followed by centroids of the peaks
file = open('C:\Isotope
shift\Final_try\ChannelCentroids_alldata.txt','w')

for k in range(0,AllSheet.ncols-2):
    Isotope=int(str(Spectrum[k+2][0])[0:3])
    SpectrumNumber=int(str(Spectrum[k+2][1])[3:6])
    Centroids=''
    for i in range(0,len(MidCh)):
        Centroids+=' '+str(CentroidsAll[k][i])
    file.write(str(Isotope)+' '+str(SpectrumNumber)+Centroids+'\n')

file.close()
```

 # Compute the centroid using the Gaussian fit.

```
import xlrd
import numpy as np
import pylab as plt
from math import sqrt, exp
from scipy.optimize import curve_fit

def gaussian(x, a, b, c):
    what1234 = a * np.exp(-(x - b)**2 /(2*c**2))
    return what1234

# This excel file contains the list of lines and ranges
Peaks = xlrd.open_workbook('C:\Isotope shift\Final_try\data_try_1.xlsx')
Sheet = Peaks.sheet_by_index(0)

# Loading the lower and higher limits. MidCh is the estimated line
position.

BlockSize=7

#Mean = []

no_extracol=1
no_extrarow=1

for k in range(no_extracol+1,(Sheet.ncols)):
    rn=0
    for l in range(0,(Sheet.nrows)/BlockSize):

        x=[]
        y=[]
        for i in range(no_extrarow+rn*BlockSize,
no_extrarow+(rn+1)*BlockSize-1):
            x.append(Sheet.cell(i,0+no_extracol).value)
            #print x
            y.append(Sheet.cell(i,k).value)

        mn=np.mean(x)
        sigma=np.std(x)
        #print mn
        popt, pcov = curve_fit(gaussian, x, y, p0 = [1,mn,sigma])
        print popt[1]
        #print popt
        plt.figure
        plt.plot(x,y,'r', label='data')
        plt.plot(x,gaussian(x, *popt),label='fit')
        plt.show()
        rn=rn+1
        #print rn
```

#Compute the shift (Xe-124 – Xe-136) using the residual binned distribution.

```
import xlrd
import numpy as np
from math import sqrt, exp
from scipy.optimize import curve_fit


def gaussian(x, a, b, c):
    gau = a * np.exp(-(x - b)**2 / (2*c**2))
    return gau


def simpTkwy(spec, l1 , z, p, peakval):
    '''
This function takes the centroid values of a peak in each spectrum and
subtracts a polynomial fit over them.
    spec = list with spec numbers,
    l1 = list with centroids,
    z = list of polyfit coefficients,
    p = polyfit order
    returns with newList = list of the subtracted values
    '''
    x = 0
    r = p
    newList = []
    while x < len(spec):
      specs = spec[x]
      result1 = 0
      y, p = 0, r
      while p >=0:
            result1 += z[y]*pow(specs, p)
            p -= 1
            y +=1
      newList.append(l1[x] - result1+peakval)
      x += 1
#newList includes the differences between the fit values and the
centroids
    return newList

def getStanDev(avg, alist):
    '''
This function calculates the standard devidation of the data from the
average value.
    avg = average
    alist = list for which deviation should be calculated
    '''
    difference = []
    deviation = 0
    devi=0

    for i in alist:
      difference.append(i-avg)
```

```
    for i in difference:
        devi += i**2
    deviation = sqrt(devi)/(len(alist)-1)
    return deviation

def getRes(avg, alist):
    '''
This function calculates the differences from the average and creates a
list with these.
    avg = average
    alist = list for which deviation should be calculated
    '''
    residual = []
    for i in alist:
      residual.append(i-avg)
    return residual

def getData(x): #fills up all the needed lists

      bothLowThird = [] #136 and 124 in low third
      bothMiddleThird = [] #136 and 124 in middle third
      bothHighThird = [] #136 and 124 in high third
      bothLowThirdX = [] #spec number of 136 and 124 in low third
      bothMiddleThirdX = [] #spec number of 136 and 124 in middle third
      bothHighThirdX = [] #spec number of 136 and 124 in high third

      threeLowThird = [] #136 in low third
      threeMiddleThird = [] #136 in middle third
      threeHighThird = [] #136 in high third
      threeLowThirdX = [] #spec number of 136 in low third
      threeMiddleThirdX = [] #spec number of 136 in middle third
      threeHighThirdX = [] #spec number of 136 in high third

      twoLowThird = [] #124 in low third
      twoMiddleThird = [] #124 in middle third
      twoHighThird = [] #124 in high third
      twoLowThirdX = [] #spec number of 124 in middle third
      twoMiddleThirdX = [] #spec number of 124 in high third
      twoHighThirdX = [] #spec number of 124 in middle third

# loop through the excel file reading in all lists
      for row in range(first.nrows):
            #check if spec is an exception
            if first.cell(row, 1).value in exception:
                  continue
            #if spec is in the lower third
            if first.cell(row, 1).value < 120:
                  #if spec is in lower third and is 136
                  if first.cell(row, 0).value == 136:
                        threeLowThird.append(first.cell(row, x).value)
                        threeLowThirdX.append(first.cell(row, 1).value)
                  #if spec is in lower third and is 124 if in middle
                  if first.cell(row, 0).value == 124:
                        twoLowThird.append(first.cell(row, x).value)
```

```
                        twoLowThirdX.append(first.cell(row, 1).value)
                  #adds both 136 and 124 to list
                  bothLowThird.append(first.cell(row, x).value)
                  bothLowThirdX.append(first.cell(row, 1).value)
            elif first.cell(row, 1).value >= 121:
                  #if spec is in middle third
                  if first.cell(row, 1).value <437:
                        #if spec is in middle third and is 136
                        if first.cell(row, 0).value == 136:
                              threeMiddleThird.append(first.cell(row,
x).value)
                              threeMiddleThirdX.append(first.cell(row,
1).value)
                        #if spec is in middle third and is 124
                        if first.cell(row, 0).value == 124:
                              twoMiddleThird.append(first.cell(row,
x).value)
                              twoMiddleThirdX.append(first.cell(row,
1).value)
                        #adds both 136 and 124 to list if in middle
                        bothMiddleThird.append(first.cell(row, x).value)
                        bothMiddleThirdX.append(first.cell(row, 1).value)
                  #if spec is in high third
                  elif first.cell(row, 1).value >=438:
                        #if spec is in high third and is 136
                        if first.cell(row, 0).value == 136:
                              threeHighThird.append(first.cell(row,
x).value)
                              threeHighThirdX.append(first.cell(row,
1).value)
                        #if spec is in high third and is 124
                        if first.cell(row, 0).value == 124:
                              twoHighThird.append(first.cell(row,
x).value)
                              twoHighThirdX.append(first.cell(row,
1).value)
                        #adds both 136 and 124 to list if high
                        bothHighThirdX.append(first.cell(row, 1).value)
                        bothHighThird.append(first.cell(row, x).value)

      allX = []
      bothoX= [(bothLowThird, bothLowThirdX), (bothMiddleThird,
bothMiddleThirdX), (bothHighThird, bothHighThirdX)]
      twooX = [(twoLowThird, twoLowThirdX), (twoMiddleThird,
twoMiddleThirdX), (twoHighThird, twoHighThirdX)]
      threeoX= [(threeLowThird, threeLowThirdX), (threeMiddleThird,
threeMiddleThirdX), (threeHighThird, threeHighThirdX)]
      allX.append(bothoX)
      allX.append(twooX)
      allX.append(threeoX)
#returns 3d list
# The first index is the isotope (0=both, 1=124, 2=136), the second is
the region(0=low, 1=mid, 2=high), the third index (0=centroid, 1=spectrum
number)
```

```
      return allX

# These are the outlier spectra, that are excluded from the analysis
exception = [15, 284, 285, 286, 287, 288, 289, 290, 291, 292, 293, 294,
295, 296, 297, 298,
                348, 349, 350, 351, 352, 353, 354, 355, 356, 357, 358,
359, 360,
                438, 439, 440, 441, 442, 443, 444, 445, 446, 447]

peakbook = xlrd.open_workbook('C:\Isotope shift\Final_try\Lines.xlsx')
strongsheet = peakbook.sheet_by_index(0)
peakv=[]
for i in range(1,21):
    peakv.append(strongsheet.cell(i,13).value)

book = xlrd.open_workbook('C:\Isotope
shift\Final_try\WavelengthCentroids_7pixels_1.xlsx')
first = book.sheet_by_index(0)

oneTwoFourAll = []
oneThreeSixAll = []
oneTwoFourResAll=[]
oneThreeSixResAll=[]

# Order of the polynomial used to fit the centroids across the files
p = 3

# Looping through the different peaks
for col in range(2,22):
      oneTwoFourAverage = []
      oneThreeSixAverage = []
      oneTwoFourStanDev = []
      oneThreeSixStanDev = []
      oneTwoFourRes = []
      oneThreeSixRes = []
      oneTwoFour = []
      oneThreeSix = []
      x = getData(col) #x includes all data, first index is the isotope
(0=both, 1=124, 2=136), the second is the region(0=low, 1=mid, 2=high),
the third index (0=centroid, 1=spectrum number)
      region = 0
      while region < 3:
              #xx=x[0][region][1]
              #xy=x[0][region][0]
              #print xx
            z = np.polyfit(x[0][region][1], x[0][region][0], p) #polyfit
returns a list of coefficients for the different orders
            oneTwoFour.extend(simpTkwy(x[1][region][1],
x[1][region][0],z, p, peakv[col-2]))
            oneThreeSix.extend(simpTkwy(x[2][region][1], x[2][region][0],
z, p, peakv[col-2]))
            region += 1

      #print chi_squared_124
```

```
      oneTwoFourAverage.append(float(sum(oneTwoFour))/len(oneTwoFour))
      oneThreeSixAverage.append(float(sum(oneThreeSix))/len(oneThreeSix))
      oneTwoFourStanDev.append(getStanDev(float(sum(oneTwoFour))/len(oneT
woFour), oneTwoFour))
      oneThreeSixStanDev.append(getStanDev(float(sum(oneThreeSix))/len(on
eThreeSix), oneThreeSix))
#residual is calulcated with respect to the average of isotope 136
#
      oneTwoFourRes.append(getRes(float(sum(oneThreeSix))/len(oneThreeSix
), oneTwoFour))
#
      oneThreeSixRes.append(getRes(float(sum(oneThreeSix))/len(oneThreeSi
x), oneThreeSix))
#residual is calulcated with respect to the literature peak value
      oneTwoFourRes.append(getRes(peakv[col-2], oneTwoFour))
      oneThreeSixRes.append(getRes(peakv[col-2], oneThreeSix))


      #print 'fin', col
      oneTwoFourAll += zip(oneTwoFourAverage, oneTwoFourStanDev)
      oneThreeSixAll +=zip(oneThreeSixAverage, oneThreeSixStanDev)
      oneTwoFourResAll +=zip(oneTwoFourAverage, oneTwoFourRes)
        oneThreeSixResAll +=zip(oneThreeSixAverage, oneThreeSixRes)

file = open("residual124_7pixels.txt", "w")

#print>>file, '----------------------------------------'
#print >>file, 'Residuals 124:'
#print>>file, '----------------------------------------'

peakNo124=[]
for i in range(0,len(oneTwoFourResAll)):
    print>>file, i+1,
    peakNo124.append(i+1)
print>>file, ''
ave124=[]
for i in range(0,len(oneTwoFourResAll)):
    print>>file, oneTwoFourResAll[i][0],
    ave124.append(oneTwoFourResAll[i][0])
print>>file, ''
resi124=[]
for j in range(0,len(oneTwoFourResAll[0][1])):
    resipeak124=[]
    for i in range(0,len(oneTwoFourResAll)):
        # i is the peak number, j runs throught the spectra
        # oneTwoFourResAll[i][1][j] is the residual with respect to the
average
        print>>file, oneTwoFourResAll[i][1][j],
        resipeak124.append(oneTwoFourResAll[i][1][j])
    resi124.append(resipeak124)
    print>>file, ''

#checking standard deviation ...
#su=0
```

```
#for j in range(0,len(oneTwoFourResAll[0][1])):
#    su+=oneTwoFourResAll[0][1][j]**2
#print sqrt(su)/(len(oneTwoFourResAll[0][1])-1)

file.close()

file = open("residual136_7pixels.txt", "w")

#print>>file, '----------------------------------------'
#print >>file, 'Residuals 136:'
#print>>file, '----------------------------------------'
peakNo136=[]
for i in range(0,len(oneThreeSixResAll)):
    print>>file, i+1,
    peakNo136.append(i+1)
print>>file, ''
ave136=[]
for i in range(0,len(oneThreeSixResAll)):
    print>>file, oneThreeSixResAll[i][0],
    ave136.append(oneThreeSixResAll[i][0])
print>>file, ''
resi136=[]
for j in range(0,len(oneThreeSixResAll[0][1])):
    resipeak136=[]
    for i in range(0,len(oneThreeSixResAll)):
        # i is the peak number, j runs throught the spectra
        # oneThreeSixResAll[i][1][j] is the residual with respect to the
average
        print>>file, oneThreeSixResAll[i][1][j],
        resipeak136.append(oneThreeSixResAll[i][1][j])
    resi136.append(resipeak136)
    print>>file, ''

#checking standard deviation ...
#su=0
#for j in range(0,len(oneThreeSixResAll[0][1])):
#    su+=oneThreeSixResAll[0][1][j]**2
#print sqrt(su)/(len(oneThreeSixResAll[0][1])-1)

file.close()
binum=(-0.0045, -0.0042, -0.0039, -0.0036, -0.0033, -0.003, -0.0027, -
0.0024, -0.0021, -0.0018, -0.0015, -0.0012, -0.0009, -0.0006, -0.0003,
0.0, 0.0003, 0.0006, 0.0009, 0.0012, 0.0015, 0.0018, 0.0021, 0.0024,
0.0027, 0.003, 0.0033, 0.0036, 0.0039, 0.0042)
file = open("histogram_7pixels.txt", "w")
filebin = open("histogrambin_7pixels.txt", "w")

listofhistograms=[]
histogram136 = []
histogram136bin = []
for i in range(0, 20):
#    binum=(peakv[i]-0.0045, peakv[i]-0.0042, peakv[i]-0.0039, peakv[i]-
0.0036, peakv[i]-0.0033, peakv[i]-0.003, peakv[i]-0.0027, peakv[i]-
0.0024, peakv[i]-0.0021, peakv[i]-0.0018, peakv[i]-0.0015, peakv[i]-
```

```
0.0012, peakv[i]-0.0009, peakv[i]-0.0006, peakv[i]-0.0003, peakv[i]+0.0,
peakv[i]+0.0003, peakv[i]+0.0006, peakv[i]+0.0009, peakv[i]+0.0012,
peakv[i]+0.0015, peakv[i]+0.0018, peakv[i]+0.0021, peakv[i]+0.0024,
peakv[i]+0.0027, peakv[i]+0.003, peakv[i]+0.0033, peakv[i]+0.0036,
peakv[i]+0.0039, peakv[i]+0.0042, peakv[i]+0.0045, peakv[i]+0.0048)
      listofhistograms.append(np.histogram(oneThreeSixResAll[i][1],bins=b
inum,density=False))
for j in range(0, len(listofhistograms)):
      a = []
      b = []
      print>>file, str(j+1)+' -------- '+'136'+' -------- '+
'delta:'+str((ave124[j]-ave136[j])*1000)+ ' 136:'+str((ave136[j])*1000)+
' Peak:'+str((peakv[j])*1000)
      print>>filebin, str(j+1)+' -------- '+'136'+' -------- '+
'delta:'+str((ave124[j]-ave136[j])*1000)+ ' 136:'+str((ave136[j])*1000)+
' Peak:'+str((peakv[j])*1000)
      for i in range(0,len(listofhistograms[2][0])):
            a.append(listofhistograms[j][0][i])
            b.append((listofhistograms[j][1][i]+ave136[j])*1000)
            print>>filebin,
str((listofhistograms[j][1][i]+ave136[j])*1000)
            print>>file, listofhistograms[j][0][i]

      histogram136.append(a)
      histogram136bin.append(b)

#for i in range(20):
#     histogram124.append(listofhistograms[i][0])
#     histogram124bin.append(listofhistograms[i]+ave136[j])*1000)

#print histogram124
listofhistograms=[]
histogram124 = []
histogram124bin = []
for i in range(0, 20):
      listofhistograms.append(np.histogram(oneTwoFourResAll[i][1],bins=bi
num,density=False))
for j in range(0, len(listofhistograms)):
      a = []
      b = []
      print>>file, str(j+1)+' -------- '+'124'+' -------- '+
'delta:'+str((ave124[j]-ave136[j])*1000)+ ' 136:'+str((ave136[j])*1000)+
' Peak:'+str((peakv[j])*1000)
      print>>filebin, str(j+1)+' -------- '+'124'+' -------- '+
'delta:'+str((ave124[j]-ave136[j])*1000)+ ' 136:'+str((ave136[j])*1000)+
' Peak:'+str((peakv[j])*1000)
      for i in range(0,len(listofhistograms[2][0])):
            a.append(listofhistograms[j][0][i])
            b.append((listofhistograms[j][1][i]+ave136[j])*1000)
            print>>filebin,
str((listofhistograms[j][1][i]+ave124[j])*1000)#it prints different x
axis for 124.
            print>>file, listofhistograms[j][0][i]
```

```
      histogram124.append(a)
      histogram124bin.append(b)


file.close()

gaussXo124 = []
gaussW124 = [] #width

for i in range(20):
      y = histogram124[i]
      x = histogram124bin[i]
      popt, pcov = curve_fit(gaussian, x, y, p0 = [50,
histogram124bin[i][10], 1])
      gaussXo124.append(popt[1])
      gaussW124.append(popt[2])
        print popt[1], popt[2]

gaussXo136 = [] #235
gaussW136 = [] #width

for i in range(20):
      y = histogram136[i]
      x = histogram136bin[i]
      popt, pcov = curve_fit(gaussian, x, y, p0 = [50,
histogram136bin[i][10], 1])
      gaussXo136.append(popt[1])
      gaussW136.append(popt[2])
      print popt[1], popt[2]

deltaXo124 = []
deltaXo136 = []

for i in range(20):
      deltaXo124.append(gaussW124[i]/sqrt(189))
      deltaXo136.append(gaussW136[i]/sqrt(239))
#print deltaXo124
#print deltaXo136

shift = []
deltaShift = []
for i in range(20):
      shift.append(gaussXo124[i] - gaussXo136[i])
      deltaShift.append(sqrt(pow(deltaXo124[i],2 )+ pow(deltaXo136[i],
2)))

with open('shift_7pixels.txt', 'w') as f:
    for s in shift:
        f.write(str(s) + '\n')

with open('deltashift_7pixels.txt', 'w') as f:
    for s in deltaShift:
        f.write(str(s) + '\n')
```

#Compute the shift and uncertainty with a polynomial fit and a constant fitting.

```
import pandas as pd
from scipy import stats
from scipy.optimize import curve_fit
import matplotlib.pyplot as plt
import numpy as np
from lmfit import Model, Parameters, fit_report, minimize
%matplotlib inline

#Na-like D1 line in 1st order
df = pd.read_csv('Na_D1_1st.csv', delimiter=',', dtype=np.float64)
df.columns = ['sn','640', '641', '642', '643', '644', '645','646', '647',
'648']
df.head()

#Calculate centroid positions in channels
sum=df[['641']].squeeze()+df[['642']].squeeze()+df[['643']].squeeze()+df[
['644']].squeeze()+df[['645']].squeeze()+df[['646']].squeeze()+df[['647']
].squeeze()

cent=(df[['641']].squeeze()*12.3738+df[['642']].squeeze()*12.3822+df[['64
3']].squeeze()*12.3905+df[['644']].squeeze()*12.3988+df[['645']].squeeze(
)*12.4071+df[['646']].squeeze()*12.4154+df[['647']].squeeze()*12.4237)/su
m
sn=df[['sn']].squeeze()
plt.plot(sn, cent, linestyle='None', marker='o', color='y', markersize=6)

#Fit with 3rd order polynomial
df = pd.read_csv('Xe_regdata.csv', delimiter=',', dtype=np.float64)
df.columns = ['iso', 'sno', 'reg', 'x', 'NaD1 1st order', 'Mg 1st
order','NaD1 2nd over2', 'Mg 2nd over2']
df.head()

def poly3d(x, c30, c31, c32, c20, c21, c22, c10, c11, c12, c00, c01, c02,
s):
    sel04=1*((x>0)&(x<1000))
    sel14=1*((x>1000)&(x<2000))
    sel24=1*((x>2000)&(x<3000))
    sel06=1*((x>5000)&(x<6000))
    sel16=1*((x>6000)&(x<7000))
    sel26=1*((x>7000)&(x<8000))
    freg0iso124=c30*sel04*x**3+c20*sel04*x**2+c10*sel04*x+c00*sel04
    freg0iso136=c30*sel06*(x-5000)**3+c20*sel06*(x-5000)**2+c10*sel06*(x-
5000)+c00*sel06+s*sel06
    freg1iso124=c31*sel14*(x-1000)**3+c21*sel14*(x-1000)**2+c11*sel14*(x-
1000)+c01*sel14
    freg1iso136=c31*sel16*(x-6000)**3+c21*sel16*(x-6000)**2+c11*sel16*(x-
6000)+c01*sel16+s*sel16
    freg2iso124=c32*sel24*(x-2000)**3+c22*sel24*(x-2000)**2+c12*sel24*(x-
2000)+c02*sel24
    freg2iso136=c32*sel26*(x-7000)**3+c22*sel26*(x-7000)**2+c12*sel26*(x-
7000)+c02*sel26+s*sel26
```

```
fun=freg0iso124+freg0iso136+freg1iso124+freg1iso136+freg2iso124+freg2iso1
36
    return fun


model = Model(poly3d, independent_vars=['x'])

params = model.make_params()
#params['c40'].value = -2.28e-12
#params['c41'].value = 1.22e-13
#params['c42'].value = 1.57e-12
params['c30'].value = -2.28e-09
params['c31'].value = 1.22e-10
params['c32'].value = 1.57e-08
params['c20'].value = 5.59e-07
params['c21'].value = -1.21e-07
params['c22'].value = -1.06e-05
params['c10'].value = -2.19e-05
params['c11'].value = 3.54e-05
params['c12'].value = 0.010203
params['c00'].value = 12.395
params['c01'].value = 12.397
params['c02'].value = 12.4
params['s'].value = 3e-5

fx = df[['x']].squeeze()
fdata = cent
#Regions to exclude
a = list(range(0,14))
a.append(11)
a.append(106)
a.extend(range(414,428))

x=fx.drop(fx.index[a])
data=fdata.drop(fdata.index[a])

result = model.fit(data, params, x=x, nan_policy='omit')
result.params
fitfunc = result.best_fit

plt.figure(1)
plt.plot(x, data, linestyle='None', marker='o', color='b', markersize=6)
plt.plot(x-5000, data, linestyle='None', marker='o', color='b',
markersize=6)
plt.plot(x, fitfunc, linestyle='None', marker='o', color='r',
markersize=2)
plt.plot(x-5000, fitfunc, linestyle='None', marker='o', color='r',
markersize=2)
plt.xlim(18, 120)
#plt.ylim(12.394,12.397)
plt.ylim(12.3945,12.3975)

plt.figure(2)
```

```
plt.plot(x, data, linestyle='None', marker='o', color='y', markersize=6)
plt.plot(x, fitfunc, linestyle='None', marker='o', color='r',
markersize=2)
plt.plot(x-5000, data, linestyle='None', marker='o', color='c',
markersize=6)
plt.plot(x-5000, fitfunc, linestyle='None', marker='o', color='b',
markersize=2)
plt.xlim(1115, 1445)
#plt.ylim(12.395,12.397)
plt.ylim(12.3945,12.4005)

plt.figure(3)
plt.plot(x, data, linestyle='None', marker='o', color='y', markersize=6)
plt.plot(x, fitfunc, linestyle='None', marker='o', color='r',
markersize=2)
plt.plot(x-5000, data, linestyle='None', marker='o', color='c',
markersize=6)
plt.plot(x-5000, fitfunc, linestyle='None', marker='o', color='b',
markersize=2)
plt.xlim(2448, 2493)
#plt.ylim(12.398,12.400)
plt.ylim(12.3945,12.4005)

shift=result.params['s'].value

print(fit_report(result))

ls=np.linspace(-0.001,0.001, num=15)

xdr=pd.DataFrame({'x':x, 'd':data, 'r':fitfunc})
xdr.loc[ xdr['x'] < 5000, ['d'] ] = np.nan
res4=xdr['d']-xdr['r']
bin_counts4, bin_edges, binnumber = stats.binned_statistic(res4, ls,
statistic='count', bins=ls)

xdr=pd.DataFrame({'x':x, 'd':data, 'r':fitfunc})
xdr.loc[ xdr['x'] > 5000, ['d'] ] = np.nan
res6=xdr['d']-xdr['r']
bin_counts6, bin_edges, binnumber = stats.binned_statistic(res6, ls,
statistic='count', bins=ls)

bin_width = (bin_edges[1] - bin_edges[0])
bin_centers = bin_edges[1:] - bin_width/2

def gaussian(x, amp, cen, wid):
    return (amp / (np.sqrt(2*np.pi) * wid)) * np.exp(-(x-cen)**2 /
(2*wid**2))

gmodel = Model(gaussian, independent_vars=['x'])

gparams = gmodel.make_params()
gparams['amp'].value = 15
gparams['cen'].value = 0
gparams['wid'].value = 0.0005
```

```
fls=np.linspace(-0.001,0.001, num=150)
result4 = gmodel.fit(bin_counts4, gparams, x=bin_centers)
fitgauss4 = gaussian(fls, result4.params['amp'].value,
result4.params['cen'].value,result4.params['wid'].value)
result6 = gmodel.fit(bin_counts6, gparams, x=bin_centers)
fitgauss6 = gaussian(fls, result6.params['amp'].value,
result6.params['cen'].value,result6.params['wid'].value)

plt.figure(4)
plt.plot(bin_centers, bin_counts4, linestyle='None', marker='o',
color='r', markersize=6)
plt.plot(fls, fitgauss4, linestyle='dashed', marker='None', color='r',
markersize=6)
plt.plot(bin_centers, bin_counts6, linestyle='None', marker='o',
color='b', markersize=6)
plt.plot(fls, fitgauss6, linestyle='dashed', marker='None', color='b',
markersize=6)
plt.xlim(-0.001,0.001)
plt.ticklabel_format(style='sci', axis='x', scilimits=(0,3))

centdiff=result6.params['cen'].value-result4.params['cen'].value

print(fit_report(result4))
print(fit_report(result6))
centdiff
```

Bibliography

[AJP+92] E. Avgoustoglou, W. R. Johnson, D. R. Plante, J. Sapirstein, and S. Sheinerman. Many-body perturbation-theory formulas for energy levels of excited states of closed-. *Physical Review Letters*, 46(9):5478–5488, 1992.

[AK16] K. M. Aggarwal and F. P. Keenan. Radiative rates for E1, E2, M1, and M2 transitions in F-like ions with 37Z53. *Atomic Data and Nuclear Data Tables*, 109-110:205–338, 2016.

[AM13] I. Angeli and K. P. Marinova. Table of experimental nuclear ground state charge radii: An update. *Atomic Data and Nuclear Data Tables*, 99(1):69–95, 2013.

[Ang04] I. Angeli. A consistent set of nuclear rms charge radii: Properties of the radius surface R(N,Z). *Atomic Data and Nuclear Data Tables*, 87(2):185–193, 2004.

[ASD] https://physics.nist.gov/cgi-bin/ASD/lines_pt.pl.

[BAN+89] W. Borchers, E. Arnold, W. Neu, R. Neugart, K. Wendt, and G. Ulm. Xenon isotopes far from stability studied by collisional ionization laser spectroscopy. *Physics Letters B*, 216(1-2):7–10, 1989.

[BBH65] R. T. Brockmeier, F. Boehm, and E. N. Hatch. Observation of the isotope shift of K alpha1 X rays of Uranium. *Physical Review Letters*, 15(4), 1965.

[BBP+87] S. A. Blundell, P. E. G. Baird, C. W.P. Palmer, D. N. Stacey, and G. K. Woodgate. A reformulation of the theory of field isotope shift in atoms. *Journal of Physics B: Atomic and Molecular Physics*, 20:3663–3681, 1987.

[BBR+86] W. E. Behring, C. M. Brown, J. Reader, M. C. Richardson, U. Feldman, and J. F. Seely. Transitions of the type 2s2p in oxygenlike Y, Zr, and Nb. *Journal of the Optical Society of America B*, 3(8):1113, 1986.

[Bei09] P Beiersdorfer. Precision energy-level measurements and QED of highly charged ions. *Canadian Journal of Physics*, 87(1):9–14, 2009.

[BKM+09] C. Brandau, C. Kozhuharov, A. Müller, D. Bernhardt, S. Böhm, F. J. Bosch, D. Boutin, J. Currell, C. Dimopoulou, B. Franzke, A. Gumberidze, Z. Harman, U. D. Jentschura, C. H. Keitel, H. J. Kluge, S. Kozhedub, R. Krücken, Yu A Litvinov, F. Nolden, B. O'Rourke, R. Reuschl, S. Schippers, M. Shabaev,

U. Spillmann, Z. Stachura, M. Steck, Th Stöhlker, I. I. Tupitsyn, D. F.A. Winters, and A. Wolf. Isotope shifts in dielectronic recombination: From stable to in-flight-produced nuclei. *Journal of Physics: Conference Series*, 194, 2009.

[BLF+05] B. Blagojević, E. O. Le Bigot, K. Fahy, A. Aguilar, K. Makonyi, E. Takács, J. N. Tan, J. M. Pomeroy, J. H. Burnett, J. D. Gillaspy, and J. R. Roberts. A high efficiency ultrahigh vacuum compatible flat field spectrometer for extreme ultraviolet wavelengths. *Review of Scientific Instruments*, 76(8):1–6, 2005.

[Blu93] S. A. Blundell. Calculations of the screened self-energy and vacuum polarization in Li-like, Na-like, and Cu-like ions. *Physical Review A*, 47(3):1790–1803, 1993.

[BOS+98] P. Beiersdorfer, A. L. Osterheld, J. H. Scofield, J. R. Crespo López-Urrutia, and K. Widmann. Measurement of QED and Hyperfine Splitting in the 2s12 - 2p32 X-Ray Transition in Li-like 209Bi80+. *Physical Review Letters*, 80(14), 1998.

[BR09] C. Biedermann and R. Radtke. Spectroscopy of highly charged tungsten relevant to fusion plasmas. *AIP Conference Proceedings*, 1125:107–112, 2009.

[BS03] H.F Beyer and V .P. Shevelko. *Introduction to the Physics of Highly Charged Ions*. CRC Press, 2003.

[CBSW96] J. R. Crespo López-Urrutia, P. Beiersdorfer, D. W. Savin, and K. Widmann. Direct observation of the spontaneous emission of the hyperfine transition f=4 to f=3 in ground state hydrogenlike 165ho66+ in an electron beam ion trap. *Physical Review Letters*, 77(5):826–829, 1996.

[Cow81] R. D Cowan. *The Theory of Atomic Structure and Spectra*. University of California Press, 1981.

[CRTBW02] S. S. Churilov, A. N. Ryabtsev, W-Ü. L. Tchang-Brillet, and J. F. Wyart. Analysis of the Spectra of Pd-like Ions from Xe IX Through Ce XIII. *Physica Scripta*, 66(4):293–307, 2002.

[DMJ89] B. Denne, G. Magyar, and J. Jacquinot. Berylliumlike Mo XXXIX and lithiumlike Mo XL observed in the Joint European Torus tokamak. *Physical Review A*, 40(7), 1989.

[Don83] E. D. Donets. The Electron Beam Method of Production of Highly Charged Ions and Its Applications. *Physica Scripta*, T3:11–18, 1983.

[EBC96] S. R. Elliott, P. Beiersdorfer, and M. H. Chen. Trapped-ion technique for measuring the nuclear charge radii of highly charged radioactive isotopes. *Physical Review Letters*, 76(7):1031–1034, 1996.

[EFSB89] J. O. Ekberg, U. Feldman, J. F. Seely, and C. M. Brown. Transitions and Energy Levels in Mg-like Ge XXI-Zr XXIX Observed in Laser-Produced Linear Plasmas. *Physica Scripta*, 40:643–651, 1989.

[FBH+95] G. Fricke, C. Bernhardt, K. Heilig, L. A. Schaller, L. Schellenberg, E. B. Shera, and C. W. Dejager. Nuclear Ground-State Charge Radii From Electromagnetic-Interactions, 1995.

[FHKS74] W. Fischer, H.. Hühnermann, G. J Krömer, and H.J Schäfer. Isotope shifts in the atomic spectrum of xenon and nuclear deformation effects. *Zeitschrift für Physik*, 270(2):113–120, 1974.

[Foo05] Christopher J Foot. Atomic Physics. *Oxford University Press, U.S.A.*, pages 1–331, 2005.

[FR53] V. L. Fitch and J. Rainwater. Studies of X-rays from Mu-mesonic atoms. *Physical Review*, 92(3):789–800, 1953.

[FSO+07] K. Fahy, E. Sokell, G. O'Sullivan, A. Aguilar, J. M. Pomeroy, J. N. Tan, and J. D. Gillaspy. Extreme-ultraviolet spectroscopy of highly charged xenon ions created using an electron-beam ion trap. *Physical Review A - Atomic, Molecular, and Optical Physics*, 75(3), 2007.

[Gal17] A. C. Gall. *Investigation of the contribution of lower charger state Ar ions to the unknown faint x-ray feature found in the stacked spectrum of galaxy clusters*. PhD thesis, Clemson University, 2017.

[GDR+09] J. D. Gillaspy, I. N. Draganić, Yu Ralchenko, J. Reader, J. N. Tan, J. M. Pomeroy, and S. M. Brewer. Measurement of the D -line doublet in high- Z highly charged sodiumlike ions. *Physical Review A - Atomic, Molecular, and Optical Physics*, 80(1):1–4, 2009.

[Gil99] J. D. Gillaspy. *Trapping Highly Charged Ions: Fundamentals and Applications*. NOVA Science Publishers, Inc., Huntington, NY, USA, 1999.

[Gil01] J. D. Gillaspy. Highly Charged Ions. *J. Phys. B: At., Mol. Opt. Phys.*, 34:R93–R130, 2001.

[Gil10] J. D. Gillaspy. Testing QED in sodium-like gold and xenon: Using atomic spectroscopy and an EBIT to probe the quantum vacuum. *Journal of Instrumentation*, 5(10), 2010.

[GMR85] W. Greiner, R. Muller, and J. Rafelski. *Quantum Electrodynamics of Strong Fields: With an Introduction into Modern Relativistic Quantum Mechanics*. Springer-Verfag, 1985.

[GOR+13] J. D. Gillaspy, D. Osin, Yu Ralchenko, J. Reader, and S. A. Blundell. Transition energies of the D lines in Na-like ions. *Physical Review A - Atomic, Molecular, and Optical Physics*, 87(6):1–13, 2013.

[Gri97] H.R Griem. *Principles of Plasma Spectroscopy*. Cambridge University Press, Cambridge, 1997.

[Gu08] M.F. Gu. The flexible atomic code. *Canadian Journal of Physics*, 86(5):675–689, 2008.

[HBC+86] E. Hinnov, F. Boody, S. Cohen, U. Feldman, J. Hosea, K. Sato, J. L. Schwob, S. Suckewer, and A. Wouters. Spectrum lines of highly ionized zinc, germanium, selenium, zirconium, molybdenum, and silver injected into Princeton Large Torus and Tokamak Fusion Test Reactor tokamak discharges. *Journal of the Optical Society of America B*, 3(10):1288, 1986.

[HBS+05] G. E. Holland, C. N. Boyer, J. F. Seely, J. N. Tan, J. M. Pomeroy, and J. D. Gillaspy. Low jitter metal vapor vacuum arc ion source for electron beam ion trap injections. *Review of Scientific Instruments*, 76(7), 2005.

[HE30] D. S. Hughes and C. Eckart. The effect of the motion of the nucleus on the spectra of Li I and Li II. *Physical Review*, 36, 1930.

[Her58] Gabriel Herrmann. Optical theory of thermal velocity effects in cylindrical electron beams. *Journal of Applied Physics*, 29(2):127–136, 1958.

[Hin76] E. Hinnov. Highly ionized atoms in tokamak discharges. *Physical Review A*, 14(4):1533–1541, 1976.

[HK80] Tatsuo Harada and Toshiaki Kita. Mchanically ruled aberration-corrected concave gratings. *Applied Optics*, 19(23):3987–3993, 1980.

[Hof56] R. Hofstadter. Electron scattering and nuclear structure. *Reviews of Modern Physics*, 28(3):214–254, 1956.

[HT10] I.G. Hughes and P. A. Thomas. *Measurements and their Uncertainties, A Practical Guide to Modern Error Analysis*. Oxford University Press Inc., New York, NY, USA, 2010.

[JAG13] P Jönsson, A Alkauskas, and G Gaigalas. Energies and E1, M1, E2 transition rates for states of the 2s22p5 and 2s2p6 configurations in fluorine-like ions between Si VI and W LXVI. *Atomic Data and Nuclear Data Tables*, 99(4):431–446, 2013.

[JBS88a] W. R. Johnson, S. A. Blundell, and J. Sapirstein. Many-body perturbation-theory calculations of energy levels along the lithium isoelectronic sequence. *Physical Review A*, 37(8):2764–2777, 1988.

[JBS88b] W. R. Johnson, S. A. Blundell, and J. Sapirstein. Many-body perturbation-theory calculations of energy levels along the sodium isoelectronic sequence. *Physical Review A*, 38(6):2699–2706, 1988.

[JGR+17] P. Jönsson, G. Gaigalas, P. Rynkun, L. Radžit, J. Ekman, S. Gustafsson, H. Hartman, K. Wang, M. Godefroid, C. Froesce Fischer, I. Grant, T. Brage, and G. D. Zanna. Multiconfiguration Dirac-Hartree-Fock Calculations with Spectroscopic Accuracy: Applications to Astrophysics. *Atoms*, 5(2):16, 2017.

[JHFG07] P. Jönsson, X. He, C. Froese Fischer, and I. P. Grant. The grasp2K relativistic atomic structure package. *Computer Physics Communications*, 177:597–622, 2007.

[JMD90] C. Jupén, I. Martinson, and B. Denne. Transitions in Al-like, Mg-like and Na-like Kr and Mo, observed in the JET Tokamak. *Physica Scripta*, 41(5):669–674, 1990.

[Joh31] H H Johann. Die Erzeugung lichtstarker Röntgenspektren mit Hilfe von Konkavkristallen. *Zeitschrift für Physik*, 69(3):185–206, may 1931.

[JS85] W. R. Johnson and G. Soff. The lamb shift in hydrogen-like atoms, 1 Z 110. *Atomic Data and Nuclear Data Tables*, 33(3):405–446, 1985.

[Jun01] K. P. Jungmann. Muon Physics Possibilities at a Muon-Neutrino Factory. *Hyperfine Interactions*, 138(1):463–473, dec 2001.

[KBI91] Y.-K. Kim, D. H. Baik, and P. Indelicato. Resonance transition energies of Li-, Na-, and Cu-like ions Y.-K. *Physical Review A*, 44(1), 1991.

[KGA+16] I. Khatri, A. Goyal, S. Aggarwal, A. K. Singh, and M. Mohan. Extreme ultraviolet and x-ray transition wavelengths in Rb XXIV. *Chinese Physics B*, 25(3), 2016.

[KHNK83] T. Kita, T. Harada, N. Nakano, and H. Kuroda. Mechanically ruled aberration-corrected concave gratings for a flat-field grazing-incidence spectrograph. *Applied Optics*, 22(4), 1983.

[Kin63] W. H. King. Comments on the Article Peculiarities of the Isotope Shift in the Samarium Spectrum. *Journal of the Optical Society of America*, 53(5):638, 1963.

[KRRN18] A. Kramida, Yu. Ralchenko, J. Reader, and NIST ASD Team. No Title, 2018.

[Kun09] H. J. Kunze. *Introduction to Plasma Spectroscopy*. Springer, New York, NY, USA, 2009.

[KVA+10] Y. S. Kozhedub, A. V. Volotka, A. N. Artemyev, D. A. Glazov, G. Plunien, V. M. Shabaev, I. I. Tupitsyn, and Th Stöhlker. Relativistic recoil, electron-correlation, and QED effects on the 2pj-2s transition energies in Li-like ions. *Physical Review A - Atomic, Molecular, and Optical Physics*, 81(4):1–15, 2010.

[LMH+88] M. A. Levine, R. E. Marrs, J. R. Henderson, D. A. Knapp, and M. B. Schneider. The Electron Beam Ion Trap: A New Instrument for Atomic Physics Measurements. *Phys. Scr.*, T22:157–163, 1988.

[LNG+12] J. Li, C. Nazé, M. Godefroid, S. Fritzsche, G. Gaigalas, P. Indelicato, and P. Jönsson. Mass- and field-shift isotope parameters for the 2s-2p resonance doublet of lithiumlike ions. *Physical Review A - Atomic, Molecular, and Optical Physics*, 86(2):1–7, 2012.

[LRS07] J. Libert, B. Roussière, and J. Sauvage. Signs of dynamical effects for Cd, Sn, Te, Xe, Ba and Sm nuclear charge radii. *Nuclear Physics A*, 786(1-4):47–70, 2007.

[MHR+85] D. L. Matthews, P. L. Hagelstein, M. D. Rosen, M. J. Eckart, N. M. Ceglio, A. U. Hazi, H. Medecki, B. J. MacGowan, J. E. Trebes, B. L. Whitten, E. M. Campbell, C. W. Hatcher, A. M. Hawryluk, R. L. Kauffman, L. D. Pleasance, G. Rambach, J. H. Scofield, G. Stone, and T. A. Weaver. Demonstration of a soft x-ray amplifier. *Physical Review Letters*, 54(2):110–113, 1985.

[MJM+94] R Myrnäs, C Jupén, G Miecznik, I Martinson, and B Denne-Hinnov. Transitions in boronlike Ni XXIV, Ge XXVIII, Kr XXXII and Mo XXXVIII and fluorinelike Zr XXXII and Mo XXXIV, observed in the JET tokamak. *Physica Scripta*, 49(4):429–435, 1994.

[opt] https://en.wikipedia.org/wiki/Optical_spectrometer.

[ORGR12] D Osin, J Reader, J D Gillaspy, and Yu Ralchenko. Extreme ultraviolet spectra of highly charged xenon observed with an electron beam ion trap. *Journal of Physics B: Atomic, Molecular and Optical Physics*, 45(24), 2012.

[Ost74] D.E. Osterbrock. *Astrophysics of Gaseous Nebulae*. W.H. Freeman and Co, 1974.

[Pal87] C. W.P. Palmer. Reformulation of the theory of the mass shift. *Journal of Physics B: Atomic and Molecular Physics*, 20(22):5987–5996, 1987.

[Pál10] Adriana Pálffy. Nuclear effects in atomic transitions. *Contemporary Physics*, 51(6):471–496, 2010.

[PGRR14] Y. A. Podpaly, J. D. Gillaspy, J. Reader, and Yu Ralchenko. EUV measurements of Kr XXI-Kr XXXIV and the effect of a magnetic-dipole line on allowed transitions. *Journal of Physics B: Atomic, Molecular and Optical Physics*, 47(9), 2014.

[PKG00] J. V. Porto, I. Kink, and J. D. Gillaspy. Direct imaging of highly charged ions in an electron beam ion trap. *Review of Scientific Instruments*, 71(8):3050–3058, 2000.

[Ral16] Yu. Ralchenko. *Modern Methods in Collisional-Radiative Modeling of Plamsas, Springer Series on Atomic, Optical and Plasma Physics*. Springer Series on Atomic, Optical and Plasma Physics, 2016.

[Ral17] Yu. Ralchenko. Atomic Structure: 2017 Joint ICTP-IAEA School on Atomic Processes in Plasmas, 2017.

[RC93] A. Redfors and C. R. Cowley. Elemental abundances of yttrium and zirconium in the mercury-manganese stars phi-Herculis, kappa-Cancri and iota-Coronae Borealis. *Astron. Astrophys.*, 271:273–275, 1993.

[RDO+11] Yu Ralchenko, I N Draganić, D Osin, J D Gillaspy, and J Reader. Spectroscopy of diagnostically important magnetic-dipole lines in highly charged 3dn ions of tungsten. *Physical Review A - Atomic, Molecular, and Optical Physics*, 83(3), 2011.

[RDT+08] Yu Ralchenko, I. N. Draganic, J. N. Tan, J. D. Gillaspy, J. M. Pomeroy, J. Reader, U. Feldman, and G. E. Holland. EUV spectra of highly-charged ions W54+-W63+ relevant to ITER diagnostics. *Journal of Physics B: Atomic, Molecular and Optical Physics*, 41(2), 2008.

[Rea82] J. Reader. 2s22p5 – 2s2p6 transitions in the flourinelike ions Sr29+ and Y30+. *Physical Review A*, 26(1), 1982.

[RKS+87] Joseph Reader, Victor Kaufman, Jack Sugar, Jan Olof Ekberg, U Feldman, C M Brown, J F Seely, W L Rowan, Joseph Reader, W L Rowan, Victor Kaufman, U Feldman, C M Brown, Jack Sugar, and J F Seely. 3S3P, 3P3D, and 3D4F Transitions of Sodiumlike Ions. *Journal of the Optical Society of America B*, 4(11):1821, 1987.

[RM01] Yu. Ralchenko and Y. Maron. Accelerated recombination due to resonant deexcitation of metastable states. *Journal of Quantitative Spectroscopy & Radiative Transfer*, 71:609–621, 2001.

[RR99] L P. Ratliff and J R. Roberts. Highly Charged Ion Studies at the NIST EBIT. NOVA Science Publishers, Inc., Huntington, NY, USA, 1999.

[RRP+07] Yu Ralchenko, J. Reader, J. M. Pomeroy, J. N. Tan, and J. D. Gillaspy. Spectra of W39+-W47+ in the 12-20 nm region observed with an EBIT light source. *Journal of Physics B: Atomic, Molecular and Optical Physics*, 40(19):3861–3875, 2007.

[SAB+94] V M Shabaev, A N Artemyev, T Beier, G Plunien, V A Yerokhin, and G So. Relativistic Nuclear Recoil Corrections to the Energy Levels of Hydrogenlike Ions Relativistic Nuclear Recoil Corrections to the Energy Levels of Hydrogenlike Ions. *Journal of Physics B: Atomic, Molecular and Optical Physics*, 27:1307, 1994.

[SC08] J. Sapirstein and K. T. Cheng. Tests of quantum electrodynamics with EBIT. *Canadian Journal of Physics*, 86(1):25–31, 2008.

[SC11] J. Sapirstein and K. T. Cheng. S-matrix calculations of energy levels of the lithium isoelectronic sequence. *Physical Review A - Atomic, Molecular, and Optical Physics*, 83(1):1–15, 2011.

[SCS05] U. I. Safronova, T. E. Cowan, and M. S. Safronova. Relativistic many-body calculations of electric-dipole lifetimes, transition rates and oscillator strengths for 2l-13l states in Ne-like ions. *Journal of Physics B: Atomic, Molecular and Optical Physics*, 38(15):2741–2763, 2005.

[SCW+92] G.M. Shimkaveg, M.R. Carter, R.S. Walling, J.M. Ticehurst, J.A. Koch, S. Mrowka, J.E. Trebes, B.J. MacGowan, L.B. Da Silva, D.L. Matthews, R.A. London, , and R.E. Stewart. The x-ray laser coherence experiments in neon-like yttrium. In *Proceedings of the International Conference on Lasers*, pages 84–92, 1992.

[sel] https://en.wikipedia.org/wiki/Selection_rule.

[SHC+82] S. Suckewer, E. Hinnov, S. Cohen, M. Finkenthal, and K. Sato. Identification of magnetic dipole lines above 2000 A in several highly ionized Mo and Zr ions on the PLT tokamak. *Physical Review A*, 26(2), 1982.

[SKIR89] J. Sugar, V Kaufman, P. Indelicato, and W. L. Rowan. Analysis of magnesiumlike spectra from Mo XXXI to Cs XLIV. *J. Opt. Soc. Am. B*, 6(8), 1989.

[SLM+05] R. Schuch, E. Lindroth, S. Madzunkov, M. Fogle, T. Mohamed, and P. Indelicato. Dielectronic resonance method for measuring isotope shifts. *Physical Review Letters*, 95(18):1–4, 2005.

[SSR+18] S.C. Sanders, R. Silwal, B.H. Rudramadevi, A.C. Gall, and E. Takacs. High-resolution x-ray spectroscopy of highly charged tungsten plasma a potential, fusion-device diagnostic tool (submitted to NIMB). 2018.

[STD+17] R. Silwal, E. Takacs, J. M. Dreiling, J. D. Gillaspy, and Yu. Ralchenko. Identification and Plasma Diagnostics Study of Extreme Ultraviolet Transitions in Highly Charged Yttrium. *Atoms*, 5(3), 2017.

[SW90] J.F. Seely and R. A. Wagner. QED contributions to the 3s-3p transitions in highly charged Na-like ions J. *Physical Review A*, 41(9), 1990.

[TEO+17] K. Tsukada, A. Enokizono, T. Ohnishi, K. Adachi, T. Fujita, M. Hara, M. Hori, T. Hori, S. Ichikawa, K. Kurita, K. Matsuda, T. Suda, T. Tamae, M. Togasaki, M. Wakasugi, M. Watanabe, and K. Yamada. First Elastic Electron Scattering from 132Xe at the Scrit facility. *Physical Review Letters*, 118(26):262501, 2017.

[TKB+15] E. Takacs, T. D. Kimmel, K. H. Brandenburg, R. K. Wilson, A. C. Gall, J. E. Harriss, and C. E. Sosolik. Diagnostic measurements of CUEBIT based on the dielectronic resonance process. *AIP Conference Proceedings*, 1640(154), 2015.

[TSC+03] I. I. Tupitsyn, V. M. Shabaev, J. R. Crespo López-Urrutia, I. Draganić, R. Soria Orts, and J. Ullrich. Relativistic calculations of isotope shifts in highly charged ions. *Physical Review A - Atomic, Molecular, and Optical Physics*, 68(2):5, 2003.

[VIT06] M. J. Vilkas, Y. Ishikawa, and E. Träbert. Relativistic multireference many-body perturbation theory calculations on F-, Ne-, Na-, Mg-, Al-, Si- and P-like xenon ions. *Journal of Physics B: Atomic, Molecular and Optical Physics*, 39(9):2195–2216, 2006.

[WCNS09] Glenn M. Wahlgren, Kenneth G. Carpenter, Ryan P. Norris, and Eric Stempels. Heavy Elements and Cool Stars. *AIP Conference Proceedings*, pages 892–895, 2009.

[ZH12] Y. Zou and R. Hutton. *Handbook on Highly Charged Ion Spectroscopic Research*. CRC Press, Boca Raton, FL, 2012.

[ZM91] G. Zhao and P. Magain. Abundances of neutron capture elements in metal-poor dwarfs I. Yttrium and zirconium *. *Astron. Astrophys.*, 244:425–432, 1991.

[ZST+84] J.D. Zumbro, E.B. Shera, Y. Tanaka, C.E. Bemis Jr., R.A. Naumann, M.V. Hoehn, and M.V. Reuter. E2 and E4 Deformations in 233,234,235,238U. *Physical Review Letters*, 53(20):1888–1892, 1984.